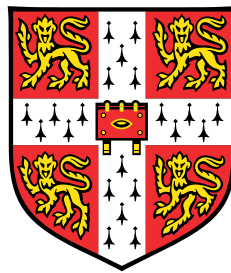


Characterizing sub-mm observations of protoplanetary disks at super-resolution scales



Jeffrey Michael Jennings

Department of Astronomy
University of Cambridge

This dissertation is submitted for the degree of
Doctor of Philosophy

Trinity Hall College

July 2022

Declaration

This thesis is the result of my own work and includes nothing which is the outcome of work done in collaboration except as declared in the Preface and specified in the text. I further state that no substantial part of my thesis has already been submitted, or, is being concurrently submitted for any such degree, diploma or other qualification at the University of Cambridge or any other University or similar institution except as declared in the Preface and specified in the text. It does not exceed the prescribed 60,000 word limit for the Physics & Chemistry Degree Committee, including summary/abstract, tables, footnotes, and appendices.

Jeffrey Michael Jennings

July 2022

Abstract

Characterizing sub-mm observations of protoplanetary disks at super-resolution scales Jeffrey Michael Jennings

Current advancements in telescope and instrumentation technology enable us to observe planets as astrophysical objects across epochs that span Gyr of evolution, from their formation in protoplanetary disks and continued growth in debris disks to their dynamical evolution in exoplanetary systems and ultimate accretion onto white dwarfs. Measurements in each of these eras can be used to inform study in the others. Interferometry affords the highest angular resolution of any observing technique in astronomy, and the use of radio interferometry with instruments such as the Atacama Large Millimeter Array (ALMA) and the Karl G. Jansky Very Large Array (VLA) is markedly advancing the protoplanetary disk field. By further improving our methods to reconstruct high fidelity (in terms of both resolution and sensitivity) images from the interferometric observable, we can not only characterize these disks, but detect the dynamical effects of planets within them. Over a large ensemble of sources, this offers the potential to both progress disk science and connect inferences on the embedded planet population to the study of these objects in later epochs.

This thesis centers on a new imaging framework for radio interferometric observations and its specific application to detect and characterize substructures in protoplanetary disks. Chapter 1 introduces the basics of protoplanetary disk theory and observations, with a focus on the principles of radio interferometry and its application for disk science. Chapter 2 then presents Frankenstein (`frank`), the open source code we have developed and applied to fit sub-mm observations of disks in order to search for substructure. Chapter 3 applies `frank` to the high resolution (30 mas) DSHARP mm sample of 20 disks to identify new substructure in these sources and more accurately constrain known disk features. Major results include discovery of more structured inner disks (at separations within 30 au of the host star). In Chapter 4 we apply `frank` to the moderate resolution (120 mas) Taurus mm survey, finding that compact disks (those with radii <50 au) routinely exhibit substructure. Chapter 5 concludes by summarizing the `frank` algorithm and our novel scientific results with this tool, then places this evolving imaging approach in the context of future disk science.

To my mom – though I don't say it enough, it's no less true; your selfless love both grounds
and inspires me.

Acknowledgements

So many people have devoted their time and energy to teach and support me, more even than I remember. Emily, Scott, Gabe, AJ, Ryan, Barbara, Giovanni, Tommaso, Eric, Rodrigo, Cathie, Richard, Marco. I'm grateful to each of them, and together they've given me an immense motivation to do the same for others.

Table of contents

List of figures	xv
1 Introduction: Protoplanetary disks and radio interferometry	1
1.1 Theory and observation of protoplanetary disks	1
1.1.1 Theory of disk structure and evolution	2
1.1.1.1 Disk formation	2
1.1.1.2 Gas disk evolution	3
1.1.1.3 Dust disk evolution	4
1.1.1.4 Dynamics of a disk-embedded planet	5
1.1.1.5 Disk dispersal	7
1.1.2 Observational tracers of disk structure	7
1.2 Basics of radio interferometry	8
1.2.1 Measurement with an interferometer	8
1.2.2 Indirect imaging and image restoration	9
1.2.2.1 The CLEAN algorithm	9
1.2.2.2 Super-resolution imaging	10
1.3 Radio interferometry for disk observations	12
1.3.1 Observed dust disk substructures in the sub-mm	12
1.3.2 Inferring the presence of embedded planets from substructures	13
1.3.3 Connecting disk and exoplanet observations	15
2 Frankenstein: Protoplanetary disk brightness profile reconstruction at sub-beam resolution with a rapid Gaussian process	19
2.1 Background	20
2.2 Model	21
2.2.1 Representing the brightness profile as a Fourier-Bessel series	22
2.2.2 Fitting the visibilities using the discrete Hankel transform	25
2.2.3 Regularizing the fit using a nonparametric Gaussian process	28

2.2.4	Jointly inferring the brightness profile and power spectrum parameters	30
2.2.5	p_{MAP} and its use as a prior on I_ν	33
2.2.6	The reconstructed brightness profile’s sensitivity to the hyperparameters	39
2.2.7	Model limitations	41
2.2.8	Code performance	44
2.3	Demonstration & analysis	44
2.3.1	Demonstration on mock observations	44
2.3.1.1	Fits can attain sub-beam resolution	44
2.3.1.2	Baseline-dependent signal-to-noise determines the achievable fit resolution	49
2.3.2	Demonstration on real observations	51
2.3.2.1	Sub-beam fits: Characterizing fine structure in real, high resolution observations	51
2.3.2.2	A dataset’s effective resolution can be much less than the longest baseline	56
2.3.2.3	Sub-beam fits: Identifying underresolved features in real, moderate resolution observations	56
2.4	Conclusions	61
2.5	Appendix A: Spectral smoothness hyperprior	64
2.6	Appendix B: Signal-to-noise threshold	65
2.7	Appendix C: Nonnegative fits	67
2.8	Appendix D: Mock disk functional forms	69
3	A super-resolution analysis of the DSHARP survey: Substructure is common in the inner 30 au	71
3.1	Background	72
3.2	Model	72
3.2.1	Point source-corrected fits	74
3.2.2	Model limitations	75
3.3	Methodologies – Assessing effective CLEAN resolution and fit accuracy	78
3.3.1	CLEAN model and image resolution	78
3.3.2	Using the visibilities to quantify the accuracy of CLEAN model, CLEAN image, and frank brightness profiles	81
3.3.3	A general note on comparing frank to CLEAN	87
3.4	Results	87
3.5	Analysis	88
3.5.1	The compact DSHARP disks all show substructure	89

3.5.2	Extended disks show brighter rings, deeper gaps, and hints of inner disk substructure	91
3.5.3	Two of the oldest DSHARP disks appear to have inner cavities	91
3.5.3.1	Improved constraints on dust trapping	94
3.5.4	Spiral arms appear to extend into the spiral disks' cores	95
3.5.5	The most structured DSHARP sources have morphologically similar inner disks	97
3.5.6	Deep gap morphologies in frank profiles potentially indicate embedded planets	98
3.5.7	A geometric viewing effect traces disk vertical structure	98
3.6	Conclusions	101
3.7	Appendix A: Point source-corrected fits	104
3.8	Appendix B: Residual image brightness asymmetries	106
4	Super-resolution trends in the ALMA Taurus survey: Structured inner disks and compact disks	109
4.1	Background	110
4.2	Model	111
4.2.1	Data reduction	112
4.3	Methodologies – Advantages and limitations of a 1D, nonparametric visibility fit	113
4.3.1	Advantages – A highly accurate fit to the observed data	113
4.3.2	Limitations – Extrapolating the fit to unobserved baselines	117
4.3.3	Limitations – Distinguishing azimuthally symmetric from asymmetric substructure	118
4.4	Results & Analysis	119
4.4.1	New substructure in compact disks	125
4.4.1.1	Occurrence rate of substructure in compact disks	127
4.4.2	New substructure in extended disks	128
4.4.2.1	Sources with an inner and outer disk	128
4.4.2.2	Sources with an apparent inner cavity	135
4.5	Conclusions	138
4.6	Appendix A: Effect of phase center uncertainty on imaged frank residuals	139
4.7	Appendix B: Parametric fit to DL Tau	142
4.8	Appendix C: frank fit to high resolution observations of CI Tau	145

5	Conclusions	147
5.1	The frank modeling framework and scientific applications	147
5.2	The role of super-resolution imaging in future disk science	148
	References	151

List of figures

1.1	Imaging a protoplanetary disk with radio interferometry	2
2.1	frank: Fourier-Bessel series representation of a brightness profile	24
2.2	frank: Fit regularization	26
2.3	frank: Model framework	33
2.4	frank: Effect of the hyperparameter w_{smooth}	34
2.5	frank: Effect of the hyperparameter α ; effect of a Jeffreys prior	37
2.6	frank: Underestimated model uncertainty	43
2.7	frank: Performance on different disk morphologies using mock observations	45
2.8	frank: Fit methodology using mock observations	48
2.9	frank: Fit sensitivity to baseline-dependent SNR using mock observations	50
2.10	frank: Fit to real, high resolution observations – AS 209	52
2.11	frank: Fit sensitivity to hyperparameters – AS 209	55
2.12	frank: CLEAN model profile extraction – AS 209	57
2.13	frank: Comparison of moderate and high resolution fits – AS 209	59
2.14	frank: Snapshot from an animation of AS 209 fit evolution with baseline .	60
2.15	frank: Fit to real, moderate resolution observations – DR Tau	62
2.16	frank: Fit sensitivity to hyperparameters – DR Tau	63
2.17	frank: Comparison of standard and nonnegative fits	68
3.1	DSHARP: Effect of CLEAN beam convolution (and other factors) on substructure recovery	77
3.2	DSHARP: CLEAN and frank fit accuracies	80
3.3	DSHARP: Recovered brightness profiles	84
3.4	DSHARP: Visibility fits at long baseline	85
3.5	DSHARP: Substructure in compact disks	90
3.6	DSHARP: Substructure in extended disks	92
3.7	DSHARP: Evidence for inner cavities	93

3.8	DSHARP: Tracing spiral arms into their disk's cores	97
3.9	DSHARP: Highly structured disks	99
3.10	DSHARP: Morphologies for deep and structured gaps	100
3.11	DSHARP: A geometric viewing effect tracing disk vertical structure	102
3.12	DSHARP: Effects of a point source-corrected fit	105
3.13	DSHARP: frank imaged residuals	108
4.1	Taurus: Improved visibility fit accuracy better resolves disk structure	113
4.2	Taurus: frank brightness profile accuracy decreases as a ring becomes increasingly super-resolution	114
4.3	Taurus: Low contrast, asymmetric substructure emulates an underresolved annular ring in a brightness profile	116
4.4	Taurus: Improved visibility model accuracy in frank fits to compact disks .	120
4.5	Taurus: Improved visibility model accuracy in frank fits to extended disks	121
4.6	Taurus: New substructure in frank fits to compact disks	122
4.7	Taurus: Noisy visibility distributions for compact disks	123
4.8	Taurus: New substructure in frank fits to extended disks with outer rings .	129
4.9	Taurus: CLEAN image asymmetries	130
4.10	Taurus: Ten Gaussian parametric fit to DL Tau	131
4.11	Taurus: New substructure in frank fits to extended disks with cavities . . .	132
4.12	Taurus: Shoulder morphology in high resolution observations	133
4.13	Taurus: Effect of fitted phase center on imaged residual visibilities	140
4.14	Taurus: Varying the phase center to minimize the imaged residual visibilities	141
4.15	Taurus: Corner plot for parametric fit to DL Tau	144
4.16	Taurus: frank fit to high resolution CI Tau observations	146

Chapter 1

Introduction: Protoplanetary disks and radio interferometry

This thesis will focus on a new technical tool we have developed for aperture synthesis, i.e., interferometric imaging, in radio astronomy, with scientific application to protoplanetary disks. **Fig. 1.1** shows three realizations of an image for the DL Tau disk in the Taurus star-forming region, observed at 1.33 mm with ALMA, the Atacama Large Millimeter/submillimeter Array. These realizations demonstrate both the remarkable observational capability of the instrument and the challenge of aperture synthesis. The left panel of Fig. 1.1 shows the raw Fourier transform of the interferometric observable (native to the Fourier domain), which contains artifacts due to convolution of the on-sky brightness with the instrument's point spread function. The middle panel shows an image realization with the standard community modeling technique, CLEAN. And the right panel shows the resolving power of 'super-resolution' imaging using the tool presented in this work, frank.

In Sec. 1.1 of this chapter I begin with an overview of basic disk theory and what observations across wavelength regimes have taught us about these objects thus far. Focusing on the utility of radio interferometric observations, I then summarize the principles of radio interferometry and the techniques to image interferometric observations in Sec. 1.2. Lastly in Sec. 1.3 I describe how we can use interferometry at mm and cm wavelengths to learn about disk structure and the disk-embedded planet population.

1.1 Theory and observation of protoplanetary disks

I will begin with a summary of how disks form and evolve (in both the gas and dust), as well as how a planet interacts with the disk, and how the gas disk ultimately disperses.

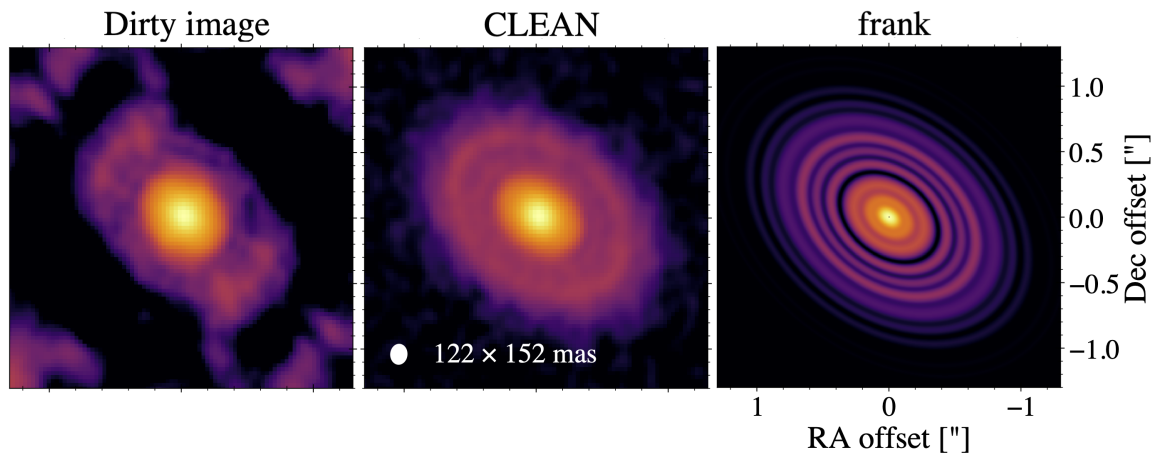


Fig. 1.1. Imaging a protoplanetary disk with ALMA

Left: The dirty image (Sec. 1.2.2) of the protoplanetary disk DL Tau, observed at 1.33 mm with ALMA.

Middle: A realization of the on-sky brightness produced by applying the CLEAN nonlinear deconvolution algorithm (Sec. 1.2.2.1) to the dirty image.

Right: A pseudo-2D realization of the on-sky brightness using the super-resolution tool frank (Chapter 2).

1.1.1 Theory of disk structure and evolution

1.1.1.1 Disk formation

Following the onset of gravitational collapse in a molecular cloud core in hydrostatic disequilibrium, the cold (≈ 10 K) and dense (molecule number density $\sim 10^6$ cm $^{-3}$) gas forms a protostar. The residual surrounding gas, if it had zero net angular momentum, would then fall radially onto the star, acted upon solely by the gravitational force F_g . However a gas parcel with nonzero angular momentum will additionally feel a centrifugal force F_c , and the net force directs it into the plane perpendicular to the cloud's angular momentum vector at the radial location where $F_g = F_c$. This is the centrifugal radius, $r_c = GM_*/\omega_c^2$. The aggregate result of this non-radial infall over all gas parcels, as a consequence of angular momentum conservation, is coalescence into a rotating protoplanetary disk around the central star (Bate, 2011) with Keplerian angular velocities $\omega_c = \Omega = (GM_*/r_c^3)^{1/2}$. The disk also contains a dust component with relative mass assumed to be the ISM average, $M_{\text{dust}} = 0.01M_{\text{gas}}$, giving a rough dust mass $\sim 1 M_{\text{Jup}}$ in $\sim \mu\text{m}$ grains (assuming a total disk mass $\approx 0.1M_*$). The gas/dust mass ratio may be smaller by virtue of systematically underestimated dust disk masses, given evidence that the inner disk is highly optically thick at observing wavelengths in objects such as TW Hya at ≤ 3.1 mm (Macías et al., 2021).

1.1.1.2 Gas disk evolution

The gas disk secularly evolves due to angular momentum redistribution (Pringle, 1981), with the evolution of an annulus in the disk Δr at radius r understood through mass and angular momentum conservation. For a radial velocity v_r , whose sign is negative radially inward (i.e., for accretion), mass transport through the inner edge of the annulus is (Armitage, 2007)

$$\dot{M}_{\text{in}} = 2\pi r \Sigma(r) v_r(r). \quad (1.1)$$

Mass transport through the annulus' outer edge is

$$\dot{M}_{\text{out}} = 2\pi(r + \Delta r) \Sigma(r + \Delta r) v_r(r + \Delta r), \quad (1.2)$$

and the mass flux through this ring is then

$$\dot{M}_{\text{out}} - \dot{M}_{\text{in}} = 2\pi r \Delta r \frac{\partial \Sigma}{\partial t}. \quad (1.3)$$

In the $\Delta r \rightarrow 0$ limit, the equation of continuity for mass becomes

$$r \frac{\partial \Sigma}{\partial t} + \frac{\partial}{\partial r} (r \Sigma v_r) = 0. \quad (1.4)$$

Applying angular momentum conservation, in the case of a constant torque in the annulus, there is no net angular momentum flux across it,

$$r \frac{\partial}{\partial t} r^2 \Omega \Sigma + \frac{\partial}{\partial r} r^2 \Omega r \Sigma v_r = 0. \quad (1.5)$$

Accounting for a varying torque G , the right-hand side of Equation 1.5 becomes $1/2\pi \partial G / \partial r$. Treating the torque as resulting from a fluid viscosity, G takes the form

$$G = 2\pi r r \nu \Sigma \frac{d\Omega}{dr} r, \quad (1.6)$$

where ν is the kinematic viscosity. Equation 1.5 then becomes

$$\frac{\partial}{\partial t} (r^2 \Sigma \Omega) + \frac{1}{r} \frac{\partial}{\partial r} (r^3 \Sigma v_r \Omega) = \frac{1}{r} \frac{\partial}{\partial r} \left(r^3 \nu \Sigma \frac{d\Omega}{dr} \right). \quad (1.7)$$

Taking the mass and angular momentum continuity equations together and assuming Keplerian rotation gives a diffusion equation for the viscous evolution of the disk,

$$\frac{\partial \Sigma}{\partial t} = \frac{3}{r} \frac{\partial}{\partial r} \left[r^{1/2} \frac{\partial}{\partial r} (\nu \Sigma r^{1/2}) \right]. \quad (1.8)$$

A solution to this equation can be expressed as (Lynden-Bell and Pringle, 1974)

$$\Sigma(r, t) = \frac{M_d(2-\gamma)}{2\pi r_0^2 r^\gamma} \tau^{-(5/2-\gamma)/(2-\gamma)} \exp\left(-\frac{r^{2-\gamma}}{\tau}\right), \quad (1.9)$$

where γ is a dimensionless parameter of order unity to encapsulate the power law relation between viscosity and radius, M_d the disk mass, and $R = r/r_0$, where r_0 is a scaling radius of order 10 au. $\tau = t/t_v + 1$ is a characteristic dimensionless time defined using the diffusion timescale ('viscous time'), $t_v \approx r^2/\nu$. This is the time for viscous evolution to perturb the local surface density by a factor of order unity, and in the absence of other processes, the disk evolves on the viscous timescale of its outermost radius. The physical origin of viscosity in accretion disks is an open question; most often turbulence is evoked, with the α -disk prescription of Shakura and Sunyaev (1973) approximating the viscosity as $\nu = \alpha c_s H$, where c_s is the local isothermal sound speed and H the disk scale height. Here $\alpha \leq 1$, with a range of $\alpha \sim 10^{-4} - 10^{-2}$ typically used in disk models.

Two central implications of these relations for the gas disk are: 1) $\Sigma(r) \propto r^{-\gamma}$ and thus the gas disk has an effective maximum radius beyond which the gas surface density is several orders of magnitude below its value in the inner disk, and 2) the gas disk evolves by mass flow inward (accretion at a rate $\dot{M}_{\text{acc}} = M_d(r)/t_v(r)$) and therefore angular momentum transport outward (carried by a trivial fraction of the disk mass), with $\Sigma(t)$ falling as a power law $\Sigma \propto \dot{M} t^{-x}$ (Hartmann et al., 1998).

1.1.1.3 Dust disk evolution

Analogous to the diffusion equation for the evolution of the gas disk, the governing equation for the dust disk evolution must include terms for turbulent diffusion and the dust radial drift. This drift is a consequence of a negative radial pressure gradient dP/dr in the gas that causes it to orbit at a sub-Keplerian speed; dust particles massive enough to decouple from the gas orbit at the local Keplerian speed, thus feeling a headwind – a drag force due to the gas that extracts angular momentum, resulting in inward radial drift.

Here we will neglect the effects of collisions leading to grain growth and fragmentation (and a discussion of the processes involved in dust coagulation, planetesimal and planet

formation generally) for brevity. The dust evolves as

$$\frac{\partial \Sigma_{\text{dust}}}{\partial t} = \frac{1}{r} \frac{\partial}{\partial r} \left[R \Sigma_{\text{dust}} v_{\text{drift}} - D R \Sigma_{\text{g}} \frac{\partial}{\partial r} \left(\frac{\Sigma_{\text{dust}}}{\Sigma_{\text{gas}}} \right) \right], \quad (1.10)$$

where the first term describes radial drift of the dust, v_{drift} being the radial drift velocity; and the second term describes turbulent diffusion (Birnstiel et al., 2010; Clarke and Pringle, 1988), where D is the dust diffusion coefficient (often equated to the gas kinematic viscosity ν).

v_{drift} can be calculated as (Takeuchi and Lin, 2002)

$$v_{\text{drift}} = \frac{\text{St}^{-1} v_{\text{gas}} - \eta v_{\text{k}}}{\text{St} + \text{St}^{-1}}, \quad (1.11)$$

where v_{gas} is the radial velocity of the gas induced by accretion and $v_{\text{k}} = (GM_*/r)^{1/2}$ the Keplerian velocity. $\text{St} = \pi a_{\text{dust}} \rho_{\text{dust}} / (2 \Sigma_{\text{gas}})$ is the Stokes number of a dust grain of radius a_{dust} and bulk density ρ_{dust} . This quantifies the strength of coupling between the gas and dust as the ratio $\text{St} = \tau_{\text{stop}} / \tau_{\text{eddy}}$ (Birnstiel et al., 2010). A grain's stopping time τ_{stop} is the ratio of its momentum to the drag force on it ($F_{\text{drag}} = -m \Delta u / \tau_{\text{stop}}$, where m is the grain's mass and Δu its velocity relative to the gas). $\tau_{\text{eddy}} = 1 / \Omega_{\text{k}}$ is the eddy turnover time that quantifies the amount of turbulence in the medium (the equality belies some simplifying assumptions). Thus $\text{St} = \tau_{\text{stop}} \Omega_{\text{k}}$; smaller dust grains have lower Stokes numbers and are well coupled to the gas, while larger grains orbit nearer to the Keplerian velocity. Because the gas orbits at sub-Keplerian speed, larger grains feel a stronger headwind and drift inward approaching their radial terminal velocity. Finally η measures the importance of the pressure gradient with respect to gravity and is given by

$$\eta = - \left(\frac{H}{R} \right)^2 \left(\frac{d \log \Sigma_{\text{gas}}}{d \log R} + (\zeta - 3) \right), \quad (1.12)$$

where H/R is the disk aspect ratio and $\zeta = 5/4$ assuming a flared disk, i.e., the aspect ratio increases with radius.

1.1.1.4 Dynamics of a disk-embedded planet

Observations find a stark absence of disks with inferred ages beyond \approx few – 5 Myr (Haisch et al., 2001), with disks older than \approx 5 Myr showing upper limits of $\Sigma \leq 10^{-5} \text{ g cm}^{-2}$ (Ingleby et al., 2009), implying gas loss is almost total. Gas giant planets thus have a brief, few Myr window to form their cores and accrete their envelopes, placing an upper bound on

the timescale for (giant) planet formation processes. Key aspects of planet formation and early orbital evolution are not yet well understood, from the mechanism that initiates planet formation (for recent reviews see [Armitage, 2018](#); [Morbidelli and Raymond, 2016](#)) to the rate of planet migration as a function of planet mass (for a review see [Nelson, 2018](#)).

While planet formation is beyond the scope of this work, a brief overview of disk-planet dynamics is useful for appreciating how a planet can perturb the disk structure. In the presence of a giant planet that is migrating in a disk, Equation 1.8 for the evolution of the gas disk becomes

$$\frac{\partial \Sigma}{\partial t} = \frac{3}{r} \frac{\partial}{\partial r} \left[r^{1/2} \frac{\partial}{\partial r} (\nu \Sigma r^{1/2}) - \frac{2\Lambda \Sigma r^{3/2}}{(GM_*)^{1/2}} \right], \quad (1.13)$$

where we recall the first term on the right-hand side describes the viscous evolution of the disk, while the added second term describes the migration of the planet due to torques from the disk [Lin and Papaloizou \(1986\)](#). Λ is the rate of specific angular momentum transfer from the planet to the disk, which can be expressed – using the modification by [Armitage et al. \(2002\)](#) to the form proposed by [Lin and Papaloizou \(1986\)](#) – as

$$\Lambda(r, a) = \begin{cases} \frac{-Q^2 GM_*}{2r} \left(\frac{r}{\Delta_p} \right)^4 & r < a \\ \frac{Q^2 GM_*}{2r} \left(\frac{a}{\Delta_p} \right)^4 & r > a. \end{cases} \quad (1.14)$$

Here Q is the mass ratio between the planet and the star, a is the semimajor axis of the planet’s orbit (assumed to be circular), and $\Delta_p = \max(H, |R - a|)$; H is the disk scale height.

When the planet mass exceeds the local thermal mass in the disk (typically $\gtrsim 1 M_J$), the body can dynamically clear the dust and gas in its orbit, carving a gap of width Δ , with $1 r_H \lesssim \Delta \lesssim 4 r_H$ (e.g., [Baruteau et al., 2014](#); [Duffell and MacFadyen, 2013](#); [Kley and Nelson, 2012](#); [Takeuchi et al., 1996](#)). Here r_H is the planet’s Hill radius, $r_H = a [m_p / (3M_*)]^{1/3}$, with a and m_p its semimajor axis and mass. The gap width depends not only on the planet mass but also the Stokes number of the local dust grain population, with $St \propto \Sigma_{\text{gas}}^{-1}$. Perturbations in the gas can induce local pressure maxima that trap and accumulate inwardly migrating dust grains in the $St \gtrsim 0.1$ regime (smaller dust grains are well coupled to the gas and thus do not ‘see’ the trap). This in turn causes a measured gap width that is narrower for $St \approx 0.1$ particles and broader for those with $St \approx 1.0$ (whose surface density distribution is more sharply peaked in the trap).

1.1.1.5 Disk dispersal

One may expect that accretion of disk gas onto the central star drives much if not all of the protoplanetary disk's evolution; as noted in [Armitage \(2015\)](#), a disk with initial mass $M_d \approx 5 \times 10^{-3} M_\odot$ (the median disk mass in the Taurus cluster, [Andrews and Williams, 2005](#)) and accretion rate $\dot{M} \approx 10^{-8} M_\odot \text{ yr}^{-1}$ suggests a viscous evolution timescale of 0.5 Myr. While this simple result is subject to order-of-magnitude uncertainties, the larger question in this context is the relative paucity of observed stars with weak (i.e., optically thin) disk indicators; if the disk viscosity scales as $\nu \propto r^\gamma$, the surface density should scale as in Equation 1.9, namely $\Sigma \propto \tau^{-(5/2-\gamma)/(2-\gamma)}$, such that for $\gamma = 1$ (corresponding to $\Sigma \propto r^{-1}$), $\Sigma \propto \tau^{-3/2}$. This gradual decline predicts a continuum of observations from young, massive, optically thick disks to old, depleted, optically thin disks. Such a population is inconsistent with the aforementioned observational absence of disks older than $\approx \text{few} - 5$ Myr. Physical mechanisms are thus invoked to initiate rapid gas disk dispersal, typically one or both of photoevaporative (e.g., [Clarke et al., 2001](#)) and magnetohydrodynamic winds (e.g., [Bai et al., 2016](#)).

Planetesimals are decoupled from the gas and thus not entrained in a potential dispersive wind, remaining in orbit around the central star. At this point the system transitions to the debris disk regime, wherein planetesimal belts collisionally erode while also gravitationally interacting with planets and dwarf planets formed during the gas disk phase ([Wyatt, 2018](#)).

1.1.2 Observational tracers of disk structure

While the gas comprises the bulk of the disk by mass, it is difficult to observe because it is predominantly molecular hydrogen, which has no permanent dipole moment and thus shows no bright emission lines ([Williams and Cieza, 2011](#)). Emission lines from more complex molecules such as CO ([Dutrey et al., 2014](#); [Öberg et al., 2021](#), e.g.,) offer some information on the gas. The rate of gas accretion onto the stellar surface gives the most readily available insight, with observed accretion rates of $10^{-9} - 10^{-7} M_\odot \text{ yr}^{-1}$ that decrease over the $\approx \text{few}$ Myr of the gas disk lifetime ([Manara et al., 2016](#)).

The dust component of the disk is substantially easier to observe and strongly influences the gas temperatures throughout the disk; the dust grain size distribution and number density, both as a function of radius in the disk and scale height, are the primary determinants of the disk opacity. Observable dust diagnostics span multiple wavelength regimes. While the infrared ($\sim 1 \mu\text{m}$) can probe dust thermal emission in the optically thick, hot (few 10^2 K) region of the disk within ≈ 1 au of the star (as well as scattered light out to much larger radii), the sub-mm – mm ($\approx 0.3 - 3$ mm) traces dust thermal emission in the (generally) optically

thin, cold (~ 10 K) outer disk midplane. It is this continuum emission observed with radio interferometry – namely the accurate modeling of these observations – that will be the focus of the thesis.

1.2 Basics of radio interferometry

Because this thesis centers on modeling radio interferometric observations of disks, I will give a technical overview here of the measurement technique in general, then examine in more depth the step of producing an image of the field of view on the sky.

1.2.1 Measurement with an interferometer

A synthesis array of radio telescopes is effectively composed of several pairs of antennae, each forming an interferometer. Each interferometer measures the spectral power flux density [units: $1 \text{ Jy} = 10^{-26} \text{ W m}^{-2} \text{ Hz}^{-1}$] of a source on the sky. The flux density emitted per unit solid angle subtended by the astrophysical source [Jy sr^{-1}] is the specific intensity I_ν , the brightness, in two dimensions. This is the real space representation of the source, while the interferometric measurement is native to the Fourier domain, with complex-valued visibilities observed at discretized spatial frequencies (Clark, 1999; Thompson, 1999; Thompson et al., 2017). The visibility function V_ν of a source as sampled by an interferometer is the 2D Fourier transform of the source brightness (Cornwell et al., 1999),

$$V_\nu(u, v) = \int \int_S I_\nu(l, m) \exp(-2\pi i(ul + vm)) \, dl dm. \quad (1.15)$$

Here S indicates the region of the sky over which the integral is taken (which is assumed to be small, such that $|l^2 + m^2| \ll 1$); and $I_\nu(l, m)$ is the 2D sky brightness at real space antenna coordinates (l, m) and corresponding Fourier domain coordinates (u, v) . (l, m) are measured in radians, (u, v) in the observing wavelength λ . The (u, v) plane is normal to the source direction, with u oriented east–west and v north–south. The visibilities are measured in Jy, with their amplitude giving the intensity and their phase the position of emission on a given angular scale. The source’s intensity distribution in the image plane is reconstructed by inverse Fourier transforming the visibilities.

The largest synthesis array for protoplanetary disk science is ALMA, the Atacama Large Millimeter/submillimeter Array. This collection of two-element interferometers is capable of angular resolution exceeding that of the largest single dishes in radio astronomy by a significant factor. Observations at 1.3 mm with a $D = 100$ m diameter antenna have an angular

resolution $R \approx 1.2\lambda/D = 3.2''$, while ALMA's angular resolution in the array's most extended configuration is $0.018''$, a factor of ≈ 150 improvement. In the limit of a well-sampled visibility plane, the instrument's angular resolution is set by the longest 'baseline,' i.e., antenna pair separation – the effective dish diameter $\sqrt{u^2 + v^2}$, in a given configuration of the synthesis array. The baseline is often given in units of λ , obtained by normalizing the physical distances between antennas by the observing wavelength. The largest antenna separation currently obtainable, 16 km, corresponds to a baseline of $12.3 M\lambda$ at an observing wavelength of 1.3 mm.

1.2.2 Indirect imaging and image restoration

The challenge in using an interferometric measurement to reconstruct the observed 2D sky brightness (or even 1D) is that the instrument response function resides in the Fourier domain, where the observations are an incomplete (sparse) representation of the source, sampled only at individual spatial frequencies. The reconstruction of a model image from an interferometric measurement by inverse Fourier transforming the visibilities thus requires some methodology to infer visibility amplitudes at the unsampled spatial frequencies. A direct inverse Fourier transform of the weighted visibilities at sampled spatial frequencies (and thus an assumption of zero power on unsampled scales) yields a 'dirty image.' This image is equivalent to the sky brightness convolved with the instrument's point spread function (PSF; 'dirty beam'). The dirty beam is generated from the inverse Fourier transform of the weighted (u, v) distribution. This convolution introduces artifacts into the dirty image due to the PSF's significant sidelobe structure. The standard approach in the protoplanetary disk field for reconstructing images is the inverse modeling CLEAN nonlinear deconvolution algorithm (Clark, 1980; Cornwell, 2008; Högbom, 1974). Super-resolution methods, i.e., those that can yield an image with resolution exceeding that in a CLEAN image, include forward modeling regularized maximum likelihood techniques that operate in the image plane, such as the maximum entropy method (e.g., Narayan and Nityananda, 1986); and forward modeling by fitting a model directly to the visibilities.

1.2.2.1 The CLEAN algorithm

The CLEAN algorithm is a nonlinear, procedural approach to remove artifacts of the PSF in the dirty image through 'deconvolution,' constructing an empirical model for the sky brightness using the dirty image. To do this, CLEAN begins with a 'residual image' that is equal to the dirty image, then iteratively: finds the brightest pixel in the residual image; adds a fraction of this brightness amplitude, a CLEAN 'component' – typically a point source (Dirac δ function)

or a Gaussian (Abrantes et al., 2009) – to the ‘CLEAN model’ (an image composed only of the CLEAN components); and subtracts this component convolved with the dirty beam from the residual image. The iteration proceeds until ideally the residual image contains only noise. At the end of this iteration, the CLEAN model is convolved with the ‘CLEAN beam’ (typically an elliptical Gaussian fit to the primary lobe of the dirty beam) in order to suppress the extrapolation of the model to scales below the beam (Cornwell et al., 1999). The final state of the residual image is then added to this to form the ‘CLEAN image’ commonly presented as the astronomical observation.

While the CLEAN algorithm is the standard and highly successful technique used across much of radio interferometry, the procedure imposes artificial resolution loss in image reconstruction, primarily due to convolution of the CLEAN model with the CLEAN beam. This causes all features in the CLEAN image, regardless of their scale, to be smeared in resolution over the size of the beam (the effect is most severe for sub-beam structures, but still alters even those resolved by the beam). Deprojecting and azimuthally averaging a CLEAN 2D model image is the most common technique used to obtain a 1D (radial) brightness profile of a source, which is often useful to characterize substructure in a protoplanetary disk. However, convolution with the CLEAN beam induces a reduction in amplitude of all disk substructures, an overestimate of ‘ring’ (annular brightness excess) widths, and an underestimate of ‘gap’ (annular brightness deficit) widths. CLEAN beam convolution thus places an intrinsic resolution limit on brightness profile extraction from the disk image. And as I will show in subsequent chapters, even the CLEAN model itself (the collection of CLEAN components) is in practice often at sub-optimal resolution.

1.2.2.2 Super-resolution imaging

‘Super-resolution’ imaging techniques can overcome the resolution limits of the CLEAN algorithm. By ‘super-resolution’ I mean an achieved fit resolution higher than the achieved CLEAN resolution, which I will subsequently quantify as distinct from the CLEAN beam width. These methods thus have the capacity to provide new insights into a source’s substructure *from existing datasets*, better informing physical inference and follow-up observing strategies.

Super-resolution fitting techniques used in (and in some cases tailored to) the protoplanetary disk field can be divided into image plane and Fourier domain approaches. Image plane procedures include the maximum entropy method (Casassus et al., 2006, 2013; Chael et al., 2016; Gull and Daniell, 1978; Narayan and Nityananda, 1986; Sutton and Wandelt, 2006) and sparse modeling (Akiyama et al., 2017; Honma et al., 2014; Kuramochi et al., 2018; Nakazato et al., 2019), with the broad class of regularized maximum likelihood techniques being actively used in Very Long Baseline Interferometry (Event Horizon Telescope Collaboration

et al., 2019, and references therein) and for application to protoplanetary disks (Czekala et al., 2021). Fourier domain approaches include fitting the visibilities parametrically (Perkins et al., 2015; Tazzari et al., 2018) and nonparametrically (Jennings et al., 2020).

An alternative approach to CLEAN is the forward modeling class of regularized maximum likelihood methods (RML). RML techniques for image reconstruction in radio interferometry have been used for decades (e.g., Ables, 1974; Cornwell and Evans, 1985; Gull and Daniell, 1978) and have recently evolved rapidly, driven largely by their application to Event Horizon Telescope (EHT) observations and intent to apply them to Next Generation Very Large Array (ngVLA) observations (e.g., Akiyama and Matthews, 2019; Chael et al., 2016; Honma et al., 2014; Johnson et al., 2017; Lu et al., 2014). The broad approach is to construct an image (among the infinite set of images consistent with the sparsely sampled visibilities) that simultaneously maximizes the likelihood (minimizes χ^2) and minimizes an additional constraint, such as the pixel brightness or image entropy (Event Horizon Telescope Collaboration et al., 2019; Narayan and Nityananda, 1986). Importantly, RML methods have demonstrated success in attaining sub-beam resolution, including in the EHT observations of M87 (Event Horizon Telescope Collaboration et al., 2019).

A second alternative to CLEAN is to directly fit a forward model in the visibility domain. This avoids the resolution loss from beam convolution in CLEAN by inferring the unconvolved brightness distribution. Current forward models of this type (e.g., the `galario` code of Tazzari et al., 2018) require the user to specify a parametric functional form for the brightness profile (existing applications include the disks AS 209 and CI Tau; Clarke et al., 2018a; Fedele et al., 2017; Guzmán et al., 2018). This approach advantageously allows predictions from physical models that consider disk properties such as the optical depth and temperature to be folded into the visibility fitting through the prescribed function form for the brightness profile. However when the goal is simply to accurately fit the highest resolution information in a dataset, a parametric approach can face practical limitations.

These limitations are most evident with high resolution (baselines $\gtrsim 5 M\lambda$) data, which almost all show fine structure in their visibilities at long baselines. The accuracy of the fit to this structure can strongly influence the recovered profile's identification and accurate characterization of sub-beam features. While there is no intrinsic resolution limit to a parametric fit of the visibilities, choosing a parametric model profile to closely match this long baseline structure is challenging. The functional form is often motivated by the CLEAN image, which for partially resolved, shallow or blended image features is not a trivial choice. Moreover the problem's dimensionality is typically high, making an exploration of multiple model profiles expensive. A disk with a single gap and ring has 15 – 20 free parameters, and more structured disks can require >50 . Parameter inference with a Markov Chain Monte

Carlo (MCMC) sampler in this high dimensional space can take hundreds of CPU hours to converge. By comparison, a nonparametric approach can offer greater flexibility and speed to accurately fit long baseline, highly structured visibility distributions.

1.3 Radio interferometry for disk observations

High resolution interferometric observations in the sub-mm – mm and cm regimes are central to the current generation of disk observations. These observations, with telescopes such as ALMA and the Karl G. Jansky Very Large Array (VLA), trace the disk’s cold, midplane dust distribution through reprocessed starlight (continuum emission) as well as molecular line tracers of the gas disk. Interferometric datasets provide the highest resolution information available on the structure of protoplanetary disks, and in the sub-mm – mm and cm are able to identify substructures in this continuum emission, both in the form of annular and azimuthally asymmetric features. Characterizing these features allows us to examine the planetary companions and/or disk processes responsible. Identifying and accurately characterizing disk substructures is therefore critical to probing the physics of circumstellar accretion disks, planet formation, and early planetary system evolution.

1.3.1 Observed dust disk substructures in the sub-mm

Observations at the highest spatial resolutions with ALMA (beam widths of $\approx 25 - 75$ mas corresponding to $\approx 1 - 10$ au) increasingly show that annular features are common – perhaps ubiquitous – at least in bright disks around single stars (e.g., [ALMA Partnership et al., 2015](#); [Andrews et al., 2018](#); [Andrews et al., 2016](#); [Benisty et al., 2021](#); [Casassus et al., 2021](#); [Cieza et al., 2021](#); [Clarke et al., 2018a,b](#); [Dong et al., 2017, 2018](#); [Hashimoto et al., 2021](#); [Huang et al., 2020](#); [Keppler et al., 2019](#); [Kudo et al., 2018](#); [Macías et al., 2021](#); [Pérez et al., 2019a](#); [Pinte et al., 2019](#); [Sheehan and Eisner, 2018](#); [Tsukagoshi et al., 2019](#)). These results suggest the occurrence rate of symmetric gaps and rings is in the tens of percent. Unbiased disk surveys at moderate resolution support this trend, with annular substructure present in at least 38% (12 / 32) of disks in the Taurus survey at ≈ 120 mas (≈ 15 au; [Long et al., 2018](#)) and hinted at in $\approx 5\%$ (3 / 53) Ophiuchus disks at ≈ 200 mas (≈ 28 au; [Cieza et al., 2019](#)). Several individual disks exhibit multiple concentric gaps and rings (e.g., [Guzmán et al., 2018](#); [Pérez et al., 2019b](#)), with a broad distribution of feature widths from ≈ 1 au in TW Hydra ([Andrews et al., 2016](#)) to several tens of au in high resolution (≈ 4 au) observations of CI Tau ([Clarke et al., 2018a](#)).

Intriguingly, even in the high resolution (35 mas corresponding to ≈ 5 au) DSHARP survey of 20 bright disks, several disk features are only partially resolved (Huang et al., 2018a), suggesting some may even split into multiple substructures. Disks such as AS 209 (Fedele et al., 2018; Guzmán et al., 2018) and HD 169142 (Fedele et al., 2017; Pérez et al., 2019b), which initially showed features at the beam width when observed at moderate resolution, were re-observed at high resolution in DSHARP, with apparently single features in the moderate resolution data in some cases resolving into multiple narrower substructures in the high resolution observations.

Azimuthally asymmetric substructures also occur at a nontrivial rate, seen for example in the DSHARP survey (Andrews et al., 2018; Huang et al., 2018a). This nonaxisymmetric dust substructure takes the form of spirals arms (e.g., Huang et al., 2018b; Kurtovic et al., 2018), azimuthally localized brightness arcs (e.g., Isella et al., 2018; Pérez et al., 2018), warps (e.g., Marino et al., 2015) and kinks (e.g., Flaherty et al., 2013).

1.3.2 Inferring the presence of embedded planets from substructures

Numerous physical mechanisms are capable of producing axisymmetric (and in many cases also asymmetric) substructures in protoplanetary disks, with the list of candidates growing. Categories include forming and newly formed planets (e.g., Goldreich and Tremaine, 1979; Kley and Nelson, 2012; Lin and Papaloizou, 1986), with one system to-date, PDS 70, presenting clear detection of embedded planets (Benisty et al., 2021; Haffert et al., 2019; Keppler et al., 2018; Müller et al., 2018); opacity effects due to ice sublimation fronts (e.g., Hu et al., 2019; Okuzumi et al., 2016; Zhang et al., 2016); gas-dust coupling effects, including preferential dust growth in localized regions (e.g., Dullemond et al., 2018; Pinilla et al., 2012; Sierra et al., 2019), gravitational instability (e.g., Dipierro et al., 2015; Dong et al., 2018; Hall et al., 2018), dynamical effects of a central binary (e.g., Longarini et al., 2021; Price et al., 2018; Ragusa et al., 2017), and internal photoevaporation (e.g., Alexander et al., 2006; Clarke et al., 2001; Ercolano et al., 2009); and magnetic field effects including dead-zone boundaries (e.g., Flock et al., 2015; Pinilla et al., 2016; Varnière and Tagger, 2006), magnetic flux concentration and zonal flows (e.g., Bai and Stone, 2014; Cui and Bai, 2021; Johansen et al., 2009), and the vertical shear instability (e.g., Flock et al., 2017; Manger and Klahr, 2018; Pfeil and Klahr, 2020).

Determining which of these mechanisms dominate in observed systems requires both in-depth studies of individual sources and a large ensemble of disks with accurately characterized substructure. For example, highly accurate characterization of axisymmetric features can place constraints on potential mechanisms for gap and ring creation such as the required dust properties (see applications in, e.g., Clarke et al., 2018a; Dullemond et al., 2018; Fedele

et al., 2018; Rosotti et al., 2016). Precise measurements of gap and ring morphologies – including their widths, depths, and the structure within and on the edges of gaps – could be compared to hydrodynamic simulations of a gap-opening planet (e.g., Meru et al. 2018) to assess whether these features are due to planetary companions. These results could be further paired with additional diagnostics to assess the planet hypothesis, such as the detection of a circumplanetary disk or line emission from gas accretion.

Alternatively, gaps and rings could be produced by disk hydrodynamical processes in the absence of any companion, such as zonal flows that can concentrate magnetic flux in radial annuli to create depletions in the gas and thus yield gaps in the dust, as well as adjacent particle traps that induce rings in the dust (e.g., Simon and Armitage, 2014). In this case measuring the magnetic field strength in the vicinity of gaps/rings would be a discriminating diagnostic. In yet another class of candidate mechanisms for annular features, icelines are condensation fronts at which ice grains sublimate as they drift inward. Modeling of the disk temperature through radiative transfer simulations can predict the radii at which icelines of different species should occur and thus where in the disk rings and adjacent gaps should be present (e.g., van der Marel et al., 2019). Icelines do not require pressure bumps in the gas to trap dust, and thus measurement of the gas radial density profile in disks with annular substructure could test this mechanism for gap/ring formation. Discriminating between so many mechanisms as the origin of substructures will benefit from fully exploiting the resolution and sensitivity information in interferometric datasets.

If as seems increasingly likely planets are responsible for at least some of the observed substructures, accurate quantification of these features could be used jointly with hydrodynamic simulations to infer key planetary properties. These include planet mass derived from either gap width (Akiyama et al., 2016; Rosotti et al., 2016) or location of a detectable gas pressure maximum using multiwavelength observations (de Juan Ovelar et al., 2013; Rosotti et al., 2016), as well as planetary migration rate calculated from spectral indices of the dust emission on either side of the circumplanetary gap in multiwavelength observations (Nazari et al., 2019). From a theoretical perspective this would advance our understanding of planetary interaction with the disk and inform models for planet formation and early dynamical evolution.

While there are promising avenues to characterize planetary properties from disk observations, inferring information from substructures is sensitive to observational and theoretical uncertainties. If as seems plausible, disk processes produce at least some of the observed substructures, misidentification of the origin of these features would contaminate a study on planet properties inferred from gaps and rings. Under the assumption substructures are due to planets, recent hydrodynamic simulations suggest a single planet can interact with the disk to produce a network of multiple gaps and rings (e.g., Bae et al., 2017; Dong et al.,

2017), complicating efforts to discern multiplicity, as well as individual planet masses and orbital radii, in a disk observed with multiple substructures. Moreover [Miranda and Rafikov \(2019\)](#) demonstrate that hydrodynamic models making the simplifying assumption of a locally isothermal equation of state can overestimate the degree to which the planet induces substructures in the disk.

On a methodological front, most studies that seek to match specific disk observations tailor their hydrodynamic simulations to emulate the observed image, including choices for the planet's location and mass, but also the gas disk surface density as a function of radius, the gas disk mass and initial dust-to-gas ratio, the dust size distribution and thus opacities, the disk temperature profile, and the disk viscosity parameter α . While this approach explores a physically reasonable range space in free parameters, choices can be motivated by how well the simulation reproduces the observations, with one of multiple degenerate solutions chosen potentially subjectively. A key way to reduce and mitigate uncertainties is a highly accurate characterization of disk substructures recorded in interferometric datasets.

1.3.3 Connecting disk and exoplanet observations

The mechanisms and conditions in a disk present during planet formation and envelope accretion set the initial physical properties of these bodies and the young, embedded planetary system. At some non-trivial level it seems reasonable to expect that disk conditions imprint on the observed demographics of evolved exoplanetary systems, allowing observed trends in protoplanetary disks to be extrapolated to the evolved exoplanet population and vice versa. However several processes subsequent to a planet's formation do erase information encoded at that time and location in the disk, precluding a simple mapping of disk substructure locations and inferred planet masses to the evolved exoplanet population. Bulk composition and atmospheric abundances can be perturbed by, e.g., planet migration in the disk ([Booth and Ilee, 2019](#)), volatile delivery from planetesimal accretion ([Schlichting et al., 2015](#)), impacts after the gas disk dissipates ([Wyatt and Jackson, 2016](#)), and atmospheric mass loss ([Ginzburg et al., 2018](#); [Owen and Wu, 2017](#)). Similarly a planetary system's orbital architecture and multiplicity can evolve after formation. In the disk, mechanisms such as eccentricity pumping ([Ragusa et al., 2018](#); [Terquem and Ajmia, 2010](#)) can drive orbital reshuffling. In the post-disk phases, dynamic interactions over Gyr can reshape a system by, e.g., planet-planet scattering ([Chatterjee et al., 2008](#)) and tidal circularization of ultra-short period companions ([Ogilvie and Lin, 2004](#)).

In addition to the open question of how much of the disk's conditions remain imprinted on an evolved planetary system, challenges in linking disk and exoplanet observations are also statistical. The number of disks with observed substructures (<80, of which ≈ 20 have

structures resolved at $\lesssim 5$ au) is and will continue for at least a decade to be more than an order of magnitude less than the number of confirmed exoplanetary systems, currently ≈ 4000 in ≈ 700 systems. The next generation Very Large Array (ngVLA, [Selina et al., 2018](#)) that could attain the spatial resolution to detect gaps induced by sub-giants in the inner dust disk ([Ricci et al., 2018](#)) – the most abundant exoplanet mass and period regime – has first science operations projected for 2028. Current and nearer term instruments in the near-IR (SPHERE on the VLT and GPI on the Gemini Telescope, [Macintosh et al., 2014](#); [Vigan et al., 2016](#)) and mid-IR (the proposed METIS spectrograph on the E-ELT, [Brandl et al., 2008](#)) will significantly increase planet detections in disks, though not with the rapidity of exoplanet yields, predicted to grow by as much as a factor of 5 only in the next few years with NASA’s TESS (Transiting Exoplanet Survey Satellite) mission ([Barclay et al., 2018](#); [Ricker et al., 2015](#)). As the first era of planet detections in disks evolves over the next decade, comparisons can begin to be made with observed and extrapolated occurrence distributions in the exoplanet population (for a recent review see [Winn and Fabrycky, 2015](#); for updates see [Fernandes et al., 2019](#); [Petigura et al., 2017](#)).

With the current generation of radio interferometers, detection of the optically thin gaps opened by giant planets and even of circumplanetary disks is achievable. This in principle allows an occurrence rate calculation that is fairly complete at ≈ 5 au resolution for disk substructures that may be due to gas giants, given a sufficiently large sample size (obtainable in the next several ALMA cycles). To this end recent studies are beginning to establish tenuous links between theoretical and observed processes in disks and the evolved exoplanet population. [Lodato et al. \(2019\)](#) propose that if giant planets at > 10 au separations are invoked to form observed gaps in disks, their subsequent inward migration in the disk could lead to rough agreement with extrapolated observations for occurrence rates of giants at 1 – 10 au separations in evolved exoplanetary systems. However there are important limitations that at present preclude drawing robust, quantitative connections between disk and exoplanet observations, a consequence of the compounded effect of many theoretical uncertainties, as well as a currently small number of disks (≈ 20) with substructures observed at high resolution ($\lesssim 5$ au).

Current progress in disk studies thus precludes robust extrapolation of observed disk features to confidently motivate exoplanet trends. There is not yet enough known from disk observations to select between multiple, viable hypotheses for disk substructure origins. And statistical trends across disks are not yet sufficient to complement the rapidly growing amount of information on evolved exoplanetary systems and discern the extent to which these influence subsequent planetary system evolution (relative to the extent this information is retained or erased by later processes). Motivated by the potential for inferences that could be

drawn from a larger sample of accurately characterized disk substructures, this thesis will focus on building and applying a tool to more highly resolve – and detect new – substructure in protoplanetary disks. Application of such a tool is a next step toward a statistical ensemble of well-characterized disk substructures. These can ultimately be paired with hydrodynamic simulations to robustly extrapolate the trends we observe in disks to exoplanetary systems.

Chapter 2

Frankenstein: Protoplanetary disk brightness profile reconstruction at sub-beam resolution with a rapid Gaussian process

Super-resolution imaging techniques have the capacity to improve the fidelity of radio interferometric images relative to the community standard imaging framework, CLEAN. This can provide new insights into protoplanetary disk science through a more accurate characterization of disk substructure. To these ends, this chapter presents a novel, super-resolution imaging technique for radio interferometry, tailored to protoplanetary disk observations. Frankenstein (`frank`) is a 1D, open source imaging code that recovers axisymmetric disk structures at sub-beam resolution. `frank` is the core modeling framework used throughout the thesis to analyze sub-mm observations of disks, and the model as presented in this chapter is a successor to the parametric fitting approach `galario` (Tazzari et al., 2018).

Richard Booth, Marco Tazzari and I developed `frank`. Richard developed and coded the fundamental model framework, which is set out in detail in Sec. 2.2 and further described in Sec. 2.5, 2.6, and 2.7. I then conducted the suite of tests and analysis presented in Sec. 2.3 and Sec. 2.7. Marco provided a synthetic image pipeline that I used to produce the mock observations shown in Sec. 2.3. I aided Richard in developing some of the ancillary code components used in the analysis. The chapter, with some modifications to the introduction, was published as Jennings et al. (2020). Richard, Marco and I co-wrote the paper, with Richard's primary contributions in what is Sec. 2.2 below, Marco's in Sec. 2.4, and mine in Sec. 2.3. There were additional refinements resulting from feedback provided by the other coauthors.

`frank` reconstructs a disk's 1D radial brightness profile by fitting the observed visibilities directly and nonparametrically, using a fast ($\lesssim 1$ min) Gaussian process. The code avoids limitations of current methods that obtain the radial brightness profile by either extracting it from the disk image via nonlinear deconvolution at the cost of reduced fit resolution, or by assumptions placed on the functional forms of disk structures to fit the visibilities parametrically. Here we use mock ALMA observations to quantify the method's intrinsic capability and its performance as a function of baseline-dependent signal-to-noise. Comparing the technique to profile extraction from a CLEAN image, we motivate how our fits accurately recover disk structures at a sub-beam resolution. Demonstrating the model's utility in fitting real high and moderate resolution observations, we conclude by proposing applications to address open questions on protoplanetary disk structure and processes.

2.1 Background

As discussed in Sec. 1.3.1, many protoplanetary disks that appear smooth in fact harbor unresolved gaps and rings. This is true for compact disks that are covered by a small number of resolution elements in current datasets, as well as for high resolution observations of large disks – the DSHARP survey at 35 mas (≈ 5 au; [Andrews et al., 2018](#); [Huang et al., 2018a](#)) shows evidence of disks with only partially resolved substructure. These findings motivate the utility of a high resolution technique that can recover annular features on sub-beam scales and thus inform both theory and follow-up observations. Even in the presence of non-axisymmetric disk structure such as spirals, accurate recovery of the background radial profile is often an important first step, allowing isolation of the asymmetric features ([Meru et al., 2017](#); [Pérez et al., 2016](#)). More accurate characterization of azimuthally averaged radial brightness profiles can thus aid in distinguishing the origins of both symmetric and asymmetric morphologies. While this could alternatively be achieved through higher resolution and/or deeper observations, extracting this information from existing datasets is more practically achievable.

To overcome the intrinsic resolution limit of CLEAN and the practical limitations of forward modeling in the visibility domain, we have developed a technique that fits the visibilities directly (avoiding beam convolution) and nonparametrically (affording the flexibility to fit complicated structure in the visibility distribution) to yield a reconstructed brightness profile. This empirical Bayes method, falling between a forward model with a fully explored posterior and a RML approach, imposes no assumptions on the functional form of the disk or its substructures, is autonomous (requiring no iterative, manual tuning of fit parameters), fast, and consistently achieves sub-beam fit resolution. This chapter will present a robust and

accurate method to reconstruct an azimuthally averaged radial brightness profile by directly fitting the interferometric dataset. We will use several mock and real datasets to compare brightness profile extraction from a CLEAN image to our model, as well as the DSHARP observations of AS 209 (Andrews et al., 2018) to compare a parametric visibility fit to our nonparametric approach.

This chapter presents `frank`, an open source code to reconstruct the 1D radial brightness profile of an axisymmetric protoplanetary disk.¹ Sec. 2.2 details the code’s methodology and assesses its prior sensitivities. Sec. 2.3 characterizes the model’s performance, both intrinsic and as a function of data quality, using mock and real datasets. This includes application to low, moderate and high resolution datasets, and a detailed comparison to brightness profile extraction from a CLEAN image. Sec. 2.4 concludes by summarizing `frank`’s properties and outlining use cases for interferometric observations of protoplanetary disks.

2.2 Model

Our goal is to infer the true brightness $I_\nu(r)$ of a source under the assumption of azimuthal symmetry. To do this we will reconstruct $I_\nu(r)$ at a set of radial locations r_k by directly fitting the observed visibilities in the Fourier domain. This is possible by exploiting the properties of the *discrete Hankel transform (DHT)* detailed in Sec. 2.2.1 and 2.2.2. Via the DHT, we can model the brightness profile as a sum of Bessel functions by nonparametrically fitting the visibilities to determine the coefficients in a Fourier-Bessel series expression for $I_\nu(r)$.

We will show, however, that the direct fit is prone to find solutions with strong oscillations on small spatial scales. This is because the observed visibilities only sample the (u, v) plane out to a finite baseline. To solve this we introduce a Gaussian process in Sec. 2.2.3 to smooth the reconstructed profile. The Gaussian process acts to regularize the Bessel series expression for the brightness profile, assigning a length scale over which there is positive correlation in brightness. We will assume that the covariance matrix of the Gaussian process can be nonparametrically estimated from the data (visibilities) under the assumption that this matrix is diagonal in Fourier space. The free parameters (diagonal elements) of the matrix can be identified as the power spectrum of the reconstructed brightness profile. In visibility space, the power spectrum at the observed baselines is to zeroth order the square of the observed visibility amplitudes. A similar approach, but based on log-normal priors, has previously been applied successfully to the more general problem of inferring 2D brightness distributions

¹The code is available at <https://github.com/discsim/frank> (and the docs at <https://disksim.github.io/frank>) under the open source GNU Lesser General Public License v3.

from radio observations (Arras et al., 2019, 2018; Greiner et al., 2016; Janklewitz et al., 2015, 2016; Sutter et al., 2013).

The necessary first step in fitting the visibilities is deprojection, correcting for the disk’s on-sky inclination, position angle (rotation) and phase offset (departure from centering on the origin in the (u, v) plane). For mock observations in this chapter we will always consider face-on, phase-centered disks. For real observations we will use published geometry values (which we confirm by fitting a 2D Gaussian to the visibilities) to deproject the data prior to applying our model. Importantly, if a disk has an appreciable vertical thickness or if limb darkening from the optically thick surface is important, many of the assumptions underlying a deprojection approach such as fitting a 2D Gaussian to the visibilities would be invalidated.

Then for an azimuthally symmetric function (in our case a deprojected, assumed azimuthally symmetric disk) this 2D Fourier transform between the disk brightness and visibilities reduces to 1D as a Hankel transform with Bessel function kernels (Bracewell, 2000; Thompson et al., 2017),

$$I_\nu(r) = \int V_\nu(q) J_0(2\pi qr) 2\pi q \, dq, \quad (2.1)$$

$$V_\nu(q) = \int I_\nu(r) J_0(2\pi qr) 2\pi r \, dr. \quad (2.2)$$

Here r is the radial coordinate in the disk, $q = \sqrt{u^2 + v^2}$ the baseline distance in the (u, v) plane, and J_0 the order 0 Bessel function of the first kind.

2.2.1 Representing the brightness profile as a Fourier-Bessel series

To evaluate Equations 2.1 – 2.2, we make use of their relation to Fourier-Bessel series via the DHT. For more information about the DHT see Baddour and Chouinard (2015)²; here we reproduce only the details necessary for our application in Sec. 2.2.2.

Imposing the assumption that the real space brightness profile $I_\nu(r) = 0$ beyond some radial distance R_{out} , or that the visibilities $V_\nu(q) = 0$ beyond some spatial frequency Q_{max} ,

²N.B. The definition of the Hankel transform used here differs from that in Baddour and Chouinard (2015) by factors of 2π .

enables the expansion of $I_\nu(r)$ or $V_\nu(q)$ in a Fourier-Bessel series. Respectively

$$I_\nu(r) = \sum_{k=1}^{\infty} \alpha_k J_0\left(\frac{j_{0k}r}{R_{\text{out}}}\right), \quad (2.3)$$

$$V_\nu(q) = \sum_{k=1}^{\infty} \beta_k J_0\left(\frac{j_{0k}q}{Q_{\text{max}}}\right), \quad (2.4)$$

where j_{0k} is a scalar representing the k th root of $J_0(r)$, i.e., $J_0(j_{0k}) = 0$.

The coefficients α_k in Equation 2.3 can be computed via the orthogonality relationship of Bessel functions with subscripts k and j ,

$$\int_0^{R_{\text{out}}} J_0\left(\frac{j_{0k}r}{R_{\text{out}}}\right) J_0\left(\frac{j_{0j}r}{R_{\text{out}}}\right) 2\pi r dr = \pi R_{\text{out}}^2 J_1^2(j_{0j}) \delta_{jk}, \quad (2.5)$$

where δ_{ij} is the Kronecker δ and J_1 the first order Bessel function. Substituting Equation 2.3 into Equation 2.5,

$$\begin{aligned} & \int_0^{R_{\text{out}}} I_\nu(r) J_0\left(\frac{j_{0k}r}{R_{\text{out}}}\right) 2\pi r dr \\ &= \sum_{j=1}^{\infty} \alpha_j \int_0^{R_{\text{out}}} J_0\left(\frac{j_{0k}r}{R_{\text{out}}}\right) J_0\left(\frac{j_{0j}r}{R_{\text{out}}}\right) 2\pi r dr \\ &= \alpha_k \pi R_{\text{out}}^2 J_1^2(j_{0k}). \end{aligned} \quad (2.6)$$

Noting that the left-hand side of this is just the Hankel transform of I_ν , the brightness profile can be written entirely in terms of its visibilities at a specific set of spatial frequencies $q_k = j_{0k}/(2\pi R_{\text{max}})$ and the Fourier-Bessel series coefficients α_k . Analogously the visibility at any q can be computed in terms of the brightness at the set of radial locations (collocation points) $r_k = j_{0k}/(2\pi Q_{\text{max}})$ and the Fourier-Bessel series coefficients β_k ,

$$\alpha_k = \frac{1}{\pi R_{\text{out}}^2 J_1^2(j_{0k})} V_\nu\left(\frac{j_{0k}}{2\pi R_{\text{out}}}\right), \quad (2.7)$$

$$\beta_k = \frac{1}{\pi Q_{\text{max}}^2 J_1^2(j_{0k})} I_\nu\left(\frac{j_{0k}}{2\pi Q_{\text{max}}}\right). \quad (2.8)$$

In practice we must truncate the infinite sums in Equation 2.3 and Equation 2.4 to a finite value N . From Equation 2.3, the brightness profile then becomes entirely determined by spatial frequencies below some $2\pi q = j_{0N_+}/R_{\text{out}}$, where j_{0N_+} is j_{0k} for $k = N + 1$. Similarly the visibilities are entirely determined by radii smaller than $2\pi r = j_{0N_+}/Q_{\text{max}}$. Choosing

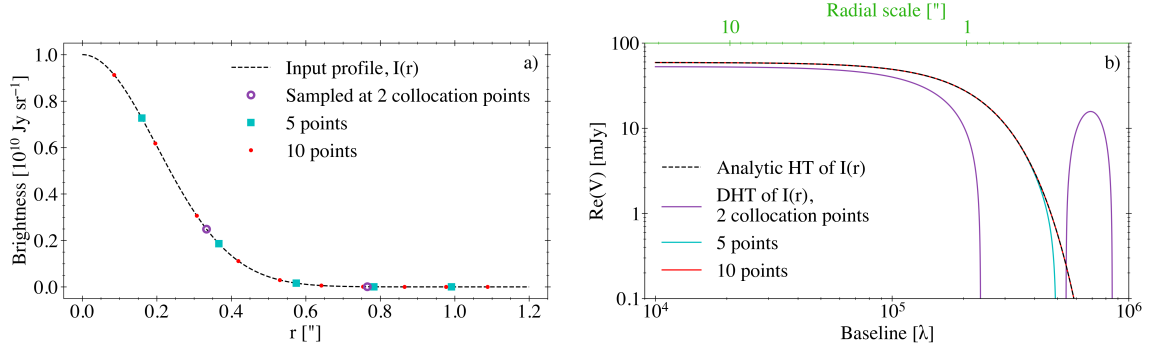


Fig. 2.1. Fourier-Bessel series representation of a brightness profile

a) An input mock brightness profile for a Gaussian disk, with samplings at an increasing number of radial collocation points and $R_{\text{out}} = 1.2''$.

b) The discrete Hankel transform (DHT) of a Fourier-Bessel series representation of the input profile at these sets of collocation points, showing that an approximation with a small number of points can closely match the analytic Hankel transform (HT) of the input profile. The second x-axis shows the spatial scale corresponding to a given baseline, $r_{\text{scale}} = 1/q$.

$2\pi Q_{\text{max}} = j_{0N_+}/R_{\text{out}}$ then produces the DHT (Baddour and Chouinard, 2015). The rules for the backward (visibility space \rightarrow real space) and forward (real space \rightarrow visibility space) transforms of the DHT are

$$I_k = \frac{j_{0N_+}}{2\pi R_{\text{out}}^2} \sum_{j=1}^N Y_{kj} V_j, \quad (2.9)$$

$$V_k = \frac{2\pi R_{\text{out}}^2}{j_{0N_+}} \sum_{j=1}^N Y_{kj} I_j, \quad (2.10)$$

where

$$Y_{kj} = \frac{2}{j_{0N_+} J_1^2(j_{0j})} J_0\left(\frac{j_{0k} j_{0j}}{j_{0N_+}}\right). \quad (2.11)$$

The intensities $I_k = I_v(r_k)$ and visibilities $V_k = V_v(q_k)$ are evaluated at the collocation points of the Fourier-Bessel series in real and visibility space respectively,

$$r_k = R_{\text{out}} j_{0k} / j_{0N_+}, \quad (2.12)$$

$$q_k = j_{0k} / (2\pi R_{\text{out}}). \quad (2.13)$$

We illustrate the correspondence between the brightness profile and visibilities using the example of a Gaussian brightness profile in **Fig. 2.1**. A small number of collocation points

($\lesssim 10$, corresponding to the same number of terms in the Bessel series) yields, via the DHT, a visibility profile $V_\nu(q)$ that is in good agreement with the analytic Hankel transform of the input profile up to frequencies $q \sim Q_{\max}$. In practice to account for more complicated profiles we use 100 – 300 collocation points.

It is convenient to absorb the normalization coefficients from Equations 2.9 – 2.10 into backward and forward transform matrices respectively³,

$$\mathbf{Y}_b = \frac{j_{0N_+}}{2\pi R_{\text{out}}^2} \mathbf{Y}, \quad (2.14)$$

$$\mathbf{Y}_f = \frac{2\pi R_{\text{out}}^2}{j_{0N_+}} \mathbf{Y}, \quad (2.15)$$

which obey

$$\mathbf{Y}_b \mathbf{Y}_f = \mathbf{Y} \mathbf{Y} \approx \mathbf{I}, \quad (2.16)$$

where \mathbf{I} is the identity matrix. The last approximation is exact only for $N \rightarrow \infty$, though the error is small at modest N ; for $N > 30$ the largest error is $< 10^{-7}$. In the code the impact is even less significant because only the forward transform matrices are used explicitly.

These matrices can be used to specify the transformation rules for vectors,

$$\mathbf{f} = \mathbf{Y}_b \tilde{\mathbf{f}}, \quad (2.17)$$

$$\tilde{\mathbf{f}} = \mathbf{Y}_f \mathbf{f}, \quad (2.18)$$

where we explicitly use a tilde (e.g., $\tilde{\mathbf{f}}$) to distinguish Fourier domain quantities from a real space vector (e.g., \mathbf{f}). For the visibilities \mathbf{V} we will drop the tilde.

It will also be useful to define the transformation rules for a covariance matrix \mathbf{S} and its inverse. These can be derived from the equivalence of scalars in real and visibility space, $\mathbf{f}^T \mathbf{S}^{-1} \mathbf{f} = \tilde{\mathbf{f}}^T \tilde{\mathbf{S}}^{-1} \tilde{\mathbf{f}}$, where $\tilde{\mathbf{S}}$ is the visibility space representation of the covariance matrix. From this relation we have

$$\tilde{\mathbf{S}}^{-1} = \mathbf{Y}_b^T \mathbf{S}^{-1} \mathbf{Y}_b, \quad (2.19)$$

$$\tilde{\mathbf{S}} = \mathbf{Y}_f^T \mathbf{S} \mathbf{Y}_f. \quad (2.20)$$

2.2.2 Fitting the visibilities using the discrete Hankel transform

Using the Fourier-Bessel series and DHT from Sec. 2.2.1, we now develop a method to reconstruct a disk's brightness profile given a set of N_{vis} visibilities. To keep the notation

³Notation: We use boldface for matrix quantities, e.g., $\mathbf{Y} = Y_{kj}$.

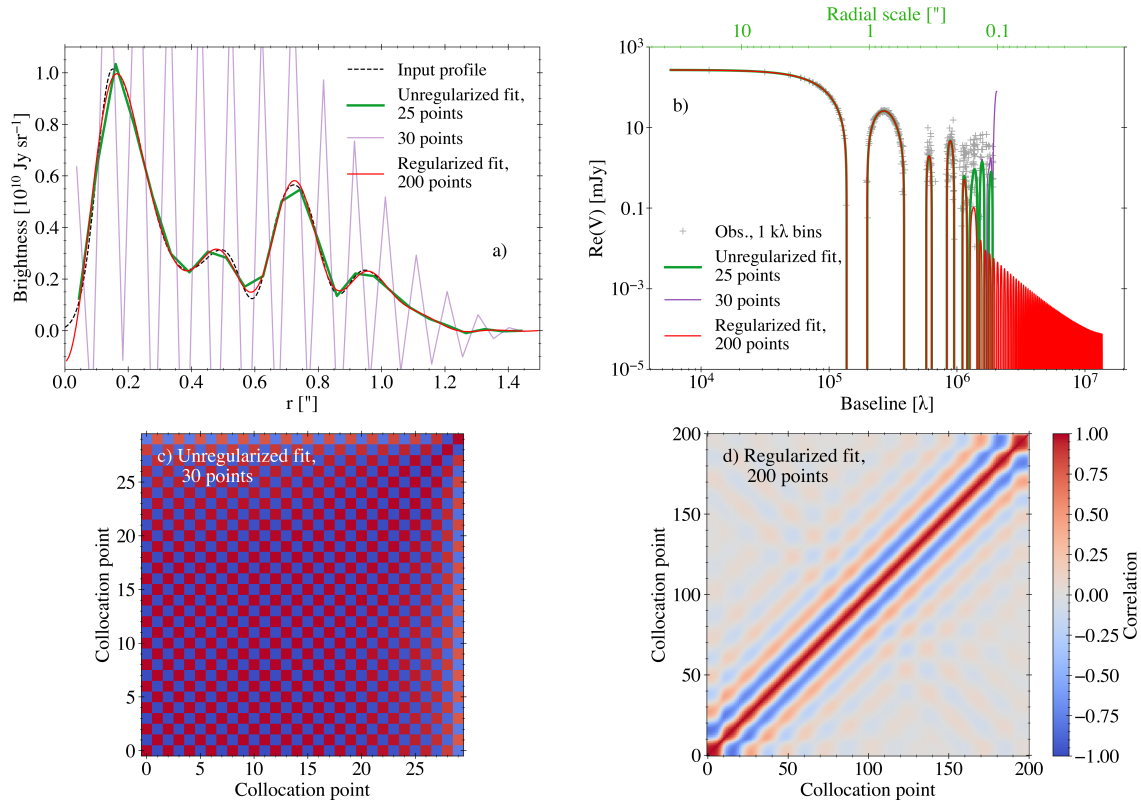


Fig. 2.2. Fit regularization

a) For a multi-Gaussian mock disk observed with the ALMA C43-6 configuration (beam FWHM $0.13 \times 0.17''$, Briggs=0.5; see Table 2.2), a fit with regularization and using 200 collocation points. Fits derived from Equation 2.23 without regularization are shown for comparison, demonstrating instability at only 30 collocation points.

b) Visibilities for the mock observation in (a) and fits corresponding to the brightness profiles in (a). The unregularized fits place erroneously high (noise) power beyond the data’s longest baseline, while the regularized fit yields a more reasonable prediction for power on these unobserved scales.

c) 30×30 correlation matrix for the 30-point unregularized fit in (a), showing that the high amplitude oscillations in (b) are a result of almost perfectly strong anticorrelation between adjacent points.

d) 200×200 posterior correlation matrix for the regularized fit in (a), with the regularization providing stability by damping correlations. This in turn prevents regions of erroneously high power in (b) and thus spurious oscillations in (a).

succinct we will denote the visibilities by the vector \mathbf{V} , with associated baselines \mathbf{q} and corresponding weights \mathbf{w} . For a radio interferometer it is reasonable to assume that the noise on each visibility is drawn from an independent Gaussian distribution with variance $\sigma_j^2 = 1/w_j$, such that the covariance matrix of the noise is $\mathbf{N} = \text{diag}(1/\mathbf{w})$. That is, \mathbf{N} has $1/w_j$ along the diagonal and is 0 otherwise.

Fixing R_{out} (to a distance beyond the edge of the disk) and choosing the number of brightness points N fixes the radial collocation points r_k . We can then use the Fourier-Bessel series representation (Equation 2.4) to link the observed visibilities \mathbf{V} to $I_\nu(r_k)$, which we seek to infer. The likelihood for \mathbf{V} is a Gaussian,

$$\mathcal{L}_G = P(\mathbf{V}|\mathbf{I}_\nu) = \mathcal{G}(\mathbf{V} - \mathbf{H}(\mathbf{q})\mathbf{I}_\nu, \mathbf{N}), \quad (2.21)$$

where generically $\mathcal{G}(M, \mathbf{\Sigma})$ refers to a multidimensional Gaussian with mean M and covariance $\mathbf{\Sigma}$. The vector \mathbf{I}_ν is the brightness at the radial collocation points (i.e., it has the components $I_\nu(r_k)$), and we have introduced the $N_{\text{vis}} \times N$ matrix $\mathbf{H}(\mathbf{q})$, defined by the components

$$H_k(q_j) = \frac{4\pi R_{\text{out}}^2}{j_{0N_+}^2 J_1^2(j_{0k})} J_0\left(2\pi q_j R_{\text{out}} \frac{j_{0k}}{j_{0N_+}}\right), \quad (2.22)$$

which comes from the Fourier-Bessel series expansion.

One way to derive $I_\nu(r_k)$ would be to maximize \mathcal{L}_G . The solution would be

$$\mathbf{I}_\nu = \mathbf{M}^{-1} \mathbf{j}, \quad (2.23)$$

where

$$\mathbf{M} = \mathbf{H}(\mathbf{q})^T \mathbf{N}^{-1} \mathbf{H}(\mathbf{q}), \quad (2.24)$$

$$\mathbf{j} = \mathbf{H}(\mathbf{q})^T \mathbf{N}^{-1} \mathbf{V}. \quad (2.25)$$

The model's dependence on the visibility data enters entirely through \mathbf{M} and \mathbf{j} . Note that the construction of \mathbf{M} scales as $\mathcal{O}(N^2 N_{\text{vis}})$, and the construction of \mathbf{j} scales as $\mathcal{O}(N N_{\text{vis}})$, while the solution of these equations and subsequent expressions in Sec. 2.2.3 scale as $\mathcal{O}(N^3)$, where we recall N is the number of collocation points. Because \mathbf{M} and \mathbf{j} are constructed using all unbinned visibilities, the code does not regrid the visibilities onto the spatial frequency collocation points; we are evaluating the full set of observed visibilities. A value of $N \approx 100 - 300 \ll N_{\text{vis}}$ is sufficient to fit data at the highest resolutions of current interferometers.

The problem with maximizing \mathcal{L}_G directly is that for sufficiently large N , \mathbf{M} will become singular. This occurs because the relationship between nearby points in the brightness profile is determined by high frequency components. For sufficiently large N these components are either not present in, or are poorly constrained by, the visibilities. Yet the requirement that N is small enough that we are able to invert \mathbf{M} will be too restrictive, limiting our ability to accurately fit high signal-to-noise (SNR), short baseline data. We would need to fit a large number of data points under the constraint that the profile is smooth on sufficiently small scales. Fitting a brightness profile with a reasonable number of radial points therefore requires regularizing the solution on small spatial scales.

Fig. 2.2 shows how attempting to fit a brightness profile without regularization yields numerical instability in \mathbf{M} at a modest number of collocation points, $N = 30$. While at $N = 25$ the fit is stable, the resulting brightness profile is undersampled, with variations between adjacent radial collocation points. Adding more points to the unregularized fit causes these oscillations to increase in amplitude and frequency, with the visibility domain fit in Fig. 2.2(b) having erroneously high amplitude near and beyond the data’s longest baselines. In Sec. 2.2.3 we will describe how the fit can be regularized using a nonparametric Gaussian process model. The regularized fit with `frank` shown in Fig. 2.2(a) is smooth and insensitive to the number of collocation points (we show the case for $N = 200$), yielding an accurate recovery of the input profile. The visibility domain fit in Fig. 2.2(b) correspondingly decreases in amplitude at the longest baselines and beyond (note the data are noise-dominated beyond $\approx 1.2 M\lambda$).

This difference in behavior between the unregularized and `frank` fits is a consequence of the correlations between radial collocation points in each model. In the unregularized fit, adjacent points are almost perfectly anticorrelated for $N = 30$ in Fig. 2.2(c), inducing strong brightness profile oscillations. By contrast the regularized `frank` fit introduces a positive correlation between adjacent points in Fig. 2.2(d), damping oscillations in the recovered brightness profile.

2.2.3 Regularizing the fit using a nonparametric Gaussian process

Regularization corresponds to an a priori assumption that the brightness should be highly correlated at adjacent points and more weakly correlated at distant points. This assumption is well suited to the framework of a Gaussian process, in which the prior on \mathbf{I}_v is a Gaussian,

$$P(\mathbf{I}_v|\mathbf{p}) = \mathcal{G}(\mathbf{I}_v, \mathbf{S}(\mathbf{p})), \quad (2.26)$$

where $\mathbf{S}(\mathbf{p})$ is the prior covariance in the real space brightness profile at the radial collocation points. We explicitly specify that the covariance structure $\mathbf{S}(\mathbf{p})$ has some dependence on a

set of parameters \mathbf{p} , which we will relate to an estimate of the power spectrum based on the DHT of I_v , $\tilde{I}_v^2 = (\mathbf{Y}_f I_v)^2$. Given \mathbf{p} , the posterior probability for I_v can be used to reconstruct the brightness,

$$P(I_v | \mathbf{V}, \mathbf{p}) = \frac{P(\mathbf{V} | I_v, \mathbf{p}) P(I_v | \mathbf{p})}{P(\mathbf{V} | \mathbf{p})} \quad (2.27)$$

$$= \frac{\mathcal{G}(\mathbf{V} - \mathbf{H}(\mathbf{q}) I_v, \mathbf{N}) \mathcal{G}(I_v, \mathbf{S}(\mathbf{p}))}{P(\mathbf{V} | \mathbf{p})}. \quad (2.28)$$

The numerator here is the product of two Gaussians, which is also a Gaussian, and has covariance \mathbf{D} and mean $\boldsymbol{\mu}$,

$$\begin{aligned} \mathbf{D} &= \left(\mathbf{M} + \mathbf{S}(\mathbf{p})^{-1} \right)^{-1}, \\ \boldsymbol{\mu} &= \mathbf{D} \mathbf{j}. \end{aligned} \quad (2.29)$$

Explicitly,

$$P(I_v | \mathbf{V}, \mathbf{p}) \propto \mathcal{G}(I_v - \boldsymbol{\mu}, \mathbf{D}), \quad (2.30)$$

which we will use to infer I_v given \mathbf{p} . The remaining challenge is how to specify $\mathbf{S}(\mathbf{p})$. Typically in a Gaussian process the covariance structure is parameterized in terms of a simple function, such as a Gaussian with some length scale ([Rasmussen and Williams, 2006](#)). This length scale could then be optimized or better yet marginalized over. We follow an alternative approach, the empirical Bayes method, in which we use a nonparametric form for the covariance matrix that can be estimated from the visibilities simultaneously with the brightness profile. This approach follows the work of [Oppermann et al. \(2013\)](#); see also [Enßlin and Frommert \(2011\)](#).

We make the ansatz that the prior covariance matrix is diagonal in visibility space, i.e.,

$$\tilde{\mathbf{S}}(\mathbf{p}) = \mathbf{Y}_f^T \mathbf{S}(\mathbf{p}) \mathbf{Y}_f = \text{diag}(\mathbf{p}), \quad (2.31)$$

thus

$$\mathbf{S}(\mathbf{p}) = \mathbf{Y}_b^T \text{diag}(\mathbf{p}) \mathbf{Y}_b, \quad (2.32)$$

where we have now defined the parameters \mathbf{p} as the diagonal elements of the visibility space representation of the covariance matrix (with the off-diagonal elements set to zero). In the code, we construct $\mathbf{S}(\mathbf{p})^{-1}$ directly from $1/\mathbf{p}$ and \mathbf{Y}_f .

To understand the effect of this prior, we consider \tilde{I}_v – the Fourier space representation of I_v – which is equivalent to the predicted visibility at the spatial frequency collocation points

q_k . In visibility space the prior takes the form

$$\begin{aligned} \log P(\mathbf{I}_v | \mathbf{S}(\mathbf{p})) &\equiv \log P(\tilde{\mathbf{I}}_v | \tilde{\mathbf{S}}(\mathbf{p})) \\ &= -\frac{1}{2} \mathbf{I}_v^T \mathbf{S}(\mathbf{p})^{-1} \mathbf{I}_v - \frac{1}{2} \log |2\pi \mathbf{S}(\mathbf{p})| \\ &= -\frac{1}{2} \sum_k \left(\frac{\tilde{I}_{\cdot,k}^2}{p_k} + \log p_k \right) + \text{const}, \end{aligned} \quad (2.33)$$

where $\tilde{I}_{\cdot,k}$ and p_k refer to the k th element of $\tilde{\mathbf{I}}_v$ and \mathbf{p} . The last line follows from the definition of $\tilde{\mathbf{I}}$ and the relation between the determinant of a matrix product and the product of determinants,

$$|2\pi \mathbf{S}(\mathbf{p})| = |\mathbf{Y}_b^T| \cdot |2\pi \text{diag}(\mathbf{p})| \cdot |\mathbf{Y}_b| = |\mathbf{Y}_b|^2 \prod_k 2\pi p_k. \quad (2.34)$$

From Equation 2.33 we see that if $\tilde{I}_{\cdot,k}^2$ (the power in the brightness profile on a scale k) is large relative to p_k , the prior probability will be small. Thus the prior acts to suppress power on scales where p_k is small. We examine the prior's effect on the reconstructed brightness profile in greater depth in Sec. 2.2.5.

2.2.4 Jointly inferring the brightness profile and power spectrum parameters

Because we do not know a priori the optimal choice for \mathbf{p} , reconstructing the brightness profile is now a problem of jointly inferring \mathbf{I}_v and \mathbf{p} . The joint posterior probability $P(\mathbf{I}_v, \mathbf{p} | \mathbf{V}, \boldsymbol{\beta})$ is constructed using the posterior for \mathbf{I}_v given \mathbf{p} , $P(\mathbf{I}_v | \mathbf{V}, \mathbf{p})$, and a prior probability distribution for \mathbf{p} , $P(\mathbf{p} | \boldsymbol{\beta})$, via

$$P(\mathbf{I}_v, \mathbf{p} | \mathbf{V}, \boldsymbol{\beta}) = P(\mathbf{I}_v | \mathbf{V}, \mathbf{p}) P(\mathbf{p} | \boldsymbol{\beta}). \quad (2.35)$$

Here we have noted explicitly the dependence of $P(\mathbf{p} | \boldsymbol{\beta})$ on a set of hyperparameters $\boldsymbol{\beta} = \{\alpha, p_0, w_{\text{smooth}}\}$, which also introduces the dependence on $\boldsymbol{\beta}$ into the posterior probability $P(\mathbf{I}_v, \mathbf{p} | \mathbf{V}, \boldsymbol{\beta})$. The set of parameters $\boldsymbol{\beta}$ will be held fixed in any given inference of \mathbf{I}_v and \mathbf{p} . We will refer to $P(\mathbf{p} | \boldsymbol{\beta})$ as the hyperprior to distinguish it from $P(\mathbf{I}_v | \mathbf{p})$. We define the components of $\boldsymbol{\beta}$ below.

To estimate the parameters of the covariance matrix \mathbf{p} using the data, our general approach will be to produce small values for \mathbf{p} on scales that are unconstrained by the data, in order to suppress them, but otherwise allow \mathbf{p} to be sufficiently large that the reconstructed brightness profile is controlled by the data. To achieve this we specify $P(\mathbf{p} | \boldsymbol{\beta})$ as the product of a

spectral smoothness term and inverse Gamma functions,

$$P(\mathbf{p}|\boldsymbol{\beta}) = P_{\text{smooth}}(\mathbf{p}|w_{\text{smooth}}) \prod_{k=1}^N \frac{1}{p_0 \Gamma(\alpha - 1)} \left(\frac{p_k}{p_0}\right)^{-\alpha} \exp\left(-\frac{p_0}{p_k}\right). \quad (2.36)$$

The exponential part of the inverse Γ function disfavors values of $p_k < p_0$, while the power law disfavors $p_k \gg p_0$ for $\alpha > 1$. Neglecting the spectral smoothness hyperprior, the limit $\alpha \rightarrow 1$ and $p_0 \rightarrow 0$ yields a Jeffreys prior (flat in log space). We typically choose a small but nonzero value of p_0 (e.g., 10^{-15} Jy^2) for practicality; low p_0 allows frank to find a solution with very low power on scales unconstrained by the data, strongly regularizing those scales. Though we do not want p_0 to be arbitrarily small, as this leads to numerical instability when evaluating Equation 2.29.

The spectral smoothness hyperprior follows [Oppermann et al. \(2013\)](#) and is included for two reasons. It first prevents regions of artificially low power arising from narrow gaps in the visibilities and at unconstrained scales beyond the data's longest baseline, ensuring the brightness profile does not exhibit artificially high correlation at the corresponding spatial scales. Secondly it introduces a coupling between adjacent points in the power spectrum. This has the effect of 'averaging' the squared visibility amplitude over a range of scales, suppressing the impact of noise on the power spectrum. Overall we have not found the brightness reconstruction to be highly sensitive to the inclusion of the smoothing hyperprior, which takes the form

$$P_{\text{smooth}}(\mathbf{p}|w_{\text{smooth}} \equiv 1/\sigma_s^2) \propto \exp\left(-\frac{1}{2\sigma_s^2} \int d\log(q) \left(\frac{\partial^2 \log(p)}{\partial \log(q)^2}\right)^2\right). \quad (2.37)$$

This hyperprior penalizes power spectra with large second derivatives in log space, i.e., those that deviate from a power law (a straight line in log space). σ_s , which is parameterized in terms of w_{smooth} , controls the allowed amount of variation (departure from a power law) in the power spectrum at a given q . We implement this hyperprior using a numerical estimate of $\partial^2 \log(p)/\partial \log(q)^2$, which can be written in the form

$$P_{\text{smooth}}(\mathbf{p}|w_{\text{smooth}}) \propto \exp\left(-\frac{1}{2} \log(\mathbf{p})^T \frac{\mathbf{T}}{\sigma_s^2} \log(\mathbf{p})\right), \quad (2.38)$$

where \mathbf{T} is a constant, pentadiagonal matrix that depends only on the spatial frequency collocation points q_k . For the exact form of \mathbf{T} , see Sec. 2.5.

With $P_{\text{smooth}}(\mathbf{p}|w_{\text{smooth}})$ specified, we now have a form for $P(\mathbf{p}|\boldsymbol{\beta})$. Ideally we would proceed to obtain the posterior for \mathbf{I}_ν by marginalizing over \mathbf{p} , but the high dimensionality of the parameter space makes this impractical. We instead maximize $P(\mathbf{p}|\mathbf{V}, \boldsymbol{\beta})$ to obtain and use the maximum a posteriori value \mathbf{p}_{MAP} as the prior on \mathbf{I}_ν . The marginal posterior $P(\mathbf{p}|\mathbf{V}, \boldsymbol{\beta})$ is obtained from $P(\mathbf{I}_\nu, \mathbf{p}|\mathbf{V}, \boldsymbol{\beta})$ by integrating over all \mathbf{I}_ν , i.e., $\int P(\mathbf{I}_\nu, \mathbf{p}|\mathbf{V}, \boldsymbol{\beta}) d\mathbf{I}_\nu$. Since $P(\mathbf{I}_\nu|\mathbf{V}, \mathbf{p})$ is a multivariate Gaussian, this can be done analytically (e.g., Appendix A of [Rasmussen and Williams, 2006](#)) as in [Oppermann et al. \(2013\)](#),

$$\begin{aligned} \log P(\mathbf{p}|\mathbf{V}, \boldsymbol{\beta}) = & \frac{1}{2} \mathbf{j}^T \mathbf{D} \mathbf{j} + \frac{1}{2} \log |\mathbf{D}| - \frac{1}{2} \log |\mathbf{S}(\mathbf{p})| \\ & - \sum_k \left[(\alpha - 1) \log p_k + \frac{p_0}{p_k} \right] - \frac{1}{2} \log(\mathbf{p})^T \frac{\mathbf{T}}{\sigma_s^2} \log(\mathbf{p}) \\ & + \text{const.} \end{aligned} \quad (2.39)$$

(see also [Enßlin and Frommert, 2011](#)). Finding the maximum entails finding the location where the derivative of Equation 2.39 with respect to $\log p_k$,

$$\begin{aligned} \frac{d \log P(\mathbf{p}|\mathbf{V}, \boldsymbol{\beta})}{d \log p_k} = & \frac{1}{2p_k} \left[\left(\mathbf{Y}_f(\boldsymbol{\mu}\boldsymbol{\mu}^T + \mathbf{D})\mathbf{Y}_f^T \right)_{kk} \right] - \frac{1}{2} \\ & - \left[(\alpha - 1) - \frac{p_0}{p_k} \right] - \left(\frac{\mathbf{T}}{\sigma_s^2} \log \mathbf{p} \right)_k, \end{aligned} \quad (2.40)$$

is zero. We find the maximum using the fixed point iteration

$$\begin{aligned} \left(\mathbf{I} + \frac{\mathbf{T}}{\sigma_s^2} \right) \log \mathbf{p}^{\text{new}} = & \log \mathbf{p} \\ & + \frac{1}{p_i} \left[p_0 + \frac{1}{2} \text{diag} \left(\mathbf{Y}_f(\boldsymbol{\mu}\boldsymbol{\mu}^T + \mathbf{D})\mathbf{Y}_f^T \right) \right] - \left[(\alpha - 1) + \frac{1}{2} \right] \end{aligned} \quad (2.41)$$

(recall that \mathbf{I} is the identity matrix). Here the application of the $\text{diag}(\mathbf{M})$ operator to a matrix should be understood as selecting the vector formed from the diagonal elements of that matrix. At each iteration $\boldsymbol{\mu}$ and \mathbf{D} are computed using \mathbf{p} from the previous iteration, and the linear system is solved using a sparse linear solver. Each iteration requires $\mathcal{O}(N^3)$ operations. The iterations are terminated when the relative change in \mathbf{p} is $< 10^{-3}$. We have confirmed with tests that the final solution is not sensitive to the initial choice of \mathbf{p} ; we use as an initialization a power law with slope of -2 to coarsely match the typical decline in visibility amplitude as a function of baseline in high resolution ALMA observations.

For the final reconstructed brightness profile, we use our best-fitting (maximum a posteriori) values for the power spectrum coefficients \mathbf{p}_{MAP} in Equation 2.29. This provides

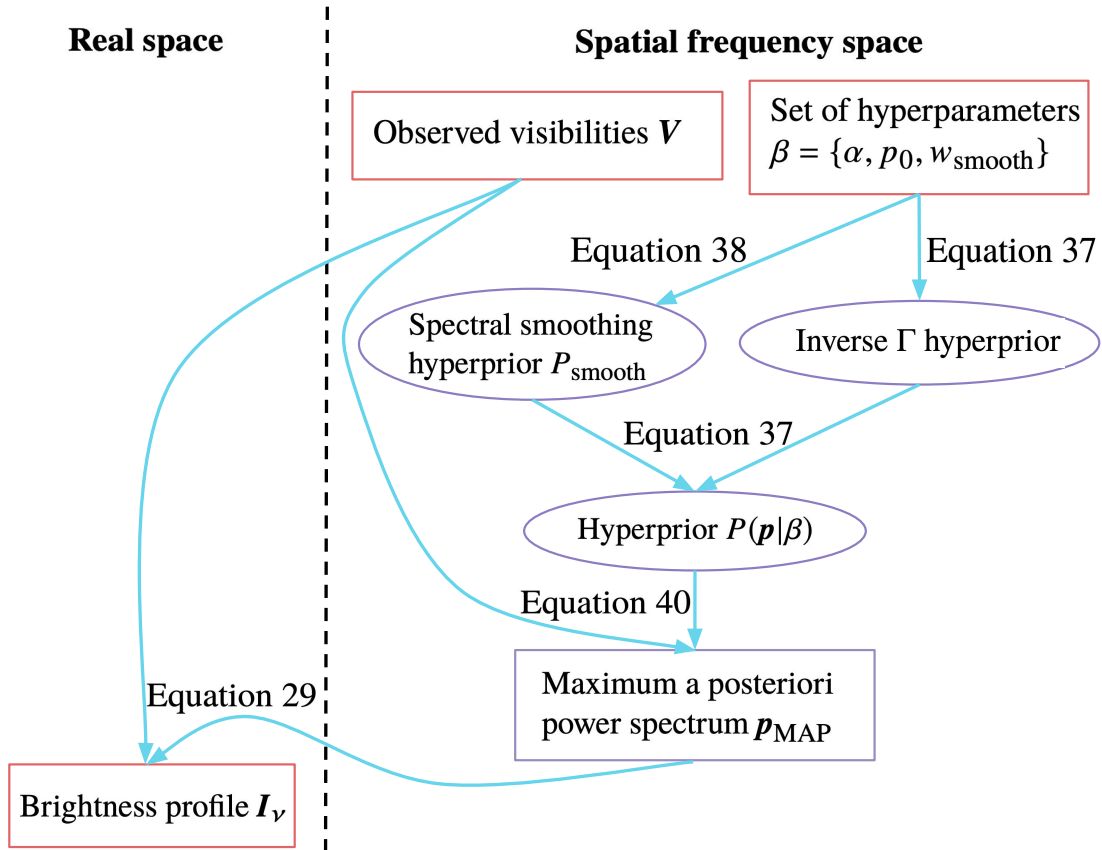


Fig. 2.3. Model framework

Diagram of the probabilistic model framework in frank. Squares represent variables, purple indicates the quantity is either a hyperprior or a prior (note p_{MAP} is an inferred variable that is used as a prior). The set of hyperparameters β determine the hyperpriors placed on the power spectrum reconstruction from V , yielding p_{MAP} . This is then used as a prior for the reconstruction of I_v from V .

our estimate for the profile's mean μ and covariance \mathbf{D} . In general $\text{diag}(\mathbf{D})$ will underestimate the uncertainty on the brightness at each collocation point, as discussed in Sec 2.2.7. We summarize the overall model framework diagrammatically in **Fig. 2.3**.

2.2.5 p_{MAP} and its use as a prior on I_v

The maximum a posteriori power spectrum p_{MAP} tends to one of two limiting forms, depending primarily on the visibility SNR at each spatial frequency. To understand this we consider the converged maximum a posteriori values (i.e., $\log p^{\text{new}} = \log p$), neglecting the spectral smoothness hyperprior for now ($w_{\text{smooth}} \rightarrow 0$).

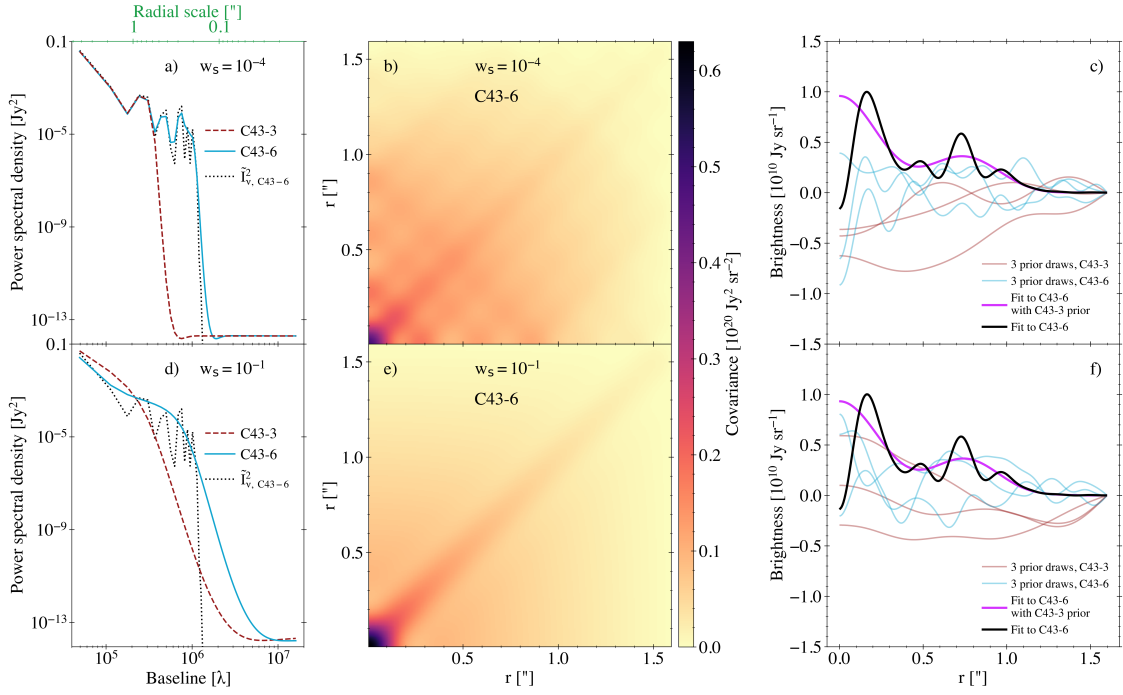


Fig. 2.4. Effect of the hyperparameter w_{smooth}

a) Maximum a posteriori power spectra \mathbf{p}_{MAP} for a multi-Gaussian mock disk observed separately with the ALMA C43-3 (synthesized beam FWHM $0.59 \times 0.70''$, Briggs=0.5) and C43-6 (beam FWHM $0.13 \times 0.17''$, Briggs=0.5) configurations (see Table 2.2). These \mathbf{p}_{MAP} are obtained for each dataset using $P(\mathbf{p}|\mathbf{V}, \boldsymbol{\beta})$, the frank posterior marginalized over all realizations of \mathbf{I}_v , under the hyperparameters $\boldsymbol{\beta} = \{\alpha, p_0, w_{\text{smooth}}\} = \{1.05, 10^{-15} \text{ Jy}^2, 10^{-4}\}$. For comparison the power spectrum estimate $\tilde{\mathbf{I}}_{v, \text{C43-6}}^2 = (\mathbf{Y}_f \mathbf{I}_{v, \text{C43-6}})^2$ based on the frank fitted brightness profile for the C43-6 dataset is shown.

b) Real space representation of the covariance matrix $\mathbf{S}(\mathbf{p}_{\text{MAP}})$ for the C43-6 configuration (that for the C43-3 looks qualitatively similar), showing covariance between not only adjacent but also nonadjacent points. The overall covariance decreases from the lower left to upper right because the disk brightness as represented in the visibilities decreases (on average) as a function of disk radius.

c) Draws from the prior on the brightness distribution $\mathcal{G}(\mathbf{I}_v, \mathbf{S}(\mathbf{p}_{\text{MAP}}))$ for both the C43-3 and C43-6 datasets. For reference the posterior mean (the frank fit for the brightness profile, Equation 2.29) is shown for the C43-6 dataset, separately realized using \mathbf{p}_{MAP} estimated from the C43-6 and C43-3 dataset.

d) – f) As in (a) – (c) but using $w_{\text{smooth}} = 10^{-1}$ to generate the power spectra, which are comparatively smooth in response to this stronger hyperparameter value, resulting in reduced covariance between nonadjacent points but higher covariance between adjacent points in $\mathbf{S}(\mathbf{p}_{\text{MAP}})$ as visualized in (e). The reduced covariance between nonadjacent points in (e) relative to (b) results in draws from the prior in (f) that show fewer small amplitude oscillations on corresponding spatial scales. However the effect on the posterior mean frank fit is small, indicating the relative insensitivity of the recovered brightness profile to the value of the hyperparameter w_{smooth} .

First, at spatial frequencies where the visibility SNR is sufficiently high, the term involving the mean $\boldsymbol{\mu}$ in Equation 2.41 dominates and thus

$$\mathbf{p}_{\text{MAP}} = \frac{(\mathbf{Y}_f \boldsymbol{\mu})^2}{1 + 2(\alpha - 1)}. \quad (2.42)$$

In this case the power spectrum is set by an estimate using the DHT of the mean brightness profile, which is approximately the square of the visibility amplitude (its power). This demonstrates the aforementioned association between \mathbf{p}_{MAP} and the power spectrum and provides the justification for calling \mathbf{p}_{MAP} the power spectrum.

Conversely, where the visibility SNR is sufficiently low, \mathbf{p}_{MAP} is small enough that the $\mathbf{S}(\mathbf{p})$ term in \mathbf{D} dominates. In this case

$$\mathbf{p}_{\text{MAP}} = \frac{p_0 + \frac{1}{2} \text{diag}(\mathbf{Y}_f \mathbf{S}(\mathbf{p}) \mathbf{Y}_f^T)}{\alpha - 1 + 1/2} \sim \frac{p_0 + \mathbf{p}_{\text{MAP}}/2}{\alpha - 1 + 1/2} \sim \frac{p_0}{\alpha - 1/2}. \quad (2.43)$$

The SNR threshold that separates these behaviors depends on α (Sec. 2.6); at $\alpha = 1$ the threshold is at SNR = 1, and the threshold increases as α increases (because for larger α , the inverse Γ hyperprior decays faster with increasing p_k). Thus given the same data, a larger α will cause p_k to be pulled more strongly downward toward p_0 .

Secondary to the effect of the visibility SNR, the spectral smoothness hyperprior modifies the power spectrum. Fig. 2.4(a) and (d) (presented below) demonstrate that increasing w_{smooth} reduces structure in the power spectrum, driving its shape toward a power law. A similar effect is evident in Fig. 2.5 (presented in Sec. 2.2.6), where the oscillations in the power spectrum under a Jeffrey's prior (using $w_{\text{smooth}} = 0$) are large compared with those generated under $w_{\text{smooth}} = 10^{-4}$. This demonstrates that in regions of low SNR at long baseline, the constraint of a smooth power spectrum can dominate the inverse Γ hyperprior's preference for low p_i . Though this is typically isolated to the case of $\alpha = 1$, because the inverse Γ hyperprior does not damp the power spectrum coefficients under this choice.

Given a form for the maximum a posteriori power spectrum \mathbf{p}_{MAP} , we now consider its effects as a prior on the reconstructed brightness profile I_ν . **Fig. 2.4** shows multiple power spectra generated using `frank` fits to the mock brightness profile in Fig. 2.2. Under different ALMA configurations and values of w_{smooth} , the power spectra in Fig. 2.4(a) and (d) are truncated (drop off) at different maximum baselines (and thus minimum spatial scales) and also show different degrees of smoothness. The covariance matrices $\mathbf{S}(\mathbf{p})$ in Fig. 2.4(b) and (e), and the draws from the prior $P(I_\nu | \mathbf{p})$ in Fig. 2.4(c) and (f), then motivate the two effects that \mathbf{p}_{MAP} has as a prior on I_ν .

First, because the power spectra have little power on long baselines, the prior draws are correlated on small spatial scales. The shortest length scale over which a brightness profile is correlated is controlled by the longest baseline at which the prior has significant power. In contrast, because the amplitude of the power spectra is large on short baselines, the large scale form of the brightness is free to vary, with the posterior brightness on these scales being ultimately determined by the data rather than the prior. If instead adjacent points were not correlated (if the prior were diagonal in real space), the prior draws would not appear smooth. Fig. 2.4(c) and (f) additionally show the posterior means (Equation 2.29) – the fitted brightness profiles for the C43-6 mock data using either the C43-3 or C43-6 prior – which reflect constraints introduced by the priors. For each of the priors, the mean matches the true (input) brightness on large scales, but only shows structure on the scales allowed by the prior. For the priors generated under the C43-3 mock observations, the power on long baselines is thus too strongly damped, and the reconstructed profiles are a poor recovery of the input profile. By contrast the reconstructed profiles using the C43-6 priors recover the input profile to high accuracy. This emphasizes the importance of correctly identifying the scale on which to regularize the brightness profile so as not to damp the fit on scales where true variations exist in the visibility distribution.

Second, substructure in the power spectrum causes differences in the real space representation of the prior. The localized areas of lower power in the structured power spectra of Fig. 2.4(a) introduce correlations between nonadjacent radial collocation points at the corresponding spatial scales. This correlation manifests as the crosshatching in Fig. 2.4(b), and consequently draws of I_ν from the prior in Fig. 2.4(c) are more oscillatory than those in (f), for which the power spectra are smooth. However because this increased correlation corresponds to baselines at which the visibility amplitude is also small, the impact on the posterior mean brightness profiles in Fig. 2.4(c) is small. This need not be the case generally, but is typical of the power spectra generated by `frank` because these regions of low power have been determined from the visibilities. The power spectrum estimate $\tilde{I}_{\nu, C43-6}^2$ in Fig. 2.4(a) and (d) further demonstrates this relative insensitivity. The comparatively large discrepancy between it and p_{MAP} in Fig. 2.4(d) relative to that in (a) is a result of the power spectrum estimate using $w_{\text{smooth}} = 10^{-1}$ having higher amplitudes than that using $w_{\text{smooth}} = 10^{-4}$ and thus providing a weaker constraint on the reconstructed brightness profile, yet this does not correspond to a less accurate brightness profile reconstruction in (f) relative to that in (c).

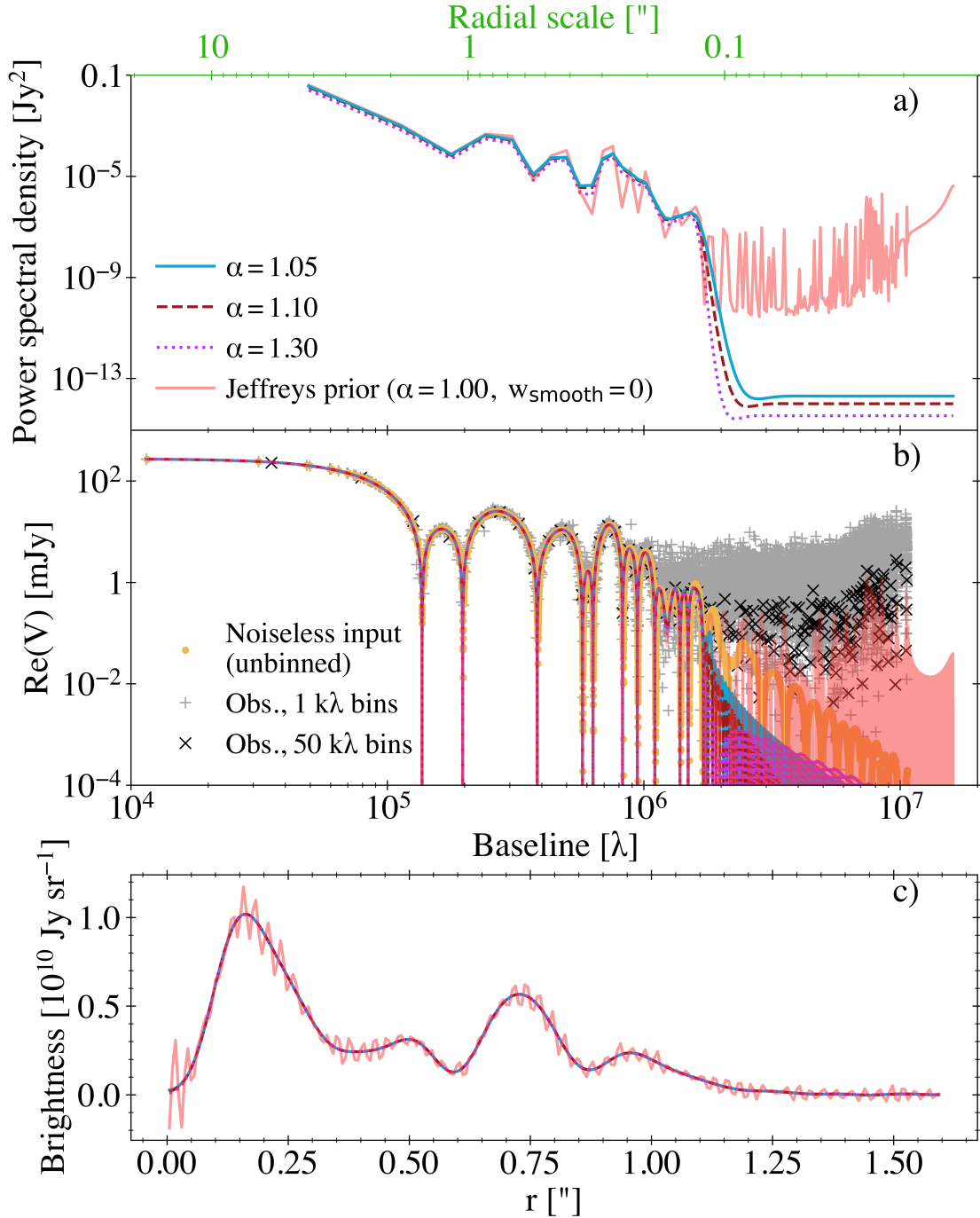


Fig. 2.5. Effect of the hyperparameter α ; effect of a Jeffreys prior

a) Maximum a posteriori power spectra p_{MAP} (under different values of the α hyperparameter) for frank fits to the mock disk in Fig. 2.4, here observed with the ALMA C43-6 + C43-9 configurations (beam FWHM $0.024 \times 0.030''$, Briggs=0.5; see Table 2.2). Also shown is p_{MAP} under a Jeffreys prior.

b) The mock observation's noisy visibilities in 1 and 50 k λ bins and the true, unbinned visibility distribution (the Hankel transform of the input profile). Also shown are the frank fits to the unbinned, noisy data and the fit under a Jeffreys prior (which forces the fit to the longest baseline, noise-dominated visibilities, imprinting oscillations on the corresponding brightness profile in (c)).

c) The fitted frank brightness profiles for the cases in (a) – (b). Varying α has a negligible effect on the fit, while the Jeffreys prior (flat in log space) allows oscillations on spatial scales corresponding to the noise-dominated visibility region (beyond $\approx 1.5 \text{ M}\lambda$).

Table 2.1. Model hyperparameters, their default values, and reasonable ranges to optionally vary these (discussed in Sec. 2.2.6).

Hyperparameter	Default value (suggested range)	Referenced in
Brightness profile hyperparameters		
N , number of collocation points	300 (100 – 300)	Text following Equation 2.8
R_{out} , fit's maximum radius	2'' ($\approx 1.5 \times$ disk's outer edge)	Equation 2.3
Maximum a posteriori power spectrum hyperparameters		
α , order parameter for the power spectrum's inverse Γ distribution hyperprior	1.05 (1.00 – 1.30)	Equation 2.38
p_0 , scale parameter for the power spectrum's inverse Γ distribution hyperprior	10^{-15} Jy^2 ($> 0, \ll 1$)	Equation 2.36
w_{smooth} , strength of smoothing applied to the power spectrum	10^{-4} ($10^{-4} - 10^{-1}$)	Equation 2.37

2.2.6 The reconstructed brightness profile’s sensitivity to the hyperparameters

Our model for the deprojected brightness profile has five free hyperparameters: two specifying the radial points at which the profile is reconstructed, N and R_{out} ; and three on the power spectrum, denoted collectively as $\boldsymbol{\beta} = \{\alpha, p_0, w_{\text{smooth}}\}$, where $w_{\text{smooth}} = 1/\sigma_s^2$ (analogous to the definition of the visibility weights). Definitions, default values and reasonable bounds to optionally vary these hyperparameters are summarized in **Table 2.1**. Here we motivate the default values and discuss the fit’s sensitivity to these choices.

We have found the reconstructed brightness profile to be insensitive to R_{out} and N so long as they are sufficiently large, and also to p_0 so long as it is small relative to the power in the visibilities ($\ll 1$). The default $R_{\text{out}} = 2''$ is sufficiently large for a protoplanetary disk. Alternatively if the disk radius is known, R_{out} can be set to a value somewhat (e.g., 50%) larger than this, the main constraint being that the model assumes the flux is 0 beyond R_{out} . By default N is set to 300 points to ensure that Q_{max} exceeds the maximum baseline in a dataset (which is important for fit stability).

The hyperparameters α and w_{smooth} do not appear directly in Equation 2.29; their effects on the brightness profile reconstruction enter entirely through their effects on p_{MAP} .

As motivated in Sec. 2.2.5, increasing w_{smooth} reduces structure in the fit’s power spectrum, reducing correlation in the brightness profile at scales for which the power spectrum has low local amplitude, while increasing correlation between adjacent radial collocation points. However we have demonstrated in Fig. 2.4 that varying w_{smooth} within sensible bounds often has a negligible effect on the frank reconstructed brightness profile. As also discussed in Sec. 2.2.5, increasing α beyond 1.0 increases the SNR threshold below which the power spectrum falls toward p_0 , damping variations in the brightness profile on scales where the visibility SNR is low (primarily at unconstrained scales beyond a dataset’s longest baseline).

Fig. 2.5 examines a fit’s typical sensitivity to the value of α . With $\alpha = 1.00$ (not a recommended value, shown only for pedagogy), frank will fit noise-dominated data, introducing noise into the reconstructed brightness, as in the Jeffreys prior fit in Fig. 2.5 that is placing significantly more power in baselines beyond $\approx 2 \text{ M}\lambda$ than exists in the noiseless input visibilities. Increasing α to 1.05 is a conservative choice, mildly damping the power on scales where the SNR is low (causing the corresponding fit in Fig. 2.5 to walk off the data at $\approx 1.5 \text{ M}\lambda$). This value of 1.05 is our default choice for α because many moderate to high resolution ($\gtrsim 0.1 \text{ M}\lambda$) datasets for protoplanetary disks exhibit noise-dominated visibilities at their longest baselines (a consequence of sampling density decreasing strongly at the most extended ALMA configurations for typical integration times). Further increasing α will more aggressively damp power on scales with low SNR, though in some cases this can lead to the

Table 2.2. Observational quantities for all *mock* datasets. All mock observations observe at 230 GHz (1.3 mm) with 7.5 GHz continuum bandwidth.

Mock observational setup	ALMA configuration (all in Band 6)	Synthesized beam FWHM [mas] (longest baseline [$10^6 \lambda$])	Integration time [min] (sampling time [s])	Peak I [$10^{10} \text{ Jy sr}^{-1}$] (integrated I [$10^{10} \text{ Jy sr}^{-1}$])
Mock profiles shown in Fig. 2.7				
low resolution	C43-3	590×700 (≈ 0.4)	2 (10)	1.00 (0.25 – 0.51)
moderate resolution	C43-6	130×170 (≈ 2)	10 (10)	1.00 (0.25 – 0.51)
high resolution	C43-6 + C43-9	24×30 (≈ 10)	10 + 50 (10)	1.00 (0.25 – 0.51)
Mock profile based on AS 209				
low noise	C43-7	86×106 (≈ 3)	40 (10)	5.00 (0.87)
moderate noise	C43-7	86×106 (≈ 3)	2 (10)	5.00 (0.87)
high noise	C43-7	86×106 (≈ 3)	1 (10)	5.00 (0.87)

fit attaining a lower effective resolution (if a significantly wider range of scales are damped). That said, comparing the $\alpha = 1.05$, 1.10 and 1.30 fits in Fig. 2.5 shows that varying α within sensible bounds often has an insignificant effect on the brightness profile, especially if the visibilities' SNR is dropping rapidly at long baselines. For a scenario in which varying α has a more significant impact, we will consider a disk with sub-beam features sampled at low SNR over a wide range of baselines in Fig. 2.9 (presented in Sec. 2.3.1.2).

In our tests the effect on the brightness profile of varying α and/or w_{smooth} is thus often trivial. Nonetheless, as a precaution *we recommend varying the hyperparameters used in a fit within sensible bounds* (see Table 2.1) *to assess the brightness profile's resulting sensitivity*. We have found that especially for lower resolution datasets, setting α and/or w_{smooth} too high can average over real, underresolved features, causing them to appear broader and shallower. Hence our default values for these hyperparameters are at the lower bound of our suggested ranges in Table 2.1.

2.2.7 Model limitations

1. Our axisymmetric model is 1D, fitting for the azimuthal average of the visibility data at each spatial scale. In the presence of deviations from axisymmetry the model is thus biased. For mild asymmetries the effect is not severe, averaging over brightness asymmetries azimuthally. However for major asymmetries (such as a prominent spiral) and/or when (u, v) coverage results in broad gaps over a given baseline range, the model can break down. This also holds for observations in which there is more than one source.
2. Since a centered axisymmetric model has only real visibilities, we do not fit $\text{Im}(V)$.
3. The model makes the flat sky approximation (Equation 1.15), which assumes that the observation's region of the sky is sufficiently small.
4. Before fitting for the brightness profile, the visibilities must first be deprojected and phase-centered. `frank` can optionally do this by fitting a 2D Gaussian to the visibilities, though this deprojection operation may yield an erroneous result if a disk has an appreciable vertical thickness or if limb darkening from the optically thick surface is important.
5. The fitted brightness profile does not include primary beam correction. For sources that were observed close to the center of the primary beam, the correction is typically small and can be obtained by dividing the reconstructed brightness profile by the primary beam profile $\mathcal{A}(\theta)$, where θ is the radial angular coordinate.

6. Regions in the visibilities with sparse and/or sufficiently noisy sampling can cause a lack of constraint on the local spatial frequency scale, inducing oscillations in the brightness profile on the corresponding spatial scale. This can potentially mimic real structure. The model typically prevents this by damping power on scales with low SNR, but when it does occur the oscillations in the brightness profile can be diagnosed by their frequency, which corresponds to the unconstrained spatial frequency scale. *Varying the hyperparameter values for a fit as noted in Sec. 2.2.6 is useful to assess and potentially suppress this behavior.*
7. The uncertainty on the fitted brightness profile is typically underestimated. For this reason we do not show the uncertainty on frank brightness profiles in this chapter. The model framework produces an estimate of the uncertainty on the brightness profile (diag (**D**)), but this is not reliable because reconstructing the brightness from Fourier data is an ill-posed problem. For example if the visibility amplitude were to spike at any point beyond the data’s maximum baseline, this would imprint high amplitude variations in the brightness profile on small spatial scales. Unless we know a priori (which is not generally the case) that the visibilities are decreasing sufficiently rapidly with increasing baseline, the uncertainty is therefore formally infinite. While it is reasonable to assume that for real disk brightness profiles the visibilities do decrease rapidly at long baseline, it is not straightforward to generically extrapolate the slope of this decline beyond a dataset’s longest baseline; a robust error estimate is thus difficult to obtain.

Fig. 2.6 shows the frank uncertainty estimate, diag (**D**) estimated at the maximum a posteriori power spectrum, for the mock Gaussian ring presented in Sec. 2.3.1. This confidence interval approximately represents the fit’s statistical uncertainty (that due to the uncertainty on the observed baselines), which is correct if the visibility weights are an accurate representation of the pointwise visibility uncertainty. But the confidence interval does not capture the fit’s ill-defined systematic uncertainty (that due to sparse sampling in the (u, v) plane). A bootstrap on the visibilities in Fig. 2.6 also fails to yield a reasonable estimate of the systematic uncertainty. Though this does confirm that diag (**D**) is a reasonable estimate of the statistical uncertainty. *We therefore urge caution before using uncertainty estimates to interpret the significance of the result in the recovered profile.*

To test whether including the uncertainty on p has a significant effect on the final uncertainty of the reconstructed brightness, we used the estimate for the uncertainty on p given by [Oppermann et al. \(2013\)](#). We translated the effect of this on the

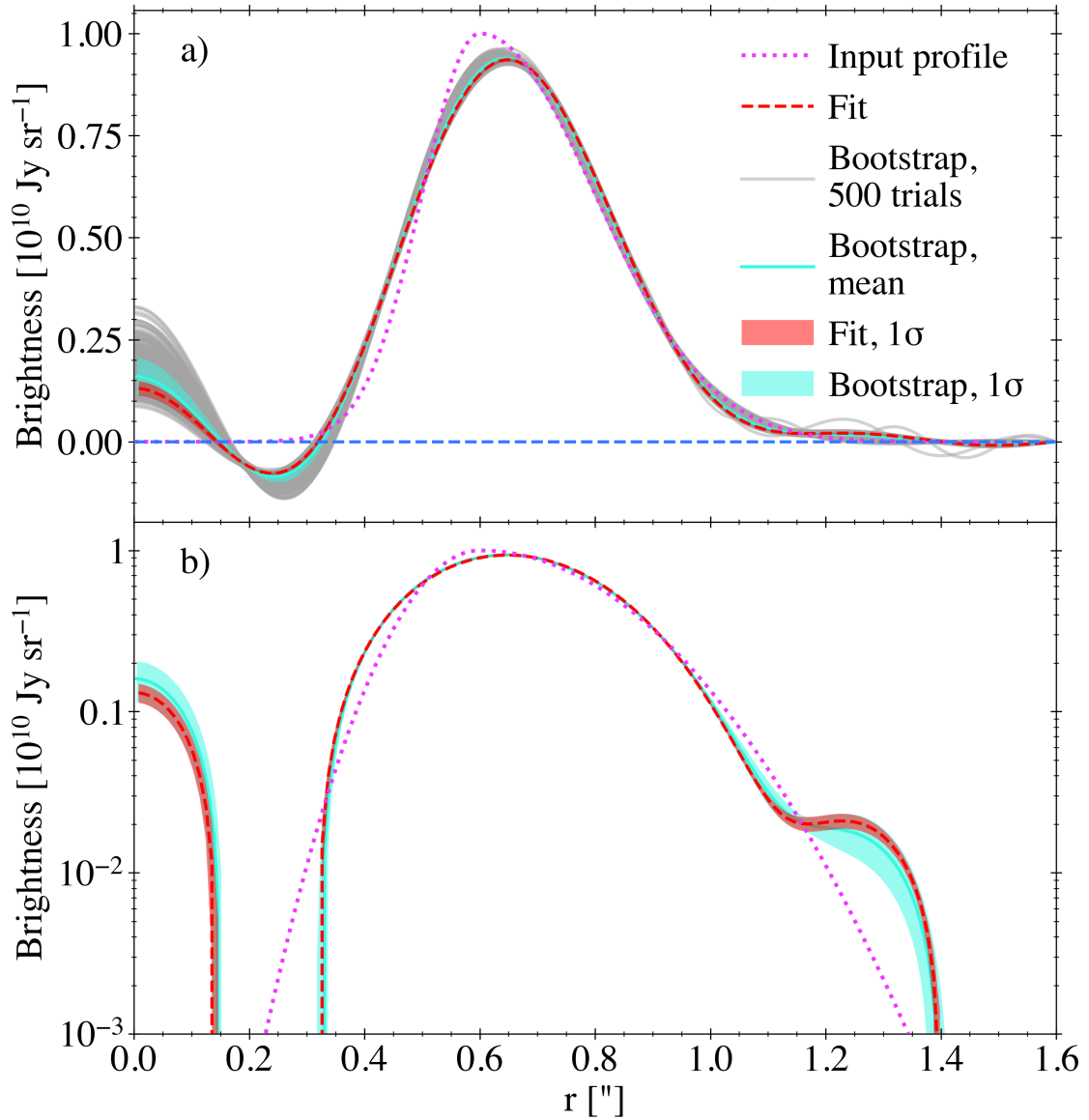


Fig. 2.6. Underestimated model uncertainty

a) Input and reconstructed brightness profiles for a mock Gaussian ring (two joined sigmoids) observed with the ALMA C43-3 configuration (synthesized beam FWHM $0.59 \times 0.70''$, Briggs=0.5; see Table 2.2). The fit's 1σ uncertainty estimate, diag (**D**) estimated at the maximum a posteriori power spectrum, is shown. Additionally shown are 500 realizations of bootstrapping on this mock dataset, as well as the resulting distribution's mean and 1σ uncertainty. Both the frank fit's uncertainty and the bootstrap uncertainty are clearly underestimated as discussed in Sec. 2.2.7.

b) As in (a) on a logarithmic scale.

brightness profile by Taylor expanding $P(\mathbf{V}, \mathbf{p})$ about its maximum to make a Gaussian approximation to $P(\mathbf{V}, \mathbf{p})$. Using this approximation, we then drew samples and compared the variance of the reconstructed brightness at each radial collocation point to that estimated by $\text{diag}(\mathbf{D})$. Except for an uninformative Jeffreys prior ($\alpha = 1.0$ and $w_{\text{smooth}} = 0$), the effect was negligible.

8. The fitted brightness profile can have negative regions corresponding to spatial scales un- or underconstrained by the visibilities. There is an argument for choosing a fitting strategy that enforces the solution be nonnegative (as in [Junklewitz et al. 2016](#)), and we have investigated the effect of negative fit regions by finding the most probable nonnegative intensity profile given $\mathbf{p} = \mathbf{p}_{\text{MAP}}$. The effect on the recovered brightness profile is localized to the regions of negative flux, with otherwise minor differences. We explore a pedagogical nonnegative fit in Sec. 2.7.

2.2.8 Code performance

The code’s computation time is dominated by two components, constructing the matrix \mathbf{M} and iterating the fit. The construction of \mathbf{M} is only done once at the start of the fit and has computational cost $\mathcal{O}(N_{\text{collocation points}}^2 N_{\text{visibilities}})$, while solving the linear systems in each iteration scales as $\mathcal{O}(N_{\text{collocation points}}^3) \sim 100^3$.

To limit memory requirement, the matrix \mathbf{M} is assembled in blocks, avoiding the need to hold the $N_{\text{collocation points}} \times N_{\text{visibilities}}$ matrix $\mathbf{H}(\mathbf{q})$ in memory. Typical computational requirements were estimated using real datasets: with 10^4 visibilities and 200 collocation points the fit took 10 s and used ≈ 100 MB, while with 10^6 visibilities it took 40 s and used ≈ 200 MB. These tests were conducted on a 2017 MacBook Pro with a 7th generation Intel Core i5 processor (7360U) running at 2.3 GHz with 8 GB RAM.

2.3 Demonstration & analysis

2.3.1 Demonstration on mock observations

2.3.1.1 Fits can attain sub-beam resolution

To demonstrate frank’s fitting approach and characterize its performance, we begin in [Fig. 2.7](#) with a series of mock observations for disks of archetypal smooth and sharp structure at both well resolved and underresolved scales. We generate these mock datasets using the default fit hyperparameters in [Table 2.1](#) and the observational setups in [Table 2.2](#).

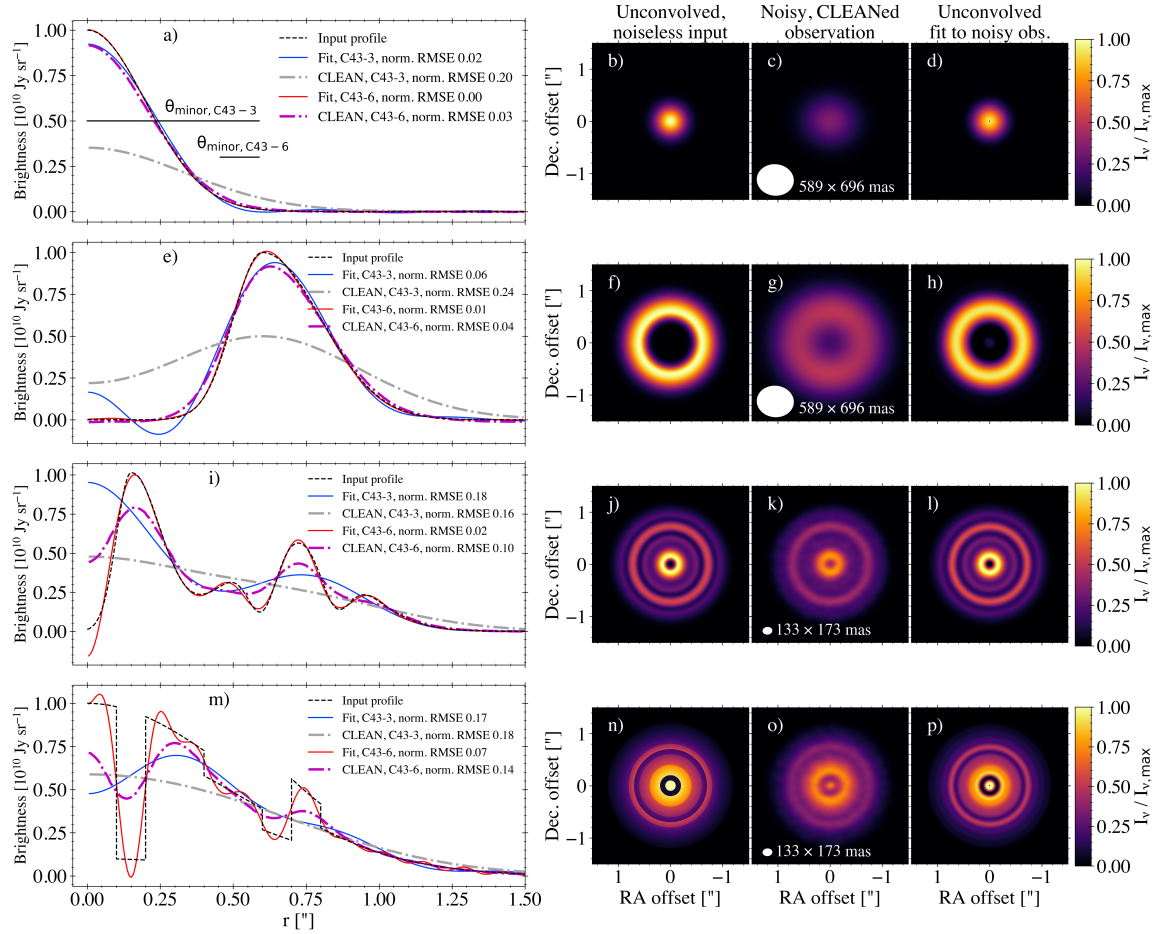


Fig. 2.7. Performance on different disk morphologies using mock observations

a) Input and reconstructed brightness profiles for a mock Gaussian disk with FWHM $0.2''$, observed separately with the ALMA C43-3 (synthesized beam FWHM $0.59 \times 0.70''$, Briggs=0.5) and C43-6 (beam FWHM $0.13 \times 0.17''$, Briggs=0.5, factor of 5 longer integration time than C43-3; see Table 2.2) configurations. The beams' minor axes are shown for reference. The frank fit to each of the 2 mock observations is shown, as are CLEAN image-extracted profiles. The normalized RMS error of each profile is given.

b) Input profile swept over 2π , noiseless and at infinite resolution.

c) Mock CLEAN image (C43-3 + noise), with brightness normalized to (b).

d) Image of the frank fit to the noisy C43-3 mock observation, *not* convolved with the beam, with brightness normalized to (b).

e) – h) As in (a) – (d) but for a Gaussian ring (two joined sigmoids) with width $\approx 0.4''$.

i) – l) As in (a) – (d) but for a more complicated, smooth-featured disk. The feature widths vary from $0.10 - 0.15''$. The images correspond to the C43-6 observation.

m) – p) As in (i) – (l) but for a disk with step features, the narrowest of which is $0.1''$.

Fig. 2.7(a) compares the brightness reconstructed by `frank` to the CLEAN image-extracted profile for a Gaussian disk centered at 0. The Gaussian’s width is resolved by the CLEAN beam for the C43-6 ALMA configuration, yet importantly the CLEAN profile is slightly too broad and shallow as a result of beam convolution⁴. By comparison `frank` recovers the profile to <1% RMS error (note this is the standard definition of RMS error, unrelated to the RMS noise in a CLEAN image). For the same disk observed at the lower resolution C43-3 configuration, the beam’s minor axis underresolves the Gaussian by a factor of 2.3, and the effect of beam convolution on the CLEAN profile is exacerbated. The `frank` fit by comparison retains high accuracy, comparable to the CLEAN profile from the C43-6 observation. Fig. 2.7(b) – (d) show the 2D images for the C43-3 case, with the `frank` image recovering the input image from the noisy, low resolution observation. This simple Gaussian case illustrates that because the model does not at any stage require beam convolution, `frank`’s *achievable resolution is sub-beam*.

Fig. 2.7(e) – (h) next consider a slightly more complex disk, a Gaussian ring. Here again the `frank` fit to the C43-3 observation achieves a similar accuracy to the CLEAN profile extracted from the higher resolution C43-6 dataset. This is despite the C43-3 beam’s minor axis underresolving the Gaussian by a factor of ≈ 1.5 . The `frank` profile reconstructed from the C43-3 dataset does however misidentify the Gaussian’s centroid and also shows a region of negative brightness allowed by the model as detailed in Sec. 2.2.7. We discuss a fit with enforced brightness positivity for this disk in Sec. 2.7.

As well as reproducing simple profiles, `frank` adapts effectively to more complicated disks such as that in Fig. 2.7(i) – (l). Here the C43-3 beam’s minor axis is a factor of >3 broader than the profile’s widest feature, and `frank` is unable to reconstruct the profile accurately. However it does discern that there are two well-separated peaks, while the CLEAN profile does not show any substructure. Increasing the resolution to C43-6, `frank` retains its resolving power advantage, recovering the input brightness profile to high accuracy.

To strain the model, Fig. 2.7(m) – (p) introduces perfectly sharp-edged features (step functions) to be recovered. `frank` fits this disk to reasonable fidelity in the C43-6 case but does show some oscillations. These are a consequence of Gibbs phenomenon, which arises when representing an infinitely sharp feature in Fourier space. By comparison the CLEAN profiles at both resolutions do not show these oscillations, but do smear the disk features over the beam. `frank`’s ability to recover arbitrarily sharp features with comparatively low error

⁴As a simple illustration of this effect, noiseless Gaussians with FWHM 25, 50, 75, and 100 mas would respectively be broadened by convolution with a FWHM 50×50 mas Gaussian beam to FWHM 56, 71, 90, and 112 mas (a factor of 2.24, 1.42, 1.20, and 1.12 increase), and their amplitudes would be reduced to 45, 70, 83 and 89% their true values.

demonstrates utility in more accurately recovering a disk’s often steep outer edge and its peak flux.

Together these mock disks show `frank`’s ability to fit smooth and sharp, partially and well-resolved, faint and bright features, at sub-beam resolution. In practice this can enable similar fit resolution to a CLEAN profile obtained with a more extended array configuration (e.g., the `frank` fit to the C43-3 data in Fig. 2.7(a) is comparable to the CLEAN profile for the C43-6 data). The `frank` fits for all 8 mock datasets shown in Fig. 2.7 recover the disks’ total flux to within a mean 0.8% (standard deviation 0.2%), compared to a mean 1.6% (standard deviation 1.6%) for the CLEAN profiles. This error in total flux recovery increases as a disk’s features become increasingly sub-beam, an effect that is more severe for CLEAN than `frank`. All `frank` fits shown here are negligibly sensitive to the choice of hyperparameter values within the suggested ranges listed in Table 2.1. As discussed in Sec. 2.2.8 these fits – and all others shown in this chapter – are performed in $\lesssim 1$ min, and the computation speed is independent of the complexity of disk substructures; *frank fits simple and complicated disk profiles equally fast*.

To illustrate how `frank` is attaining a sub-beam fit resolution, **Fig. 2.8** characterizes its performance using a mock profile based on observational data rather than a simple functional form. We use the CLEAN image-extracted fit to the real DSHARP observations (C40-5/8/9 + archival short and moderate baseline datasets) of AS 209 ([Andrews et al., 2018](#)) as the input profile to be recovered from mock observations. This profile was obtained in that work with a beam of FWHM 36×38 mas; we generate the mock data at a factor of ≈ 2.6 worse resolution using the C43-7 configuration (beam FWHM 86×106 mas, see Table 2.2). Much of the structure in the profile is thus sub-beam in the mock observation. The mock visibilities’ SNR as a function of baseline is similar to the real dataset.

`frank` accurately recovers the input profile’s sub-beam features to within 1% RMS error for the noiseless case in Fig. 2.8(a) – (b). It shows minor difference between the fit under the default hyperparameter values and under values at the other extrema of our suggested range (Table 2.1) as shown in Fig. 2.8(c), despite the difference in prior structure in Fig. 2.8(f). The brightness profile recovery’s high fidelity is a result of the model fitting the visibility distribution in Fig. 2.8(d) – (e) to high accuracy. As in previous cases the CLEAN profile extracted from the C34-7 mock image underresolves these features. The `frank` fit recovers the mock disk’s total flux to within 0.6%, while the analogous CLEAN error is 30.4%. The nontrivial CLEAN error is primarily a result of the mock observations containing no baselines shorter than those in the ALMA C43-7 configuration; i.e., the nominal maximum recoverable scale for C43-7, Band 6 is $1.12''$ ([Remijan et al., 2019](#)), while the disk extends to $1.25''$. By comparison, `frank` is able to extrapolate the fit accurately to short baselines despite this

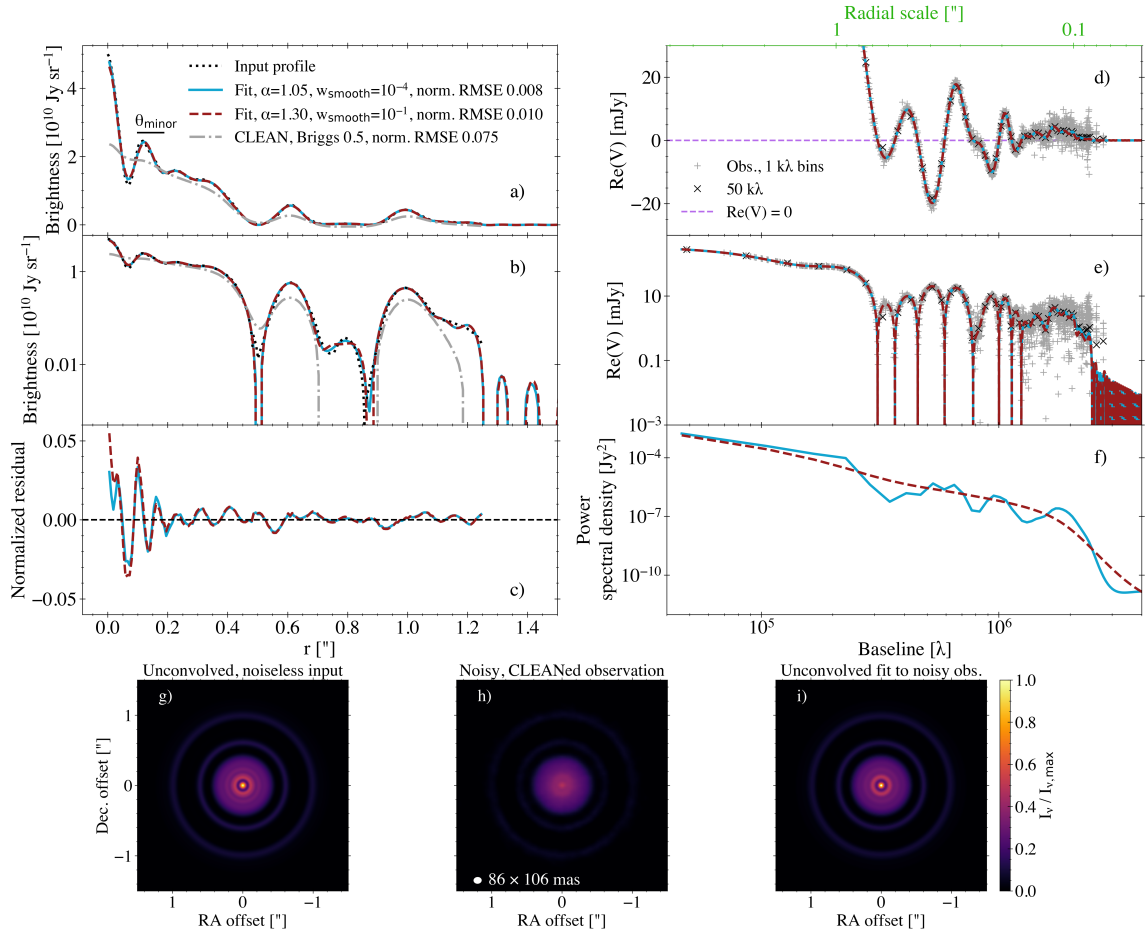


Fig. 2.8. Fit methodology using mock observations

a) Input and reconstructed brightness profiles under different hyperparameter values for a mock disk that uses as input the CLEAN image-extracted fit to the real DSHARP AS 209 observations (ALMA configurations C40-5/8/9, synthesized beam FWHM $36 \times 38 \text{ mas}$; Andrews et al. 2018). The mock observation uses only the C43-7 configuration (beam FWHM $86 \times 106 \text{ mas}$, Briggs=0.5; see Table 2.2). This beam’s minor axis is shown for reference. The CLEAN image-extracted profile for the mock C43-7 observation is also shown, with the normalized RMS error of all fits given.

b) As in (a) on a logarithmic y-scale. The fit’s oscillations beyond the disk’s outer edge indicate the model’s noise floor.

c) Normalized residual for the frank fits under different hyperparameter values.

d) Visibilities for the mock C43-7 observation in (a). The brightness profile fits in (a) are the discrete Hankel transforms of these visibility domain fits.

e) As in (d) on a logarithmic y-scale.

f) The fit’s maximum a posteriori power spectrum p_{MAP} for different hyperparameter values. These power spectra are used as the priors on the brightness profile reconstructions in (a).

g) Input profile swept over 2π , noiseless and at infinite resolution.

h) Mock CLEAN image (C43-7 + noise), with brightness normalized to (g).

i) Image of the frank fit to the noisy C43-7 mock observation, *not* convolved with the beam, with brightness normalized to (g).

lack of data (though this behavior may not always be robust). In Fig. 2.8(f) the maximum a posteriori power spectrum p_{MAP} has low power at the unconstrained spatial frequencies beyond the data’s longest baseline, preventing large amplitude oscillations in the reconstructed brightness profile at equivalent spatial scales (these oscillations, damped, are seen in the residuals of Fig. 2.8(c)). In Fig. 2.8(g) – (i) the 2D images of the input model, mock CLEANed observation and fit demonstrate the amount of structure `frank` is recovering that is smeared out by the beam.

*Beam convolution is the primary difference in achievable resolution between `frank` and CLEAN. Convoluting either `frank` fit in Fig. 2.8(a) – (b) with the 2D CLEAN beam yields a profile that is similar to the CLEAN profile. The CLEAN beam size does depend on the visibility weighting, with the choice affecting the resulting CLEAN profile. For the disk in Fig. 2.8, setting the Briggs robust parameter to -2.0 (approximating uniform weighting), 0.5 and 2.0 (natural weighting) sets the beam FWHM as $0.08'' \times 0.10''$, $0.09'' \times 0.10''$ and $0.10'' \times 0.12''$. However the resulting profiles vary only slightly, with the RMSE changing at most by 3%, and each profile still underresolves the disk features relative to `frank`. This highlights that *`frank` can recover disk features underresolved even by uniform weighting, while retaining high sensitivity.**

2.3.1.2 Baseline-dependent signal-to-noise determines the achievable fit resolution

We next characterize the model’s SNR sensitivity by decrementing the integration time for mock observations of the input profile from Fig. 2.8. This increasingly degrades the (u, v) coverage, in turn worsening the data’s effective SNR at a given baseline. **Fig. 2.9(a) – (b)** first show the method’s intrinsic capability by fitting the *noiseless* data, with the (u, v) coverage determined by the mock observation’s C43-7 configuration and integration time. The fits using both values for the α hyperparameter accurately match the full visibility distribution, the reconstructed brightness profiles showing $<1\%$ RMS error.

Then fitting the same baseline distribution but with the mock observation’s noise included in Fig. 2.9(c) – (d), both fits remain able to recover the noiseless visibilities to high accuracy. However as the data’s SNR worsens beyond $\approx 1.8 \text{ M}\lambda$ the fits do show some error, including tending toward 0 prior to the longest baselines. These errors manifest in the recovered brightness profiles in Fig. 2.9(c) as a slightly less accurate recovery of the peak brightness and of the innermost gap’s depth. The fit using the stronger $\alpha = 1.30$ is slightly less accurate at the longest baselines because the mock observations do not have sufficiently high SNR there for the model to fit them with $\alpha = 1.30$. However the differences in the reconstructed profile are minor for this case.

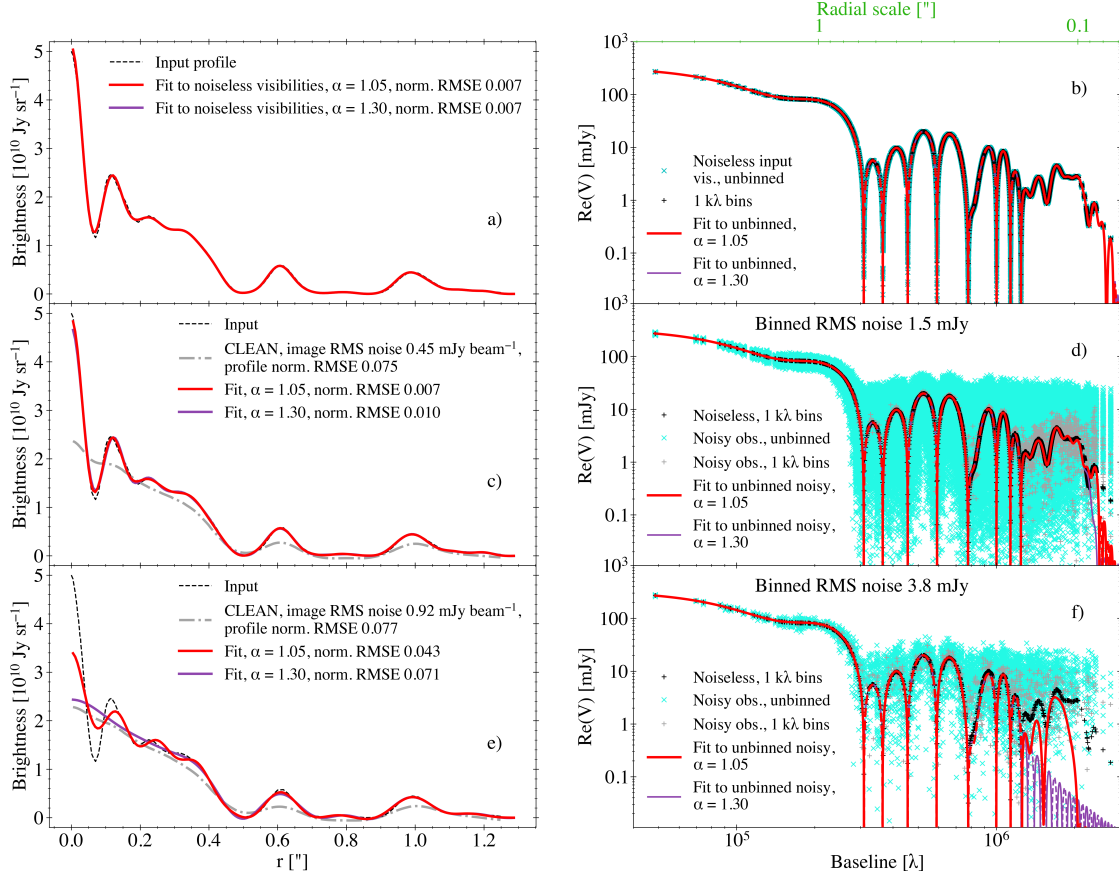


Fig. 2.9. Fit sensitivity to baseline-dependent SNR using mock observations

a) The input profile from Fig. 2.8 is used to generate noiseless mock observations, with frank fits to these noiseless data shown and their normalized RMS errors given under two values of the α hyperparameter (both fits use $w_{\text{smooth}} = 10^{-4}$).

b) Noiseless visibilities corresponding to the input profile in (a). frank fits the *unbinned* visibilities shown. Also shown are the data in 1 $k\lambda$ bins. The data (and the fits') negative regions are denoted by the fit lines' dashed sections. The $\alpha = 1.30$ fit is behind the $\alpha = 1.05$ fit.

c) – d) As in (a) – (b) but with noise added to the mock observation. The fits shown are to the unbinned, noisy data. The CLEAN image-extracted profile is shown for comparison. The apparently larger scatter in the observations in (d) (compared with (f)) is due to the larger number of data points rather than higher intrinsic error.

e) – f) As in (c) – (d) but with a higher RMS noise due to shorter integration time. The binned RMS noise (1 $k\lambda$ bins) does not increase dramatically because the number of empty bins has also increased.

As the integration time is further decremented in Fig. 2.9(e) – (f), the fits’ fidelity is degraded primarily beyond $\approx 1.2 M\lambda$ as the visibility distribution becomes more sparse. By consequence the highest resolution structural information – the depths and centroids of the narrowest features in the input brightness profile, including the peak brightness – are only partially recovered. The effect is more severe for the $\alpha = 1.30$ case because the data beyond $1.2 M\lambda$ have low effective SNR, and as α increases, the SNR threshold below which frank does not fit the visibilities increases. Since these data clearly contain meaningful information, $\alpha = 1.05$ is the more sensible choice.

In contrast to frank’s SNR sensitivity, the CLEAN image-extracted profiles in Fig. 2.9(c) and (e) vary marginally when the visibilities’ SNR is decreased. This is because convolution with the C43-7 beam, rather than the data’s SNR, is primarily limiting the CLEAN image resolution. While frank’s resolving power is sensitive to variations in the baseline dependence of the data’s SNR, the CLEAN profile is largely determined by the pure baseline distribution. This entails that *improving an observation’s SNR via the on-source integration time can significantly enhance the resolving capability of frank, while it may make little difference for CLEAN.*

2.3.2 Demonstration on real observations

Mock datasets are useful to test and characterize frank’s performance, though real data have more complex noise properties to which the model must also be well suited.

2.3.2.1 Sub-beam fits: Characterizing fine structure in real, high resolution observations

To this end **Fig. 2.10** demonstrates frank’s performance with real data, fitting the high resolution DSHARP observations of AS 209 (synthesized beam FWHM 36×38 mas ≈ 5 au at 121 pc)⁵.

Fig. 2.10(a) – (b) show the frank fit (using the default hyperparameter values) and the CLEAN image-extracted profile from [Andrews et al. \(2018\)](#). frank recovers additional substructure and higher amplitude features in the inner disk, a higher peak brightness, and slightly narrower rings in the outer disk. These results are consistent with those using mock observations in Sec. 2.3.1. That the frank fit finds a negative innermost gap indicates that

⁵We downloaded the AS 209 self-calibrated and multi-configuration combined continuum measurement sets from <https://bulk.cv.nrao.edu/almadata/lp/DSHARP>. Before extracting the visibilities using the `export_uvtable` function of the `uvplot` package ([Tazzari, 2017](#)), we applied channel averaging (to obtain 1 channel per spectral window) and time averaging (30 sec) to all spectral windows and multi-configuration datasets in the original MS table.

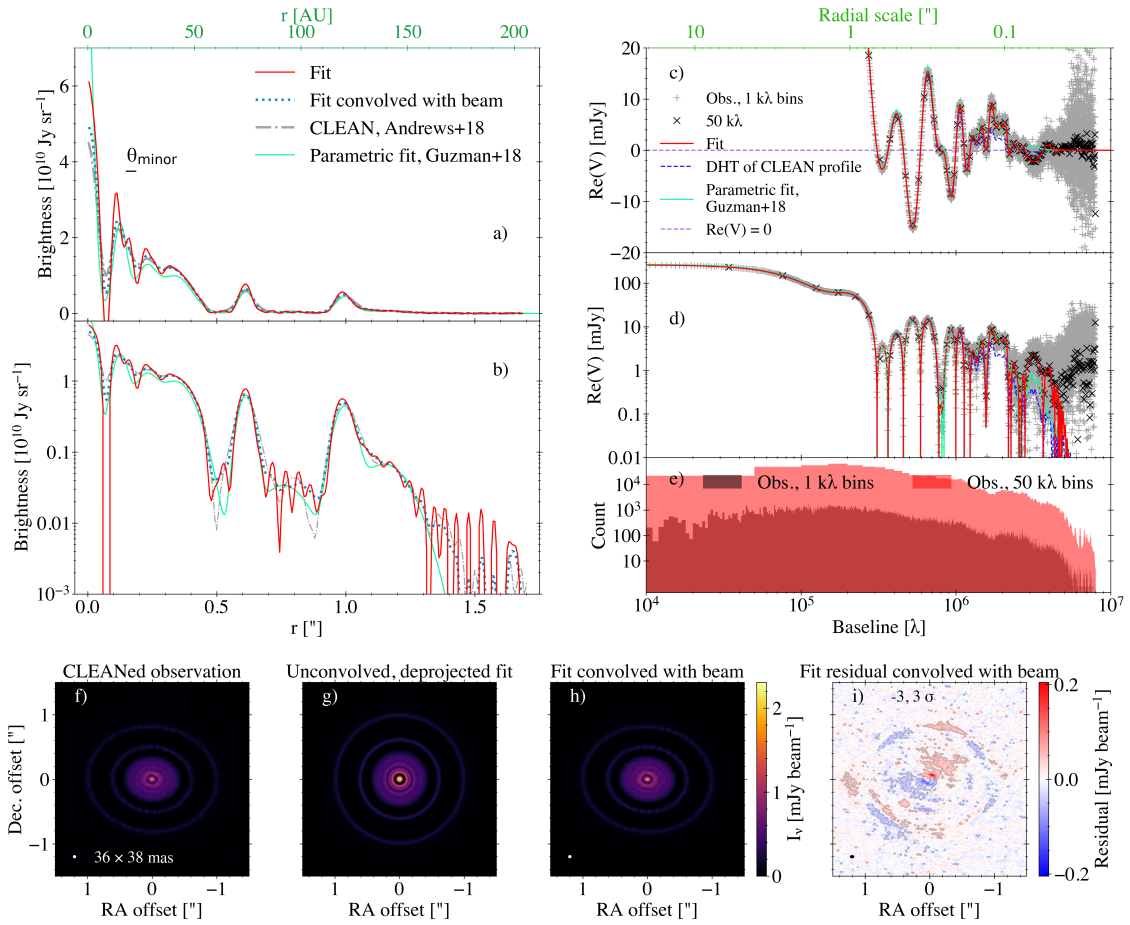


Fig. 2.10. Fit to real, high resolution observations: AS 209

a) Reconstructed brightness profile for the real, high resolution (beam FWHM 36×38 mas) DSHARP observations of AS 209 in Andrews et al. (2018). The CLEAN image-extracted profile from that work and the beam’s minor axis are shown. frank achieves a higher fit resolution (narrower, higher amplitude features) than the CLEAN technique. The presence of additional structure in the inner disk relative to the CLEAN image-extracted profile is robust to variations of the model. Also shown is the frank brightness profile convolved with the observations’ 2D synthesized beam and the brightness profile for the parametric visibility domain fit in Guzmán et al. (2018).

b) As in (a) on a logarithmic y-scale. The outermost radii show the fit’s noise floor.

c) Zoom on the region around 0 of the observed DSHARP visibilities in 1 and 50 k λ bins. The frank fit, the discrete Hankel transform of the CLEAN profile in (a), and the parametric fit from Guzmán et al. (2018) corresponding to the profile in (a) are shown. The strong increase in scatter at $\geq 4.5 M\lambda$ sets the data’s effective resolution, beyond which frank does not attempt to fit the noise-dominated visibilities.

d) As in (c) on a logarithmic y-scale. The data (and the frank fit’s) negative regions are denoted by the frank fit line’s dashed sections.

e) Histogram of (binned) visibility counts, showing the strong decrease beyond $\approx 4.5 M\lambda$ responsible for the increased scatter in (c) – (d).

f) CLEANed observation.

g) Image of the unconvolved and deprojected frank reconstruction.

h) Image of the frank reconstruction reprojected and convolved with the observations’ synthesized beam.

i) Residual map of the frank reconstruction (the fit’s residual visibilities imaged with CLEAN), showing evidence of non-axisymmetric structure (contour $\sigma = 10 \mu\text{Jy beam}^{-1}$, peak residual 12σ).

the innermost disk's features are not fully resolved; forcing the fit to be positive results in the innermost gap having zero flux and alters the profile's integral by 4%, but otherwise has a negligible effect (see Sec. 2.7 for a discussion of nonnegative fits). The `frank` fit agrees with the CLEAN profile in finding that the gaps centered at ≈ 0.5 and $0.8''$ are not empty⁶. However the fine structure in these gaps remains uncertain because their brightness is near the fit's noise floor (which can be approximated by the amplitude of the oscillations beyond $\approx 1.3''$).

The `frank` fit convolved with the synthesized beam is also shown in Fig. 2.10(a) – (b), its similarity to the CLEAN profile giving credence to `frank` correctly finding real higher resolution structural information. The sub-beam resolution of the reconstructed brightness profile is enabled by `frank` accurately fitting the visibilities in Fig. 2.10(c) – (d) out to ≈ 4.5 $M\lambda$. This is equivalent to an angular scale $\sim 1/(4.5 M\lambda) = 46$ mas = 5.5 au, which is an indication of the data's effective resolution beyond which the visibilities are noise-dominated. In Fig. 2.10(e) a histogram of the binned visibilities commensurately decreases sharply in counts beyond $\approx 4.5 M\lambda$. Fitting longer baselines with our current modeling approach only imprints noise on the brightness profile as discussed in Sec. 2.3.2.2.

Although the CLEAN beam has a FWHM 36×38 mas that is less than the 46 mas equivalent of the `frank` visibility fit, these two values are not directly comparable. A more direct comparison can be made in Fourier space; the DHT of the CLEAN profile in Fig. 2.10(c) – (d) demonstrates how convolution with the CLEAN beam effectively acts as a lowpass filter, downweighting the contribution to the CLEAN brightness profile from visibilities beyond $\approx 2.4 M\lambda \Leftrightarrow 86$ mas = 10.4 au. This is the baseline at which the DHT of the CLEAN profile begins to show discrepancies with the observed visibilities. Convolution with the beam thus suppresses features in the profile on spatial scales smaller than 10.4 au, causing them to appear broader and shallower than in the `frank` reconstruction, which fits the visibilities out to $\approx 4.5 M\lambda \Leftrightarrow 46$ mas = 5.5 au.

The DHT of the CLEAN profile more generally shows a less accurate agreement with the visibilities than `frank` beyond $\approx 1.5 M\lambda$, motivating that the `frank` brightness profile is correctly identifying high resolution structure. For comparison the *parametric* visibility domain fit in Guzmán et al. (2018) uses the CLEAN image to motivate an 8 Gaussian functional form for the brightness profile, shown in Fig. 2.10(a) – (b). The Fourier transform of this parametric form in Fig. 2.10(c) – (d) accurately fits the visibilities out to $\approx 2.5 M\lambda$ but begins to show discrepancies at longer baselines. The brightness profile has less structure in the inner disk and lower amplitude features than the `frank` fit. Because the `frank` fit accurately traces the data out to $\approx 4.5 M\lambda$, its higher achieved resolution finds the disk features to be

⁶Although the SNR in the gaps is low, this noise is dominated by the uncertainty on scales $\lesssim 0.05''$; it is the lower uncertainty on scales of the approximate gap widths, $0.1''$ and $0.3''$, that suggests the average flux in the gaps is nonzero.

narrower and higher in amplitude (though the [Guzmán et al. 2018](#) fit is positive everywhere). This is an example of the comparative advantage of a nonparametric form to fit a complicated visibility distribution.

Fig. 2.10(f) – (i) compare the CLEAN image with the image of the *unconvolved and deprojected frank* fit, the fit convolved with the beam, and the convolved residual image of the fit. The latter demonstrates an additional use case of the model, identifying and isolating small deviations from axisymmetry (for large deviations from axisymmetry, our axisymmetric fits may not be reliable). Here the 5 – 10% deviations in the brightness around each ring may potentially be explained by the gaps and rings being produced by the combination of a planet and a low viscosity as suggested in ([Fedele et al., 2018](#)). In such a case these asymmetries may be expected as a result of the low viscosity ([Hallam and Paardekooper, 2020](#)).

Varying the fit hyperparameters α and w_{smooth} within sensible bounds has negligible effect on the *frank* brightness profile. **Fig. 2.11** compares the fit from Fig. 2.10 using the default values ($\alpha = 1.05, w_{\text{smooth}} = 10^{-4}$) with a fit that more strongly damps low SNR data ($\alpha = 1.30, w_{\text{smooth}} = 10^{-1}$). The latter smooths the power spectrum appreciably relative to the default choice in Fig. 2.11(a), yet the effects on the visibility fit and the reconstructed brightness in Fig. 2.11(b) – (c) are negligible; the fit is robust to how precisely the prior weights the longest (i.e., noisiest) baselines. Note that although the priors (power spectra) shown in Fig. 2.11(a) do not extend to the shortest baselines, this does not significantly impact the fit. This is because the maximum recoverable scale of the observations is much larger than the size of the disk, and *frank* recovers the brightness accurately so long as R_{out} is larger than the disk size.

Although convolving the *frank* profile with the CLEAN beam generally results in brightness profiles that are similar to CLEAN-extracted profiles, the converse is not true. In **Fig. 2.12** we compare a profile extracted from the raw (unconvolved) CLEAN point source model (*.model* image); a profile extracted from the point source model convolved with the CLEAN beam (without the addition of the residual dirty map, the *.residual* image); and a profile extracted from the final CLEAN *.image* image. One may expect that the fit resolution achieved in the CLEAN point source model profile is similar to that in the *frank* profile. While the disk’s innermost gap is narrower in the point source model profile relative to the final CLEAN image profile, the point source model profile does not show as much structure in the inner disk as the *frank* fit. Moreover the noise in the point source model profile (even when binning) can make inference on disk feature widths and amplitudes nontrivial. We have applied this same analysis to multiple real and mock datasets at various antenna configurations, finding in general that while the resolution difference between profiles extracted from the *.model* image and *.image* image is starker in lower resolution data (because the beam is larger and so

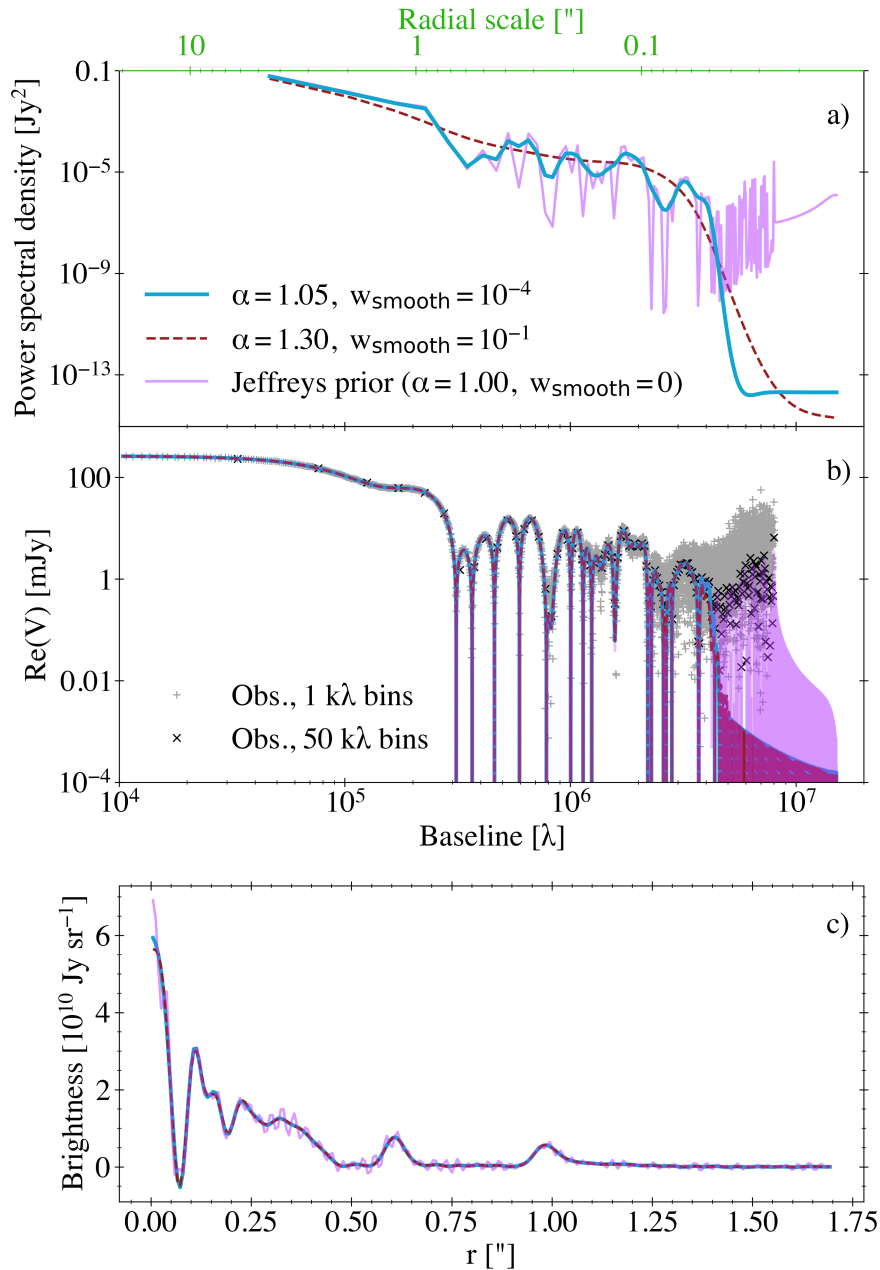


Fig. 2.11. Fit sensitivity to hyperparameters: AS 209

a) Maximum a posteriori power spectra of the frank fit under the default hyperparameter values ($\alpha = 1.05, w_{\text{smooth}} = 10^{-4}$) and stronger values ($\alpha = 1.30, w_{\text{smooth}} = 10^{-1}$). The structural differences between these spectra show negligible effect on the visibility fits in (b) and fitted profiles in (c). The power spectra are the priors placed on the respective brightness profile reconstructions. The maximum a posteriori power spectrum under a Jeffreys prior ($\alpha = 1.00, w_{\text{smooth}} = 0$) is also shown, which forces the model to fit the longest baseline, noise-dominated visibilities in (b), imprinting oscillations on the corresponding brightness profile in (c).

b) Observed visibilities in 1 and 50 k λ bins; the frank fit under the default hyperparameter values and under a stronger choice, showing minor difference; the fit under a Jeffreys prior.

c) The fitted frank brightness profile in Fig. 2.10(a) – (b) under the default hyperparameter values, as well as fits under the stronger choice and Jeffreys prior.

convolution with it has a stronger effect), the point source model profile’s noise also worsens for lower resolution data. We have confirmed this behavior with a CLEAN gain parameter as low as 10^{-3} .

2.3.2.2 A dataset’s effective resolution can be much less than the longest baseline

To further demonstrate that the longest baselines in datasets are often noise-dominated, we find that both the `frank` and CLEAN brightness profiles change negligibly if the AS 209 dataset, which extends to $8 \text{ M}\lambda \Leftrightarrow 26 \text{ mas} = 3.1 \text{ au}$, is truncated at $5 \text{ M}\lambda \Leftrightarrow 41 \text{ mas} = 5.0 \text{ au}$ *prior to* the visibilities being fit. This suggests that the data’s effective resolution as seen by both CLEAN and `frank` is $\lesssim 5 \text{ M}\lambda$, or at $\lesssim 63\%$ of the baseline distribution. In Fig. 2.10(c) the visibilities begin oscillating rapidly about 0 beyond $\approx 5 \text{ M}\lambda$, indicative of noise dominating the signal. Fitting longer baselines only imposes noise on the reconstructed brightness profile as shown by the Jeffreys prior fit in Fig. 2.11 (this behavior is consistent with that found using mock data in Fig. 2.5). The Jeffreys prior causes the model to fit the full baseline distribution, including the noise-dominated region beyond $\approx 4.5 \text{ M}\lambda$. This imposes oscillations on the brightness profile, demonstrating that these baselines in the AS 209 dataset are noise-dominated. The fit with the default hyperparameter values is thus (at least approximately) correctly identifying where the data become noise-dominated and accordingly justified in not fitting beyond $\approx 4.5 \text{ M}\lambda$. This is not to say that an alternative fitting approach could not obtain useful information on disk structures from these noise-dominated data.

Importantly though *it is common for an appreciable fraction of the long baselines in real datasets to be noise-dominated*. This occurs in high as well as low – moderate resolution observations and suggests the integration time at the most extended baselines is often too short to yield informative visibility measurements for CLEAN or `frank`. This ‘effective resolution’ is predominantly a result of sampling density dropping appreciably at the longest baselines in many real datasets (while the longest baselines also typically exhibit higher phase noise, self-calibration can often alleviate this).

2.3.2.3 Sub-beam fits: Identifying underresolved features in real, moderate resolution observations

While `frank` has utility in more accurately characterizing disk substructure in high resolution observations, it is also effective in identifying sub-beam structure in low – moderate resolution observations. **Fig. 2.13** compares the `frank` and CLEAN fits to the DSHARP AS 209 dataset from Fig. 2.10 with fits to lower resolution (longest baseline $2 \text{ M}\lambda$) observations of the same disk (Fedele et al., 2018). Relative to CLEAN, the `frank` fit to the lower resolution dataset is

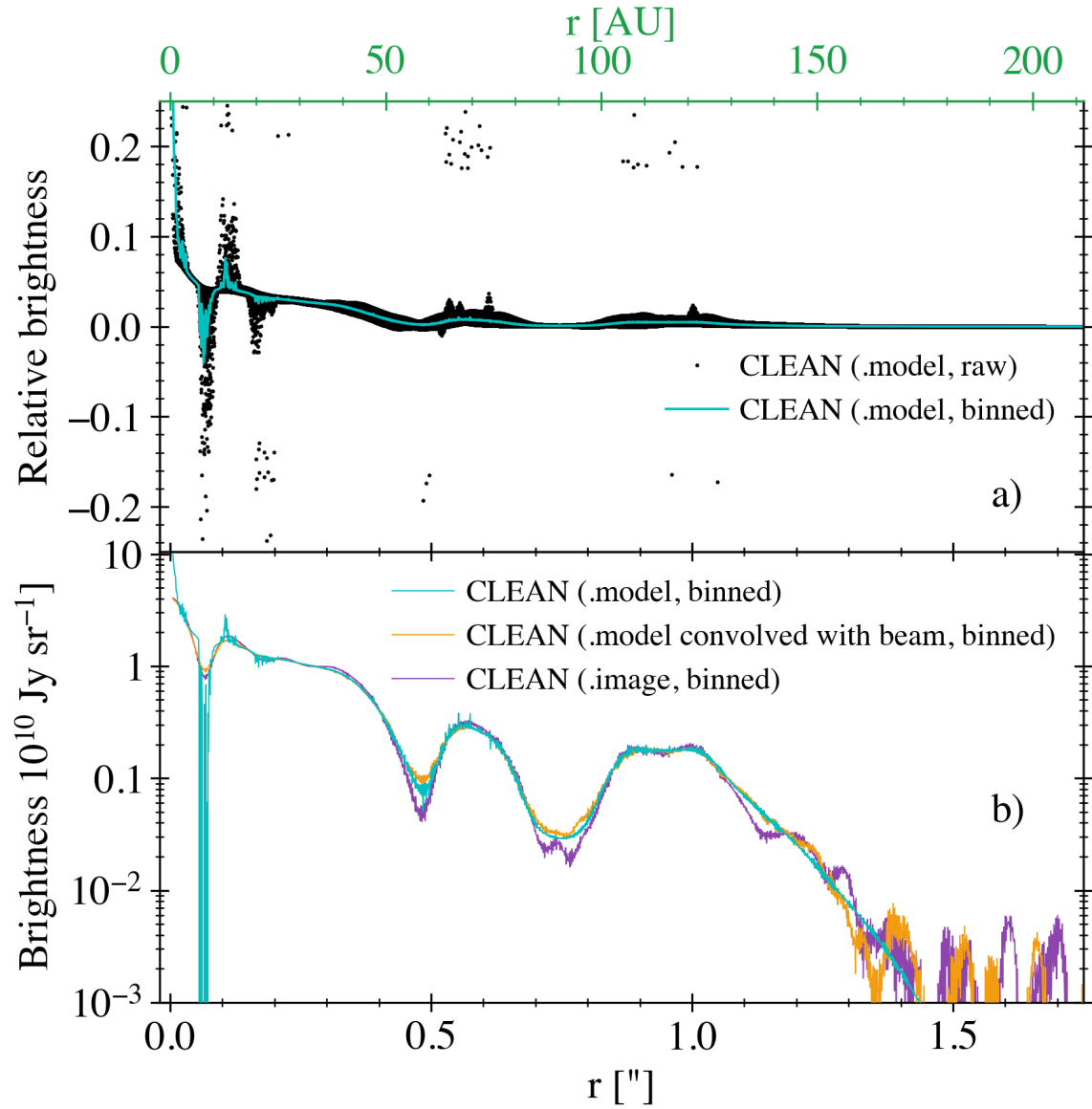


Fig. 2.12. CLEAN model profile extraction: AS 209

a) Pixel flux as a function of disk radius, extracted from the CLEAN point source model (*.model* image) for the DSHARP AS 209 dataset. A binned average (1 mas bins) of these data is also shown to estimate the radial profile underlying the noisy pixel flux.

b) Binned average from (a), compared with a profile extracted (using the same binning) from the point source model convolved with the CLEAN beam (*.image* - *.residual*), and a profile extracted from the final CLEAN image (*.image*). The lack of prominent additional disk features in the *.model* profile indicates a comparable resolution to the *.image* profile.

more accurately identifying a number of features in the brightness distribution (the centroids and widths of the outer disk’s rings, depths of the adjacent gaps, and the disk’s outer edge) as confirmed by the higher resolution DSHARP observations. The `frank` fit to the lower resolution data also shows reasonable agreement with the CLEAN fit to the high resolution DSHARP data in the outer disk. This is due to both profiles fitting the visibilities out to a similar maximum baseline (the `frank` fit to the lower resolution dataset extends to $\approx 2.1 \text{ M}\lambda$, and recall the DHT of the DSHARP CLEAN beam’s FWHM is $\approx 2.4 \text{ M}\lambda$). `frank`’s sub-beam resolving capability is thus not limited to high resolution observations, offering the potential to identify and more accurately constrain substructure relative to CLEAN in low – moderate resolution datasets.

To further show that `frank` can identify substructure in lower resolution observations, **Fig. 2.14** shows a snapshot from an animation in which the `frank` fit to the DSHARP AS 209 dataset evolves as a function of the data’s longest baseline. We first truncate the data at $1 \text{ M}\lambda \Leftrightarrow \approx 0.2''$ prior to the visibilities being fit, then successively step the maximum baseline to $5 \text{ M}\lambda$ and fit at each step. `frank` identifies with increasing accuracy the presence and detailed morphology of substructure in the disk as the truncation baseline increases, and at each step, including when $1 \text{ M}\lambda$ is the longest baseline, the model is correctly identifying and partially resolving more structure than a CLEAN profile obtained with the same truncated dataset. This again demonstrates that `frank` can correctly identify structure in low – moderate resolution data.

`frank`’s resolving capability for low – moderate resolution observations also shows utility when applied to apparently smooth disks. For the FWHM $92 \times 127 \text{ mas}$ ($\approx 15 \text{ au}$ at 140 pc) observations of the compact ($\approx 0.3''$) disk DR Tau (Long et al., 2019), the CLEAN image (even with uniform weighting) shows no clear signs of substructure, and the parametric visibility domain fit with a smooth profile in Long et al. (2019) shows significant residual error⁷. The `frank` fit using default hyperparameter values in **Fig. 2.15(a) – (b)** identifies substructure and finds a factor of ≈ 2 higher peak brightness than the CLEAN profile. This is because the `frank` fit matches the visibilities in **Fig. 2.15(c) – (d)** out to the longest baselines, $2.3 \text{ M}\lambda \Leftrightarrow 88 \text{ mas} = 12 \text{ au}$. Conversely convolution with the FWHM $92 \times 127 \text{ mas}$ synthesized beam causes the DHT of the CLEAN profile to depart the data beyond $\approx 0.8 \text{ M}\lambda$. The DHT of the CLEAN profile does track at lower accuracy the same features in the visibility distribution that `frank` closely fits, and the `frank` fit when convolved with the synthesized beam in **Fig. 2.15(a) – (b)** matches the CLEAN profile. Together these suggest the `frank` fit is correctly identifying sub-beam structure.

⁷We used the self-calibrated measurement set in Long et al. (2019). Before extracting the visibilities using the `export_uvtable` function of the `uvplot` package (Tazzari, 2017), we applied channel averaging (to obtain 1 channel per spectral window) and time averaging (30 sec) to all spectral windows in the original MS table.

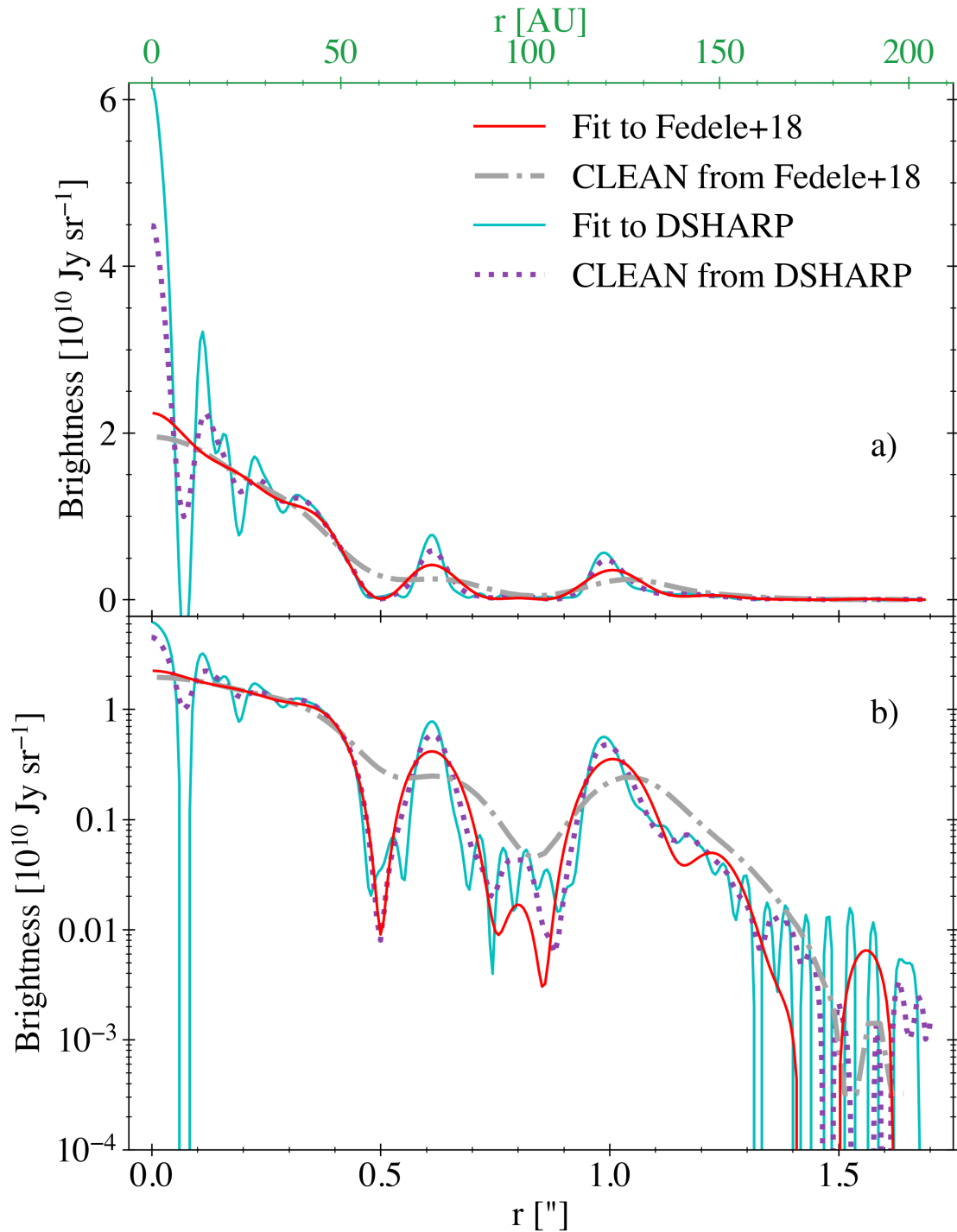


Fig. 2.13. Comparison of moderate and high resolution fits: AS 209

a) The fitted frank brightness profile in Fig. 2.10(a), as well as a fit to lower resolution (longest baseline $2 \text{ M}\lambda$) observations of the same disk (Fedele et al., 2018). Analogs for the CLEAN image-extracted profile. The frank fit to the lower resolution dataset is correctly identifying structure evident in both the frank and CLEAN fits to the higher resolution data.

b) As in (a) on a logarithmic y-scale.

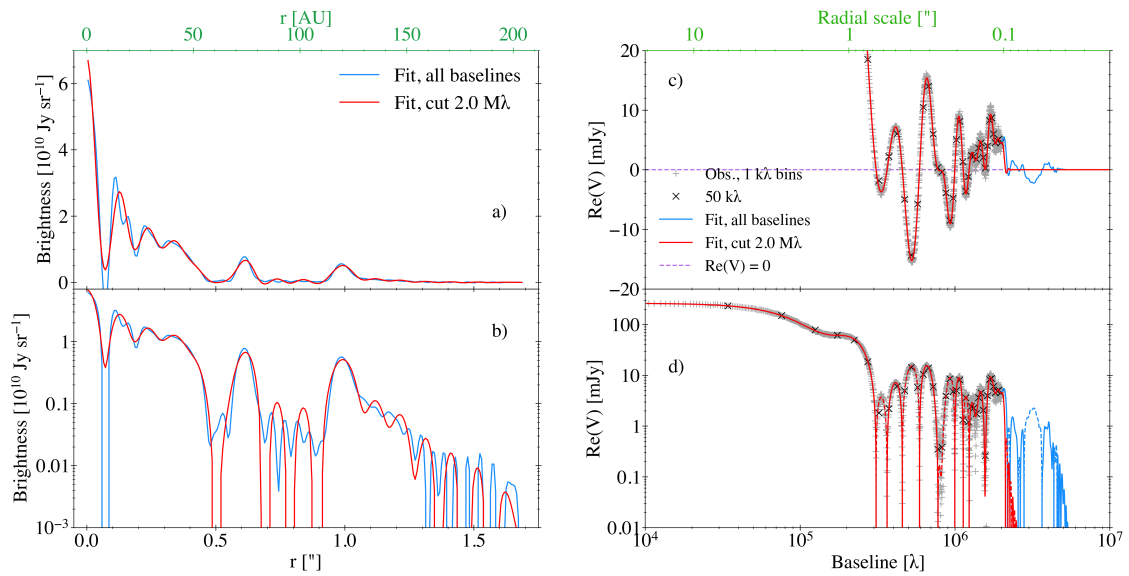


Fig. 2.14. Snapshot from an animation of AS 209 fit evolution with baseline

- a) The fitted frank brightness profile in Fig. 2.10(a) and a snapshot of the fit's evolution as the data are truncated at successively longer maximum baseline, beginning at 1 $M\lambda$.
- b) As in (a) on a logarithmic y-scale.
- c) Zoom on the region around 0 of the observed DSHARP visibilities in 1 and 50 $k\lambda$ bins. The frank fit to the dataset at a truncation baseline of 2 $M\lambda$ is shown.
- d) As in (c) on a logarithmic y-scale. The data (and fit's) negative regions are denoted by the fit line's dashed sections.

`frank` thus infers the presence of substructure (two or more gaps) in addition to the centrally peaked component in this compact disk that appears featureless in the CLEAN image and profile. Note that `frank` is still almost certainly underresolving the disk’s features, identifying and localizing the presence of substructure rather than accurately characterizing the features’ morphologies. These are governed by the longest baselines in the dataset, so while it is clear from the current data that substructure is present, its form would likely change with the addition of higher resolution data (as is the case for AS 209). We therefore caution against overinterpreting the exact form of the fitted brightness profile.

Fig. 2.15(e) – (h) compare the CLEAN image with the image of the *unconvolved and deprojected* `frank` fit, the fit convolved with the beam, and the convolved residual image of the fit. The latter shows prominent asymmetric structure whose origin is not yet clear, but is not as best we can discern an artifact of an erroneous fit.

Varying the fit hyperparameters α and w_{smooth} within sensible bounds has a fairly weak effect on the `frank` brightness profile as shown in **Fig. 2.16**. While the stronger hyperparameter choice ($\alpha = 1.30, w_{\text{smooth}} = 10^{-1}$) does fit the visibilities to shorter baseline than the default hyperparameter values ($\alpha = 1.05, w_{\text{smooth}} = 10^{-4}$), the effect of using the stronger values is fairly benign: slightly less prominent disk features and a peak brightness $\approx 10\%$ lower.

2.4 Conclusions

In this chapter we have presented `frank`, an open source code that uses a fast Gaussian process to recover the axisymmetric structure of sources observed with radio interferometers by directly fitting the real component of the visibilities. While the code is tailored to protoplanetary disk observations, it can be extended to applications in other physical contexts where an azimuthally averaged brightness profile is useful.

`frank`’s main advantages for characterizing axisymmetric structure relative to the CLEAN technique are:

- resolution: `frank` can resolve angular scales smaller than the uniform-weighted CLEAN beam while retaining sensitivity typical of a natural-weighted CLEAN image;
- flexibility: `frank` yields a nonparametric reconstruction of a source’s radial brightness profile, enabling it to fit the visibilities to high accuracy without additional input from the user;
- speed: `frank` fits are performed in <1 min for datasets of $\lesssim \text{few} \times 10^6$ visibilities;

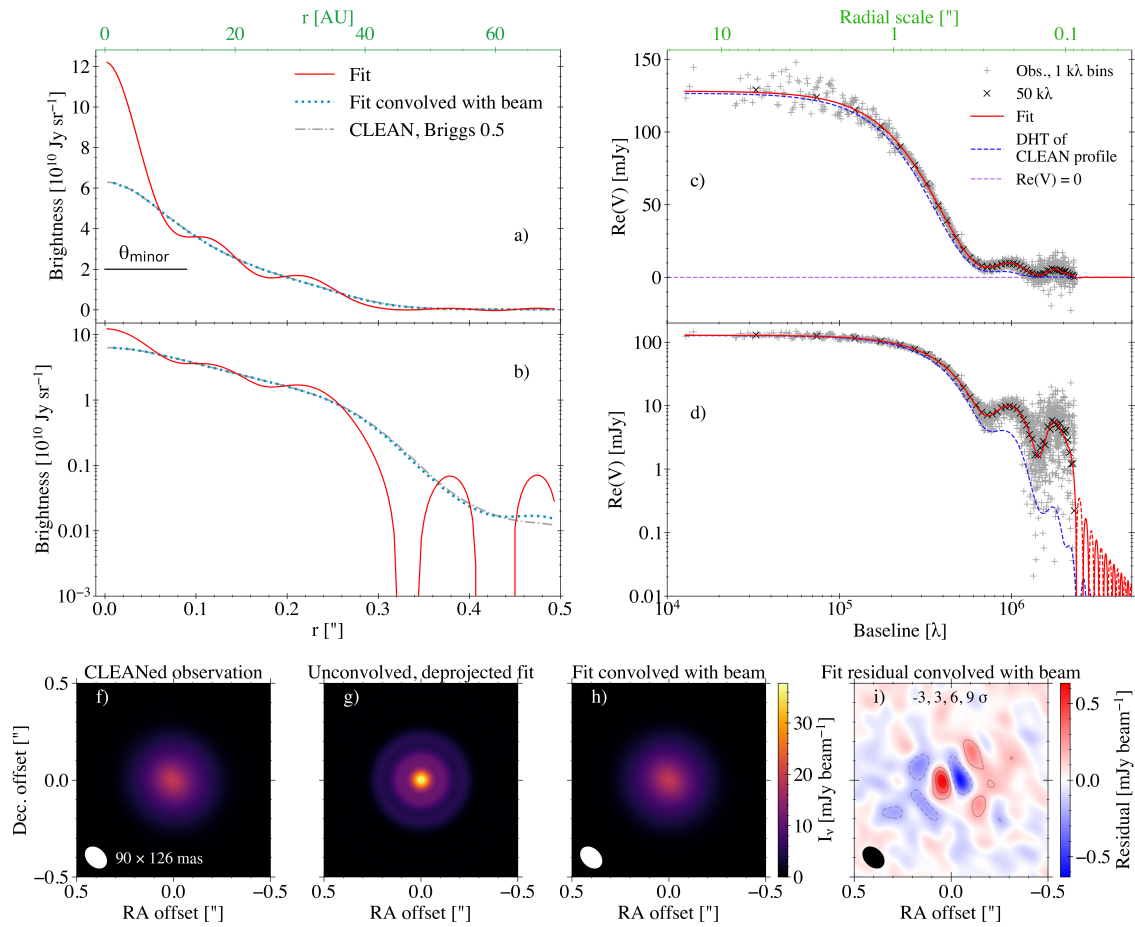


Fig. 2.15. Fit to real, moderate resolution observations: DR Tau

a) Reconstructed brightness profile for the real, moderate resolution observations of DR Tau in Long et al. (2019). A CLEAN image-extracted profile and the beam’s minor axis are also shown.

b) As in (a) on a logarithmic y-scale, emphasizing the fitted profile’s outer edge at $\approx 0.3''$ (oscillations in the frank profile beyond this indicate the fit’s noise floor).

c) Observed visibilities in 1 and 50 k λ bins. The frank fit and the discrete Hankel transform of the CLEAN profile in (a) are shown.

d) As in (c) on a logarithmic y-scale. The frank fit’s negative regions are denoted by its dashed sections.

e) CLEANed observation.

f) Image of the *unconvolved and deprojected* frank reconstruction.

g) Image of the frank reconstruction reprojected and convolved with the observations’ synthesized beam.

h) Residual map of the frank reconstruction (the fit’s residual visibilities imaged with CLEAN), showing evidence of non-axisymmetric structure (contour $\sigma = 60 \mu\text{Jy beam}^{-1}$, peak residual 12σ).

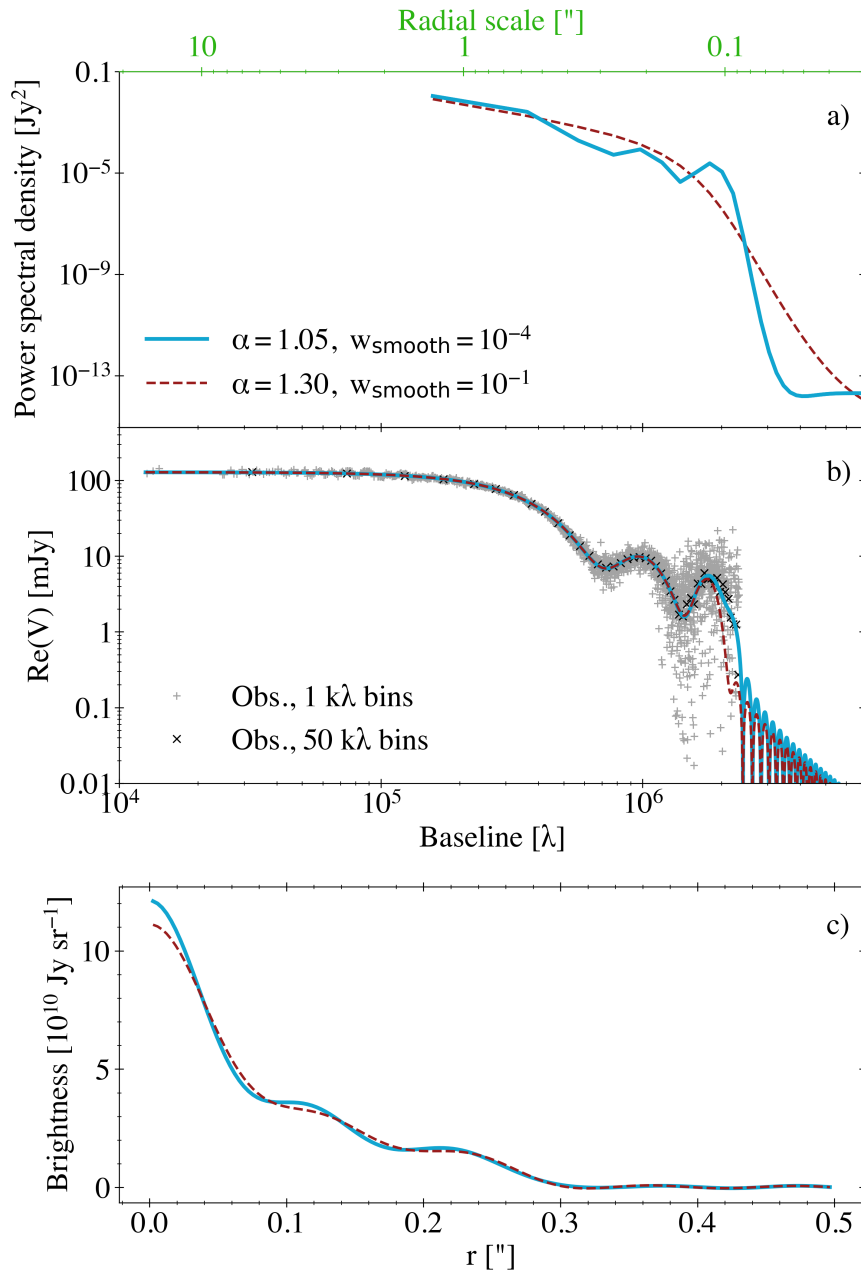


Fig. 2.16. Fit sensitivity to hyperparameters: DR Tau

a) Maximum a posteriori power spectra of the frank fit under the default hyperparameter values ($\alpha = 1.05, w_{\text{smooth}} = 10^{-4}$) and stronger values ($\alpha = 1.30, w_{\text{smooth}} = 10^{-1}$). The structural differences between these spectra show weak effect on the visibility fits in (b) and fitted profiles in (c). The power spectra are the priors placed on the respective brightness profile reconstructions.

b) Observed visibilities in 1 and 50 $k\lambda$ bins; the frank fit under the default hyperparameter values and under a stronger choice, showing fairly minor difference.

c) The fitted frank brightness profile in Fig. 2.15(a) – (b) under the default hyperparameter values, and a fit under a stronger choice.

- ease of use: `frank` is a Python package with a minimum number of dependencies that is easy to install and integrate into existing codebases.

`frank`'s resolution, flexibility, speed, and ease of use make it a high performance tool suitable for a wide range of applications on diverse interferometric datasets.

The major use case of `frank` in the protoplanetary disk context is fitting interferometric observations to find and characterize disk substructures at higher resolution than the CLEAN algorithm. Recent high resolution observations of sources previously observed at lower angular resolution have begun to show the ubiquity of disk substructure, including in disks that appeared featureless at low resolution. This motivates the utility of a technique such as `frank` to resolve features and characterize disks at sub-beam scales. The model can resolve additional structure in high resolution datasets, such as the DSHARP observations of AS 209 (Andrews et al., 2018); as well as in lower resolution datasets that show featureless CLEAN images (even with uniform weighting), such as the compact disk DR Tau (Long et al., 2018). Specific scientific applications of the code include more accurately discerning substructure widths and amplitudes, better resolving the inner disk structure including the peak brightness, and isolating disk asymmetries in a residual image.

`frank` uses all visibilities in a dataset to inform the reconstructed brightness profile. Its resolving power is thus sensitive to variations in the baseline dependence of the data's SNR. In contrast a CLEAN image-extracted profile is largely determined by the pure baseline distribution. Consequently for observations at any resolution, improving an observation's SNR via the on-source integration time can markedly enhance `frank`'s resolving capability to constrain sub-beam features, whereas it makes little difference for CLEAN.

`frank` is actively developed at <https://github.com/discsim/frank>, where users are welcome to contribute and to report issues.

2.5 Appendix A: Spectral smoothness hyperprior

The spectral smoothness hyperprior is designed to constrain the power spectrum to be close to a power law in the absence of data. We implement this hyperprior using a numerical estimate for the integral of the second logarithmic derivative of the power spectrum,

$$-\frac{1}{2\sigma_s^2} \int d\log(q) \left(\frac{\partial^2 \log(p)}{\partial \log(q)^2} \right)^2 \approx -\frac{1}{2\sigma_s^2} \sum_{n=2}^{N-1} \delta_{c,n} (\Delta \log p_n)^2, \quad (2.44)$$

as in [Oppermann et al. \(2013\)](#). Here $\delta_{c,n} = (\log q_{n+1} - \log q_{n-1})/2$ and

$$\Delta \log p_n = \frac{1}{\delta_{c,n}} \left(\frac{\log p_{n+1} - \log p_n}{\delta_{e,n}} - \frac{\log p_n - \log p_{n-1}}{\delta_{e,n-1}} \right) \quad (2.45)$$

is an approximation to the second logarithmic derivative of \mathbf{p} , where $\delta_{e,n} = \log q_{n+1} - \log q_n$. Equation 2.44 can be simplified as

$$-\frac{1}{2\sigma_s^2} \sum_{n=2}^{N-1} \delta_{c,n} (\Delta \log p_n)^2 = -\frac{1}{2\sigma_s^2} \log \mathbf{p}^T \mathbf{T} \log \mathbf{p}, \quad (2.46)$$

where the components of \mathbf{T} are

$$T_{ij} = \sum_k \gamma_{ki} \delta_{c,k} \gamma_{kj}, \quad (2.47)$$

with

$$\gamma_{ij} = \frac{1}{\delta_{c,i}} \begin{cases} -\left(\frac{1}{\delta_{e,i}} + \frac{1}{\delta_{e,i-1}}\right) & \text{if } j = i \\ +\frac{1}{\delta_{c,i\pm 1}} & \text{if } j = i \pm 1 \\ 0 & \text{otherwise.} \end{cases} \quad (2.48)$$

The matrix \mathbf{T} is constant and pentadiagonal, depending only on q_k . For large k , \mathbf{T} has the asymptotic form

$$T_{ij} = \frac{1}{(q_i R_{\max})^3} \times \begin{cases} +48 & \text{if } j = i \\ -32 & \text{if } j = i \pm 1 \\ +8 & \text{if } j = i \pm 2 \\ 0 & \text{otherwise.} \end{cases} \quad (2.49)$$

2.6 Appendix B: Signal-to-noise threshold

Here we show that it is the visibilities' SNR that determines whether a frank fit ignores the data at a given baseline. This is ultimately determined by whether the maximum a posteriori value for the power spectrum parameters tends to: Equation 2.42, in which case the power spectrum is determined by the visibility amplitude; or Equation 2.43, in which case the power spectrum's low amplitude suppresses the power on a given scale. The argument presented here is similar to that in [Enßlin and Frommert \(2011\)](#), who derive this for a general class of methods like frank.

To make the derivation tractable, we make some simplifications: we assume $p_0 = 0$, neglect smoothing, and study the simplifying case where the visibilities are observed exactly at the spatial frequency collocation points q_k . While this is somewhat unrealistic, the insights derived are useful more generally. Under our last assumption, the matrix $\mathbf{H}(\mathbf{q})$ in Equation 2.23 is just \mathbf{Y}_f . Now,

$$\begin{aligned}\boldsymbol{\mu} &= \left(\mathbf{Y}_f^T \mathbf{N}^{-1} \mathbf{Y}_f + \mathbf{Y}_f^T \text{diag}(1/p) \mathbf{Y}_f \right)^{-1} \mathbf{Y}_f^T \mathbf{N}^{-1} \mathbf{V} \\ &= \mathbf{Y}_b \left(\mathbf{N}^{-1} + \text{diag}(1/p) \right)^{-1} \mathbf{N}^{-1} \mathbf{V}.\end{aligned}\quad (2.50)$$

This means that

$$(\mathbf{Y}_f \boldsymbol{\mu})_k = \frac{V_k}{1 + \sigma_k^2/p_k} \quad (2.51)$$

and

$$(\mathbf{Y}_f^T \mathbf{D} \mathbf{Y}_f)_{kk} = \frac{\sigma_k^2}{1 + \sigma_k^2/p_k}. \quad (2.52)$$

Using these in Equation 2.41 with $p_0 = 0$, $\sigma_s = \infty$, and $\mathbf{p}^{\text{new}} = \mathbf{p}$ (convergence to the maximum likelihood) and rearranging produces the cubic equation in p_k ,

$$p_k \left\{ (p_k + \sigma_k^2)^2 [1 + 2(\alpha - 1)] - (p_k + \sigma_k^2)(V_k^2 + \sigma^2) - V_k^2 \sigma^2 \right\} = 0, \quad (2.53)$$

which always has the solution $p_k = 0$. Solutions for $p_k > 0$ can be found by completing the square of the term in brackets;

$$\begin{aligned}p_k &= \frac{1}{1 + 2(\alpha - 1)} \times \\ &\quad \frac{1}{2} \left\{ [V_k^2 - \sigma^2(1 + 4(\alpha - 1))] + \right. \\ &\quad \left. \sqrt{(V_k^2 - \sigma^2)^2 - 8V_k^2 \sigma^2 (\alpha - 1)} \right\}.\end{aligned}\quad (2.54)$$

For $V_k \gg \sigma_k$, this yields an equivalent expression to that given in Equation 2.42. However, the term inside the square root in Equation 2.54 is only positive if

$$V_k^2 > \sigma^2 \left\{ 1 + 4(\alpha - 1) + 2\sqrt{2(\alpha - 1)[1 + 2(\alpha - 1)]} \right\}, \quad (2.55)$$

otherwise $p_k = 0$ is the only solution (note that in the special case $\alpha = 1$, the term in brackets in Equation 2.54 is always positive; however the above expression still correctly denotes the region for which solutions with $p_k > 0$ exist). The implication of this is that for an SNR

below a given threshold, $V_k^2 \lesssim \sigma_k^2$, the inverse Γ hyperprior will drive the power spectrum toward zero. In practice, including a nonzero p_0 means that $p_k \rightarrow p_0/(\alpha - 1)$, as given in Equation 2.43.

Equation 2.54 also shows why we use $\alpha > 1$. At long baselines – where the visibilities are noise-dominated – we will have $V_k^2 \sim \sigma_k^2$, and there will be many statistical fluctuations causing V_k to be slightly greater than σ_k . Since for $\alpha = 1$ the threshold is exactly at $V_k = \sigma_k$, the power spectrum will contain some fraction of this power, and the model will fit the noise-dominated visibilities. Increasing α to 1.05, 1.10, 1.30, or 1.90 increases the noise threshold to 1.36, 1.54, 2.04, or 3.01 σ_k respectively. Thus using $\alpha > 1$ markedly reduces the chance that the model will attempt to fit noise-dominated data.

A similar argument can be made in the case where the visibilities are not observed directly at the spatial frequency collocation points, so long as the (u, v) plane is sampled well enough that \mathbf{M} can be approximated as a diagonal matrix in the visibility domain. In this case $V_k = \sigma_k^2 (\mathbf{Y}_b^T \mathbf{j})_k$, where $\sigma_k^2 \approx (\mathbf{Y}_f^T \mathbf{M} \mathbf{Y}_f)_{kk}^{-1}$ is the effective variance at that scale.

2.7 Appendix C: Nonnegative fits

In some circumstances it may be beneficial to have brightness profiles that are nonnegative, i.e., $I_\nu \geq 0$, as is produced by maximum entropy methods or a log-normal model for the brightness (Junkewitz et al., 2016). In `frank` we can generate nonnegative solutions by finding the most probable brightness reconstruction I_ν for a given set of power spectrum parameters and the constraint $I_\nu \geq 0$ (i.e., the maximum of $P(I_\nu | \mathbf{p})$ subject to $I_\nu \geq 0$) using the nonnegative least squares solver in the `scipy.optimize.nnls` package.

In Fig. 2.17 we show the impact of the $I_\nu \geq 0$ constraint on the reconstructed brightness profile for the mock Gaussian ring under the C43-3 mock observation. Comparing the posterior mean brightness profile and the most probable nonnegative solution under two values of w_{smooth} , Fig. 2.17(a) shows the nonnegative solution is more accurate. Correspondingly the constraint $I_\nu \geq 0$ yields a visibility fit in Fig. 2.17(b) that initially falls slower than the standard `frank` fit beyond the data’s longest baseline (0.4 $M\lambda$), predicting the visibility amplitude at unobserved baselines more accurately than the standard fit between 0.4 – 0.8 $M\lambda$.

The improvement gained by enforcing $I_\nu \geq 0$ does however depend on the hyperparameters, with the nonnegative fit using $w_{\text{smooth}} = 10^{-4}$ fitting the visibilities less accurately than the analogous standard `frank` fit. This hyperparameter dependency is a result of the need to introduce additional power on small scales when enforcing a nonnegative brightness. Large α and small w_{smooth} strongly damp power at long baseline (on small spatial scales), introducing tension between the prior and the $I_\nu \geq 0$ constraint. This can cause the nonnegative

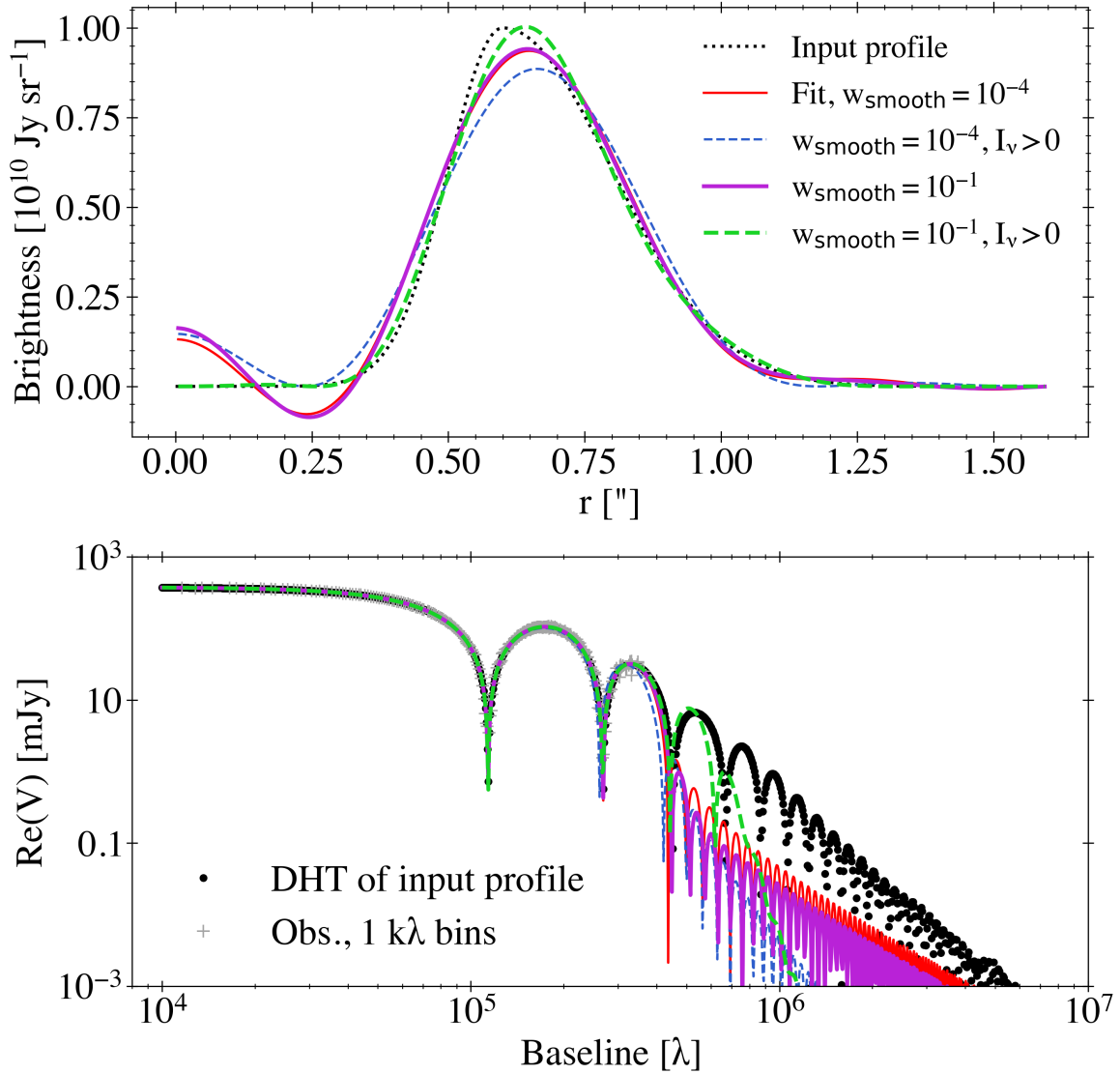


Fig. 2.17. Comparison of standard and nonnegative fits

a) Input and reconstructed brightness profiles for a mock Gaussian ring (two joined sigmoids) observed with the ALMA C43-3 configuration (synthesized beam FWHM $0.59 \times 0.70''$, Briggs=0.5; see Table 2.2 and Sec. 2.3.1.1), shown under two values of the w_{smooth} hyper-parameter, and with brightness profile positivity either unenforced or enforced. All fits use $\alpha = 1.05$.

b) Observed visibilities in $1 k\lambda$ bins, the DHT of the noiseless input profile, and the frank fits corresponding to the profiles in (a).

reconstruction to be a poor fit to the data on shorter baselines. Conversely with smaller α and larger w_{smooth} , the maximum a posteriori power spectra fall off more slowly with increasing q , and the resulting nonnegative brightness reconstruction has more power on small spatial scales.

Because this process involves extrapolating the visibilities beyond their maximum baseline (or at least into a region where they are noise-dominated), we therefore urge caution when interpreting any additional structures introduced by enforcing the profile be nonnegative.

2.8 Appendix D: Mock disk functional forms

Table 2.3 gives the functional forms of the brightness profiles for the mock disks shown in Fig. 2.7 and listed in Table 2.2.

Table 2.3. Functional forms of the brightness profiles for the archetypal mock disks listed in Table 2.2 and shown in Fig. 2.7.

Disc	Brightness profile functional form	Amplitude variables [$10^{10} \text{ Jy sr}^{-1}$]	Location variables [$''$]
Gaussian centered at 0	$I(r) = ae^{-\frac{r^2}{2c^2}}$	$a = 1.0$	$c = 0.2$
Gaussian ring	$I(r) = \begin{cases} ae^{-\frac{(r-b)^2}{2c_1^2}}, & r \leq b \\ ae^{-\frac{(r-b)^2}{2c_2^2}}, & r > b \end{cases}$	$a = 1.0$	$b = 0.6$ $c_1 = 0.1$ $c_2 = 0.2$
Multi-Gaussian	$I(r) = a_1e^{-\frac{(r-b_1)^2}{2c_1^2}} - a_2e^{-\frac{(r-b_2)^2}{2c_2^2}} - a_3e^{-\frac{(r-b_3)^2}{2c_3^2}} + \begin{cases} a_4e^{-\frac{(r-b_4)^2}{2c_4^2}}, & r \leq b_4 \\ a_4e^{-\frac{(r-b_4)^2}{2c_5^2}}, & r > b_4 \end{cases}$	$a_1 = 0.6$ $a_2 = 0.4$ $a_3 = 0.3$ $a_4 = 1.0$	$b_1 = 0.70$ $b_2 = 0.60$ $b_3 = 0.85$ $b_4 = 0.15$ $c_1 = 0.20$ $c_2 = 0.05$ $c_3 = 0.05$ $c_4 = 0.05$ $c_5 = 0.10$
Sharp-edged	$I(r) = e^{-2r^2} \cdot (a_1 + \begin{cases} a_2, & b_1 \leq r \leq b_2 \\ a_3, & b_3 \leq r \leq b_4 \\ a_4, & b_5 \leq r \leq b_6 \\ a_5, & b_7 \leq r \leq b_8 \\ 0, & \text{else} \end{cases})$	$a_1 = 1.00$ $a_2 = -0.90$ $a_3 = -0.20$ $a_4 = -0.25$ $a_5 = 0.50$	$b_1 = 0.1$ $b_2 = 0.2$ $b_3 = 0.4$ $b_4 = 0.7$ $b_5 = 0.6$ $b_6 = 0.7$ $b_7 = 0.7$ $b_8 = 0.8$

Chapter 3

A super-resolution analysis of the DSHARP survey: Substructure is common in the inner 30 au

Having presented `frank` and demonstrated its efficacy for accurately characterizing protoplanetary disk substructure in Chapter 2, this chapter details the application of (`frank`) to the DSHARP survey, which observed 20 disks at high spatial resolution (35 mas). This application provides new scientific insight on disk morphology and the physical processes responsible. Richard Booth and I co-developed the novel component of `frank` tailored to this analysis as detailed in Sec. 3.7, with the majority of the framework and code being Richard's. I conducted the analysis in Sec. 3.5. The chapter, with some modifications to the introduction, was published as [Jennings et al. \(2021\)](#). I wrote the chapter text and the paper, with refinements resulting from coauthor feedback.

The DSHARP survey evidenced the ubiquity of substructure in the mm dust distribution of large, bright protoplanetary disks. Intriguingly, these datasets have yet higher resolution information that is not recovered in a CLEAN image. We first show that the intrinsic performance of the CLEAN algorithm is resolution-limited. Then analyzing all 20 DSHARP sources using the 1D, super-resolution code Frankenstein (`frank`), we accurately fit the 1D visibilities to a mean factor of 4.3 longer baseline than the Fourier transform of the CLEAN images and a factor of 3.0 longer baseline than the transform of the CLEAN component models. This yields a higher resolution brightness profile for each source, identifying new substructure interior to 30 au in multiple disks; resolving known gaps to be deeper, wider, and more structured; and known rings to be narrower and brighter. Across the survey, high contrast gaps are an average 14% wider and 44% deeper in the `frank` profiles relative to CLEAN, and high contrast rings are an average 26% narrower. Categorizing the `frank` brightness profiles

into trends, we find that the relative scarcity of features interior to 30 au in the survey’s CLEAN images is an artifact of resolving power, rather than an intrinsic rarity of inner disk (or compact disk) substructure. Finally the rings in the `frank` profiles are narrower than the previously inferred deconvolved widths, indicating smaller α/St ratios in the local gas disk.

3.1 Background

While super-resolution approaches have been applied to individual DSHARP disks, namely parametric visibility fitting in [Guzmán et al. 2018](#), [Isella et al. 2018](#) and [Pérez et al. 2018](#), no study has yet examined the entire DSHARP sample. In this chapter we characterize substructure at super-resolution scales in all 20 DSHARP disks using the 1D code `frank` ([Jennings et al., 2020](#)), reconstructing the disks’ brightness profiles by nonparametrically fitting their azimuthally averaged visibility distributions.

Sec. 3.2 summarizes the `frank` modeling approach as relevant to this analysis and discusses its limitations. Sec. 3.3 then examines the resolution limitations of CLEAN images and models in real and visibility space (Sec. 3.3.1), compares the accuracy of brightness profiles extracted from the CLEAN images and models with the `frank` visibility fits for the DSHARP sources (Sec. 3.3.2), and summarizes the principles of comparing `frank` to CLEAN (Sec. 3.3.3). In Sec. 3.4 we present the super-resolution `frank` fits for each DSHARP source, then group the `frank` brightness profiles by previously unidentified substructure trends in Sec. 3.5. We further use the super-resolution fits to identify a geometric viewing effect that can imprint on disk images. Sec. 3.6 summarizes our findings and briefly places them in the context of super-resolution substructure that may be present in other protoplanetary disk datasets, as well as the physical inference this can inform.

3.2 Model

A full description of the `frank` model framework and its limitations is in [Jennings et al. \(2020\)](#). In short, `frank` reconstructs the 1D (axisymmetric) brightness profile of a source as a function of disk radius by directly fitting the real component of the deprojected, unbinned visibilities as a function of baseline. The brightness profile is determined nonparametrically by fitting the visibilities with a Fourier-Bessel series, which is linked to the real space profile by a discrete Hankel transform. A Gaussian process regularizes the fit, with the covariance matrix nonparametrically learned from the visibilities under the assumption that this matrix is diagonal in Fourier space. The free parameters (diagonal elements) of the matrix correspond

to the power spectrum of the reconstructed brightness profile. The fitting procedure takes $\lesssim 1$ min on a standard laptop for each dataset shown here.

For a full description of the model framework in `frank`, see [Jennings et al. \(2020\)](#). Here we briefly and qualitatively summarize the approach. `frank` reconstructs the azimuthally averaged brightness profile of a source as a function of disk radius by directly fitting the real component of the deprojected, unbinned visibilities as a function of baseline.¹ The brightness profile is determined nonparametrically by fitting the visibilities with a Fourier-Bessel series, which is linked to the real space profile by a discrete Hankel transform ([Baddour and Chouinard, 2015](#)). The Fourier transform of a circle has a Bessel function kernel, making the discrete Hankel transform (*DHT*) a natural basis for circular (at least to zeroth order) protoplanetary disks. A Gaussian process regularizes the fit, with the covariance matrix nonparametrically learned from the visibilities under the assumption that this matrix is diagonal in Fourier space. The free parameters (diagonal elements) of the matrix correspond to the power spectrum of the reconstructed brightness profile. The approach is largely built on that in [Oppermann et al. \(2013\)](#).

The model has five free parameters; variation in reasonable choices for three of these (the outer radius and number of points used in the fit, and the floor value for the power spectral mode amplitudes) has a trivial effect on the recovered profile. Of the remaining two, α sets the signal-to-noise (*SNR*) threshold at which the model stops fitting the data, with a larger α resulting in a higher *SNR* threshold. The choice of α effectively corresponds to a maximum baseline beyond which the model does not attempt to fit the visibilities. This is relevant for the DSHARP datasets, as they all become noise-dominated typically at $\gtrsim 5 M\lambda$, while the maximum baseline is $\approx 10 M\lambda$. *In practice we manually choose an α value to fit out to the baseline at which the binned visibility SNR begins to oscillate about $SNR = 1$* (due to the *uv* sampling becoming highly sparse). The *SNR* is assessed with 20 $k\lambda$ bins of the real component of the visibilities, using $SNR = \mu^2/\sigma^2$, where μ is the mean visibility amplitude in each bin and σ the standard deviation. Pushing the fit out to these long baselines always comes at the cost of fitting some noise, which imprints on the brightness profile as rapid oscillations, usually with very low amplitude (typically $< 1\%$ of the profile’s peak brightness; as an example, see the fit residuals in Fig. 8 of [Jennings et al. 2020](#)). To suppress these noisy oscillations, the remaining free parameter w_{smooth} varies the spatial frequency scale over which the visibility *SNR* is averaged when building the power spectrum. A nonzero

¹We will use the disk geometries and phase centers in [Huang et al. \(2018a\)](#) to deproject the DSHARP datasets. Those values were determined in the image plane by either fitting ellipses to individual annular rings or fitting a 2D Gaussian to the image. Across all datasets, we have tested both fitting a 2D Gaussian to the visibilities and fitting the visibilities nonparametrically to determine the geometry and phase center. In general we have found close agreement with the published values and so default to those.

w_{smooth} prevents regions of artificially steep gradient in the power spectrum that are due to undersampled baselines.

For the DSHARP datasets, we use α and w_{smooth} values within the ranges $1.01 \leq \alpha \leq 1.50$ and $10^{-4} \leq w_{\text{smooth}} \leq 10^{-1}$, tailoring choices to the unique visibility distribution and noise properties of each dataset. We favor the smaller values within these ranges in order to reduce the constraint placed by the Gaussian process prior on the brightness profile reconstruction.

To fit each dataset, we download the self-calibrated and multi-configuration combined continuum measurement sets from <https://bulk.cv.nrao.edu/almadata/lp/DSHARP>. Before extracting the visibilities using the `export_uvtable` function of the `uvplot` package (Tazzari, 2017), we apply channel averaging (to obtain 1 channel per spectral window) and time averaging (30 sec) to all spectral windows in the original MS table. The `frank` fit takes $\lesssim 1$ min for each resulting visibility distribution.

To generate images of the `frank` residual visibilities in this chapter, we produce measurement sets from the `frank` residual UV tables, then use the `tclean` scripts from the DSHARP website to image. These scripts yield CLEAN beams that are often larger than those in the `.fits` files on the website, though only by 1 – 2 mas along either axis. The only exception is HD 143006, where the CLEAN beam is 36×53 mas in the `.fits` file, while the `tclean` script yields 47×48 mas (this may be due to slightly different versions of CASA used). For consistency with the imaged `frank` residuals, we will therefore show CLEAN images generated by applying the published `tclean` scripts to the published measurement sets, rather than showing the published `.fits` images.

3.2.1 Point source-corrected fits

Eleven of the 20 DSHARP datasets do not clearly converge on zero visibility amplitude at their longest baselines, exhibiting a mean value of $0 < \text{Re}(V) < 1$ mJy (relative to a peak visibility amplitude of ≈ 100 mJy). This seems to indicate that the observations are detecting a point-like source – namely the innermost disk, whose brightness increases sharply toward $r = 0$. A `frank` visibility fit strongly drives to zero once its SNR threshold is reached (which is a deliberate choice motivated by the high uncertainty in extrapolating the fit beyond the longest well-sampled baselines). And a steep slope in the fit at any baseline is represented in the brightness profile as structure on the corresponding spatial scale. Thus for a dataset that does not converge on zero at long baselines, a steep slope in the `frank` fit prior to the baseline at which the visibilities converge on zero can impose false oscillations on the brightness profile. These oscillations manifest as a sinc-like function, at constant spatial period (the inverse of the spatial frequency location of the slope in Fourier space) and at an amplitude that diminishes away from $r = 0$.

To prevent this artifacting, we have developed an extension to `frank` for a ‘point source-corrected model’ to effectively subtract a point source from the visibilities and fit the resulting ‘residuals’, which are centered on $\text{Re}(V) = 0$ at long baseline. By doing this we have implicitly assumed that there is a strong point source at the center of the disk. This model is one of an infinite number of choices to extrapolate the fitted visibility distribution to inaccessible scales (a requirement of any imaging algorithm) while remaining consistent with the observed data. The choice is however sensible, as it is both physically and practically motivated. Discs are expected to rapidly increase in brightness towards the star, and applying no point-source correction can lead to spurious, coherent oscillations in the recovered brightness profile.

A pure point source (Delta function) in real space transforms to a constant visibility amplitude at all baselines. While the innermost disk is not physically a Delta function, we find this approximation works well in an unresolved component fit. In the point source-corrected model, we first subtract a constant amplitude from the visibilities, equal to the mean offset from zero at the dataset’s longest baselines (specifically, those beyond the point at which the binned visibility SNR begins to oscillate about $SNR = 1$). Then we perform a standard `frank` fit on the ‘residual’ visibilities, and finally add the constant amplitude offset back into the `frank` visibility fit. Empirically, we have found this approach does a reasonable job of preventing artifacting in the `frank` brightness profile for each of the 11 DSHARP datasets whose visibilities do not clearly converge on zero (we will note these disks in Sec. 3.3). However the technique does not fully suppress oscillations in the brightness profile in some sources, particularly in the innermost disk. In these cases the amplitude and spatial period of oscillations is sensitive to the point source amplitude; an example is shown in Sec. 3.7. We therefore assess the associated uncertainty by comparing, for each source, the fit that uses the point source amplitude as determined above with a fit that uses a $1.5\times$ larger point source amplitude (an example case is discussed in Sec. 3.7). This is motivated by a model with a larger point source amplitude effectively fitting the data to shorter baseline, which yields a more conservative estimate of small scale substructure in the brightness profile. In the main text we show the difference between the profiles of these two point source fits as an informal uncertainty band.

3.2.2 Model limitations

The model’s notable limitations in the context of this analysis are:

1. The 1D (axisymmetric) approach fits for the azimuthal average of the visibility data at each baseline. The model is thus inaccurate for any annulus at which the brightness is not perfectly symmetric, averaging an asymmetry over 2π in azimuth. Azimuthally

localized features such as a bright arc then appear in the 1D brightness profile as a plateau or ‘bump’ (depending on their relative brightness; we will identify specific instances). Especially for super-resolution features not seen in a CLEAN image, it can be difficult in some cases to distinguish the artifact of an asymmetry from an underresolved annular feature using only the 1D frank brightness profile and observed visibilities.

To partially resolve this ambiguity, we image the frank fit residual visibilities to exploit that the axisymmetric model fits for the average brightness at each annulus. This effectively isolates azimuthal asymmetries in the imaged residuals², allowing us to identify radii at which asymmetries are coincident with features in the reconstructed brightness profile. But for disks that have overlapping annular structures and azimuthal asymmetries (in DSHARP, disks with prominent spirals), interpretation is more ambiguous. We generate a frank residual image using the same imaging parameters as the CLEAN image of the source; the residual image is thus convolved and at lower resolution than the frank brightness profile. Assessment of these residual images is therefore not a substitute for analysis with a 2D super-resolution model.

The axisymmetric approach in frank is also incorrect for fields of view with multiple sources (AS 205 and HT Lup in the DSHARP sample), as these are asymmetric on large scales. Structure on the scale of a secondary disk must at some level bias the frank fit for the primary, and we have tested the severity of this effect by refitting the HT Lup dataset after subtracting out the secondary disk seen in the CLEAN image. We found this to only weakly alter the morphology of the frank brightness profile for HT Lup. We verified this weak sensitivity with mock datasets containing brightness asymmetries, in which we found a frank brightness profile to be trivially altered by structure on a given scale at radii where that structure is not present. Regardless, application of the model to a field of view with multiple sources is formally incorrect.

2. While frank produces an estimate of the uncertainty on the fitted brightness profile, the estimate is not reliable because reconstructing the brightness from Fourier data is an ill-posed problem (see the discussion of this in [Jennings et al., 2020](#)). In particular, we do not have a robust approach for accurately extrapolating visibility amplitudes in a given dataset beyond the longest baseline that frank fits. The uncertainty on the brightness profile produced by the model is an underestimate, and we thus do not show a formal uncertainty on any profile in this chapter (the uncertainty described in

²While azimuthal asymmetries are ‘isolated’ in the imaged frank residuals, their brightness in the image is biased because the 1D fit cannot localize flux azimuthally. The fit recovers the *total* flux in any annulus correctly. But a feature such as a bright arc that is localized in azimuth will have its imaged brightness biased low, because the fit distributes it over the full 2π in azimuth.

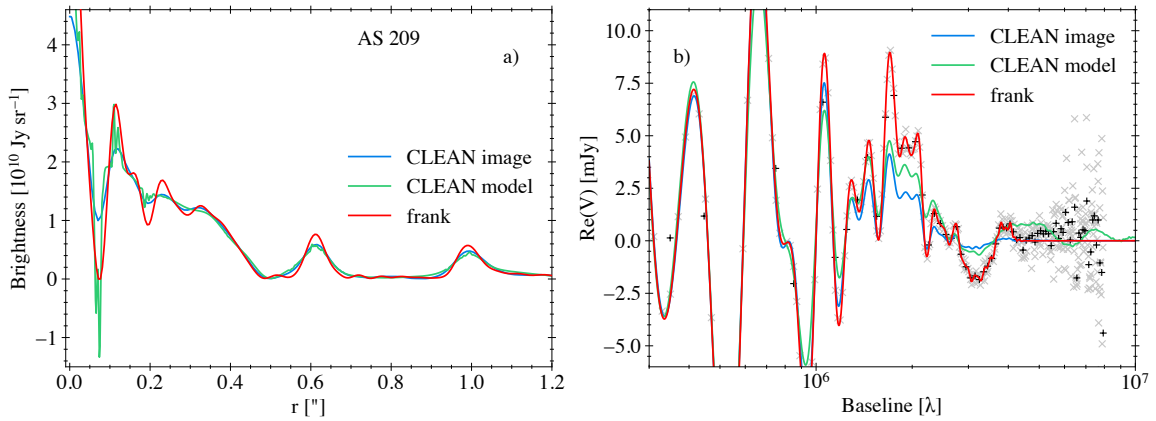


Fig. 3.1. Effect of CLEAN beam convolution (and other factors) on substructure recovery in DSHARP

- a) For the DSHARP observations of SR 4, radial brightness profiles extracted from the CLEAN image and CLEAN model, as well as the frank brightness profile. The frank profile and CLEAN model profile peak at 8 and 16×10^{10} Jy sr^{-1} respectively.
- b) The discrete Hankel transform (DHT) of the CLEAN profiles in (a), and the frank visibility fit. Data are shown in 20 and 100 k λ bins.

Sec. 3.2.1 is informal). The uncertainty on spatial scales well resolved by a frank fit is very low as demonstrated with mock data in Jennings et al. (2020). We note that the 1σ contour typically shown as an uncertainty on CLEAN brightness profiles is also often an underestimate, as will be evident by comparing the CLEAN and frank profiles in this chapter. A valuable test of systematics in the extrapolation of any model is perhaps best achieved in practice by comparing observations of the same source at different resolutions (see, e.g., Yamaguchi et al. 2020 for this comparison using sparse modeling, or Jennings et al. 2020 for such a comparison with frank fits to moderate resolution and DSHARP observations of AS 209).

3. The current frank model fits for the brightness in linear space and is not positive definite (see Appendix C in Jennings et al. 2020). Consequently the frank brightness profile for a disk with a deep gap or an inner cavity can exhibit negative brightness in this region. We will enforce that such fits must have nonnegative brightness (which trivially affects the visibility domain fit) and will note disks for which we impose this constraint.

3.3 Methodologies – Assessing effective CLEAN resolution and fit accuracy

Here we motivate resolution limitations that affect CLEAN images and CLEAN models (Sec. 3.3.1), then compare the accuracy of brightness profiles extracted from CLEAN images and CLEAN models to the `frank` fits for all DSHARP datasets, quantifying the resolution improvement in `frank` (Sec. 3.3.2). We summarize the principles of comparing `frank` fits to CLEAN in Sec. 3.3.3.

3.3.1 CLEAN model and image resolution

As noted in Sec. 3.1, convolution of the CLEAN model image with the CLEAN beam induces resolution loss in the final CLEAN image (and thus the 1D brightness profile). As an example, convolution of a circular beam whose full-width-at-half-maximum (*FWHM*) is equal to the FWHM of a Gaussian feature in a brightness profile in a broadening of the feature by $\approx 40\%$ and a reduction in its amplitude by $\approx 30\%$. Convolution in real space corresponds to multiplication in Fourier space, which induces a loss in resolution in the visibility domain via an underestimate of the observed visibility amplitudes, an effect that worsens with baseline. The FWHM of a Gaussian in real space as a function of radius r corresponds to a FWHM in Fourier space as a function of spatial frequency q by $\text{FWHM}_q = 4 \ln(2) / (\pi \text{FWHM}_r)$, obtained by relating the standard deviations in real and Fourier space.

While CLEAN beam convolution is the primary source of resolution loss in the CLEAN procedure, additional contributions can arise from, e.g., non-Gaussianity of the PSF (dirty beam). To assess the inherent performance of the CLEAN algorithm – the resolution prior to CLEAN beam convolution – it is thus useful to examine the CLEAN model image (the `.model` output of `tclean`). A brightness profile extracted from this image directly measures the algorithm’s achievable resolution and can itself be used to quantify a source’s emission features. Some real astrophysical flux may be missed because the final residual image has not been added to the model image, and the brightness profile is often noisy due to the model image’s sparse composition. But the Fourier transform of a profile extracted from the model image can quantify how well the modeling framework in the CLEAN procedure fits the observed visibility distribution as a function of baseline.

To this end, **Fig. 3.1** compares the brightness profiles extracted from the convolved CLEAN image and the CLEAN model, as well as the Fourier transform of these profiles, for the DSHARP observations of AS 209. The profiles identify the same features in Fig. 3.1(a), but the CLEAN model profile shows higher amplitudes (though also more noise) and narrower

widths for the two innermost disk features. This resolution advantage is not maintained across all disk features, as the CLEAN model profile does not recover the rings in the CLEAN image profile at $\approx 0.25''$ and $0.33''$. This is because not all of the real flux in the dirty image is incorporated into the CLEAN model. The CLEAN model profile also shows effectively identical widths and amplitudes as the CLEAN image profile for the two outer disk rings. Additionally and importantly, the CLEAN model can have negative components.

The Fourier domain equivalents of these brightness profiles in panel (b) show how the transform of the CLEAN image profile underestimates visibility amplitudes with increasing severity as baseline increases, as expected from beam convolution. The transform of the CLEAN model critically still underestimates the visibility amplitudes between $\approx 1.6 - 3.7 \text{ M}\lambda$, and overestimates amplitudes between $\approx 4.1 - 5.1 \text{ M}\lambda$. This demonstrates that additional factors beyond CLEAN beam convolution are nontrivially limiting recovery of the full information content in the long baseline data, and thus that *the inherent performance of the CLEAN modeling framework is resolution-limited*. We emphasize that all DSHARP datasets were CLEANed by experts in the field (Andrews et al., 2018; Huang et al., 2018a); these results trace practical resolution limits of CLEAN rather than the capability of a user.

For reference, if we compare the observed visibilities for a given survey dataset to the Fourier transform of a brightness profile extracted from the CLEAN image, then convolve the data with a beam that minimizes the difference with the Fourier transform of the brightness profile, the average CLEAN beam width across the survey is increased by a factor of 1.16. This simplistically treats all resolution-limiting factors in the CLEAN images as convolution operators, but it gives a sense of the aggregate resolution limitations in the CLEAN images beyond the effect of CLEAN beam convolution. PSF sidelobe structure and the compromise between resolution and sensitivity in the choice of the Briggs robust parameter in `tclean` are two notable resolution-limiting contributors.

For comparison to the CLEAN image and CLEAN model profiles, the `frank` fit to AS 209 is also shown in Fig. 3.1. The `frank` profile in panel (a) more highly resolves features seen in the CLEAN image profile and suggests a small bump at $\approx 0.16''$ not present in either the CLEAN image profile or the CLEAN model profile. In panel (b), the `frank` visibility fit is correspondingly more accurate than the transforms of both the CLEAN profile and the CLEAN model beyond $\approx 1 \text{ M}\lambda$; factors problematic for CLEAN such as PSF sidelobe structure are not limiting the `frank` fit resolution. *frank is thus outperforming the inherent resolution capability of the CLEAN algorithm*. This relative performance holds across the DSHARP survey, as we will now quantify.

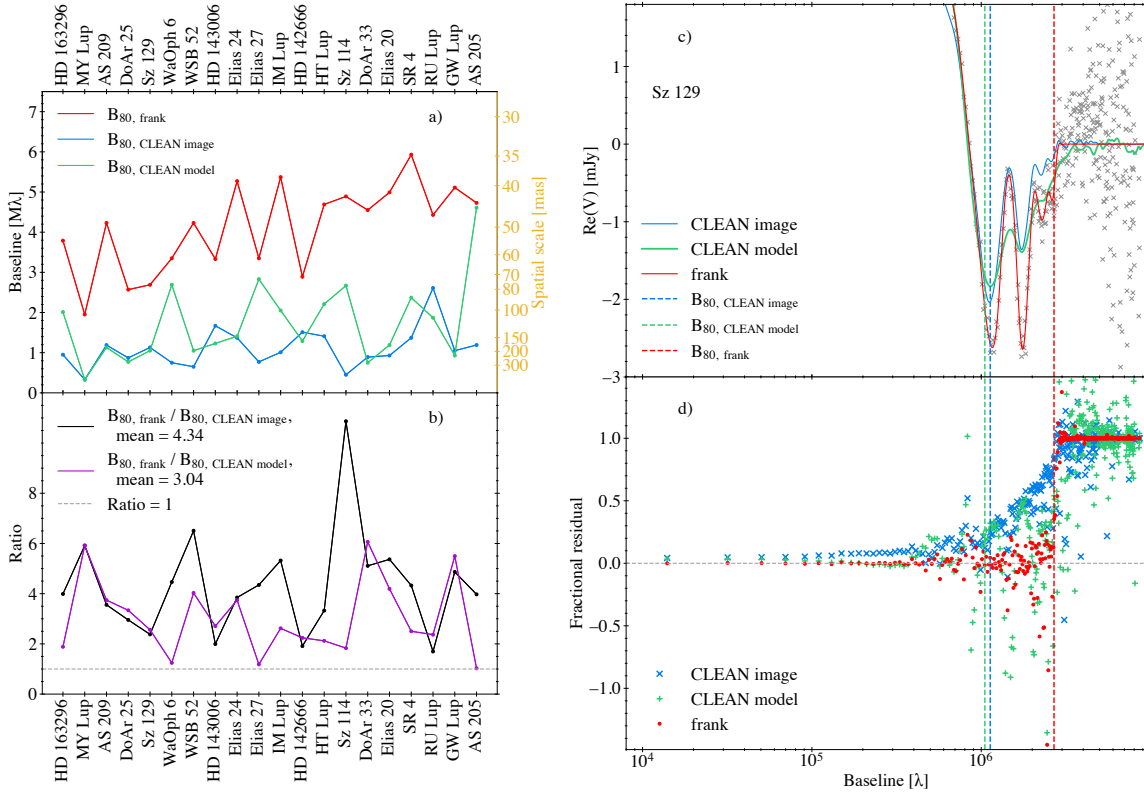


Fig. 3.2. CLEAN and frank fit accuracies in DSHARP

a) Baseline accuracy metric B_{80} for the convolved CLEAN image, CLEAN model, and frank visibility fits across the 20 DSHARP sources. The accuracy metric is the shortest baseline beyond which a fit shows $\geq 20\%$ error in visibility amplitude for a consecutive ≥ 200 k λ (Sec. 3.3.2). Sources are sorted by the expected baseline resolution of each dataset (see Equation 3.1).

b) Ratio of the frank to CLEAN baseline accuracy metric for both the convolved CLEAN image and CLEAN model visibility fits.

c) An example of the baseline accuracy calculation. The visibility distribution for Sz 129 (20 k λ bins), the frank visibility fit, and the Fourier transform of the brightness profiles extracted from the convolved CLEAN image and CLEAN model.

d) Fractional residuals [(data - model) / data; 20 k λ bins] for the convolved CLEAN image visibility fit, CLEAN model visibility fit and frank visibility fit.

3.3.2 Using the visibilities to quantify the accuracy of CLEAN model, CLEAN image, and frank brightness profiles

It is useful to consider a metric that directly quantifies the accuracy of a 1D brightness profile extracted from a CLEAN image or CLEAN model by comparing the Fourier transform of the profile to the observed visibilities. Such a metric can incorporate all sources of error in the visibility domain representation of the profile, while being agnostic to the causes of these errors. This metric also allows us to compare the fit accuracy in CLEAN and frank. We will use as a metric a simple assessment of a profile’s visibility space residuals.

We have found the most robust definition of a visibility space accuracy metric to be the shortest baseline B_{80} beyond which a fit shows $\geq 20\%$ error in visibility amplitude for a minimum consecutive 200 $k\lambda$ (using 20 $k\lambda$ binning). In practice these criteria robustly identify, across all 20 DSHARP sources, the first baseline at which the Fourier transform of a profile extracted from a CLEAN image or model, or the frank visibility fit, departs appreciably from the observed visibility amplitudes and only becomes more inaccurate with increasing baseline. Varying the 20% threshold has a weak effect on $B_{80, \text{frank}}$, while decreasing the threshold to 10% yields an average $B_{90, \text{CLEAN image}} = 0.64 B_{80, \text{CLEAN image}}$, and $B_{90, \text{CLEAN model}} = 0.87 B_{80, \text{CLEAN model}}$ across the 20 DSHARP datasets. Increasing the threshold to 50% gives an average $B_{50, \text{CLEAN image}} = 1.97 B_{80, \text{CLEAN image}}$ and $B_{50, \text{CLEAN model}} = 2.26 B_{80, \text{CLEAN model}}$. Varying the 200 $k\lambda$ threshold has a weak effect on $B_{80, \text{frank}}$, $B_{80, \text{CLEAN image}}$ and $B_{80, \text{CLEAN model}}$. The B_{80} metric approximately gives a corresponding spatial scale down to which a CLEAN or frank brightness profile *accurately* recovers substructure widths and amplitudes. A profile can of course partially recover information on smaller spatial scales, but features on these scales will be underresolved relative to the dataset’s available resolution information.

Fig. 3.2(c) – (d) show the application of the B_{80} accuracy metric to the Sz 129 DSHARP dataset. In panel (c) the Fourier transform of a brightness profile extracted from the CLEAN image begins to show error at baselines near $B_{80, \text{CLEAN image}}$, with inaccuracies growing in severity beyond $B_{80, \text{CLEAN image}}$. The transform of a profile extracted from the CLEAN model has a $B_{80, \text{CLEAN model}}$ that is highly similar to $B_{80, \text{CLEAN image}}$, with clear inaccuracy beyond $B_{80, \text{CLEAN image}}$. Applying the same metric to determine $B_{80, \text{frank}}$, the frank visibility fit in Fig. 3.2(c) accurately matches the observed visibility amplitudes out to $\approx 2.8 M\lambda$, the baseline at which the binned data’s SNR begins to oscillate about $\text{SNR} = 1$. Finally, the CLEAN (image and model) and frank residual visibilities in Fig. 3.2(d) demonstrate the higher accuracy of the frank fit even at moderate baselines. The CLEAN model residuals increase over a broad baseline range due to fundamental limitations in the CLEAN algorithm, while the CLEAN image residuals similarly increase over a broad range due additionally to

Table 3.1. Expected and achieved fit accuracy metrics shown in Fig. 3.2, as well as the baseline equivalent of the data’s expected resolution given in Equation 3.1. Standard deviations assume a Gaussian distribution. Conversions to au account for the unique distance to each source. λ is the observing wavelength; L_{80} is the eightieth percentile of the baseline distribution. The last two rows give a mean and standard deviation taken across the 20 datasets (i.e., not simply the ratio of preceding rows).

Baseline quantity, B	Mean and standard deviation
$B_{\text{data, expected}} = 0.574\lambda/L_{80}$	$4.75 \pm 1.39 M\lambda$
$B_{80, \text{ CLEAN image}}$	$1.10 \pm 0.48 M\lambda$
$B_{80, \text{ CLEAN model}}$	$1.72 \pm 0.97 M\lambda$
$B_{80, \text{ frank}}$	$4.12 \pm 1.05 M\lambda$
$B_{80, \text{ frank}}/B_{80, \text{ CLEAN image}}$	4.34 ± 1.99
$B_{80, \text{ frank}}/B_{80, \text{ CLEAN model}}$	3.04 ± 1.47

CLEAN beam convolution. The *frank* residuals remain ≈ 0 until the sharp rise at the baseline where the fit’s SNR threshold is met and the fit drives toward zero.

The ordering of the baseline accuracy measurements for Sz 129 is indicative of results across the survey: $B_{80, \text{ CLEAN image}} \lesssim B_{80, \text{ CLEAN model}} < B_{80, \text{ frank}}$. Fig. 3.2(a) shows this fit accuracy analysis for all DSHARP sources, ordered by increasing $B_{\text{data, expected}}$, the baseline equivalent of the expected angular resolution,

$$\theta_{\text{data, expected}} = 0.574\lambda/L_{80}. \quad (3.1)$$

Here λ is the observing wavelength and L_{80} is the eightieth percentile of the baseline distribution (Remijan et al., 2019). For reference, the observed visibility distributions for the DSHARP datasets typically extend to $\approx 8 - 10 M\lambda$, with a mean $B_{\text{data, expected}} = 4.72 M\lambda$. Fig. 3.2(b) shows that across the 20 DSHARP datasets, *frank* is accurately fitting the visibilities to a mean factor of 4.3 longer baseline than brightness profiles extracted from the CLEAN images, and a factor 3.0 longer baseline than profiles extracted from the CLEAN models. This reaffirms that *frank is outperforming the achieved resolution in both the CLEAN images and CLEAN models*. The resolution ratios and individual fit metrics are summarized in **Table 3.1**. For reference, increasing the accuracy metric’s error threshold from 20% to 50% decreases the mean $B_{80, \text{ frank}}/B_{80, \text{ CLEAN image}}$ from 4.3 to 3.0, and the mean $B_{80, \text{ frank}}/B_{80, \text{ CLEAN model}}$ from 3.0 to 1.9.

Table 3.2. For each DSHARP source, values for the five hyperparameters used to produce the frank fit: SNR criterion α , strength of smoothing w_{smooth} applied to the reconstructed power spectrum, outer radius of the fit R_{out} , number of radial and spatial frequency points N used in the fit, and floor value p_0 for the reconstructed power spectral mode amplitudes. Sensible choices for R_{out} , N and p_0 have a trivial effect on the fits: R_{out} is chosen to be larger than the disk’s outer edge, N is increased proportionally to R_{out} , and p_0 is the same for all fits. Sec. 3.2 gives a fuller explanation of, and motivation of the values for, α and w_{smooth} . Some fits, as indicated, are forced to be nonnegative or are fit with a combined frank and unresolved component model (in which case the visibility offset applied for the unresolved component is given); see Sec. 3.2.1–3.2.2. In the rightmost column, sources whose imaged frank residuals show the brightness asymmetry discussed in Sec. 3.5.7 are noted. All frank fits are available at <https://zenodo.org/record/5587841>.

Disc	α	$\log_{10} w_{\text{smooth}}$	R_{out} ["]	N	p_0 [Jy^2]	Fit conditions	Brightness asymmetry
AS 205	1.05	-1	2.2	457	10^{-15}		
AS 209	1.05	-4	1.9	395	"	Nonnegative fit	✓
DoAr 25	1.05	-1	3.1	500	"	Unresolved component fit; offset 0.24 mJy	
DoAr 33	1.01	-4	0.5	150	"	Unresolved component fit; offset 0.51 mJy	✓
Elias 20	1.01	-4	1.1	222	"	Unresolved component fit; offset 0.66 mJy	
Elias 24	1.01	-4	1.9	395	"	Unresolved component fit; offset 0.95 mJy	✓
Elias 27	1.25	-1	2.9	500	"	Unresolved component fit; offset 0.40 mJy	✓
GW Lup	1.05	-1	1.4	296	"	Unresolved component fit; offset 0.73 mJy	✓
HD 142666	1.50	-4	0.7	150	"		✓
HD 143006	1.01	-3	0.8	173	"		
HD 163296	1.01	-4	2.9	500	"		✓
HT Lup	1.05	-3	0.6	150	"		
IM Lup	1.10	-1	2.4	494	"	Unresolved component fit; offset 0.46 mJy	✓
MY Lup	1.01	-4	1.2	247	"	Unresolved component fit; offset 0.26 mJy	✓
RU Lup	1.05	-4	0.7	150	"		
SR 4	1.05	-4	0.5	150	"		
Sz 114	1.05	-2	0.7	150	"	Unresolved component fit; offset 0.51 mJy	
Sz 129	1.50	-4	1.0	198	"	Nonnegative fit	
WaOph 6	1.01	-4	1.9	395	"	Unresolved component fit; offset 0.83 mJy	✓
WSB 52	1.01	-4	0.5	150	"	Unresolved component fit; offset 0.33 mJy	

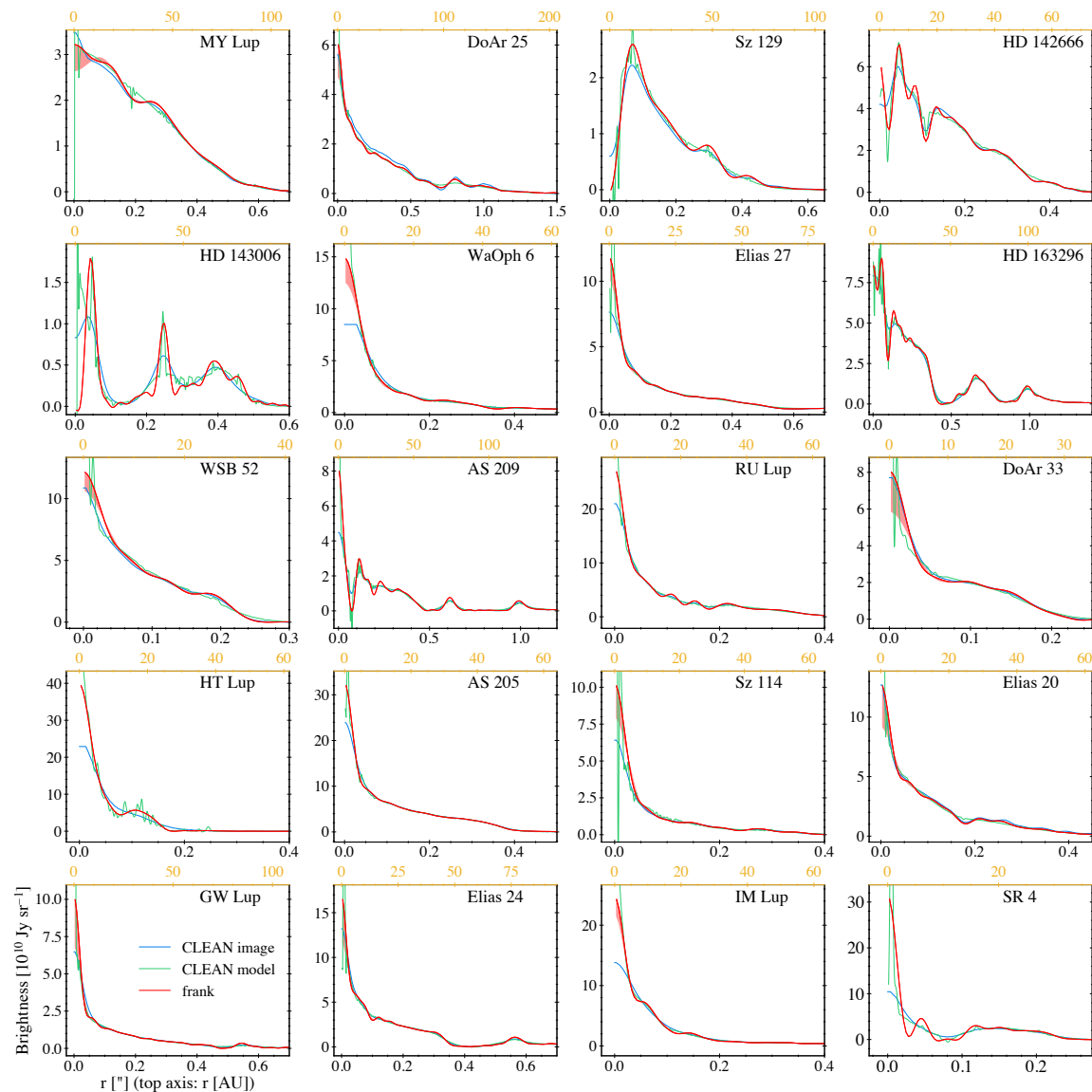


Fig. 3.3. Recovered brightness profiles

For each source in the DSHARP survey, the convolved CLEAN image, CLEAN model and frank brightness profiles. Some profiles zoom on the inner region of the disk. Discs are arranged from left to right and then top to bottom in ascending order of frank fit resolution. Informal uncertainties are shown on disks fit with the point source-corrected model (Sec. 3.2.1).

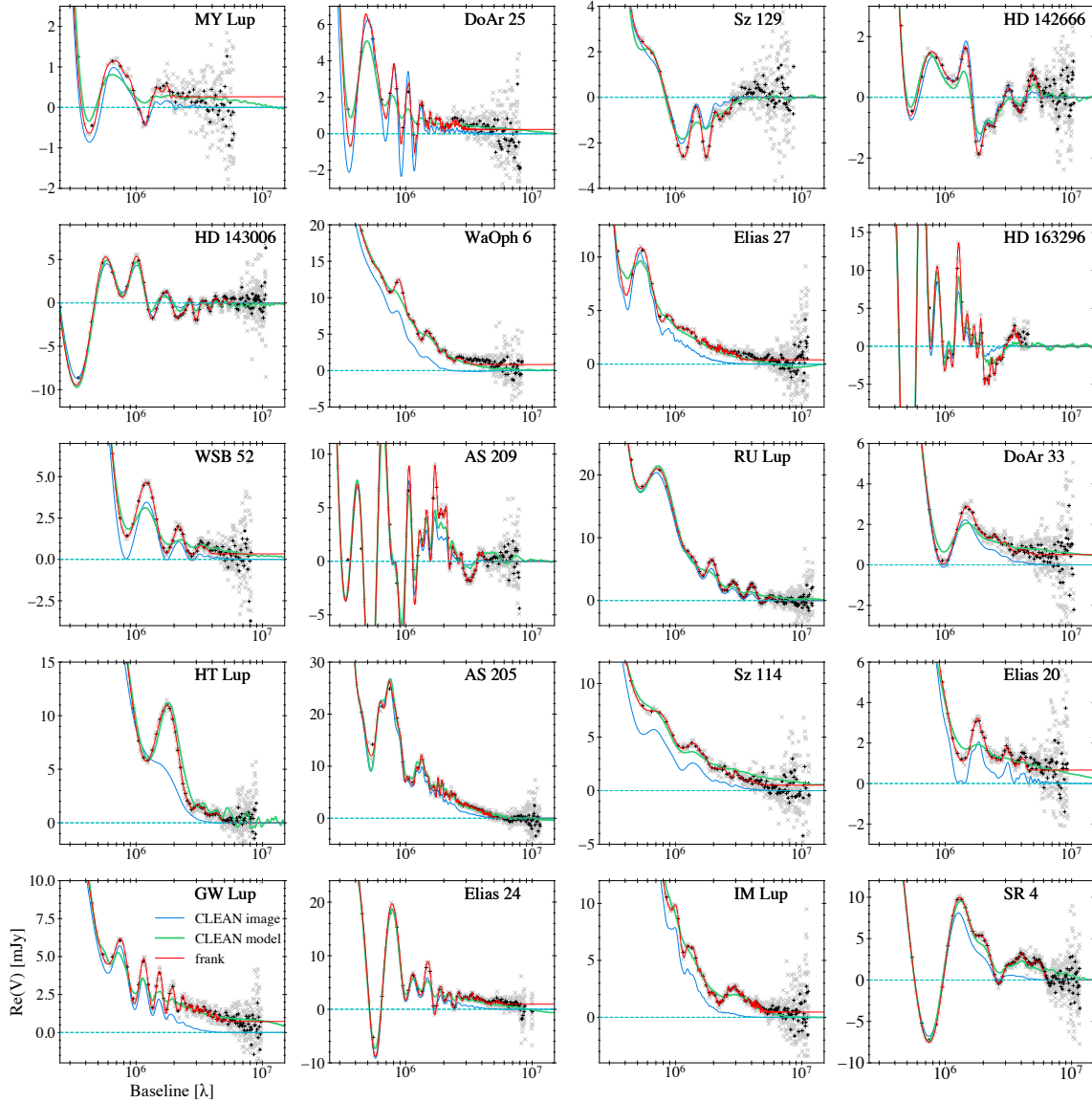


Fig. 3.4. Visibility fits at long baseline

For each source in the DSHARP survey, a zoom on the data’s long baselines ($> 0.25 \text{ M}\lambda$, corresponding to spatial scales $< 0.83'' \text{ mas}$) to show the accuracy of the CLEAN image, CLEAN model and `frank` fits in matching detailed visibility structure. Data are shown in 20 and 100 $\text{k}\lambda$ bins (gray ‘ \times ’ and black ‘+’ respectively) and become heavily noise-dominated at the longest baselines across all datasets, typically at $\geq 5 \text{ M}\lambda$. `frank` does not fit these regions, as doing so would imprint noisy oscillations on the recovered brightness profile. Discs are arranged from left to right and then top to bottom in ascending order of `frank` fit resolution.

Table 3.3. Major new and appreciably more highly resolved features identified in frank brightness profiles. Feature widths and gap depths are defined following the method in [Huang et al. \(2018a\)](#); see Sec. 3.5. The datasets’ finite resolution entail that the values for ring widths are upper bounds, and for gap widths and depths are lower bounds.

Disc	New (or better resolved) feature	Location [au]	Identifier in Huang et al. (2018a)	Width [au] (width in Huang et al. 2018a [au])	Gap depth (depth in Huang et al. 2018a)
AS 209	Deeper gap, brighter ring	9	D9	5.2 (4.7 ± 0.2)	0.00 (0.45 ± 0.02)
Elias 24	New gap	14	B14	4.9 (8.9 ± 0.2)	N/A
		14	—	2.2 (—)	0.89 (—)
GW Lup	Deeper and sharper gap, brighter and narrower ring	75	D74	11.7 (12.1 ± 0.4)	0.01 (0.31 ± 0.03)
HD 142666	New gap, brighter ring	85	B85	7.5 (11.3 ± 0.4)	N/A
		3	—	3.6 (—)	0.42 (—)
HD 143006	Cleared inner cavity, brighter rings, wider and sharper gaps [†] ,	7	B6	4.0 (5.3 ± 1.4)	N/A
		≤ 7	—	N/A	N/A
HD 163296	brighter and narrower ring	7, 41, 64	B6, B41, B65	5.3, 5.4, 9.5 (5.0 ± 1.4, 12.2 ± 1.0, 11.5 ± 1.4)	0.07, 0.43
		25, 52	D22, D51	28.4, 16.1	N/A
RU Lup	Deeper gaps	(21.7 ± 1.0, 12.8 ± 1.4)		(0.04 ± 0.02, 0.53 ± 0.02)	
		41	B41	5.4 (12.2 ± 1.0)	N/A
SR 4	wider and deeper gap [†]	10	D10	3.0 (3.2 ± 1.4)	0.47 (0.93 ± 0.03)
		13	B14	3.8 (3.6 ± 1.4)	N/A
Sz 129	Cleared inner cavity, brighter ring	14, 21, 29	D14, D21, D29	3.1, 3.4, 4.8	0.90, 0.75, 0.57
		4	—	(—, < 7, 4.5 ± 0.3)	(—, —, 0.78 ± 0.01)
Sz 129	Cleared inner cavity, brighter ring	11	D11	1.4 (—)	0.64 (—)
		≤ 11	—	8.6 (6.3 ± 1.4)	0.02 (0.23 ± 0.02)
		11	B10	N/A	N/A
				12.3 (17.6 ± 1.1)	N/A

[†] Because these gaps are structured in the frank profiles, the gap center is determined as the average of the adjacent ring centers. The gap depth is determined using the average brightness across the gap width.

3.3.3 A general note on comparing frank to CLEAN

The CLEAN algorithm is a model to deconvolve the 2D sky brightness from the instrument PSF, which requires a functional form for the fundamental brightness unit (e.g., point sources or Gaussians). By comparison, `frank` is a visibility fitter, with the express goal of accurately recovering the 1D projection of the data. This is done nonparametrically, but requires assumptions that the emission is axisymmetric and that the source geometry can be perfectly determined. These two tools can be used for different goals; in the case of accurately describing a source’s azimuthally averaged brightness, `frank` offers a clear resolution advantage over a profile extracted from a CLEAN image. The tradeoff is the potential imprint of reasonably high contrast azimuthal asymmetries on the morphology of a `frank` brightness profile; this must be diagnosed by Fourier transforming (imaging) the residual `frank` visibilities and/or examining the imaginary component of the observed data. In summary, for the purpose of obtaining a 1D brightness profile of a source (under the assumptions of axisymmetry and known source geometry), `frank` will yield a more accurate (higher resolution) result, without a loss in sensitivity, compared to extracting an azimuthally averaged profile from the CLEAN image.

3.4 Results

Fig. 3.3 shows the `frank` brightness profile for each DSHARP disk, as well as the CLEAN image profile from [Huang et al. \(2018a\)](#) and the CLEAN model profile obtained using the published `tclean` scripts. The `frank` fits exhibit more highly resolved, and in some cases new, substructure relative to the CLEAN images. Consistent with expectations from CLEAN beam convolution, the CLEAN image profiles also tend to underestimate the source’s peak brightness (`frank` must as well, albeit to a lesser extent). The `frank` profiles further identify fine substructure more clearly than the noisy CLEAN model profiles. As a general note, feature morphologies primarily in the inner disk of the `frank` profiles can be expected to evolve with higher resolution observations, which could for example find gaps to be deeper and broader, resolve rings into multiple components, or reduce the amplitude of features by placing stronger constraints on structure at the smallest scales recovered in these data. **Table 4.1** gives the values of the hyperparameters used in each `frank` fit.

Fig. 3.4 shows a zoom on the long baselines of the `frank` visibility fits and the Fourier transform of the CLEAN image and model brightness profiles across the survey. The higher resolving power evident in the `frank` brightness profiles for all 20 sources corresponds to the `frank` visibility fits matching the data at high accuracy to longer baseline than the CLEAN image profiles and (to a lesser extent) the CLEAN model profiles. Table 4.1 notes which `frank`

fits use the point source-corrected model (Sec. 3.2.1) and gives the point source visibility amplitude applied. For some sources – DoAr 25, Elias 27, HD 163296, AS 205, GW Lup, Elias 24, and IM Lup – `frank` is clearly fitting some noise on top of the signal at long baseline. This manifests as short spatial period, low amplitude ($< 1\%$ of the peak brightness) noise in the corresponding brightness profile. We accept this as a tradeoff for fitting out to baselines at which the binned data SNR approaches unity. The effect is seen most clearly in the logarithmic brightness plots for GW Lup, Elias 24 and HD 163296 in Fig. 3.10 (which will be discussed in Sec. 3.5.6).

3.5 Analysis

Table 3.3 summarizes the major new and appreciably better resolved annular features in the `frank` fits across the survey, as well as quantifies the gap/ring widths and gap depths. For the purpose of comparison, this quantification follows the approach in [Huang et al. 2018a](#) (see their §3.2). The metric measures a gap depth as the ratio of the brightness at center of the gap I_d to the brightness at the center of the ring I_b exterior to the gap, and determines a feature width by defining the edges of an adjacent gap and ring using the average $I_{\text{mean}} = 0.5(I_d + I_b)$. This does not yield a perfect comparison for feature widths and depths between CLEAN and `frank` profiles, because the `frank` profiles exhibit additional low amplitude substructure (e.g., in some gaps and on the wings of some rings). But as a coarse comparison, among the features in Table 3.3, 7 of the 12 gaps and each of the 8 rings were quantified in [Huang et al. \(2018a\)](#). For this subset, the `frank` profiles find the gaps to be a mean 14% wider and 44% deeper, and the rings to be a mean 26% narrower. This illustrates the utility of the super-resolution fits for substructure characterization.

Grouping the `frank` brightness profiles in Fig. 3.3 by morphology, we can identify new substructure trends. We will exclude the multiple systems HT Lup and AS 205 from the following analysis because, as discussed in Sec. 3.2.2, while the 1D `frank` profiles are not visibly biased by the presence of multiple sources in the field of view, application of the model to such a case is still formally incorrect. We do note here that the `frank` fit for HT Lup identifies the primary disk’s spiral structure as the bump in the profile at 15 au in Fig. 3.3.

Collectively, these trends as detailed below demonstrate two broad findings. First, the DSHARP sources – already rife with gaps and rings as identified in [Huang et al. \(2018a\)](#) – are even more structured, especially interior to 30 au. Second, the gaps and rings detected in the CLEAN images, which in many cases have widths 2 – 3 \times that of the CLEAN beam, become deeper and wider (gaps) or narrower and brighter (rings) when we fit the data with `frank`.

3.5.1 The compact DSHARP disks all show substructure

The super-resolution `frank` fits find new substructure in each of the DSHARP survey’s three compact ($R_{\max} < 50$ au), single-disk systems – WSB 52, DoAr 33 and SR 4. As a prominent example – shown in **Fig. 3.5** – the `frank` profile for SR 4 resolves the broad depression in the CLEAN profile into two distinct, deep gaps within 20 au (those listed in Table 3.3). The innermost of these is centered at 4 au; the outer, centered at 11 au, is predicted by `frank` to be at least as deep as the fit’s noise floor ($\approx 10^9$ Jy sr⁻¹, or 4% of the fitted peak brightness). Additionally, the `frank` profile for WSB 52 finds a new, shallow gap/ring pair at 13/17 au (in addition to the previously identified gap/ring pair at 21/25 au), and the `frank` fit for DoAr 33 resolves the single gap/ring pair at 9/17 au in the CLEAN profile into two gap/ring pairs.

Typical of current observations of compact disks, the shallow features in the `frank` profiles for these compact sources could be either intrinsically wide and shallow or narrow and underresolved. Sensitive observations at higher angular resolution are needed to distinguish between the two scenarios. We use a point source-corrected fit for WSB 52 and DoAr 33 (Sec. 3.2.1), with the profile’s sensitivity to the point source visibility amplitude shown as the informal uncertainty band in Fig. 3.5.³ The substructure in both sources is robust to this informal uncertainty.

The commonality of substructure `frank` finds across these three compact DSHARP sources suggests that in general compact disks, just as more extended disks, may routinely exhibit annular substructure. SR 4 is particularly notable in this context, with its effectively empty gap at 11 au analogous to the empty gap `frank` finds at 10 au in the much larger disk of AS 209 (outer radius ≈ 150 au). If compact disks are frequently structured, it may follow that the same physical processes (including companions) responsible for structure in larger disks are also efficacious in smaller disks. The improved identification of substructure in the compact DSHARP disks is also of particular interest, as compact sources represent a significant yet understudied component of the protoplanetary disk population.

³We recall from Sec. 3.2.1 that this uncertainty is calculated as the difference in brightness as a function for radius between the standard point source fit and the $1.5\times$ point source amplitude fit. In the standard point source fit, the point source amplitude is set as the mean of the visibility amplitudes beyond the baseline at which the $20\text{ k}\lambda$ binned visibility SNR begins to oscillate about unity. We note that this point can be at a baseline slightly shorter than that beyond which the visibility scatter strongly increases, which can result in the fit not perfectly bisecting the average value of the longest baseline points.

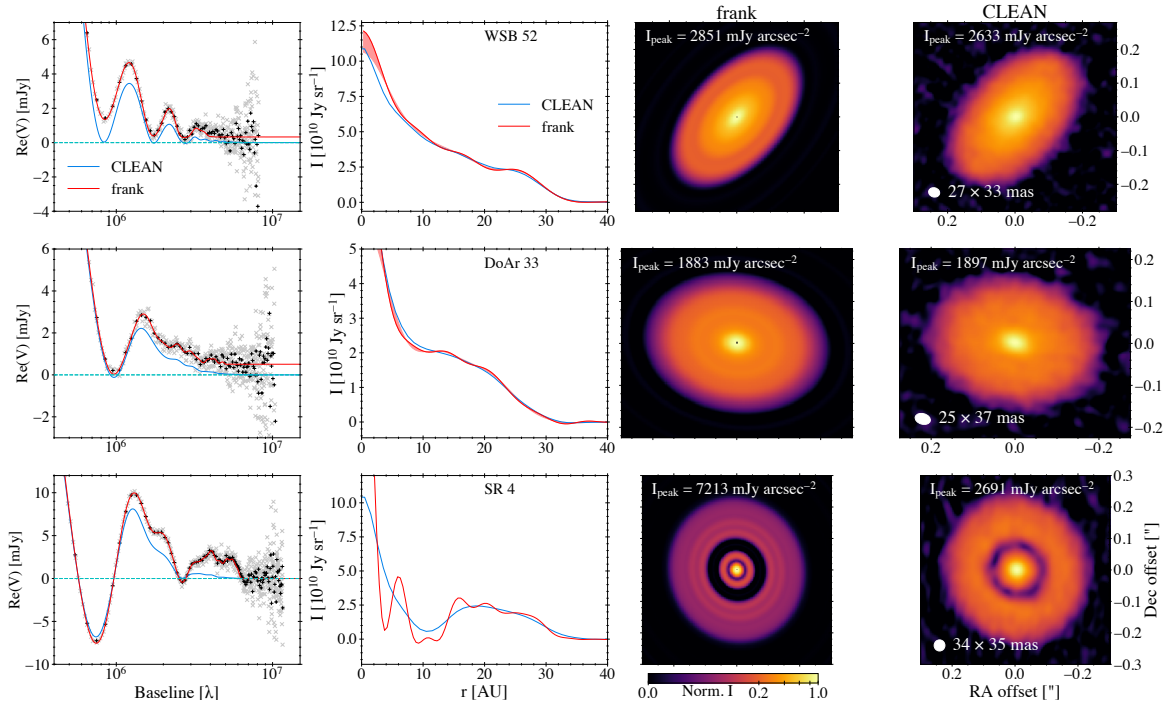


Fig. 3.5. Substructure in compact disks

For each of the compact ($R_{\max} < 50$ au) single-disk systems in DSHARP, a zoom on the data’s long baselines ($> 0.40 M\lambda$, corresponding to spatial scales $< 0.52''$ mas; data shown in 20 and 100 $k\lambda$ bins), the `frank` and CLEAN visibility domain fits, the `frank` and CLEAN brightness profiles (in some cases zoomed into lower brightness), an image of the `frank` profile swept over 2π and reprojected, and the CLEAN image. The `frank` and CLEAN images of each disk use the same arcsinh stretch color scaling ($I_{\text{stretch}} = \text{arcsinh}(I/a) / \text{arcsinh}(1/a)$, $a = 0.02$, as shown by the colorbar), but different brightness normalization. The generic color bar gives the normalized color scale, and the peak brightness is listed on each image. Discs are arranged from top to bottom by increasing `frank` fit resolution. Informal uncertainties are shown on disks fit with the point source-corrected model (Sec. 3.2.1).

3.5.2 Extended disks show brighter rings, deeper gaps, and hints of inner disk substructure

`frank` fits for several extended DSHARP sources better resolve the gaps and rings that appear shallow in the CLEAN profiles, as shown in **Fig. 3.6**. This is especially apparent in the outer gap and ring pair in GW Lup, where in the `frank` profile the brightness contrast between the gap and ring is 0.01, compared to 0.31 in the CLEAN profile (see Table 3.3); and in RU Lup, where the three consecutive gaps interior to 30 au are deeper in the `frank` profile (the contrast of the gap at 29 au for example is 0.57 in the `frank` fit, compared to 0.78 in the CLEAN profile). The `frank` fit to Elias 24 robustly finds a new gap at 13 au, and the model better resolves the faint ring at 45 au in Sz 114.

For RU Lup, Sz 114, Elias 20, GW Lup, and Elias 24, the model suggests a steep inner disk in the inner 5 – 7 au, followed by a shallower slope at slightly larger radii. This may be an indication of underresolved substructure between $\approx 7 - 12$ au. We use the point source-corrected fit (Sec. 3.2.1) for 5 of the 6 sources in Fig. 3.6 and show the profile’s sensitivity to the point source visibility amplitude as the informal uncertainty band. This suggests we should be cautious about the fit’s exact structure in the innermost disk, while the change in slope is robust to this uncertainty.

In addition to these sources, the `frank` brightness profile for a majority of the 20 DSHARP disks exhibits either gap and ring substructure interior to 30 au, or clear change in slope interior to ≈ 12 au. This suggests substructure is common not only at ≥ 30 au, but also at the smaller separations that harbor the bulk of the observed exoplanet population. The Gaussian kernel density estimate for gap and ring locations in [Huang et al. \(2018a\)](#) peaks at 30 au, while by comparison the `frank` fits suggest that the occurrence rate continues to rise toward $r = 0$. The (effectively) empty gaps at ≈ 10 au in the `frank` fits for AS 209 (gap contrast of 0.00 in the `frank` profile, compared to 0.45 in the CLEAN profile) and SR 4 (contrast of 0.02 in the `frank` profile, compared to 0.23 in the CLEAN profile) suggest that the lack of such deep features identified thus far in high resolution disk observations is an artifact of resolving power, rather than an intrinsic absence of cleared gaps in inner disks.

3.5.3 Two of the oldest DSHARP disks appear to have inner cavities

`frank` finds that 2 of the 20 DSHARP disks, HD 143006 and Sz 129, have a fully cleared inner cavity. The CLEAN profiles for these sources show a decreasing brightness toward $r = 0$, but not a full cavity in **Fig. 3.7**, and the `frank` fits also find the disks to have an appreciably brighter inner rim (noted in Table 3.3). [Huang et al. \(2018a\)](#) inferred the presence of a cleared cavity in these sources from the CLEAN images, now confirmed by the `frank` fits.

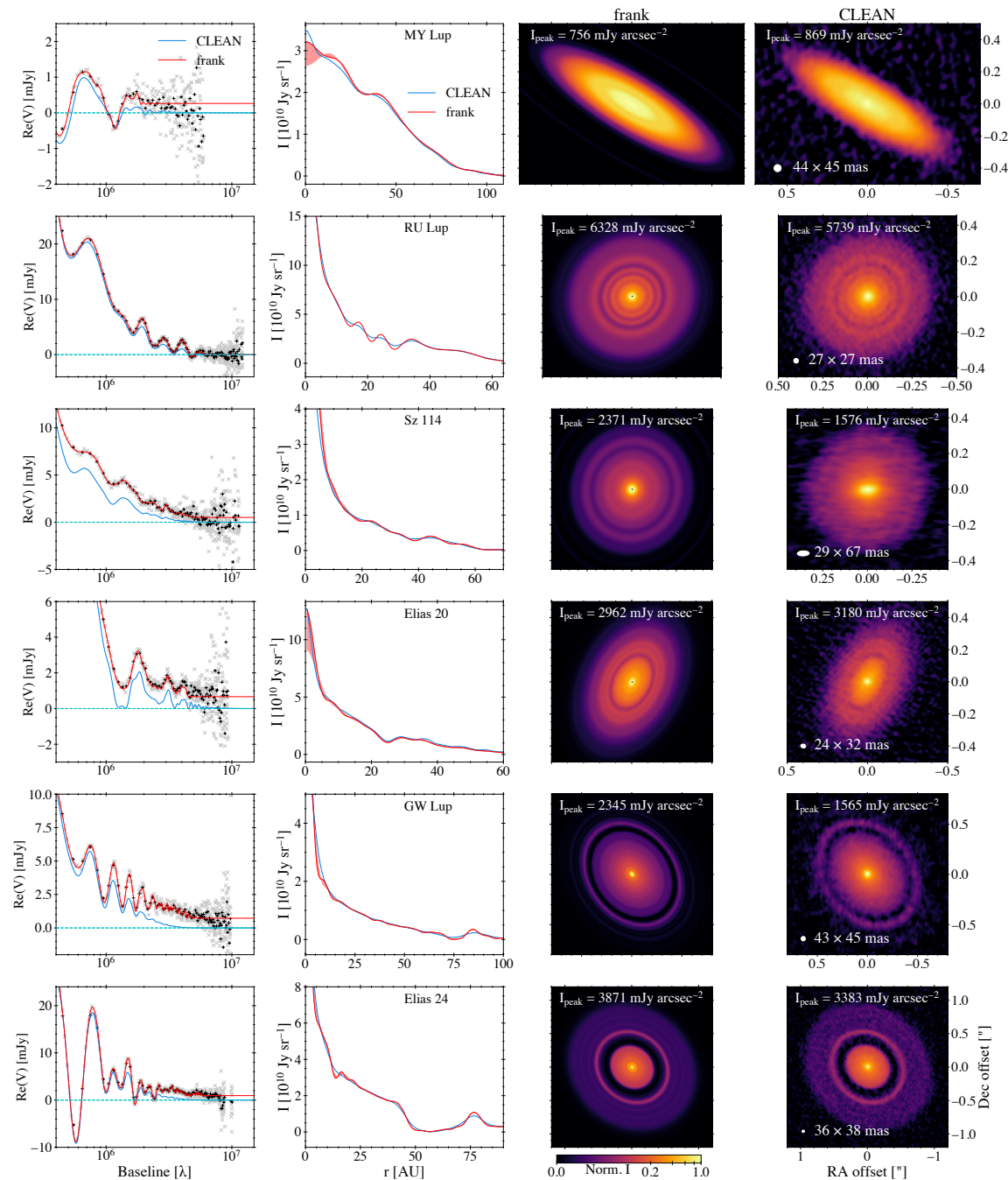


Fig. 3.6. Substructure in extended disks

As in Fig. 3.5, but for the extended (> 50 au) DSHARP disks in Sec. 3.5.2.

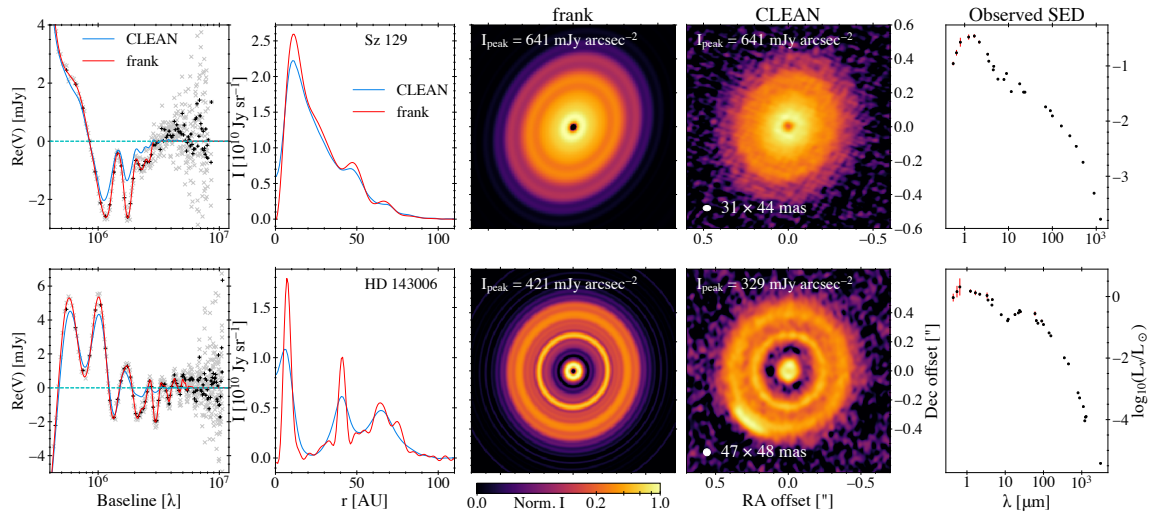


Fig. 3.7. Evidence for inner cavities

As in Fig. 3.5, but for the DSHARP disks showing indications of inner cavities. Additionally shown are the observed spectral energy distributions (Andrews et al., 2018). The azimuthally localized bright arc along the outer edge of the outer ring in the CLEAN image for HD 143006 is erroneously visualized as a symmetric feature in the frank image (because the model is 1D) and manifests in the frank brightness profiles as the ‘bump’ at 77 au.

The spectral energy distribution (SED) for HD 143006 (and potentially for Sz 129) shows a dearth in the near-IR ($\approx 10 - 20 \mu\text{m}$) and excess in the far-IR ($\approx 20 - 100 \mu\text{m}$) as shown in Fig. 3.7 (SEDs adapted from Andrews et al., 2018). These may be indications of transition disks, with the depletion of near-IR emission suggesting a lack of hot midplane dust at small radii relative to the cold, optically thin outer disk signature in the form of the far-IR excess. It is also possible that either of these sources has a sharp rise in brightness in the innermost disk that is not resolved by frank.

Intriguingly, HD 143006 and Sz 129 may be two of the oldest disks in the DSHARP sample. Among the survey’s single-disk systems, 5 of 18 orbit a star whose inferred age is > 2 Myr as reported in Andrews et al. 2018 (see specific references in their Table 1): HD 143006 (4.0 ± 2.0 Myr), Sz 129 (4.0 ± 2.5 Myr), MY Lup ($10.0^{+4.0}_{-2.0}$ Myr), HD 142666 (12.6 ± 0.3 Myr), and HD 163296 (12.6 ± 4.0 Myr). These estimates are in general subject to systematic challenges such as interpreting robust ages at high effective temperature, and Andrews et al. (2018) additionally note that the age for MY Lup may be overestimated due to the inclined and flared disk extinguishing the stellar spectrum. Of the remaining four potentially old sources, HD 143006 and Sz 129 show inner cavities in the frank fits, while HD 142666 and HD 163296 both show gaps interior to ≈ 5 au. No other frank brightness profile in DSHARP shows a turnover in brightness interior to 5 au, which may tentatively suggest that

these four objects are experiencing the later stages of disk dispersal, losing (or having already lost) their inner disk at their potentially advanced ages. The expectation is in line with the finding by [Espaillat et al. \(2014\)](#) that the fraction of transition disks in star forming regions and young clusters increases from $\approx 1\%$ to $\approx 10\%$ for ages $\gtrsim 2$ Myr (these percentages do carry large uncertainties).

More speculatively, HD 142666, HD 143006 and HD 163296 are 3 of the 4 most structured disks in the survey, perhaps indicating that even if annular substructures do form early, disks may become more structured over time (e.g., as additional planets form). AS 209 complicates this interpretation though, being the other highly structured disk in the survey and having an inferred age of only $1.0^{+2.5}_{-1.0}$ Myr.

3.5.3.1 Improved constraints on dust trapping

The narrower rings in the `frank` fits relative to CLEAN can offer improved constraints on dust trapping. [Dullemond et al. \(2018\)](#) examine the outer disk rings in the CLEAN profiles for five of the DSHARP sources – AS 209, Elias 24, GW Lup, HD 143006, and HD 163296 – and infer deconvolved widths w_{dust} to compare to the local pressure scale height h_p . If this ratio is < 1 , the rings are inferred to be the result of dust traps. With this ratio a plausible range of widths for gas pressure bumps w_{gas} at the radial location of the dust rings can also be determined, in turn yielding a range of values for the ratio of the viscosity parameter to the local Stokes number ([Dullemond et al. 2018](#), Equation 21),

$$\frac{\alpha_{\text{turb}}}{\text{St}} = \left[\left(\frac{w_{\text{gas}}}{w_{\text{dust}}} \right)^2 - 1 \right]^{-1}. \quad (3.2)$$

The lower this ratio, the lower the threshold to induce the streaming instability. [Rosotti et al. 2020](#) take a similar approach, using the dust ring widths together with deviations from Keplerian velocity inferred from the ^{12}CO observations in AS 209 and HD 163296 to measure $\alpha_{\text{turb}}/\text{St}$. According to their Equation 1,

$$\frac{\alpha_{\text{turb}}}{\text{St}} = -\frac{2w_{\text{dust}}^2}{r_0} \frac{v_k^2}{c_s^2} \frac{d}{dr} \left(\frac{\delta v_\phi}{v_k} \right). \quad (3.3)$$

Here r_0 is the radial location of the dust ring, v_k the local Keplerian velocity, c_s the sound speed, and $\delta v_\phi = v_\phi - v_k$ is the deviation from Keplerian.

Following the procedure in [Dullemond et al. \(2018\)](#) to determine dust ring widths, we find each of the 8 rings in the `frank` profiles are narrower than even the deconvolved widths in [Dullemond et al. \(2018\)](#), by a mean 24%. The `frank` widths are also narrower than the

4 of these rings examined in [Rosotti et al. \(2020\)](#) by a mean 13%. **Table 3.4** compares the frank widths to those in [Dullemond et al. \(2018\)](#) and [Rosotti et al. \(2020\)](#), as well as the corresponding estimates of w_{dust}/h_p . The narrower frank dust rings yield a reduction in estimates of $\alpha_{\text{turb}}/\text{St}$ by a mean 47% relative to [Dullemond et al. 2018](#) (for w_{min} , the minimum width of the gas pressure bump; see that work) and by a mean 25% relative to [Rosotti et al. \(2020\)](#). These results suggest the dust ring widths in [Dullemond et al. \(2018\)](#) and [Rosotti et al. \(2020\)](#) are overestimates, and that smaller values of α_{turb} (or larger values of St) are thus needed to agree with the true (unknown) ring widths. A smaller ratio of $\alpha_{\text{turb}}/\text{St}$ would in turn correspond to a lower threshold for inducing the streaming instability.

To emphasize the importance of an accurate visibility fit, we note that [Dullemond et al. \(2018\)](#) find the deconvolved ring widths are in some cases wider, but in others narrower, than the widths determined by parametrically fitting the visibilities for AS 209 ([Guzmán et al., 2018](#)), HD 163296 ([Isella et al., 2018](#)) and HD 143006 ([Pérez et al. 2018](#); see Appendix C in [Dullemond et al. 2018](#)). The frank profiles instead yield narrower rings than the deconvolved widths in [Dullemond et al. 2018](#) in all cases, because frank is fitting structure in the observed visibilities to longer baseline than the parametric visibility fits. Comparing the frank visibility fit for HD 163296 to the parametric visibility fit in [Isella et al. 2018](#) for example, frank accurately traces the visibilities to $\approx 3.8 \text{ M}\lambda$, while the parametric fit begins to show clear error beyond $\approx 0.9 \text{ M}\lambda$, and the frank ring widths are thus narrower.

3.5.4 Spiral arms appear to extend into the spiral disks' cores

The frank fits to the three single-disk systems in the survey exhibiting prominent spirals – WaOph 6, Elias 27 and IM Lup – show clear deviations from a smooth envelope in the disks' bright cores, which extend to $\approx 45, 60$ and 30 au respectively. The imaged frank residual visibilities⁴ in **Fig. 3.8** suggest these features may not be tracing symmetric gaps and rings, but instead the (azimuthally averaged) innermost components of the spiral arms. This interpretation is tentatively supported by examining polar projections of the deprojected frank imaged residuals (not shown), which appear to faintly trace the arms to moderately smaller radii than the polar plots in [Huang et al. \(2018b\)](#).

The model for each of these disks uses the point source-corrected fit (Sec. 3.2.1), with the profile's sensitivity to the point source visibility amplitude shown as the informal uncertainty band in Fig. 3.8. The exact structure in the disks' cores should thus be taken with caution,

⁴As discussed in Sec. 3.2.2, an azimuthally averaged frank brightness profile is erroneous for any radius at which the brightness is not symmetric. However because frank correctly fits for the *averaged* brightness in each annulus, subtracting the fit from the observed visibilities effectively isolates asymmetric structure in a residual image (analogous to the same procedure with CLEAN fits in Figure 1 of [Huang et al., 2018b](#)).

Table 3.4. Dust trapping constraints from frank rings (see Sec. 3.5.3.1). Column (1): Disc name. (2): Ring name in Huang et al. (2018a). (3): Measured frank dust ring widths $w_{\text{dust, frank}}$, deconvolved widths $w_{\text{dust, decon.}}$ (Dullemond et al., 2018), and widths inferred using the ^{12}CO rotation curve $w_{\text{dust, rot. curve}}$ (Rosotti et al., 2020). (4): Ratio of the ring widths in (3) to the pressure scale height h_p . (5): Ratio of turbulent viscosity to Stokes number $\alpha_{\text{turb}}/\text{St}$, using minimum gas pressure bump widths $w_{\text{gas, min.}}$ following Dullemond et al. (2018). For cases in which $w_{\text{dust}}/h_p \geq 1$, values of $\alpha_{\text{turb}}/\text{St}(w_{\text{gas, min.}})$ are not given. (6): Ratio of turbulent viscosity to Stokes number $\alpha_{\text{turb}}/\text{St}$, using gas pressure bump widths $w_{\text{gas, rot. curve}}$ following Rosotti et al. (2020). Widths w in columns (3) – (6) are defined as the standard deviation of a Gaussian.

Disc	Ring identifier	$w_{\text{dust, frank}}$ [au] ($w_{\text{dust, decon.}}$ [au]) { $w_{\text{dust, rot. curve}}$ [au]}	$w_{\text{dust, frank}}/h_p$ ($w_{\text{dust, decon.}}/h_p$) { $w_{\text{dust, rot. curve}}/h_p$ }	$\alpha_{\text{turb}}/\text{St}(w_{\text{gas, min.}, \text{ frank}})$ ($\alpha_{\text{turb}}/\text{St}(w_{\text{gas, min.}, \text{ decon.}})$)	$\alpha_{\text{turb}}/\text{St}(w_{\text{gas, rot. curve}, \text{ frank}})$ { $\alpha_{\text{turb}}/\text{St}(w_{\text{gas, rot. curve}})$ }
(1)	(2)	(3)	(4)	(5)	(6)
AS 209	B74	2.86 (3.38) {3.39 ± 0.06}	0.5 (0.6) {0.6}	0.35 (0.57)	0.13 {0.18 ± 0.04}
AS 209	B120	3.63 (4.11) {4.12 ± 0.07}	0.4 (0.4) {0.4}	0.14 (0.19)	0.10 {0.13 ± 0.02}
Elias 24	B77	3.41 (4.57)	0.5 (0.6)	0.29 (0.66)	
HD 163296	B67	6.32 (6.84) {6.85 ± 0.03}	1.5 (1.6) {1.6}	— (—)	0.19 {0.23 ± 0.03}
HD 163296	B100	3.80 (4.67) {4.66 ± 0.08}	0.5 (0.7) {0.7}	0.40 (0.77)	0.03 {0.04 ± 0.01}
GW Lup	B85	3.12 (4.80)	0.4 (0.6)	0.21 (0.68)	
HD 143006	B41	2.09 (3.90)	1.0 (1.9)	— (—)	
HD 143006	B65	4.99 (7.31)	1.4 (2.0)	— (—)	

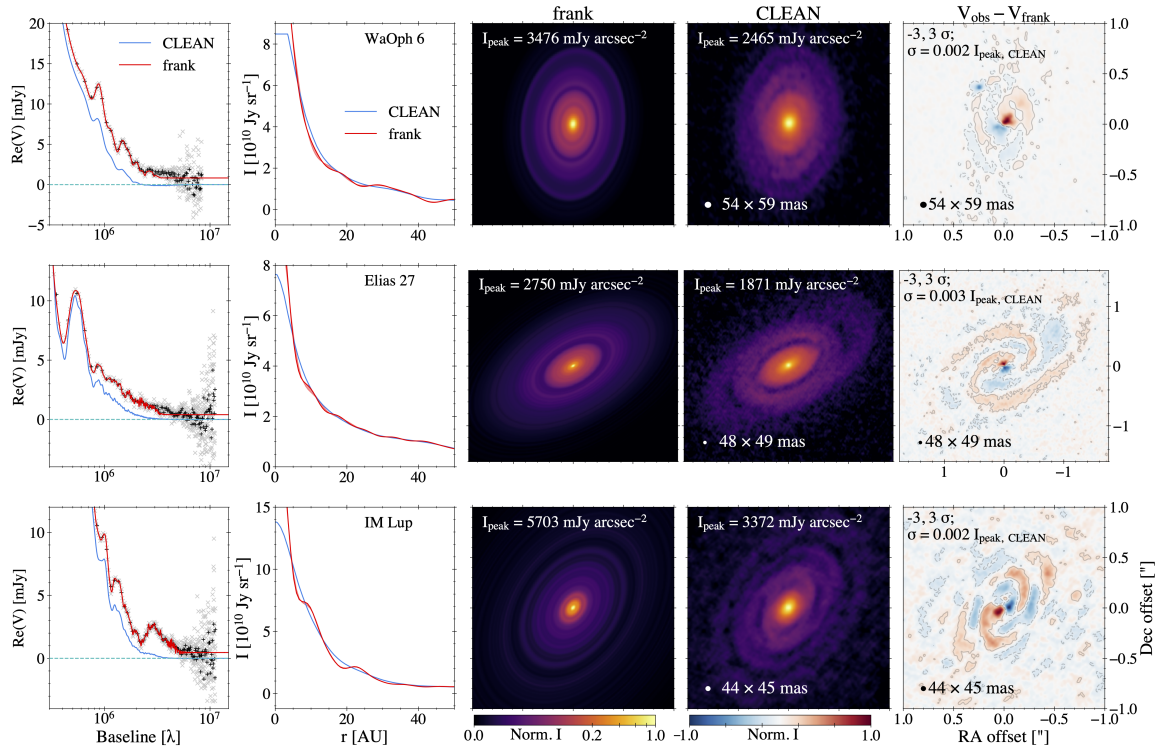


Fig. 3.8. Tracing spiral arms into their disk's cores

As in Fig. 3.5, but for the DSHARP disks exhibiting strong spiral structure. The visibility plots here zoom on baselines $> 0.30 M\lambda$ (corresponding to spatial scales $< 0.69''$). Additionally shown are the frank residual visibilities imaged (0 CLEAN iterations). Residual images use a linear color scale (a normalized color bar is shown, and the σ value for each image is given). Azimuthal asymmetries in CLEAN images are erroneously visualized as symmetric features in the frank images because the frank model is 1D.

though the features in WaOph 6 beyond ≈ 20 au, in Elias 27 beyond ≈ 15 au, and throughout the inner disk in IM Lup are robust to this informal uncertainty.

3.5.5 The most structured DSHARP sources have morphologically similar inner disks

frank fits to the three most highly structured DSHARP disks – HD 163296, AS 209 and HD 142666 – in Fig. 3.9 more fully resolve gaps and rings present in the CLEAN profiles, especially the gap-ring pair in each source interior to 15 au (noted in Table 3.3). The frank profiles also show new substructure in the inner disk of each source that is strikingly similar: a gap-ring pair, immediately exterior to which is a gap that shows a brightness excess (potentially a pressure bump) on both of its wings, and exterior to this a shallow depression (this region is highlighted for each source in Fig. 3.9). Whether this morphological similarity,

including the newly identified features, is due to the same physical process, e.g., an embedded planet, would require detailed hydrodynamic simulations that are beyond the scope of this chapter.

3.5.6 Deep gap morphologies in frank profiles potentially indicate embedded planets

The frank brightness profiles for the six DSHARP disks shown in **Fig. 3.10** – GW Lup, Elias 24, HD 163296, AS 209, SR 4, and HD 143006 – show that deep gaps which were already prominent in the CLEAN profiles become deeper and/or wider with sharper edges, as well as more structured in some cases. The detailed structure within the gaps in the frank profiles varies weakly as the fit’s SNR criterion is varied (recall that we have accepted some low amplitude, short spatial period noise in the profiles as a tradeoff for fitting the visibilities out to baselines at which the binned data SNR approaches unity). Insensitive to the exact fit is the presence of local maxima exterior to the gaps, as well as less prominent maxima or shallow slopes interior to the gaps. Some of the gap morphologies (both the structure within the gap and on its edges) are qualitatively similar to the dust surface density distribution surrounding a gap-opening planet in hydrodynamic simulations (particularly those for a stationary or slowly migrating planet in [Meru et al. 2018](#) and [Nazari et al. 2019](#)). However detailed simulations would be required to confirm agreement in any individual case; we leave this to a future work. The four gaps shaded in gray in Fig. 3.10 have a claimed planet detection: in GW Lup ([Pinte et al., 2020](#)), Elias 24 ([Jorquera et al., 2020](#)) and both gaps in HD 163296 ([Pinte et al., 2018](#); [Teague et al., 2018](#)); the gaps shaded in pink do not have a detection.

3.5.7 A geometric viewing effect traces disk vertical structure

Ten of the 20 DSHARP sources (noted in Table 4.1) have frank residual visibilities that when imaged exhibit a clear two-fold brightness asymmetry in the inner disk, oriented about the disk’s major axis. The imaged frank residuals for these sources are shown in Fig. 3.13. **Fig. 3.11** demonstrates the most prominent case, Elias 24, in which the asymmetry spans the entirety of the inner disk. This brightness asymmetry across the inner disk can be explained by a geometric viewing effect, provided the disk is optically thick, has finite thickness, and is not viewed exactly face-on. In such a case the observer sees the disk photosphere like the inclined interior of a bowl, where the angle between the local surface normal and the line of sight to the observer varies with azimuth. Since the maximum brightness is seen on the side

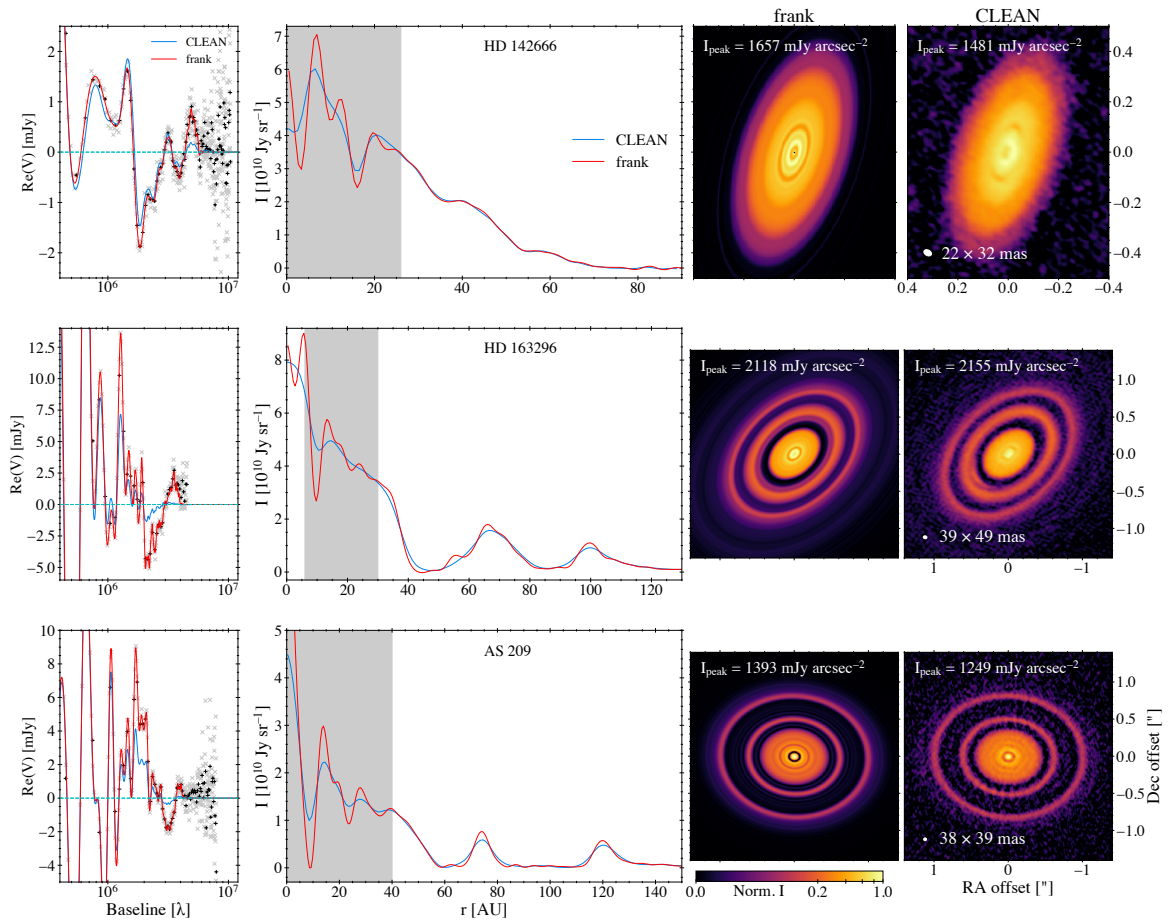


Fig. 3.9. Highly structured disks

As in Fig. 3.5, but for the DSHARP disks exhibiting the highest density of substructures. The azimuthally localized bright arc along the inner edge of the intermediate ring in the CLEAN image for HD 163296 is erroneously visualized as a symmetric feature in the frank image (because the model is 1D) and manifests in the frank brightness profile as the ‘bump’ at 55 au. The shaded regions show morphological similarities across disks as discussed in Sec. 3.5.5.

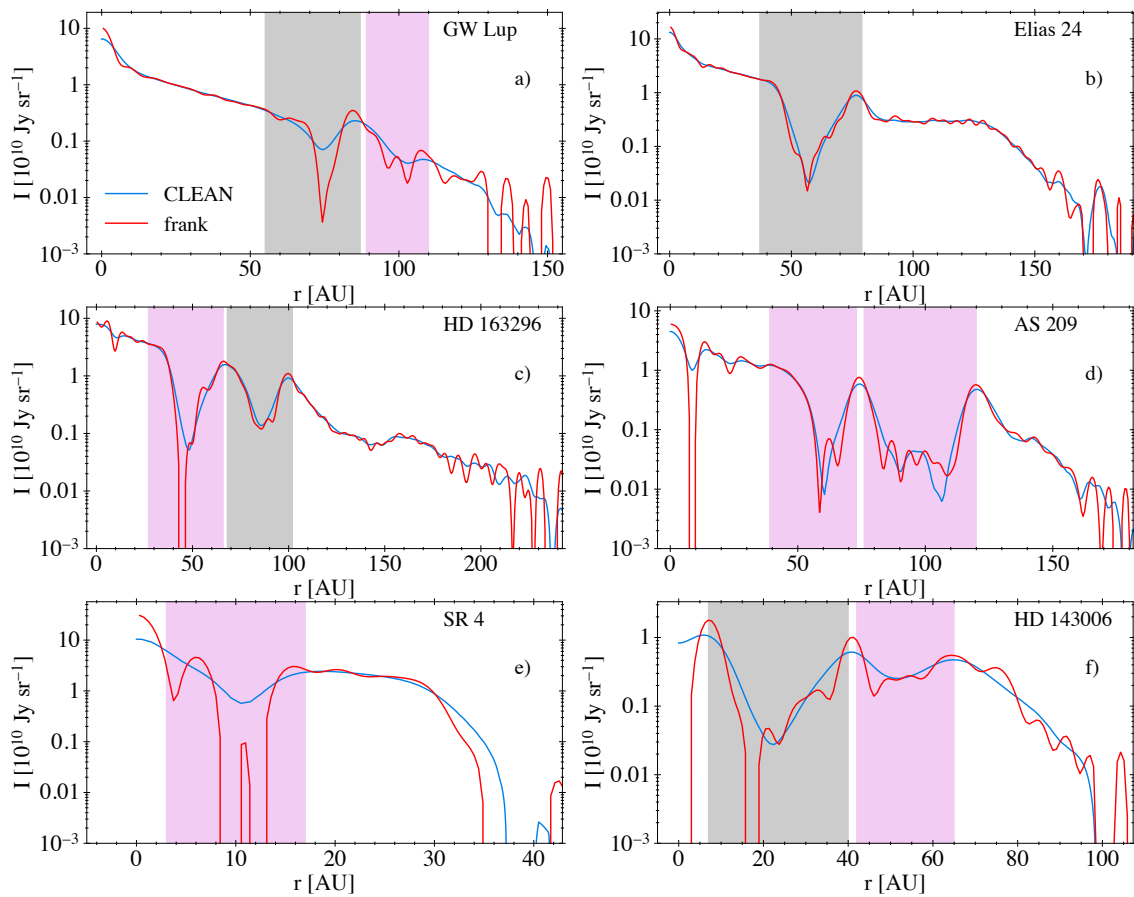


Fig. 3.10. Morphologies for deep and structured gaps

frank and CLEAN brightness profiles in logarithmic brightness for DSHARP disks whose frank profiles have gaps that are either appreciably deeper or contain more structure than seen in the CLEAN profiles. Gap regions are shaded for identification; those shaded in gray have a claimed planetary detection (either from gas kinematics or direct imaging), and those in pink have no detection.

of the disk surface that is more angled towards the observer (i.e., on the far side of the major axis), the brightness asymmetry can be used to trace the inner disk vertical structure.

This interpretation is supported by considering that among the subsample of 10 disks in which we see the asymmetry in the `frank` imaged residuals, a corresponding asymmetry was identified in the CLEAN images or their residuals for six sources: in the inner 5 – 10 au of HD 142666, HD 163296 and Sz 129 (Huang et al., 2018a); and in the core of the survey’s three disks with spiral structure, Elias 27, IM Lup and WaOph 6 (Huang et al., 2018b). The $^{12}\text{CO } J = 2 - 1$ emission indicates the brighter region is on the disk’s far side in all six cases (Huang et al., 2018a; Isella et al., 2018), consistent with our geometric interpretation. Huang et al. (2018a) posit the brightness asymmetry in HD 142666, HD 163296 and Sz 129 could be attributed to viewing the interior surface of a finite thickness ring, while we additionally see the asymmetry in sources such as Elias 24, where it spans the entirety of the (fairly smooth) inner disk. Huang et al. (2018b) attribute the brightness asymmetries in the spiral disks to an imperfect determination of the disk phase center, though they note that asymmetric brightness may also be caused by vertical structure.

Additionally, the 10 disks in which we see the brightness asymmetry all have a 1.25 mm optical depth as calculated in Huang et al. (2018a) that is ≈ 1 in the inner disk (and if the brightness asymmetry is tracing vertical structure, the true optical depth may be $\gg 1$). Placing quantitative constraints on vertical scale height and optical depth using the brightness asymmetry will be addressed in a future work. Investigating potential alternative origins of the observed brightness asymmetry in Sec. 3.8, we find that a simple warp (inclination misalignment between an inner and outer disk) does not yield an asymmetric brightness pattern oriented about the major axis, and an incorrect source phase center does not explain the presence of this asymmetry across so many of the DSHARP sources.

3.6 Conclusions

Finding the effective resolution of CLEAN images in the DSHARP survey corresponds to an increase in the CLEAN beam width by an average factor of 1.16, we used `frank` to accurately fit the 1D visibility distribution for each of the 20 DSHARP sources to a mean factor of 4.3 longer baseline than brightness profiles extracted from the CLEAN images and a factor of 3.0 longer baseline than the CLEAN models. This yielded super-resolution brightness profiles for each source that more highly resolved azimuthally symmetric (and asymmetric) disk substructure seen in the CLEAN images. The `frank` fits additionally identified new features – an extra gap in the inner 20 au of SR 4 and Elias 24, as well as new excesses and depressions in the inner 30 au of HD 142666, HD 163296 and AS 209. Overall the analysis demonstrated

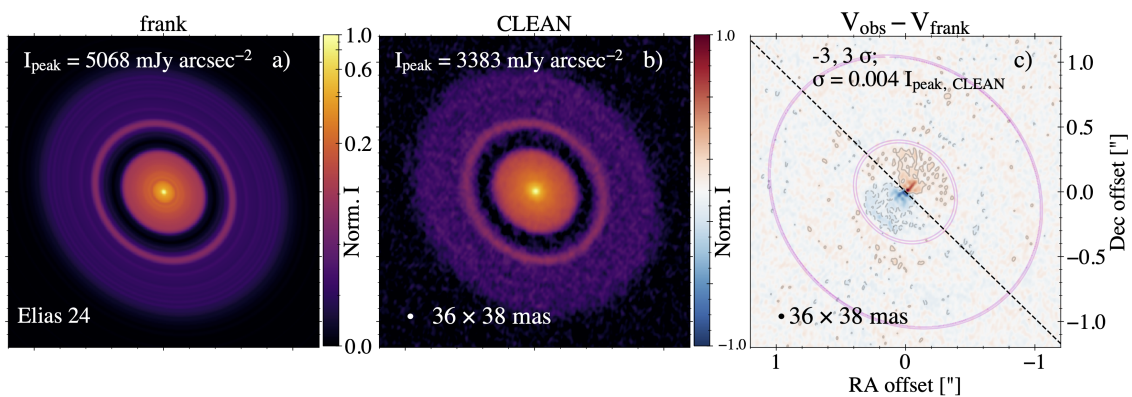


Fig. 3.11. A geometric viewing effect tracing disk vertical structure

- a) For Elias 24, an image of the frank profile swept over 2π and reprojected.
- b) The CLEAN image. The frank and CLEAN images of each disk use the same arcsinh stretch ($I_{\text{stretch}} = \text{arcsinh}(I/a) / \text{arcsinh}(1/a)$, $a = 0.02$), but different brightness normalization. The generic color bar gives the normalized color scale, and the peak brightness is listed on both images.
- c) The frank residual visibilities imaged (0 CLEAN iterations), with contours overplotted, as well as additional lines tracing the outer edge of the inner disk and the disk outer edge (from (a)), and a dashed line along the fitted position angle (as a proxy for the disk's major axis). The residual image is convolved with the published CLEAN beam and uses a linear color scale. The shown 3σ contours correspond to a residual brightness $< 1\%$ of the local average brightness in the CLEAN image at the outer edge of the inner disk, 42 au. The residual image uses a linear color scale (a normalized color bar is shown, and the σ value for each image is given).

two key points: the DSHARP sources – already found to ubiquitously contain gaps and rings in [Huang et al. \(2018a\)](#) – are even more densely structured, especially interior to 30 au; and the gaps and rings detected in the CLEAN images, despite in many cases having widths 2–3× that of the CLEAN beam, become deeper and wider (gaps) or narrower and brighter (rings) when we fit the data with a technique not subject to CLEAN beam convolution.

We further identified new trends in substructure across the survey:

- substructure in compact disks: frank profiles for all three compact ($R_{\text{max}} < 50$ au), single-disk systems showed substructure, suggesting it may be frequent in compact sources
- substructure in extended disks: frank profiles for six extended ($R_{\text{max}} > 50$ au), fairly smooth DSHARP sources found indications of a change in slope in the innermost disk, implying the interior regions of disks may commonly be structured
- potential transition disks: frank profiles for two of the oldest disks in the sample suggested they have cleared inner cavities, which may indicate they are dispersing
- spiral arms in disk cores: frank profiles for the three single-disk systems with prominent spirals suggested the spiral arms reach into the disks’ cores
- inner disk morphologies: frank profiles for the three most structured DSHARP disks exhibited highly similar substructure morphology in their inner 40 au, indicating the same physical processes, e.g., the presence of a companion, may be responsible
- gap morphologies: frank profiles for six survey disks that already had prominent gaps in the CLEAN images showed these features to have greater depth and/or more structure (both within the gap and on its wings)

We found that lower values of $\alpha_{\text{turb}}/\text{St}$ than determined in [Dullemond et al. \(2018\)](#) and [Rosotti et al. \(2020\)](#) are needed to explain the super-resolved ring widths in AS 209, Elias 24, HD 163296, GW Lup, and HD 143006. Finally, the frank fits also found clear evidence of a geometric viewing effect in 10 of the 20 DSHARP sources that traces inner disk vertical structure.

The extent to which these substructure trends are present in surveys and individual datasets with different biases (DSHARP consists primarily of bright, large disks; [Andrews et al., 2018](#)) is a question we will address in subsequent work. Those trends that do hold beyond DSHARP may offer the potential to broadly inform open questions on the physical mechanisms underlying dust substructure in protoplanetary disks.

On the technical side, the analysis in this chapter demonstrated that `frank`, and super-resolution fitting techniques more generally, can consistently extract more 1D substructure information from sub-mm disk observations than both CLEAN images and CLEAN models. There is a clear limitation with `frank` in that it reconstructs the 1D brightness of a source, rather than the 2D brightness as in a CLEAN image. However, for the purpose of obtaining a 1D brightness profile of a source (under the assumptions of axisymmetry and known source geometry), `frank` will yield a more accurate (higher resolution) result, without a loss in sensitivity, compared to extracting an azimuthally averaged profile from the CLEAN image. Super-resolution techniques can provide new insights from existing datasets, better informing physical inference without requiring deeper and/or longer baseline observations. In practice these tools can also be approachable and efficient; performing a `frank` fit requires nontrivial choices for only two hyperparameters (the parameter space for each being small), and the `frank` fits shown in this chapter all took $\lesssim 1$ min to run. All `frank` fits in this chapter are available at <https://zenodo.org/record/5587841>.

3.7 Appendix A: Point source-corrected fits

To demonstrate the effect of a point source-corrected fit, **Fig. 3.12(a) – (b)** compares a model generated with this approach to two standard `frank` fits for GW Lup. In panel (b), the observed visibilities remain systematically positive at the longest baselines, i.e., do not converge on zero. Their offset is 0.7 mJy; for reference, $\text{Re}(V)$ plateaus at 88.9 mJy at short baselines. First considering the two standard `frank` fits (which use different α values), the model with $\alpha = 1.1$ fits the visibilities out to $\approx 7 M\lambda$, at which point some of the $100 k\lambda$ binned values approach zero. However because the data are noise-dominated by this baseline, the corresponding brightness profile in **Fig. 3.12(a)** has noisy oscillations, most apparent at small radii. By comparison, increasing α to 1.3 effectively fits the data to shorter baseline, $\approx 5 M\lambda$, beyond which the binned SNR start to dither about $\text{SNR} = 1$. The model drives toward zero (by design) once its SNR threshold is reached, which is problematic if the fit's slope at this baseline is steeper than the average slope of the true, underlying signal in the data. That appears to be the case here, as the fit's slope still translates to strong oscillations in the brightness profile in panel (a).

The point source-corrected model in **Fig. 3.12(b)** fits the data out to comparable baseline to the $\alpha = 1.3$ case, but once its SNR threshold is reached, the fit takes on a constant visibility amplitude (rather than driving toward zero). This amplitude is the mean of the data beyond the baseline at which the $20 k\lambda$ binned SNR first drops below unity. The strong oscillations in the innermost disk present in the standard fits are no longer apparent in the point source-corrected

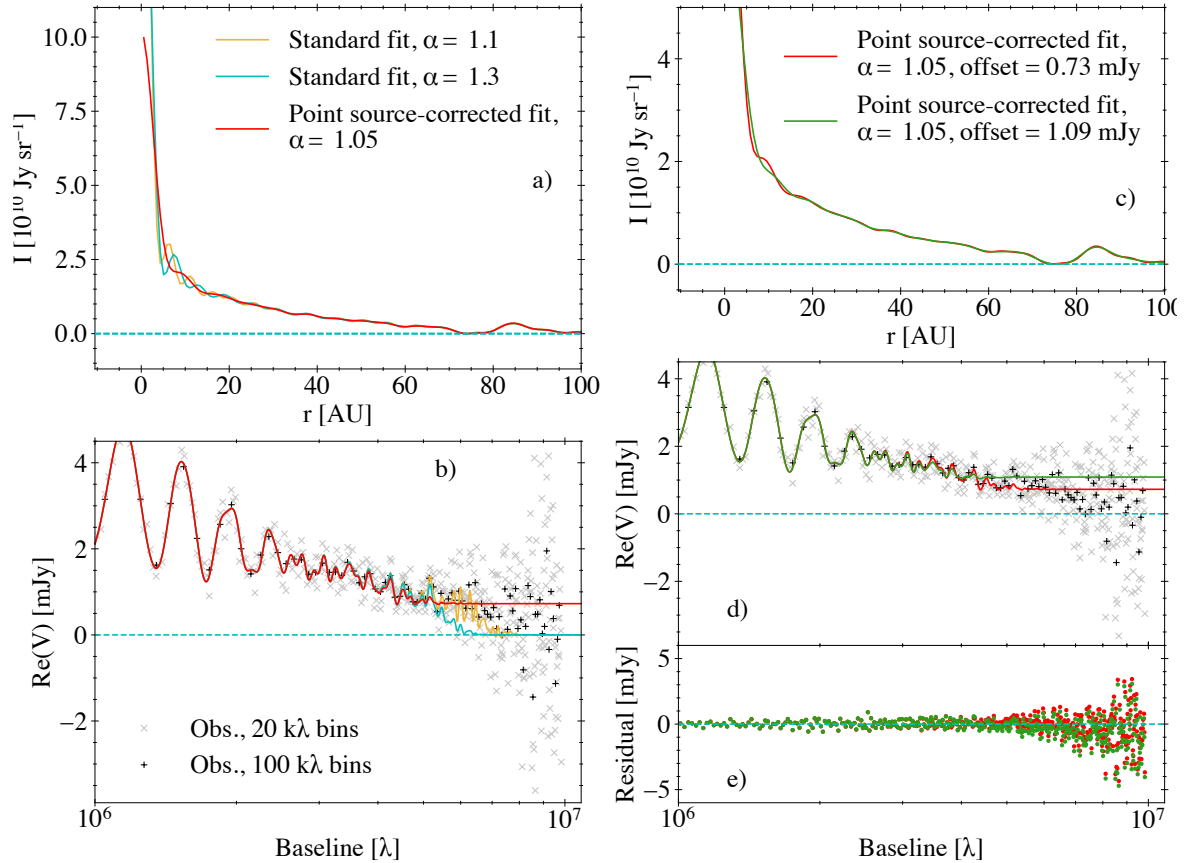


Fig. 3.12. Effects of a point source-corrected fit

- a) frank brightness profiles for two standard fits using different α , and the profile for the point source-corrected fit shown in the main text.
- b) A zoom on the data's long baselines ($> 1.0 \text{ M}\lambda$, corresponding to spatial scales $< 0.2''$; data shown in 20 and 100 $\text{k}\lambda$ bins), the two standard frank fits, and the point source-corrected fit.
- c) frank brightness profiles for the point source-corrected fit in (a), and a point source-corrected fit using a $1.5\times$ larger point source amplitude.
- d) As in (b), but for the two point source-corrected fits in (c).
- e) Residuals (in 20 $\text{k}\lambda$ bins) of the two point source-corrected fits in (d).

fit, though we do still see some small amplitude oscillations across all radii in the brightness profile, whose sensitivity we will examine below. The fit's zero slope over the data's longest baselines yields a conservative representation of features on the corresponding spatial scales in the brightness profile, which we prefer because of the ambiguity in where the true visibility signal converges on zero.

While for practical purposes the point source-corrected model is the best approach we have at present to fit a visibility distribution that does not clearly converge on zero, it has limitations. First, because it involves fitting `frank` to a visibility distribution from which we have subtracted a constant offset, the SNR of the resulting data are not identical to those of the observed data. This is why the point source-corrected model in Fig. 3.12(b) fits the visibilities beyond $\approx 4 \text{ M}\lambda$ less closely than the shown standard fits, despite using a lower α .

Second, while we have determined the point source amplitude by taking the mean of the longest baseline visibilities, they are in general dominated by noise and so not necessarily an accurate indication of the true signal. We thus test how the applied point source offset affects the `frank` visibility fit and in turn substructure in the brightness profile. Fig. 3.12(d) shows the visibility fit for GW Lup when we increase the point source offset to $1.5\times$ the mean of the long baseline data. The factor of 1.5 was chosen empirically as a liberal upper bound for the sensible range in point source visibility amplitude. This offset expectedly yields larger amplitude (negative) residuals in panel (e), while also reducing structure in the brightness profile interior to $\approx 0.1''$ in panel (c). The reduced prominence of structure seems less correct than the fit with a lower point source offset based on the residuals in (e). However it is also not clear that the structure interior to $0.1''$ in the smaller point source offset fit is real; this ambiguity motivates our treatment of the difference between these two fits as an informal uncertainty estimate in all disks where we use the point source-corrected model in the main text. Note that a point source amplitude of 0 Jy would correspond to a standard `frank` fit, and we do not consider this fit in the uncertainty estimate because we expect the standard fit to be erroneous in cases where there is need for a point source model.

3.8 Appendix B: Residual image brightness asymmetries

Considering the residual brightness asymmetries in Sec. 3.5.7, **Fig. 3.13** shows the `frank` residuals imaged for each DSHARP source. Here we present tests to determine whether the observed trend of a brightness asymmetry oriented about the major axis in 10 of the 20 sources could – instead of a geometric effect – be produced by either an incorrect source phase center or a simple warp in the form of a misalignment between the inner and outer disks (effectively an incorrect inclination). First considering a phase center error, shifting

the phase center of a flat disk generates an asymmetry in the direction of the centroid error. In order to explain the observed asymmetry pattern in 10 of the 20 DSHARP disks would thus require that some aspect of fitting for the phase center (which was done by fitting a 2D Gaussian to the image) biased the error toward alignment with the disk’s minor axis. We do not see how such a bias could arise.

Nevertheless, as a precaution we considered the 1σ uncertainties in fitted right ascension and declination offsets as determined in [Huang et al. \(2018a\)](#), which are typically $1 - 3$ mas. To test whether shifting the phase center within this range could effectively erase the brightness asymmetry in the residual maps, for each DSHARP source we applied a phase center that differed from the published value by 1 or 3 mas, with the perturbation oriented along the disk’s minor axis as well as at $\pi/4$ intervals over the full 2π in azimuth. For each of these applied phase centers, we then fit for the frank profile, and compared the resulting imaged frank residuals. Shifting the phase center in this way did change the amplitude of the brightness asymmetry in the inner disk by a factor of $\lesssim 2$, and in some cases it slightly rotated the asymmetry’s orientation. But in almost all cases the asymmetry clearly persisted, suggesting it is not an artifact of an incorrect phase center.

For the 10 DSHARP disks in which we initially did not identify a clear brightness asymmetry, shifting the phase center along the disk’s minor axis could in some cases create an asymmetry similar to that observed. The same was true for mock datasets in which we intentionally assigned an incorrect phase center. And 2 of these 10 sources, SR 4 and Sz 114, exhibited an asymmetry that was not aligned about the major axis; however shifting the phase center within published uncertainty (< 3 mas) could reorient the asymmetry about the major axis. Taking all of this together, again we do not see why fitting for the phase center as described in [Huang et al. \(2018a\)](#) would introduce a bias along the disk’s minor axis.

Next considering disk misalignment, we forward modeled mock observations emulating DSHARP datasets that have an inner disk separated from an outer ring by a deep gap. We generated images in which the inner disk’s inclination was misaligned relative to the outer ring by values between $0.1 - 3^\circ$ (the published 1σ uncertainties on inclination are $\leq 2^\circ$ in either direction). We then forced the geometry used to deproject the source to be that of the outer ring (separately, we also ran trials in which we fit for the geometry using a 2D Gaussian in visibility space), and fit the deprojected dataset with frank. We found that a misaligned inner disk produces a *four-fold symmetric* pattern oriented equivalently about the major or minor axis in the imaged frank residuals. In the real observations we instead see a *two-fold asymmetric* pattern oriented about the major axis.

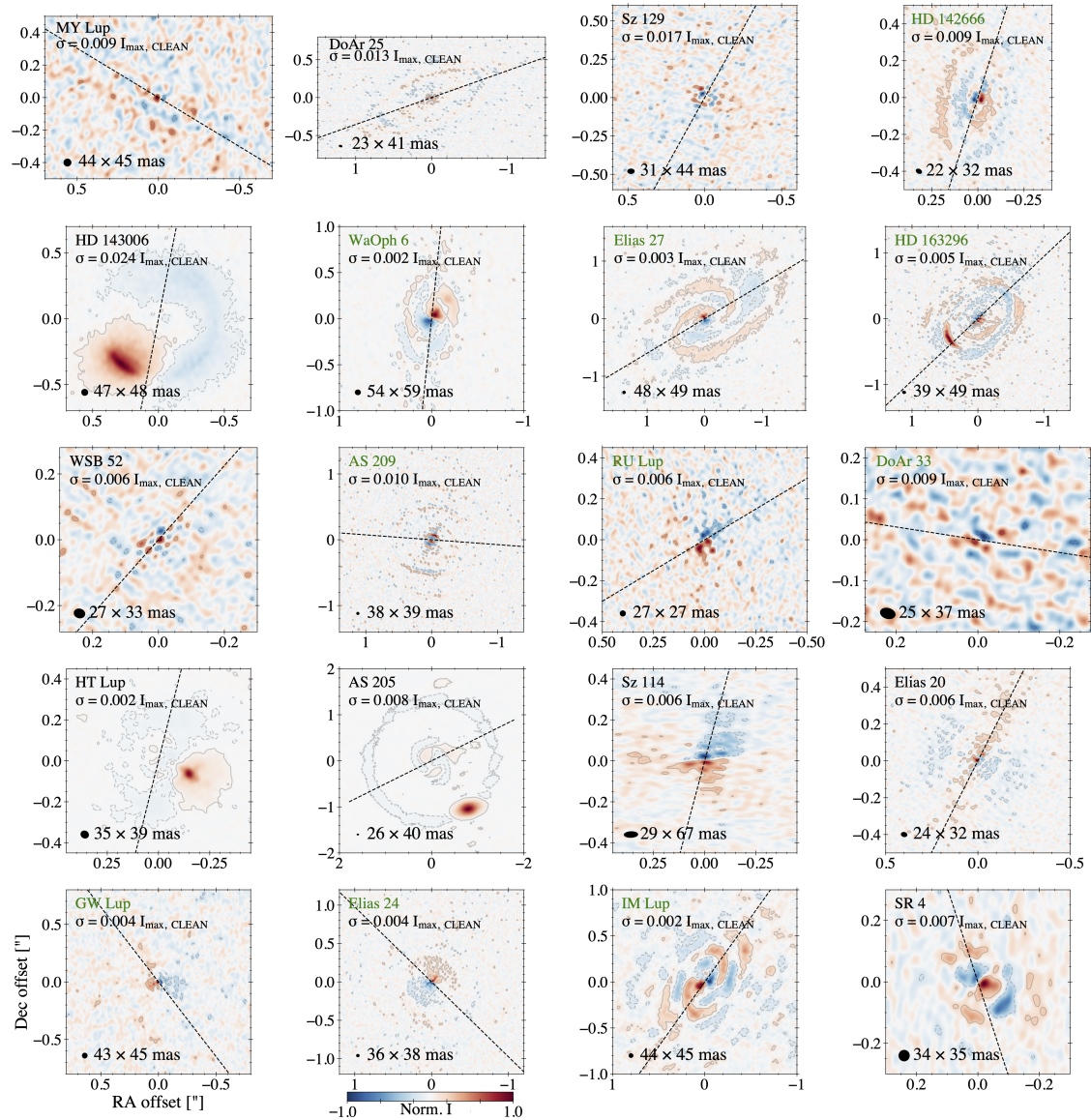


Fig. 3.13. frank imaged residuals

The frank residual visibilities imaged (0 CLEAN iterations), with $\pm 3\sigma$ contours overplotted (σ is given for each image), and a dashed line along the fitted position angle. The residual image is convolved with the published CLEAN beam and uses a linear color scale. Discs are ordered as in Fig. 3.3. The 10 sources that exhibit a clear two-fold brightness asymmetry in the inner disk have their names shown in green. All images use a linear color scale (a normalized color bar is shown, and the σ value for each image is given).

Chapter 4

Super-resolution trends in the ALMA Taurus survey: Structured inner disks and compact disks

This chapter presents the application of `frank` to ten disks in the Taurus survey, which observed these sources at moderate spatial resolution (120 mas). This application provides unique scientific insight on disk substructure, which is distinct from scientific findings in Chapter 3 with the DSHARP survey in part because here the disks are typically smaller and fainter than in that sample. I conducted the analysis in Sec. 4.3 and 4.4, while Marco Tazzari ran the parametric visibility fit shown in Sec. 4.4.2 and 4.7. The chapter, with some modifications to the introduction, has been published in MNRAS. I wrote the chapter text and the paper, with refinements resulting from coauthor feedback.

The 1.33 mm survey of protoplanetary disks in the Taurus molecular cloud found annular gaps and rings to be common in extended sources ($\gtrsim 55$ au), when their 1D visibility distributions were fit parametrically. We first demonstrate the advantages and limitations of *nonparametric* visibility fits for data at the survey's 0.12'' resolution. Then we use the nonparametric model in Frankenstein (`frank`) to identify new substructure in three compact and seven extended sources. Among the new features we identify three trends: a higher occurrence rate of substructure in the survey's compact disks than previously seen, underresolved (potentially azimuthally asymmetric) substructure in the innermost disk of extended sources, and a 'shoulder' on the trailing edge of a ring in disks with strong depletion at small radii. Noting the shoulder morphology is present in multiple disks observed at higher resolution, we postulate it is tracing a common physical mechanism. We further demonstrate how a super-resolution `frank` brightness profile is useful in motivating an accurate parametric model, using the highly structured source DL Tau in which `frank` finds two new rings. Finally

we show that sparse (u, v) plane sampling may be masking the presence of substructure in several additional compact survey sources.

4.1 Background

When applied to high resolution observations, super-resolution techniques that fit the observed visibilities directly, such as `galario` (Tazzari et al., 2018) and `frank` (Jennings et al., 2020), have found a yet greater occurrence rate of disk substructure than analysis with CLEAN images alone. This includes identification of previously unseen features across the DSHARP survey (Andrews et al., 2021; Jennings et al., 2021) and the ODISEA survey (Cieza et al., 2021); in compact sources, including those that appear featureless in a CLEAN image (Kurtovic et al., 2021; Pinilla et al., 2021); and for observations at the highest available ALMA resolutions, such as in PDS 70 (Benisty et al., 2021).

The next question is whether super-resolution techniques are also able to identify more substructure in moderate resolution observations. This would be particularly valuable for a statistical approach to substructure characterization over a large sample of disks, enabling a fuller investigation of demographic trends by exploiting the large archive of datasets at $\approx 100 - 300$ mas. This archive includes many disks that are not particularly large or bright, which current models predict should also contain substructure in order to counteract radial drift and retain reasonable dust disk sizes on few Myr timescales (Toci et al., 2021). We can ask for example whether compact disks that routinely appear smooth in CLEAN images are intrinsically featureless, or if this tends to be an artifact of observational or model resolution.

Long et al. (2018) and Long et al. (2019) demonstrated at the survey level that parametric visibility fits can identify more substructure in moderate resolution (120 mas, ≈ 16 au) observations than the CLEAN images alone. Here we will push super-resolution visibility fits to still higher resolution, using the *nonparametric* approach in `frank` to fit the observed visibilities yet more accurately. This will allow us to investigate how much more substructure in the Taurus survey data can be recovered from the observed visibilities – including in compact sources – and whether the identified features suggest new trends.

In this chapter we characterize new substructure in 10 of the Taurus survey disks using the 1D code `frank`, which reconstructs a disk’s brightness profile at super-resolution scales by nonparametrically fitting the azimuthally averaged visibility distribution. Sec. 4.2 summarizes the `frank` modeling approach and its limitations. Sec. 4.3 more closely examines the major advantages (Sec. 4.3.1) and limitations (Sec. 4.3.2 – 4.3.3) of nonparametric visibility fitting for datasets at the Taurus survey resolution, exploring how they affect substructure inference in `frank` fits to these observations. In Sec. 4.4 we present fits for the 10 sources, grouping

substructure findings into trends in compact disks (Sec. 4.4.1) and extended disks (Sec. 4.4.2). We further divide the extended sources into those with an inner and outer disk (Sec. 4.4.2.1) and those with an inner cavity (Sec. 4.4.2.2). Sec. 4.5 summarizes our findings and briefly places them in the context of super-resolution substructure found in datasets outside the survey.

4.2 Model

A full description of the `frank` model framework and its limitations is in [Jennings et al. \(2020\)](#). In short, `frank` reconstructs the 1D (axisymmetric) brightness profile of a source as a function of disk radius by directly fitting the real component of the deprojected, unbinned visibilities as a function of baseline. The brightness profile is determined nonparametrically by fitting the visibilities with a Fourier-Bessel series, which is linked to the real space profile by a discrete Hankel transform. A Gaussian process regularizes the fit, with the covariance matrix nonparametrically learned from the visibilities under the assumption that this matrix is diagonal in Fourier space. The free parameters (diagonal elements) of the matrix correspond to the power spectrum of the reconstructed brightness profile. The fitting procedure takes $\lesssim 1$ min on a standard laptop for each dataset shown here.

To obtain the results shown in this chapter, we vary three of the five `frank` model hyperparameters across datasets: R_{\max} , N and α . The hyperparameters R_{\max} and N simply set the maximum radius of the fit and number of brightness points in the fit, which we increase for larger disks. α controls the prior on the Gaussian process, effectively determining the signal-to-noise (SNR) threshold at which the model no longer attempts to fit the data. By varying α we can thus account for the unique visibility distribution and noise properties of each dataset, with higher α values imposing a stronger constraint that in practice causes the model to stop fitting the data at shorter maximum baseline. Most of the Taurus survey datasets become noise-dominated at their longest baselines, as (u, v) plane sampling becomes increasingly sparse. We will thus choose α such that we fit the datasets out to long baselines, but stop before fitting clearly noise-dominated data (using $\alpha \in [1.01, 1.10]$). Pushing a fit out to long baselines to extract higher resolution information does nonetheless come at the cost of fitting some noise. The noise imprints on the brightness profile as short period, low amplitude oscillations; we will note nontrivial instances.

There are three major limitations in the current version of `frank`:

1. A `frank` fit drives to a visibility amplitude of zero once it stops fitting the data. This is intentional given the difficulty of generically extrapolating a fit beyond the edge of the observed visibilities, but we often expect the true visibility distribution would continue

oscillating beyond the longest observed baselines if the disk is sufficiently structured. We will motivate how this affects substructure inference in datasets characteristic of the Taurus survey in Sec. 4.3.2. Ultimately this issue stems from the ill-posed nature of reconstructing the sky brightness from Fourier data, and it is also why the uncertainty on a `frank` brightness profile is easily underestimated, particularly for deep gaps (CLEAN brightness profiles can similarly exhibit underestimated uncertainties for this reason). We thus will not show uncertainties in the `frank` profiles in this chapter.

2. The 1D approach in `frank` fits for the azimuthal average of the visibility data at each baseline. While this is an accurate representation of the azimuthally averaged brightness profile, in the presence of azimuthal asymmetries the brightness profile should be interpreted with caution, as (particularly super-resolution) asymmetries can be misidentified as annular features. We will demonstrate this in Sec. 4.3.3.
3. The `frank` real space model is not positive definite and so can exhibit regions of small amplitude, negative brightness. When this unphysical behavior occurs we can enforce positivity by finding the most probable brightness profile for a given set of power spectrum parameters and the constraint that the brightness be nonnegative, using a nonnegative least squares solver. This sometimes alters features across the disk (i.e., not just in regions of negative brightness) because the enforced positivity condition affects the visibility fit at long baselines. We will remove this limitation in a forthcoming work and version of the code by fitting in logarithmic brightness space, but for the current analysis we will show nonnegative fits for those `frank` models that would otherwise exhibit regions of negative brightness; we will note which fits include this correction.

4.2.1 Data reduction

In this chapter we reanalyze the ALMA Taurus survey published by Long et al. (2018) and Long et al. (2019), to which we refer for details on the observational setup and calibration procedure. To apply `frank` to the datasets, we first apply channel averaging (1 channel per spectral window) and time averaging (60 s) to all spectral windows in the self-calibrated measurement set, then extract the unflagged visibilities. We then use the disk geometries and phase centers in Long et al. (2019) to deproject the visibilities in `frank` prior to fitting their 1D distribution. After deprojection, we re-estimate the weights by a constant factor of order unity to approximate the relation $w = 1/\sigma^2$, where w is the weight of a visibility point and σ^2 is the variance of its real and imaginary components.

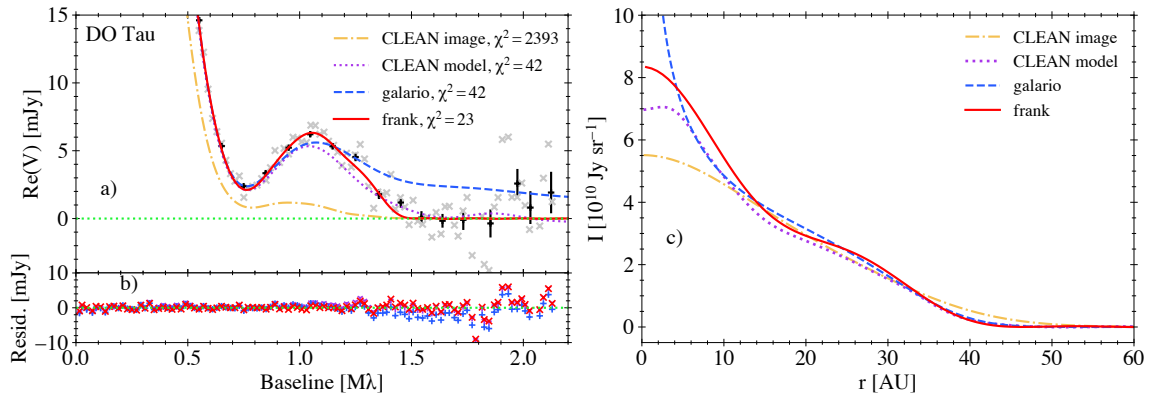


Fig. 4.1. Improved visibility fit accuracy better resolves disk structure

a) A zoom on the Taurus survey visibilities for DO Tau (20 and 100 $k\lambda$ bins, with 1σ uncertainties shown for the 100 $k\lambda$ points); the parametric fit from Long et al. (2019); the nonparametric frank fit; and the Fourier transform of brightness profiles extracted from the CLEAN image and CLEAN model.

b) Residuals of the parametric and frank visibility fits and the CLEAN model transform (20 $k\lambda$ bins).

c) Brightness profiles for DO Tau corresponding to the visibility fits in (a).

4.3 Methodologies – Advantages and limitations of a 1D, nonparametric visibility fit

Here we examine the benefits and drawbacks of 1D, nonparametric visibility fits (both generally and specific to frank) for brightness profile reconstruction at resolutions typical of the Taurus survey, ≈ 120 mas.

4.3.1 Advantages – A highly accurate fit to the observed data

Recovering super-resolution structure in a brightness profile with a 1D visibility model is a matter of fit accuracy; even a modest improvement in accuracy can correspond to new or more highly resolved profile features. To demonstrate how a nonparametric visibility fit’s improved accuracy can better constrain super-resolution structure in Taurus survey data, Fig. 4.1 compares the parametric visibility fit from Long et al. (2019) for the compact disk DO Tau with the nonparametric frank fit.¹ Long et al. (2019) inferred that structure in the visibility distribution for this source indicates a sharp outer edge in the brightness profile, and so they modeled the profile parametrically as an exponentially tapered power law. The resulting visibility fit in Fig. 4.1(a) is more accurate than the Fourier transform of a brightness

¹All visibility fits from Long et al. (2018) and Long et al. (2019) shown in this chapter are obtained by taking the 1D Fourier transform of their best-fit galario brightness profiles.

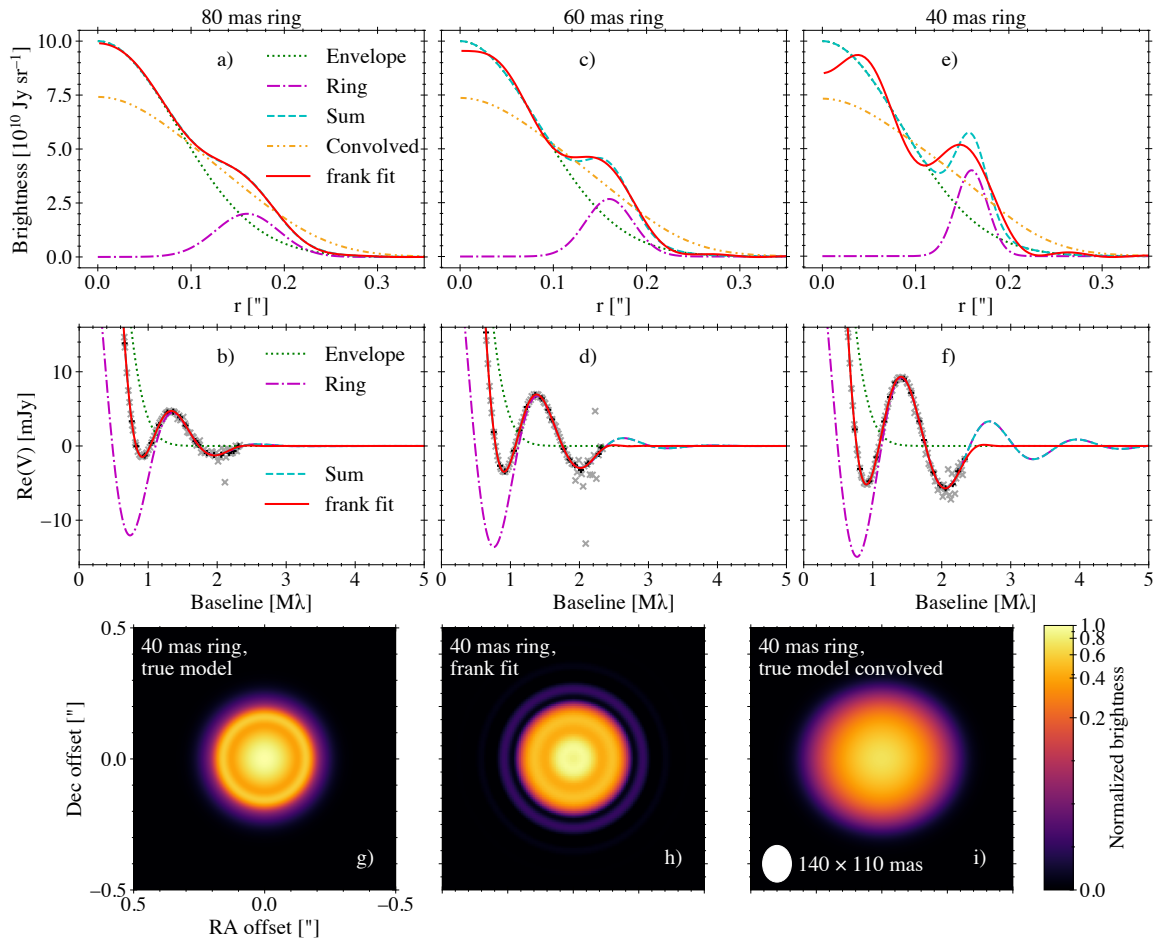


Fig. 4.2. frank brightness profile accuracy decreases as a ring becomes increasingly super-resolution

a) Mock brightness profile of a compact disk with a shallow Gaussian ring; the profile is the sum of a Gaussian envelope and Gaussian ring, with each component shown. The ring’s FWHM is given in the plot title. The frank recovery of the summed profile is also shown, as is the summed profile convolved with a 140×110 mas beam.

b) The real component of the 1D Fourier transform of the Gaussian envelope, ring, and their sum (the summed profile peaks at ≈ 150 mJy). Also shown are noisy mock observations of the summed profile (20 and 100 $k\lambda$ bins), and the frank fit to these mock data.

c) – d) and e) – f) As in (a) – (b), but with the Gaussian ring’s FWHM successively decreased and amplitude correspondingly increased to conserve the disk’s total (2D) flux.

g) – i) The noiseless, true model image of the disk in (e), the 1D frank fitted profile swept over 360° in azimuth, and the true model convolved with the 140×110 mas beam. The images use an arcsinh stretch ($I_{\text{stretch}} = \text{arcsinh}(I/a) / \text{arcsinh}(1/a)$, $a = 0.02$) and the same absolute brightness normalization.

profile extracted from the CLEAN image.² The parametric visibility fit’s improved accuracy in turn corresponds to super-resolution structure recovery in the brightness profile; this structure is also apparent in a profile extracted from the CLEAN model.³ While the parametric visibility fit is accurate at short and intermediate baselines, its residuals in Fig. 4.1(b) show nontrivial error at long baselines. By comparison, the `frank` visibility model in Fig. 4.1(a) and its residuals in (b) demonstrate a yet higher accuracy across intermediate and long baselines.

We can quantify an improvement in fit accuracy with the χ^2 statistic, $\chi^2 = \sum_{k=1}^N w_k [Re(V_{k, \text{obs}}) - Re(V_{k, \text{fit}})]^2$, where we neglect the imaginary component of the visibilities because `frank` only fits the real component. As given in the legend of Fig. 4.1(a), both the parametric fit and the Fourier transform of a brightness profile extracted from the CLEAN model exhibit a smaller χ^2 than the transform of a profile extracted from the CLEAN image by a factor of 57.0 for this source, while the `frank` fit yields a further reduction of the χ^2 value by a factor of 1.8. This comparatively small improvement in fit accuracy with `frank` corresponds to a clear change in the disk morphology in the `frank` brightness profile in panel (c), with the bump at 28 au in the `frank` profile not seen in the parametric profile and only hinted at in the CLEAN model profile. (Note that while the CLEAN model profile has lower integrated flux than the `frank` profile – because there is visibility information left in the residuals during the CLEAN process – reducing the `tclean` threshold value also results in fitting more noise.) Thus even in a dataset with a simple visibility distribution and relatively featureless brightness profile, a fairly small improvement to the accuracy of a visibility fit can nontrivially inform the scale and location of super-resolution structure in the recovered profile. This is the main advantage of a nonparametric fit, and it motivates why, for the sources in Sec. 4.4 which all exhibit more structured visibility distributions than DO Tau, a more accurate visibility fit with `frank` yields new brightness profile features (as well as more highly resolved known features) relative to the parametric fits and the CLEAN models.

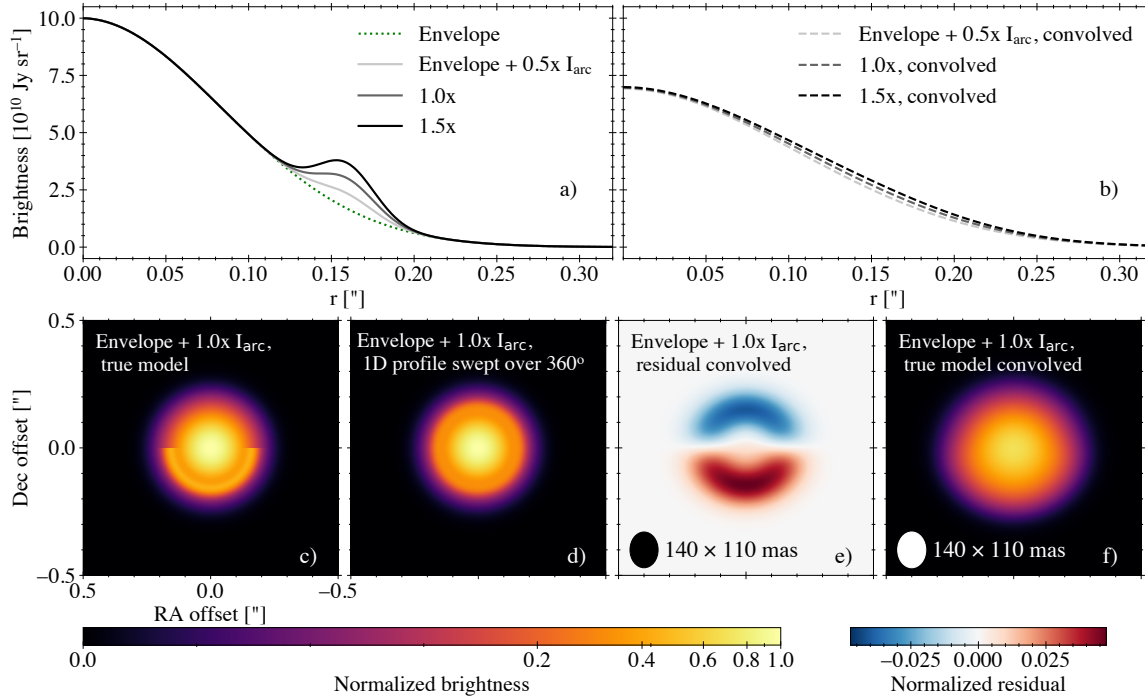


Fig. 4.3. Low contrast, asymmetric substructure emulates an underresolved annular ring in a brightness profile

a) The brightness profile of a Gaussian envelope, as well as the azimuthally averaged profile of the envelope summed with a 40 mas arc that spans 180° in azimuth. The summed profile is shown for various amplitudes of the arc (0.5x, 1.0x and 1.5x an arbitrary value of $I_{\text{arc}} = 2.67 \times 10^{10} \text{ Jy sr}^{-1}$).

b) Brightness profiles obtained from the 2D images of the envelope + arc, when convolved with a Gaussian beam whose $140 \times 110 \text{ mas}$ size is typical of the Taurus survey.

c) – f) For the 1.0x I_{arc} case: the noiseless, true model image; the 1D brightness profile extracted from this image [which is shown in (a)] swept over 360° ; the residual between these two images, convolved with the beam; and the true model image convolved with the beam [corresponding to the brightness profile in (b)]. The disk images use an arcsinh stretch ($I_{\text{stretch}} = \text{arcsinh}(I/a) / \text{arcsinh}(1/a)$, $a = 0.02$) and the same absolute brightness normalization; the residual image uses a linear stretch symmetric about zero.

4.3.2 Limitations – Extrapolating the fit to unobserved baselines

A fair question to then ask is how much we trust the morphology of features in a super-resolution profile. An important consideration is that even super-resolution fits can still be expected to underresolve most disk features (even broad ones, albeit to a lesser extent), as is evident when comparing fits to lower and higher resolution observations of the same source (differing in resolution by a factor of say 3). True features in a disk that are highly super-resolution (very roughly, a factor $\gtrsim 3$ narrower than the nominal spatial resolution) tend to be inaccurately recovered in a `frank` fit, and in some cases they can induce erroneous oscillations in the brightness profile, as we will now show.

Fig. 4.2 demonstrates the accuracy of a `frank` fit to a disk with super-resolution features using mock data. In Fig. 4.2(a) – (b), we first consider a simple disk – the sum of a Gaussian envelope and a shallow Gaussian ring whose 80 mas full width at half maximum (*FWHM*) is super-resolution relative to the ≈ 120 mas *FWHM* beam of the mock observations by a factor of ≈ 1.5 .⁴ While the profile convolved with a 140×110 mas beam (typical of the Taurus survey) in (a) shows no clear indication of the super-resolution ring, fitting the visibilities in (b) with `frank` gives an accurate recovery of the true brightness profile. But if we then narrow the ring to 60 mas (and increase its surface brightness to conserve total flux) in Fig. 4.2(c) – (d), it is now super-resolution by a factor of ≈ 2 , and the `frank` recovered profile begins to show some clear inaccuracy. It exhibits a plateau around $0.16''$, underresolving the true gap/ring pair. This is due to an inaccurate extrapolation of the `frank` visibility fit beyond the mock observation’s longest baselines, where the true profile’s visibility distribution continues to oscillate. A further consequence of the fit’s underestimated visibility amplitudes at unsampled baselines is the underestimated peak brightness in the `frank` brightness profile.

Narrowing and brightening the ring even further so that it has a 40 mas *FWHM* (super-resolution by a factor of ≈ 3) in Fig. 4.2(e) – (f), the convolved profile in panel (e) [and the 2D image of this profile swept over 2π in panel (i)] still shows no hint of the ring. The `frank` profile in (e) identifies the gap/ring pair, but underresolves the feature amplitudes and

²This difference is primarily due to the resolution loss induced by CLEAN beam convolution, which results in the transform of the CLEAN image poorly representing the observed visibilities. While we should thus not expect the transform of a CLEAN image profile to be accurate at long baselines, we will include this visibility profile in comparisons throughout this chapter because the CLEAN `.image` is the most common imaging product on which analysis is conducted in this field.

³All CLEAN brightness profiles for Taurus survey data in this chapter are extracted from CLEAN model images (the `.model` output of `tclean`) and convolved images (the `.image` output of `tclean`) generated using `tclean` in CASA 5.6.1–8 with the `multiscale` deconvolver (pixel size of 30 mas and scales of 1, 2, 4, 6 pixels); a threshold of 3σ , where σ is the RMS noise measured in a region of the image far from the source; and Briggs weighting with a robust value of 0.5.

⁴The mock dataset is generated with a baseline distribution and noise properties that emulate the Taurus survey observations of DR Tau.

misidentifies their centroids. The `frank` profile also underestimates the peak brightness more severely, showing an erroneous turnover near $r = 0$. This turnover is a consequence of the narrower ring in the true profile increasing the absolute visibility amplitudes at all baselines; accurately fitting the higher amplitude features in the visibilities introduces higher contrast structure into the brightness profile. Because the `frank` fit has a visibility amplitude of ≈ 0 beyond the edge of the data, while the true visibility distribution has nontrivial amplitude there, these higher contrast structures are not well constrained. This effect also introduces the erroneous, shallow bump into the `frank` brightness profile between $0.2 - 0.3''$, appearing in the 2D image of the swept `frank` brightness profile in Fig. 4.2(h) as a faint but fake ring [compare the true 2D image in panel (g)]. It is thus possible for highly super-resolution features in a true brightness profile to introduce erroneous oscillations into a `frank` brightness profile.

For some datasets in the Taurus survey such as DO Tau in Fig. 4.1(a), this is not much of a concern, as the observed visibilities appear to plateau at zero at the longest baselines. But for other datasets it is less clear whether higher resolution and/or deeper observations would show the visibilities to continue oscillating beyond the baselines at which the current data become noise-dominated. While any extrapolation of a fit beyond the data's longest baselines is highly uncertain, it can be useful to compare a `frank` brightness profile to that obtained with a parametric visibility fit, where the parametric profile's functional form is motivated for example by the `frank` fit or by structure in the observed visibilities (as Long et al. 2018 and Long et al. 2019 have done). We will perform an in-depth comparison in Sec. 4.4.2.1 for the most structured disk in our results, DL Tau.

4.3.3 Limitations – Distinguishing azimuthally symmetric from asymmetric substructure

If we have found a super-resolution feature in a disk, the next question is whether it is an annular ring (gap) or an azimuthally asymmetric brightness excess (depletion). Because a 1D brightness profile averages the flux in a given annulus over 2π in azimuth, a low – moderate contrast asymmetric feature within that annulus can mimic an underresolved (or shallow) ring in the profile. **Fig. 4.3** demonstrates this with mock data, using a Gaussian disk with an additional brightness ‘arc’ that is produced by sweeping a Gaussian ring only over 180° in azimuth in panel (c). The arc emulates a brightness excess on top of the background envelope, and a 1D profile in Fig. 4.3(a) extracted from the image in (c) shows a slight bump at the arc's radial location. From the brightness profile alone this could be misidentified as an annular feature, and because the arc is super-resolution by a factor of ≈ 3 , the true

model image convolved with a 140×110 mas beam in (f) – and the corresponding convolved brightness profile in (b) – show no clear indication of it. When we increase the asymmetry’s brightness by 50%, it emulates a shallow gap/ring pair in (a), while the convolved profile in (b) is effectively unchanged.

How then can we distinguish super-resolution asymmetries from annular features? We do not have an unambiguous method for this, so jointly consider three metrics: contouring the CLEAN image, identifying structure in the imaginary component of the visibilities, and imaging a frank fit’s residual visibilities. The first of these, contouring the CLEAN image at levels of the RMS noise, can be useful in identifying the convolved representation of super-resolution asymmetries. A limitation is that low contrast or sufficiently narrow features are often not identifiable. Second, while an asymmetric feature is represented in the real component of the 1D visibilities exactly as an annular feature at the same location and that has the same width and total surface brightness (as integrated over 360° in azimuth),⁵ structure in the imaginary component of the visibilities indicates scales at which there is asymmetry with respect to the phase center. A limitation here is that without a robust model to fit $\text{Im}(V)$, interpretation of its structure can be complicated by the comparatively low amplitude (and thus low binned SNR) relative to $\text{Re}(V)$, and by the typical uncertainty in the disk phase center of $\lesssim 3$ mas. Third, imaging the frank residual visibilities effectively isolates azimuthal asymmetries in the image by subtracting out the (fitted) average brightness at each radius. A limitation is that there is typically ambiguity in interpreting structure in imaged residuals, due to potential artifacts of an incorrect disk geometry and/or phase center, imaging artifacts, and loss in resolution by convolving the residuals with the CLEAN beam [as demonstrated in Fig. 4.3(e)]. While each of these three approaches is thus imperfect, together they can aid in distinguishing super-resolution asymmetries from annular features.

4.4 Results & Analysis

Of the 32 sources in the Taurus survey, our analysis focused only on the 24 single-disk systems; among these, here we show the 10 for which we obtain a brightness profile with prominent new substructure. The remaining 14 comprise four extended disks where the frank visibility fit is highly similar to the parametric fit in Long et al. (2018) and 10 compact disks whose fitted brightness profiles lack substructure. In Sec. 4.4.1 we will discuss the

⁵We can intuit this by recalling that the Fourier transform is a linear operation; the Fourier transform of a feature is equal to the sum of its’ components’ Fourier transforms. Thus the transform of a ring is equal to the sum of the transforms of its azimuthal segments.

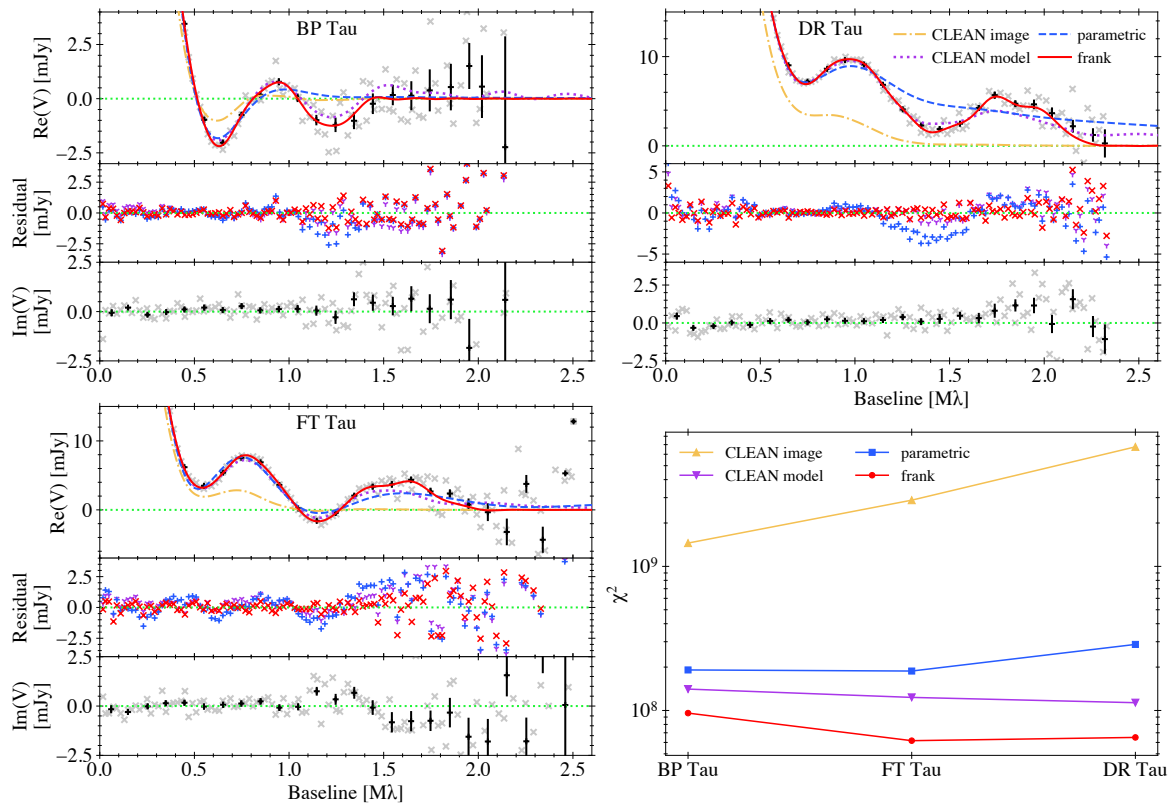


Fig. 4.4. Improved visibility model accuracy in frank fits to compact disks

For the compact disks in Sec. 4.4.1, a zoom on the visibilities ($> 0.30 M\lambda$; 20 and 100 $k\lambda$ bins, with 1σ uncertainties shown for the 100 $k\lambda$ points). The parametric visibility fit from either Long et al. (2018) or Long et al. (2019), the frank fit, and the Fourier transforms of the CLEAN image and model brightness profiles are shown. Also shown are residuals for the parametric and frank fits and the CLEAN model transform (20 $k\lambda$ bins; larger amplitude residuals at the longest baselines are beyond the y-range in some panels), as well as the imaginary component of the observed visibilities. Discs are arranged from top to bottom and then left to right in increasing frank fit resolution. The bottom-right panel shows the χ^2 statistic for each fit.

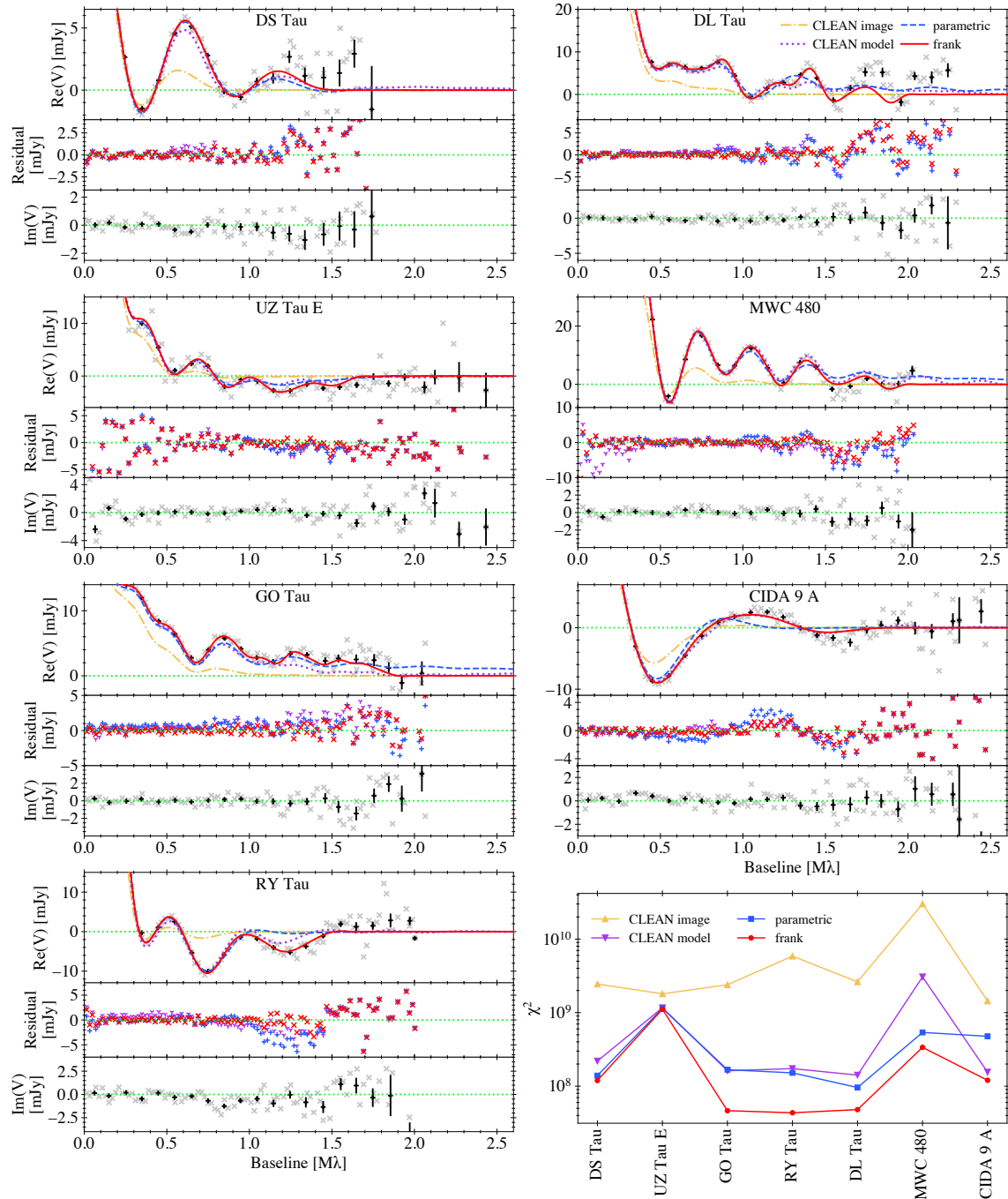


Fig. 4.5. Improved visibility model accuracy in frank fits to extended disks

As in Fig. 4.4, but for the extended disks in Sec. 4.4.2.

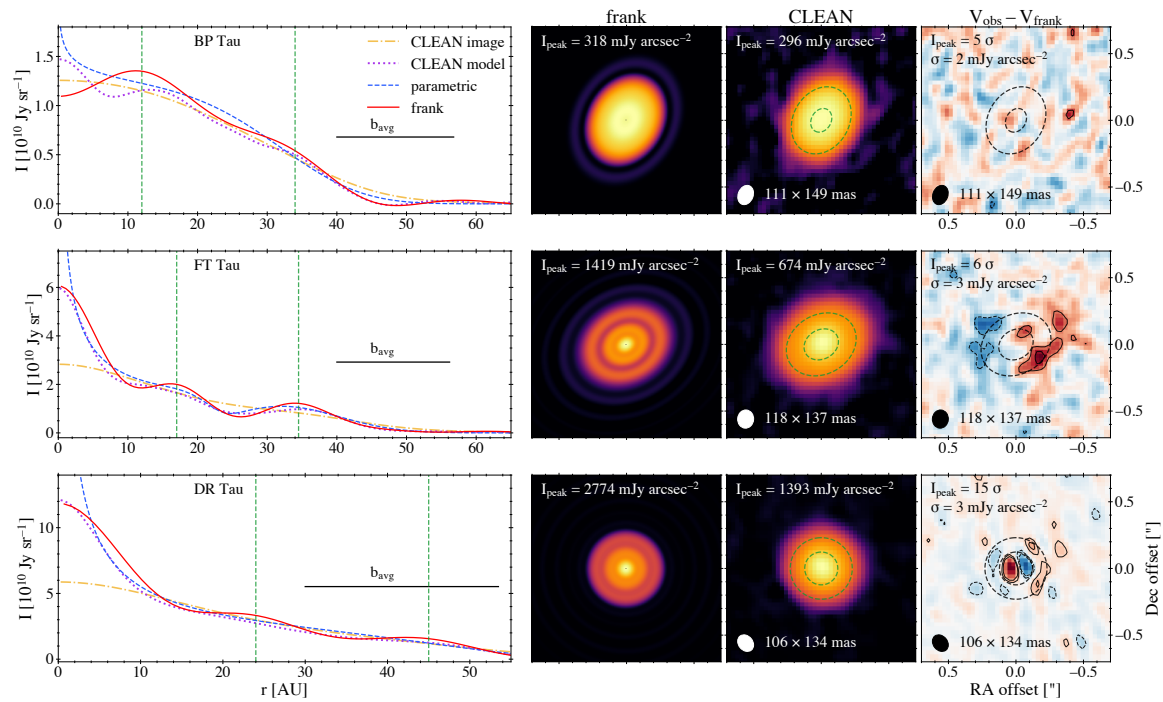


Fig. 4.6. New substructure in frank fits to compact disks

Brightness profiles extracted from the CLEAN image and model, the parametric profile and frank profile for three of the compact ($R_{\text{eff}, 90\%} \leq 50$ au) systems in the Taurus survey, corresponding to the visibility fits in Fig. 4.4 (the parametric fits are from Long et al. 2018 and Long et al. 2019; b_{avg} shows the mean of the CLEAN beam width along its major and minor axes). Also shown are an image of the frank profile swept over 2π and reprojected, the CLEAN image, and the imaged frank residual visibilities (zero CLEAN iterations; contours at $-5, -3, +3, +5\sigma$). Vertical lines in the brightness profile plots denote features that are shown as ellipses in the CLEAN image and imaged frank residuals for reference. The frank and CLEAN images use an arcsinh stretch ($I_{\text{stretch}} = \text{arcsinh}(I/a) / \text{arcsinh}(1/a)$, $a = 0.02$), but different brightness normalization (indicated by the given peak brightness). The imaged frank residuals use a linear stretch symmetric about zero. We use image brightness units of $[\text{mJy arcsec}^{-2}]$ to facilitate comparison between datasets of different beam size.

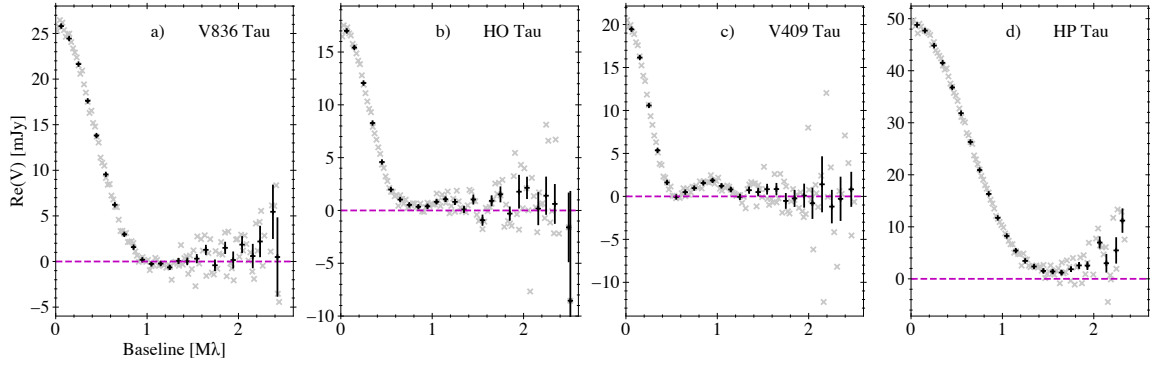


Fig. 4.7. Noisy visibility distributions for compact disks

Visibility distributions for four compact ($R_{\text{eff}, 90\%} \leq 50$ au) sources in the Taurus survey, whose structure at long baselines is unclear due to (u, v) plane sparsity.

general potential for substructure in these compact sources based on the observed visibility distributions.

The `frank` fit hyperparameters for the 10 datasets where we find new substructure are summarized in **Table 4.1**. We divide our analysis into compact and extended disks. The compact disks – BP Tau, DR Tau and FT Tau – have an effective radius $R_{\text{eff}, 90\%} \leq 50$ au, where the integrated flux $f(R_{\text{eff}, 90\%}) = 0.9 \cdot 2\pi \int_0^{r=\infty} I(r) r dr$. The extended disks – CIDA 9 A, DL Tau, DS Tau, GO Tau, MWC 480, RY Tau, and UZ Tau E – have $R_{\text{eff}, 90\%} > 60$ au. [Long et al. \(2019\)](#) fit BP Tau and DR Tau parametrically with `galario`, using an exponentially tapered power law to model the brightness profile, motivated by structure in the observed visibility distributions. [Long et al. \(2018\)](#) fit the remaining eight disks shown here with a parametric form in `galario` comprised of a sum of Gaussians (for CIDA 9 A, DS Tau, RY Tau, and UZ Tau) or an exponentially tapered power law summed with Gaussians (for DL Tau, FT Tau, GO Tau, and MWC 480). Their choice of the number of Gaussians for each source is motivated by a brightness profile extracted (along the disk’s major axis) from the CLEAN image.

For each of these 10 sources, we compare the `frank` visibility fit to the parametric fit, as well as the Fourier transform of the CLEAN brightness profile, in **Fig. 4.4** for the compact disks (the corresponding brightness profiles, discussed below, are in **Fig. 4.6**) and **Fig. 4.5** for the extended disks (brightness profiles in **Figs. 4.8** and **4.11**). In every case the parametric model matches the data more accurately than the Fourier transform of the CLEAN image profile, the transform of the CLEAN model profile is generally comparable to or in some cases slightly more accurate than the parametric model, and the residuals and χ^2 values demonstrate that the `frank` fit is more accurate than each of the CLEAN image, CLEAN model and parametric model visibility profiles. The `frank` fits that have enforced brightness profile positivity

Table 4.1. For each Taurus survey disk in Sec. 4.3 and 4.4, the distance to the source (using Gaia DR2 measurements from [Bailer-Jones et al. 2018](#)), and the values for the five frank hyperparameters: SNR criterion α , strength of smoothing w_{smooth} applied to the reconstructed power spectrum, outer radius of the fit R_{out} , number of radial (and spatial frequency) points N , and floor value p_0 for the reconstructed power spectral mode amplitudes. Sec. 4.2 gives a fuller explanation of α . All frank fits in this chapter are available at <https://zenodo.org/record/5587840>.

Disc	d [pc]	α	$\log_{10} w_{\text{smooth}}$	R_{out} ["]	N	p_0 [Jy ²]
Compact disks						
BP Tau [†]	129	1.01	-4	1.0	200	10^{-15}
DO Tau	139	"	"	"	"	"
DR Tau	195	"	"	"	"	"
FT Tau	127	"	"	"	"	"
Extended disks						
UZ Tau E	131	1.01	-4	1.0	200	10^{-15}
CIDA 9 A [†]	171	1.05	"	"	"	"
DS Tau [†]	159	1.05	"	"	"	"
RY Tau	128	1.10	"	"	"	"
DL Tau [†]	159	1.01	"	1.5	300	"
GO Tau	144	1.00	"	1.5	300	"
MWC 480 [†]	161	1.01	"	1.5	300	"

[†] These fits have enforced brightness profile positivity (see Sec. 4.2).

(BP Tau, CIDA 9 A, DL Tau, DS Tau, MWC 480) underestimate data amplitudes at long baselines. Nonetheless, we recall from Sec. 4.3.1 that even modest improvements in visibility fit accuracy can yield appreciably more highly resolved brightness profile features, and in some cases can identify new features.

In order to examine whether new features may be nonaxisymmetric, Fig. 4.4 and Fig. 4.5 also show the imaginary component of the observed visibility distributions (which frank treats as zero at all baselines). We will discuss $\text{Im}(V)$ in relation to disk asymmetries in the following subsections.

4.4.1 New substructure in compact disks

Across three compact sources in the survey – BP Tau, DR Tau and FT Tau – the frank fits in **Fig. 4.6** find new substructure. Additionally we note that for the highly compact ($R_{\text{eff}, 90\%} < 25$ au) disk T Tau N, in which [Yamaguchi et al. \(2021\)](#) recently found a gap/ring pair with their 2D, super-resolution modeling framework PRIISM, the frank fit (not shown here) demonstrates agreement in the gap/ring pair’s location and approximate amplitude.

BP Tau: The frank fit to BP Tau identifies a new turnover in the inner disk that is not seen in the [Long et al. \(2019\)](#) parametric profile because the corresponding visibility fit does not recover the negative peak in the data at $1.25 M\lambda$. The parametric model instead finds an almost flat inner disk (power law index of 0.1), resulting in a quasi-linear region of the brightness profile between $\approx 8 - 17$ au; this can be understood as a result of underresolving the turnover (which may itself be an underresolved ring). Representation of an underresolved brightness excess as a quasi-linear region in a brightness profile is demonstrated with mock data in Fig. 4.3(b). We can further motivate the turnover by the observed visibilities; their amplitudes are preferentially negative between $\approx 0.5 - 1.5 M\lambda$, which is an indication of a wide Gaussian in the brightness profile that is not centered at zero radius. Notice how the visibility distributions in Fig. 4.5 for the three disks with an apparent inner cavity (and thus, a Gaussian ring not centered at zero) – CIDA 9 A, RY Tau and UZ Tau E – also each exhibit preferentially negative visibility amplitudes at intermediate baselines. The frank profile also better localizes the structure beyond 20 au in the disk than the parametric profile, with the CLEAN model profile showing rough agreement with frank here.

To further assess the frank profile features (using BP Tau as an example for the analysis we will more succinctly cover in subsequent disks), we can consider how the model limitations in Sec. 4.3.2 and 4.3.3 may affect the fit. Given the demonstration in Sec. 4.3.2 of the difficulty in accurately extrapolating a fit to unobserved (and noise-dominated) baselines – and how this can introduce fake oscillations into a profile when the underlying disk

has highly super-resolution features – we emphasize that a more accurate visibility fit or higher resolution/deeper observations can find the features in a frank brightness profile to become either more or less prominent. This is particularly true in the innermost disk, where substructure can routinely be highly underresolved. The turnover in the frank profile for BP Tau for example may resolve into a ring or something more complicated, as may be indicated by the inner 15 au of the CLEAN model profile in Fig. 4.6. We do expect the turnover to be indicating the presence of real substructure, given the dataset’s preferentially negative visibility amplitudes at intermediate baselines as discussed above. In the outer disk, the broad, shallow feature in the frank brightness profile between $\approx 52 - 65$ au is at least partly due to noise (influenced by the visibility fit’s extrapolation of zero amplitude beyond $\approx 1.5 M\lambda$, analogous to Fig. 4.2(e)), but it may also have contributions from real, diffuse emission.

In light of the discussion in Sec. 4.3.3 on how nonaxisymmetric features can mimic the appearance of a partially resolved ring, we can also use the CLEAN image, imaginary component of the visibilities and imaged frank residuals to examine whether any super-resolution features in the frank profile may be artifacts of azimuthally asymmetric emission. Contouring the CLEAN image of the source shows no clear signs of an asymmetry; the imaginary component of the visibility distribution in Fig. 4.4 does not exhibit prominent structure, indicating that asymmetries in the image must be particularly faint and/or small-scale; and the imaged frank residuals do not have clear features within the disk (the small, 5σ blob in the west of the imaged residuals that is also in the CLEAN image). We thus infer that the profile’s features are likely annular.

FT Tau: The frank fit in Fig. 4.6 finds a new gap/ring pair around 11 – 17 au, underresolved in the parametric brightness profile as the quasi-linear region (and hinted at in the CLEAN model profile). The frank profile also determines the gap at 26 au identified in Long et al. (2018) to be wider, with a brighter adjacent ring. While the difference between the parametric and frank visibility fits for FT Tau in Fig. 4.4 may not look dramatic enough to correspond to a new gap/ring pair, it is important first that frank exhibits an improved fit accuracy over a large span in baseline ($\approx 1.0 - 1.7 M\lambda$). Second, while the frank fit converges on zero visibility amplitude at $\approx 2.0 M\lambda$, the parametric fit remains positive and continues to slowly oscillate out to the longest baselines and beyond. The data instead appear by eye to indicate that the true visibility distribution becomes negative beyond $2.0 M\lambda$ [denser (u, v) plane sampling at these baselines would be needed to confirm].

Considering disk asymmetries, the imaginary component of the visibilities for FT Tau in Fig. 4.4 have clear structure on scales between $\approx 1.2 - 1.7 M\lambda$, and this structure has amplitude comparable to the difference between the frank and parametric fit residuals for

$\text{Re}(V)$. The imaged frank residuals also have $\leq 5\sigma$ features within and beyond the gap at ≈ 26 au. Together this suggests that there may be some faint asymmetric structure in the disk, particularly in the gap centered at 26 au, where the residual amplitude is largest.

DR Tau: We find two new gaps relative to Long et al. 2019 (the frank fit to DR Tau was previously shown in Jennings et al. 2020) in Fig. 4.6. This can be motivated by the significant difference in visibility fit accuracy between the parametric and frank models in Fig. 4.4; the CLEAN model visibility profile is also more accurate than the parametric model, with the CLEAN model brightness profile having a hint of the outer ring found in the frank brightness profile. The qualitative similarity in structure between the observed visibility distributions for FT Tau and DR Tau also motivates why the frank fit shows two gaps in both disks. The visibilities for DR Tau do not exhibit a zero-crossing, indicating the data contain underresolved structure at small spatial scales; this seems most likely to be an indication of a partially resolved inner disk.

Considering the inner disk, while the imaginary component of the visibilities for DR Tau do not show clear structure, the imaged frank residuals in Fig. 4.6 do have strong features in the innermost radii ($\leq 15\sigma$, or $\lesssim 5\%$ of the background brightness in the CLEAN image). This is likely affecting the morphology of the inner gap in the frank profile to some extent. We find that the inner disk residuals in DR Tau and other disks discussed below are not attributable solely to an incorrect determination of the disk phase center (assessed by varying the applied phase center in Appendix 4.6).

4.4.1.1 Occurrence rate of substructure in compact disks

The frank fits to BP Tau and DR Tau raise the number of compact, single-disk systems with substructure from two – FT Tau and the cavity disk IP Tau (shown in Long et al. 2018) – to four, out of 14 total in the survey. Among the 14 compact disks, these four are neither the largest nor brightest, which prompts the question of whether more of the survey’s compact objects may be structured. To partially address this, we can consider whether the survey data strongly exclude the presence of substructure in the remaining 10 compact sources. The visibility distributions for four additional compact disks in Fig. 4.7 each show tentative or clear indications of structure at intermediate baselines and become highly noisy at longer baselines due to sparse (u, v) plane sampling. Whether this structure at intermediate baselines corresponds in each case only to the brightness profile becoming steeper in the outer disk (i.e., no gap/ring substructure), or instead to substructure, is not clear from these data. The visibility distributions in Fig. 4.7(b) – (d) also do not exhibit a zero-crossing at short baseline, characteristic of an underresolved inner disk and/or highly super-resolution substructure. It is

thus possible that higher resolution and/or deeper observations would identify substructure in a larger subset of the survey’s compact sources.

That the current data do show substructure in four of the survey’s compact disks – BP Tau, DR Tau, FT Tau, and IP Tau – is in line with multiple features detected in the `frank` fits to the DSHARP observations of the compact sources SR 4, DoAr 33 and WSB 52 (Jennings et al., 2021), as well as substructure recovered in the parametric visibility fits to the compact disks CIDA 1, MHO 6 and J0433 (Kurtovic et al., 2021; Pinilla et al., 2021). Collectively these results demonstrate that many compact disks are not intrinsically featureless; their lack of apparent substructure is instead in some cases an artifact of either the resolving power of the model applied to the data or of the data itself. This may be a tentative indication that a nontrivial fraction of compact dust disks follow the same evolutionary pathway as extended disks, which tend to be structured.

4.4.2 New substructure in extended disks

For each of seven extended disks – CIDA 9 A, DL Tau, DS Tau, GO Tau, MWC 480, RY Tau, and UZ Tau E – the `frank` brightness profiles identify new features and more highly resolve those found in Long et al. (2018). We divide our analysis here into sources with a deep gap separating the inner and outer disk (Sec. 4.4.2.1) and those with an apparent inner cavity (Sec. 4.4.2.2).

4.4.2.1 Sources with an inner and outer disk

In four sources with an inner disk separated from one or more outer rings by a deep gap – DS Tau, MWC 480, DL Tau, and GO Tau – we find new substructure as shown in **Fig. 4.8**.

DS Tau: The `frank` fit finds a new feature, a broad plateau, in the gap separating the inner and outer disk (at 30 au). This arises from the small improvement in visibility fit accuracy in Fig. 4.5, and it may be underresolving smaller scale substructure. The CLEAN model profile also exhibits this plateau. The improved fit accuracy with `frank` additionally yields slightly steeper gap walls. The feature in the gap may be informed to some extent by nonaxisymmetric emission, given structure in the imaginary component of the visibilities and in the imaged `frank` residuals of Fig. 4.8 in the inner disk.

GO Tau: The `frank` profile in Fig. 4.8 finds the quasi-linear region between $\approx 21 - 45$ au in the parametric profile to resolve into two rings. This may seem surprising when comparing the fairly similar `frank` and parametric visibility fits for GO Tau in Fig. 4.5, but it can

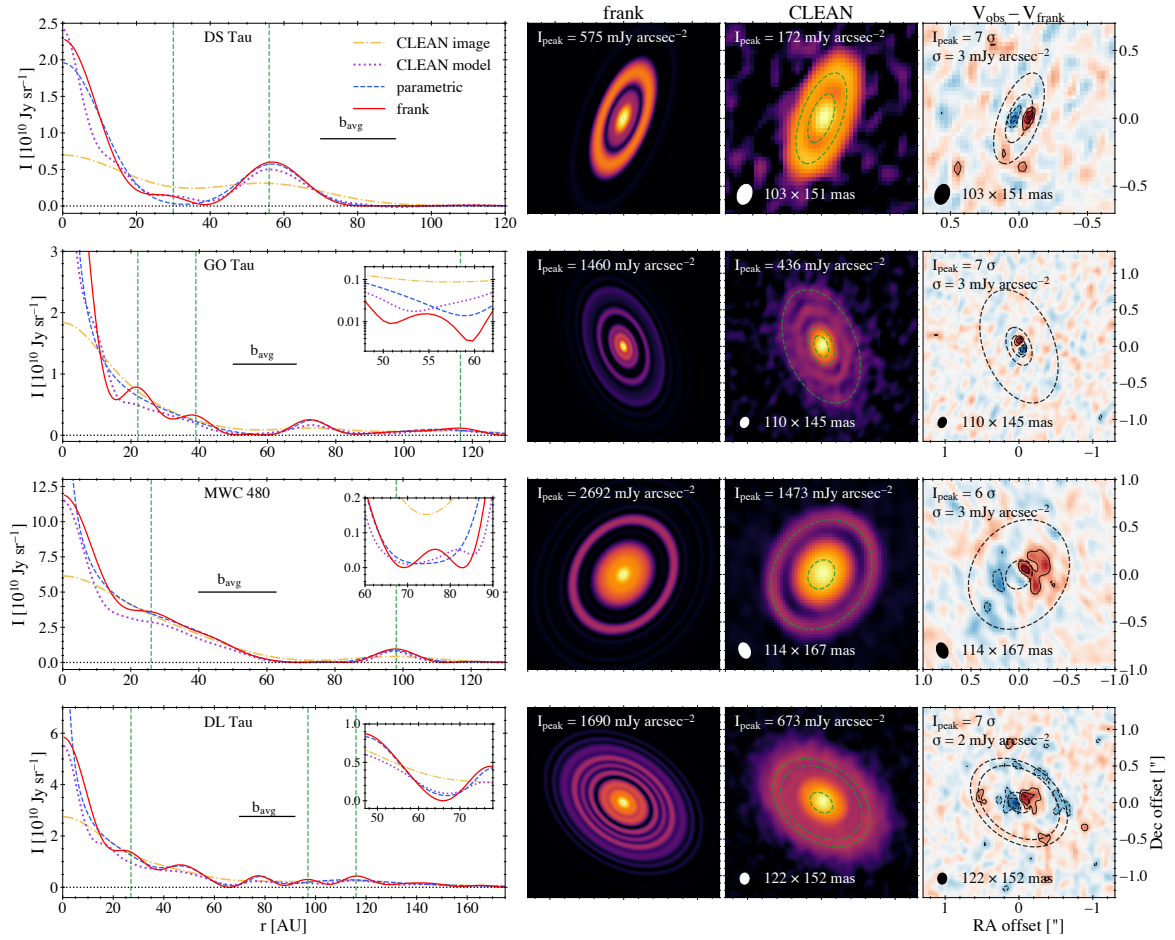


Fig. 4.8. New substructure in frank fits to extended disks with outer rings

As in Fig. 4.6, but for the four extended ($R_{\text{eff}, 90\%} > 50 \text{ au}$) systems in the Taurus survey that exhibit an inner disk and one or more outer rings, discussed in Sec. 4.4.2.1. Parametric profiles are from Long et al. 2018; the visibilities and fits for these disks are in Fig. 4.5. The inset panels zoom on deep gaps in the brightness profiles. The frank fit to GO Tau peaks at $6.2 \times 10^{10} \text{ Jy sr}^{-1}$.

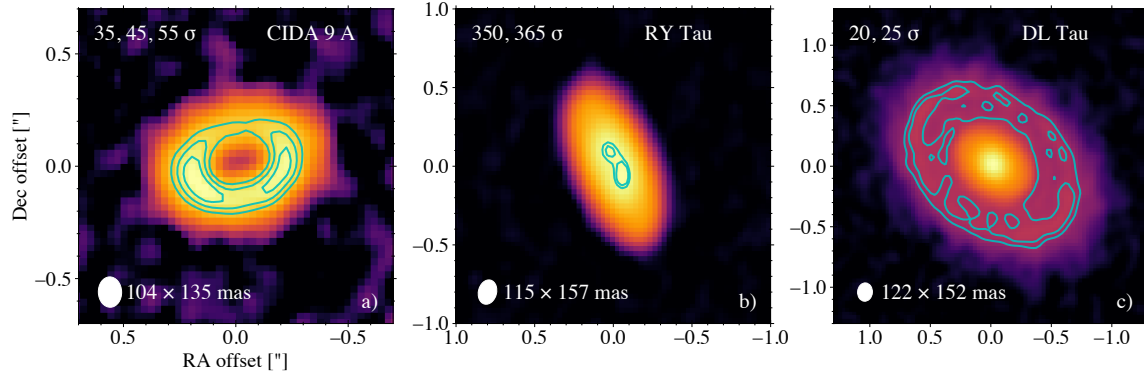


Fig. 4.9. CLEAN image asymmetries

CLEAN images for three of the Taurus survey’s extended disks (see Sec. 4.4.2), with contours chosen to highlight asymmetries. The images are identical to those in Fig. 4.8 and 4.11.

be understood by the frank visibility fit exhibiting regions of comparatively steeper slope beyond $\approx 1.1 M\lambda$ as it more closely traces the data. The inner disk features in the frank profile can nonetheless be expected to evolve with longer baseline data that more strongly condition structure on small scales. In Fig. 4.8 we also again see a bimodal pattern in the imaged frank residuals of the innermost disk, with $\geq 5\sigma$ and $\leq -5\sigma$ features interior to the inner ring. We can expect that the inner disk features may evolve considerably with higher resolution observations.

The deep gap separating inner from outer disk (at 55 au) in the frank fit exhibits a slight bump (see the inset in Fig. 4.8), suggesting it may not be empty. This is reminiscent of structure in the deep gap between inner and outer disk in the frank fits to the ≈ 35 mas resolution DSHARP observations of AS 209, Elias 24, HD 163296, and SR 4 (see Fig. 12 in Jennings et al. 2021); it may be indicative of a common gap forming mechanism. The fractional uncertainty in a frank profile is largest at faint brightness though, and the RMS noise level in the CLEAN image of GO Tau, $0.01 \times 10^{10} \text{ Jy sr}^{-1}$, is of comparable amplitude to the bump, so inference on structure within the deep gap is limited. In the outer disk, the frank profile more strongly localizes the location of the outermost ring and better resolves its faint amplitude. As a note, the two rings in the outer disk are clearly visible in the CLEAN image due to the colorscale, but are relatively faint, and imaging artifacts are likely introducing the apparent diffuse emission into the gap between the rings; these rings are thus shallow and broad in the CLEAN image profile (though visible in the CLEAN model profile).

MWC 480: The frank fit finds the inner disk for this source as well to be structured, with a new plateau between $\approx 20 - 27$ au. The profile’s broad, shallow, quasi-linear region

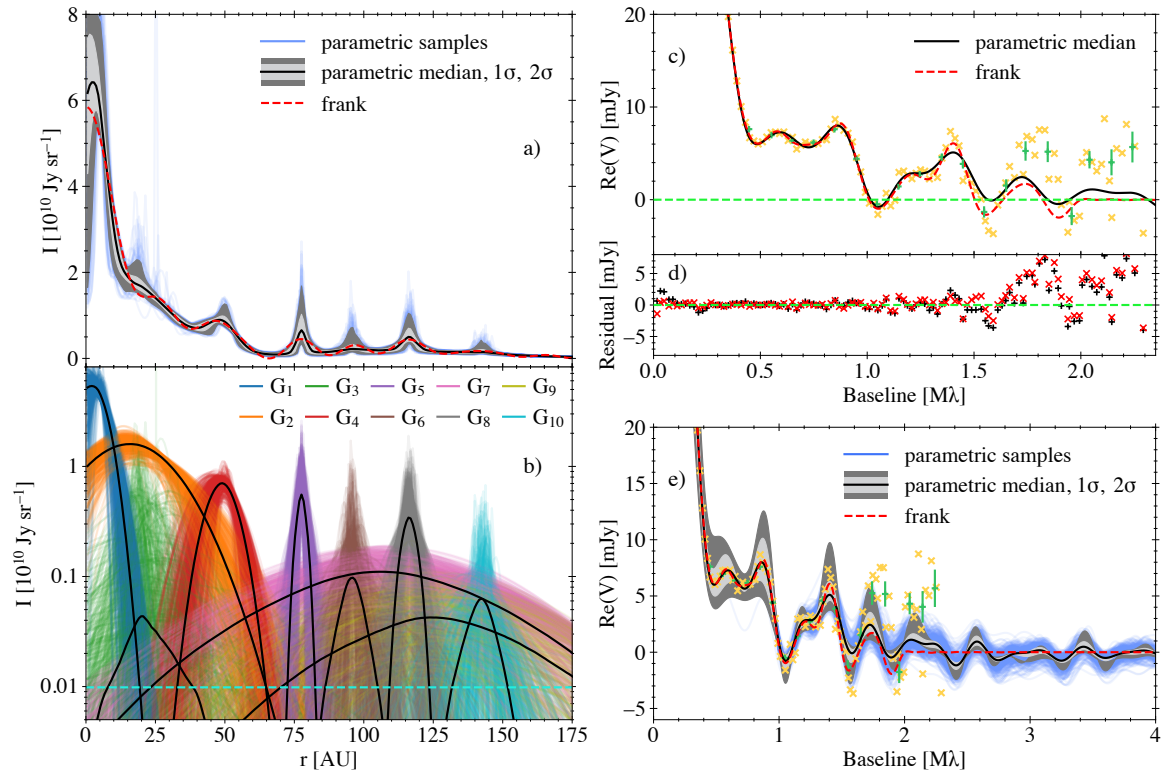


Fig. 4.10. Ten Gaussian parametric fit to DL Tau

- a) Posterior median, 1σ and 2σ confidence intervals of the 10 Gaussian fit to DL Tau, and 500 randomly drawn posterior samples. Also shown is the frank fit from Fig. 4.8.
- b) Posterior median (black lines) for each of the 10 Gaussians in the fit, and the same 500 samples. The dashed horizontal line is at the CLEAN image RMS noise level.
- c) A zoom on the observed visibilities ($> 0.30 M\lambda$; 20 and 100 $k\lambda$ bins, with 1σ uncertainties shown for the 100 $k\lambda$ points), and the parametric median and frank visibility fits.
- d) Residuals for the visibility fits (20 $k\lambda$ bins).
- e) As in (c), but with the 1σ and 2σ confidence intervals and the 500 posterior samples included. Longer baselines are shown to demonstrate the difference in fit extrapolations at unsampled scales.

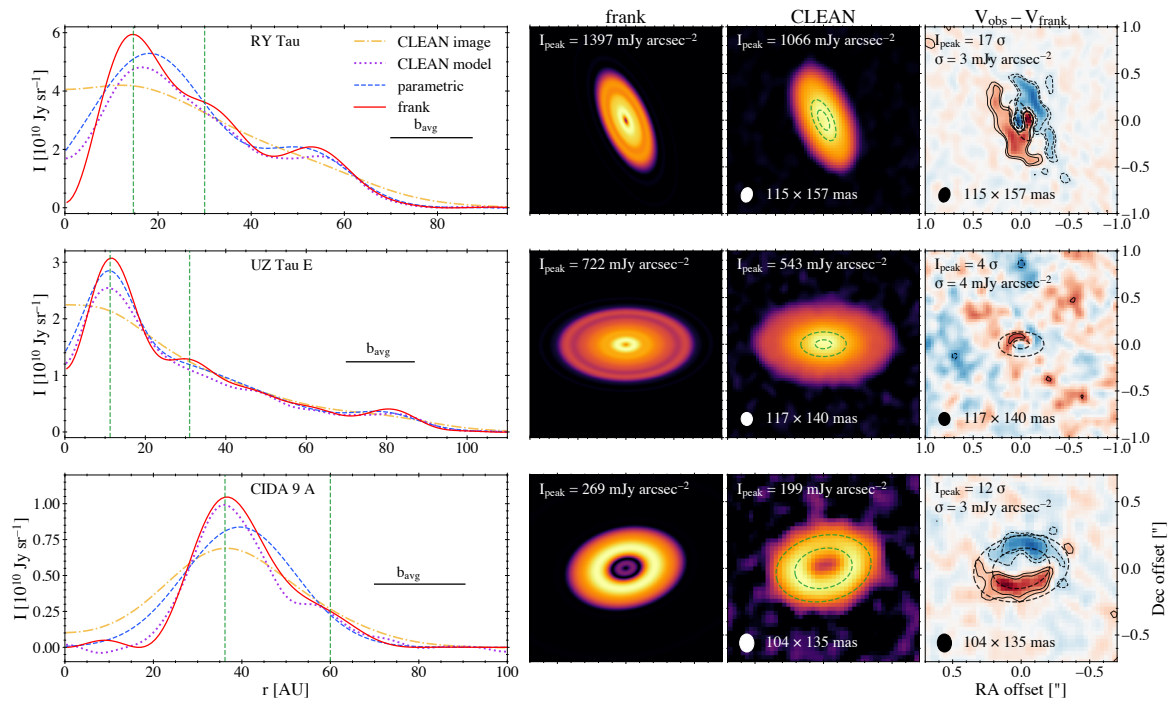


Fig. 4.11. New substructure in frank fits to extended disks with cavities

As in Fig. 4.6, but for three of the extended ($R_{\text{eff}, 90\%} > 50$ au) systems in the Taurus survey that exhibit an inner cavity, discussed in Sec. 4.4.2.2. Parametric profiles are from Long et al. 2018; the visibilities and fits for these disks are in Fig. 4.5. Vertical lines in the brightness profile plots denote the radial location of a ring and its shoulder; ellipses in the CLEAN image and imaged frank residuals correspond to these radii.

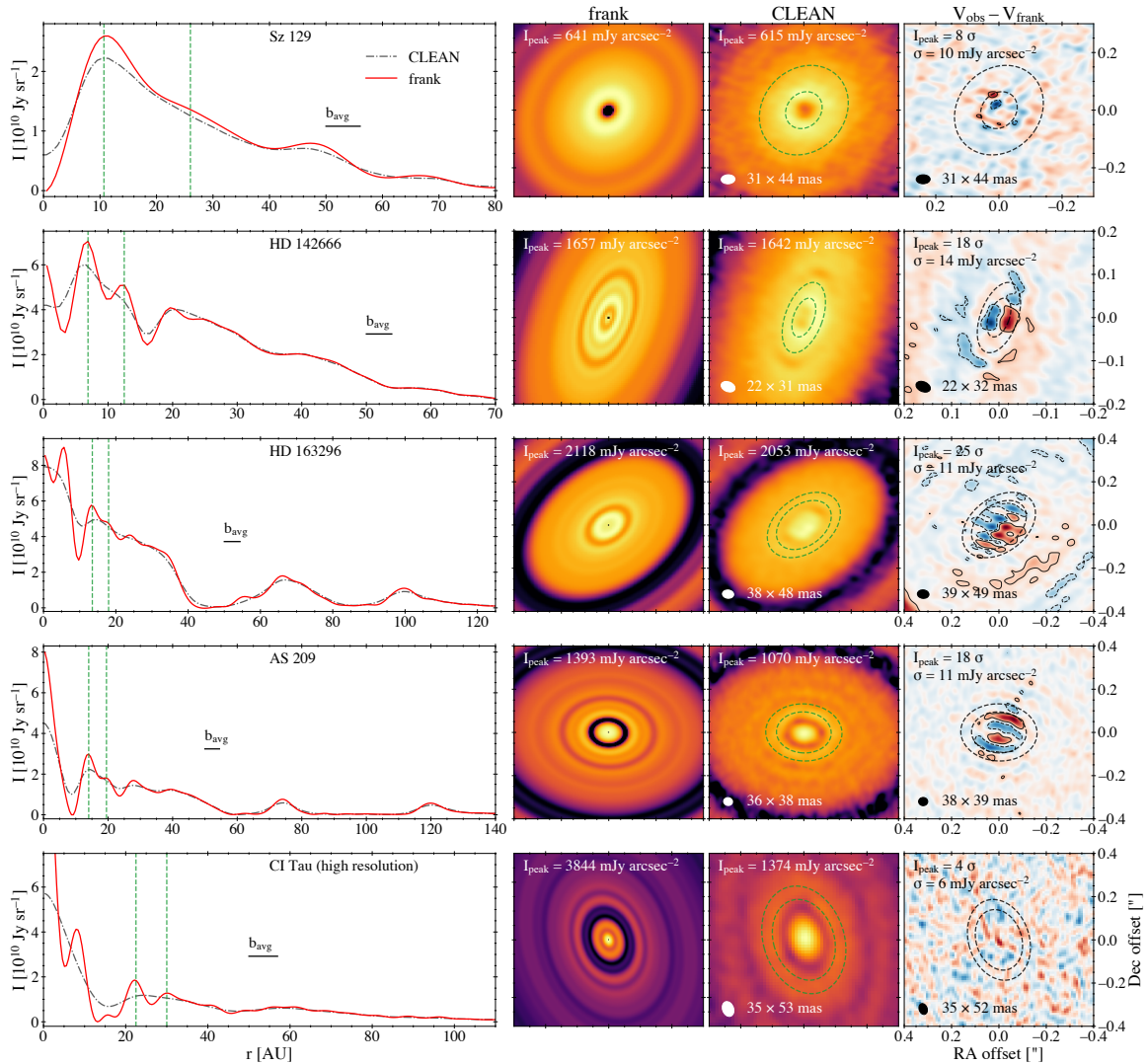


Fig. 4.12. Shoulder morphology in high resolution observations

The brightness profile extracted from the CLEAN image and the frank brightness profile for four disks in the ≈ 35 mas resolution DSHARP survey (Andrews et al., 2018; Huang et al., 2018a) and the ≈ 40 mas resolution observations of CI Tau (Clarke et al. 2018b; the y-scale zooms on lower brightness). Vertical lines in the brightness profile plots denote the radial location of a ring and its shoulder (Sec. 4.4.2); ellipses in the CLEAN image and imaged frank residuals correspond to these radii. Images zoom on the inner disk of each source. The imaged frank residuals have contours at $-5, +5\sigma$. frank fits for the DSHARP disks are from Jennings et al. (2021); the frank fit for CI Tau is previously unpublished (Appendix 4.8 shows the visibility fit).

between $\approx 30 - 50$ au may be a further indication of underresolved inner disk substructure. Additionally, the imaged `frank` residuals show $\geq 3\sigma$ asymmetries across the inner disk; from all of this we may again expect the inner disk morphology to evolve with higher resolution observations. As in GO Tau, the deep gap separating inner from outer disk (at 76 au) has a bump in the inset in Fig. 4.8. Again, at low surface brightness the relative model uncertainty is higher, although the CLEAN model profile does also suggest there may be structure in this gap.

DL Tau: Like DS Tau, GO Tau and MWC 480, DL Tau has a deep gap that separates inner from outer disk (at 66 au). Yet by comparison the gap in DL Tau is narrower and lacks the flat bottom morphology. The outer disk in DL Tau is distinct as well; while in the other three disks there is one prominent ring exterior to the gap, in DL Tau we find three (in addition to broad bumps at 144 au and 165 au that either trace faint rings, diffuse emission, or potentially artifacts of the visibility model's extrapolation). The rings at 97 au and 116 au in the `frank` profile are averaged over as a single, broad feature in the parametric profile from Long et al. (2018). Unique also to DL Tau is prominent asymmetry in the outer disk. The imaged `frank` residuals have $\geq 3\sigma$ and $\leq -3\sigma$ regions that lie roughly in the gap between the outer two prominent rings. The asymmetries have an orientation consistent with a generally brighter east side of the outer disk as identified by contouring the CLEAN image in Fig. 4.9(c). Collectively, these differences in morphology for DL Tau could indicate that the gaps in this disk are produced by a different physical process or a lower mass planet than in DS Tau, GO Tau and MWC 480. The one strong similarity between DL Tau and these other sources is a new plateau in DL Tau between $\approx 19 - 27$ au that corresponds to an asymmetry in the imaged fit residuals (note a plateau is also seen in the CLEAN model profile), suggesting the underresolved inner disk substructure may not be purely annular.

The abundance of substructure in the `frank` brightness profile for DL Tau (2 new rings in addition to the 3 rings identified in Long et al. 2018) makes this a good disk for comparing the `frank` fit to a parametric model whose functional form is motivated by the `frank` profile. Such a comparison gives a sense of how similar we can expect nonparametric and parametric fits to be for a highly structured source. This is of particular interest in the inner disk, where `frank` fits tend to find new substructure; that is, an independent parametric model can test the recovery of the features in the `frank` profile. This comparison also demonstrates the benefit of using a rapid, super-resolution `frank` brightness profile (as compared to the profile extracted from a CLEAN image or even from a CLEAN model) to motivate a parametric model which uses expensive Markov Chain Monte Carlo (MCMC).

Fig. 4.10 shows this comparison for DL Tau, between a 10 Gaussian parametric model and the `frank` fit. The parametric modelling approach and results, including the corner plot

and analysis of sampling convergence, are more fully presented in **Appendix 4.7**. The 10 Gaussian parametric form is composed of: 2 Gaussians based on the plateau and ring in the inner disk of the `frank` fit, 3 Gaussians for the 3 prominent rings in the outer disk of the `frank` fit, 1 Gaussian for the broad bump at 144 au in the `frank` fit, 2 additional Gaussians to describe the disk interior to 25 au, and 2 more Gaussians to account for the brightness profile's small offset from zero brightness out to large radii. Fig. 4.10(b) shows the median of the posterior samples for each of these 10 Gaussians, as well as the spread in randomly drawn samples for each.

The median brightness profile for the parametric model is in general agreement with the `frank` profile for DL Tau in Fig. 4.10(a), with the `frank` profile lying within the 2σ confidence interval of the parametric model at almost all radii. Both models find the outer disk between 65 – 130 au to resolve into 3 rings, and both prefer a (likely underresolved) deviation from the smooth Gaussian envelope in the inner disk, between 15 – 30 au. Relative to the `frank` profile, the parametric median profile exhibits narrower and brighter rings in the outer disk (and thus more flat-bottomed gaps between these rings), as well as a slight turnover near $r = 0$. These differences arise from the different extrapolation of the parametric median visibility fit and the `frank` fit beyond the end of the data in Fig. 4.10(e). The true visibility distribution likely continues to oscillate beyond the longest baselines sampled, but the observations of course provide no constraint on visibility amplitudes at unsampled baselines (apart from flux conservation). Since the differences between the parametric and `frank` profiles in visibility space are essentially limited to noisy or unsampled baselines, the precise ring widths, flatness of the gap bottoms, and turnover near $r = 0$ in the parametric brightness profile should thus be considered uncertain. Overall though, the general agreement between the parametric and `frank` profiles provides further evidence that DL Tau is densely structured, and the comparison illustrates the benefit of using a `frank` profile to initialize a parametric visibility fit, particularly for a disk with a large number of features.

4.4.2.2 Sources with an apparent inner cavity

For each of the three disks with an apparent inner cavity identified in the Taurus survey – CIDA 9 A, RY Tau and UZ Tau E – the `frank` fit in **Fig. 4.11** finds one or more new features.

RY Tau: The `frank` fit finds the cavity hinted at in the parametric fit to be almost fully cleared, with a steep outer wall. The adjacent ring in the parametric profile resolves into a narrower/brighter ring and an emission excess, a ‘shoulder’, in the `frank` profile (the shoulder is also hinted at in the CLEAN model profile). The contoured CLEAN image in Fig. 4.9(b) shows asymmetry in the innermost disk, and the imaged `frank` residuals in Fig. 4.11 have a strong

asymmetric pattern at small radii (roughly interior to the shoulder) that is $\leq 17\sigma$, or $\approx 5\%$ of the peak brightness in the CLEAN image. This is a smaller contrast by a factor of a few than the shoulder in the frank profile, suggesting that feature is not purely due to an asymmetry. The residual structure could be dominated by an elevated/flared emission surface, as $\geq 5\sigma$ and $\leq -5\sigma$ residuals span most of the disk, and the source has a large fitted inclination of $\approx 65^\circ$. A cleared inner cavity and inner disk asymmetry are seen in higher resolution observations (20×40 mas beam) of this source (Francis and van der Marel, 2020). In the outer disk, the plateau in the parametric profile between $\approx 40 - 50$ au becomes a gap/ring pair in the frank profile (and to a lesser extent in the CLEAN model profile), as may be expected from a higher resolution fit; note how the parametric fit in Fig. 4.5 misses the trough in the visibilities centered at $1.25 M\lambda$ that the frank fit recovers and the CLEAN model visibility profile partially recovers.

UZ Tau E: As in RY Tau, the frank profile finds the cavity to be more devoid of material than previously seen, with a steeper edge and brighter adjacent ring, and a shoulder on the ring's trailing edge. The broad region of quasi-linear slope in both the parametric and frank brightness profiles (between $\approx 40 - 70$ au in the latter) is potentially suggestive of underresolved substructure at these radii. In the outer disk, the frank fit finds the ring at 82 au to be narrower and brighter. The imaginary component of the visibilities for UZ Tau do show structure at the shortest baselines, but this is due to the disk-bearing binary system UZ Tau Wa and Wb in the field of view.

CIDA 9 A: As in RY Tau and UZ Tau E, the frank profile finds the cavity wall to be steeper, with a brighter adjacent ring and an accompanying shoulder that is also apparent in the CLEAN model profile. The imaginary component of the visibilities in Fig. 4.5 show structure across a wide range of baselines, and the contoured CLEAN image of the source in Fig 4.9(a) correspondingly traces brightness excesses in the southeast and southwest of the disk. These roughly coincide with the ring's peak location in the frank profile and the strong structure in the imaged frank residuals. The residual features have brightness up to 18% of the peak brightness in the CLEAN image; such a high contrast entails they are affecting the frank profile in the bright ring's vicinity. The profile also indicates an additional, faint ring within the cavity (at 9 au).

The shoulder morphology as a trend A shoulder is present on the trailing edge of the bright ring in all three Taurus survey disks with an apparent inner cavity, suggesting a trend. The shoulder morphology is also seen in several disks beyond the survey that have an inner

cavity or deep gap. These shoulders have been identified using a variety of fitting techniques, and over a range of observational resolutions and wavelengths. Like the Taurus disks, the shoulder's contrast varies across disks observed at similar resolution and wavelength. And like the Taurus disks there are often brightness asymmetries in the vicinity of the ring and shoulder, identified in either a CLEAN image or imaged fit residuals.

In some disks, a brightness arc in an otherwise empty annulus seen in the CLEAN image manifests in the CLEAN brightness profile as a shoulder. Examples include the arc exterior to a ring outside a deep gap in the 1.3 mm DSHARP observations of HD 143006 (Huang et al., 2018a; Pérez et al., 2018), as well as the arc exterior to a ring that surrounds an inner cavity in the 0.9 mm observations of V1247 Ori and HD 135344 B (van der Marel et al. 2019; the shoulder in HD 135344 B is also seen in the frank profile in Norfolk et al. 2021). In other cases, similar to the Taurus survey disks, the shoulder morphology is present not as the result of a clearly isolated arc, but within an annulus that in the CLEAN image appears to contain emission across all azimuthal angles. The 2.1 mm CLEAN brightness profile of GM Aur shows such a shoulder on the trailing edge of a bright ring exterior to a cavity (Huang et al., 2020), with the CLEAN image showing hints of a brightness asymmetry in the radial region of the gap and shoulder; lower resolution observations of the same source at 0.93 mm and 7 mm (Macías et al., 2018) also find a shoulder.

frank fits to four of the six DSHARP sources that have a bright ring in the inner disk – AS 209, HD 142666, HD 163296, and Sz 129 – show a shoulder on the ring's trailing edge (Jennings et al., 2021). In Sz 129 the ring is exterior to an inner cavity, while in AS 209, HD 142666 and HD 163296 it is exterior to a deep gap in the inner disk. These fits are reproduced in Fig. 4.12, with brightness asymmetries consistently present in the imaged frank residuals interior to and/or at the radial location of the ring. Asymmetries are also identified at these radii in the CLEAN image for HD 142666, HD 163296 and Sz 129 (Huang et al., 2018a). The shoulder's contrast varies across the frank brightness profiles, from a faint, wide bump in Sz 129 to an apparent ring in HD 142666. Fig. 4.12 also shows a frank fit to the 40 mas observations of CI Tau from Clarke et al. (2018b), where the broad ring in the parametric profile at 27 au resolves into an inner narrow ring and an outer, fainter ring (the shoulder) in the frank fit. The frank profile also finds the deep gap interior to the rings to be structured.

We suspect this shoulder morphology (regardless of whether a given shoulder is under-resolving a ring) is tracing some common physical mechanism whose relative effect varies between sources. Perhaps the most viable candidates are ones that can produce azimuthal brightness asymmetries in a disk with a cavity or deep gap, such as those discussed in § 3.3 of Long et al. (2018): planet-induced dust traps (Ataiee et al., 2013; van der Marel et al.,

2013) and eccentric cavities in a circumbinary disk (Ragusa et al., 2017); or migrating planets (Meru et al., 2018; Nazari et al., 2019).

4.5 Conclusions

We used `frank` to identify new features and more highly resolve known features in 10 Taurus survey disks observed at ≈ 120 mas resolution.⁶ Relative to the parametric visibility fits in Long et al. (2018) and Long et al. (2019) and the CLEAN model brightness profiles, which both yielded substantially more disk substructure than the CLEAN image brightness profiles, we demonstrated how further improvements to visibility fit accuracy with the nonparametric approach in `frank` could find yet more features. The most notable example was DL Tau, in which the `frank` fit recovered two new rings in a disk with three previously identified rings. We also used this source to show how a super-resolution `frank` profile is advantageous for motivating a parametric form that can be modeled with tools such as `galarío`, and how this parametric fit provided further confidence in the `frank` profile features. Among the substructures characterized across the 10 disks, we identified three main trends:

- increased substructure in compact disks: Of the survey’s 14 disks with radii $\lesssim 55$ au, we found two previously smooth disks (BP Tau, DR Tau) to exhibit substructure and identified a new gap in the inner disk of another (FT Tau). These disks were not systematically larger or brighter than the compact sources without detected substructure, and we motivated how sparse (u, v) plane sampling at long baselines in many of the latter does not exclude the presence of substructure at the observed spatial scales.
- increased inner disk substructure: Across the compact and extended sources considered, we found evidence of underresolved substructure at small ($\lesssim 30$ au) radii, in many cases coinciding with azimuthally asymmetric fit residuals.
- a ring/shoulder morphology in inner disks: The three survey sources with an apparent inner cavity (CIDA 9 A, RY Tau, UZ Tau E) showed a shoulder on the trailing edge of the disk’s bright ring. We noted numerous instances of this same morphology exterior to a cavity or deep gap in disks outside the survey, positing it may trace a common physical mechanism.

Identification of new substructure in Taurus survey disks complements recent applications of `frank` to the DSHARP survey (Jennings et al., 2021) and ODISEA survey (Cieza et al., 2021). Along with super-resolution fits obtained using other methods such as `galarío` in

⁶All `frank` fits in this chapter are available at <https://zenodo.org/record/5587840>.

Long et al. (2018) and Long et al. (2019), these results contribute to the growing evidence that it is not only bright, large disks that exhibit substructure. Instead a lack of substructure in a disk may often be an artifact of a dataset’s or model’s resolution. This underscores the utility of super-resolution methods across a range of observational resolutions to better constrain substructure occurrence rates and discern morphological trends. Ultimately a large ensemble of sources characterized at super-resolution scales will help to discriminate between candidate physical mechanisms producing disk features.

4.6 Appendix A: Effect of phase center uncertainty on imaged frank residuals

To assess the robustness of features in the imaged frank residuals shown in the main text, here we consider how the fitted phase center alters their morphology and brightness. We focus on the phase center, rather than the fitted inclination or position angle, or out-of-plane effects, because several of the imaged frank residuals in the main text show a bimodal asymmetry in the inner disk that may reasonably be expected as an artifact of the applied phase center (see Appendix A in Andrews et al. 2021 for a good demonstration). We seek to determine whether they may instead be indications of real asymmetries (see also Appendix B in Jennings et al. 2021).

Long et al. (2018) found the typical 1σ uncertainties in fitted right ascension and declination offsets for a source (relative to the center of the field of view) to be < 1 mas, while we have found uncertainties with mock and real data to commonly be $1 - 3$ mas. While < 1 mas shifts in phase center typically have a trivial effect on residual visibility amplitudes, shifts of $1 - 3$ mas can induce visible differences in imaged frank residuals. To test whether these shifts can remove high residual brightness in the inner disk, for each source in the main text we have applied a phase center differing from the published value by 1, 2 or 3 mas – with the shift at $\pi/4$ intervals over the full 2π in azimuth – then fit the shifted visibilities and compared the fit to that with the published phase center (this is the same test described in Appendix B of Jennings et al. 2021). The effects of a phase shift of $1 - 3$ mas on the visibilities and thus the frank brightness profile are largely imperceptible, but differences are evident in the imaged frank residuals.

As an example, the imaged frank residuals for DR Tau using the published phase center contain $> 5\sigma$, bimodal features in the inner disk. **Fig. 4.13** shows the results of the above test for a 2 mas phase center shift at each of the $\pi/4$ azimuthal angles (the imaged residuals for shifts of 1 and 3 mas are qualitatively similar). The phase shifts do result in a variation in the

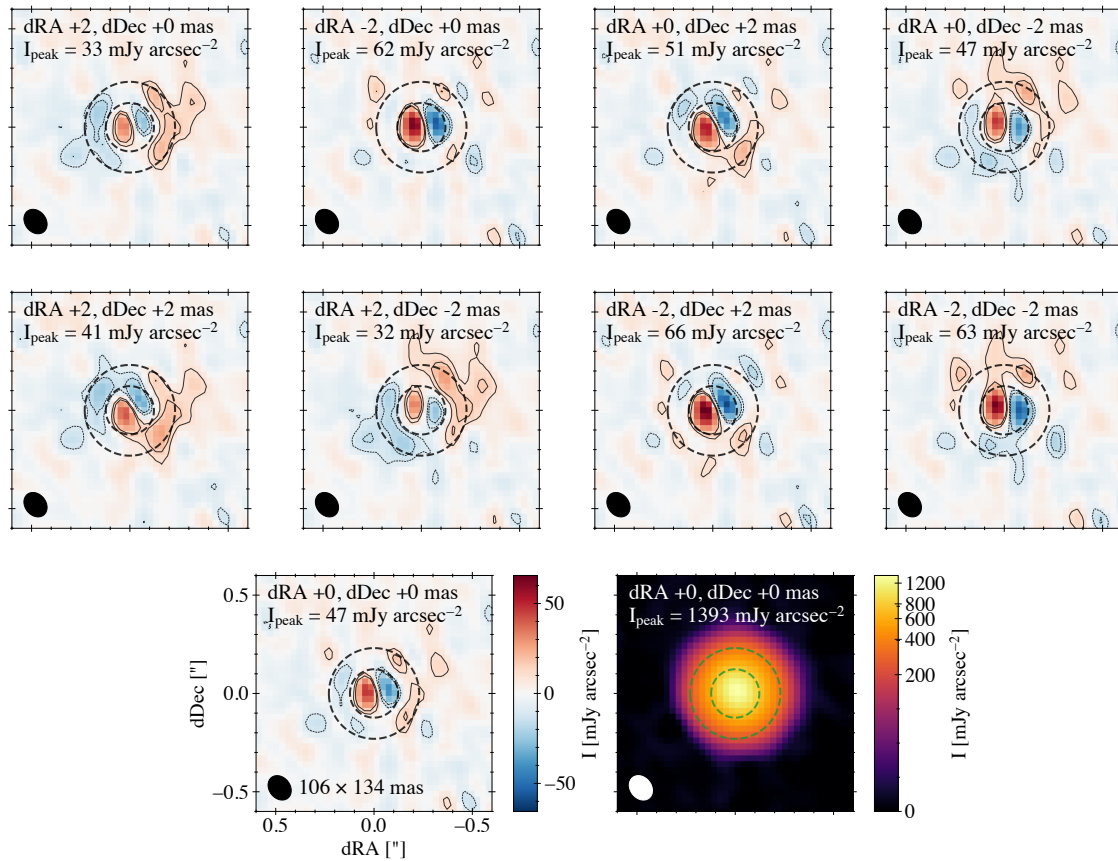


Fig. 4.13. Effect of fitted phase center on imaged residual visibilities

Bottom row: The imaged frank residual visibilities for the fit in the main text to DR Tau (zero CLEAN iterations; contours at $-5, -3, +3, +5\sigma$, with $\sigma = 3 \text{ mJy arcsec}^{-2}$), and the CLEAN image.

Top and center rows: The imaged frank residual visibilities when the fitted dRA and/or dDec is varied by $\pm 2 \text{ mas}$ (as listed in each panel). The imaged frank residual panels all use the same absolute linear stretch shown in the colorbar.

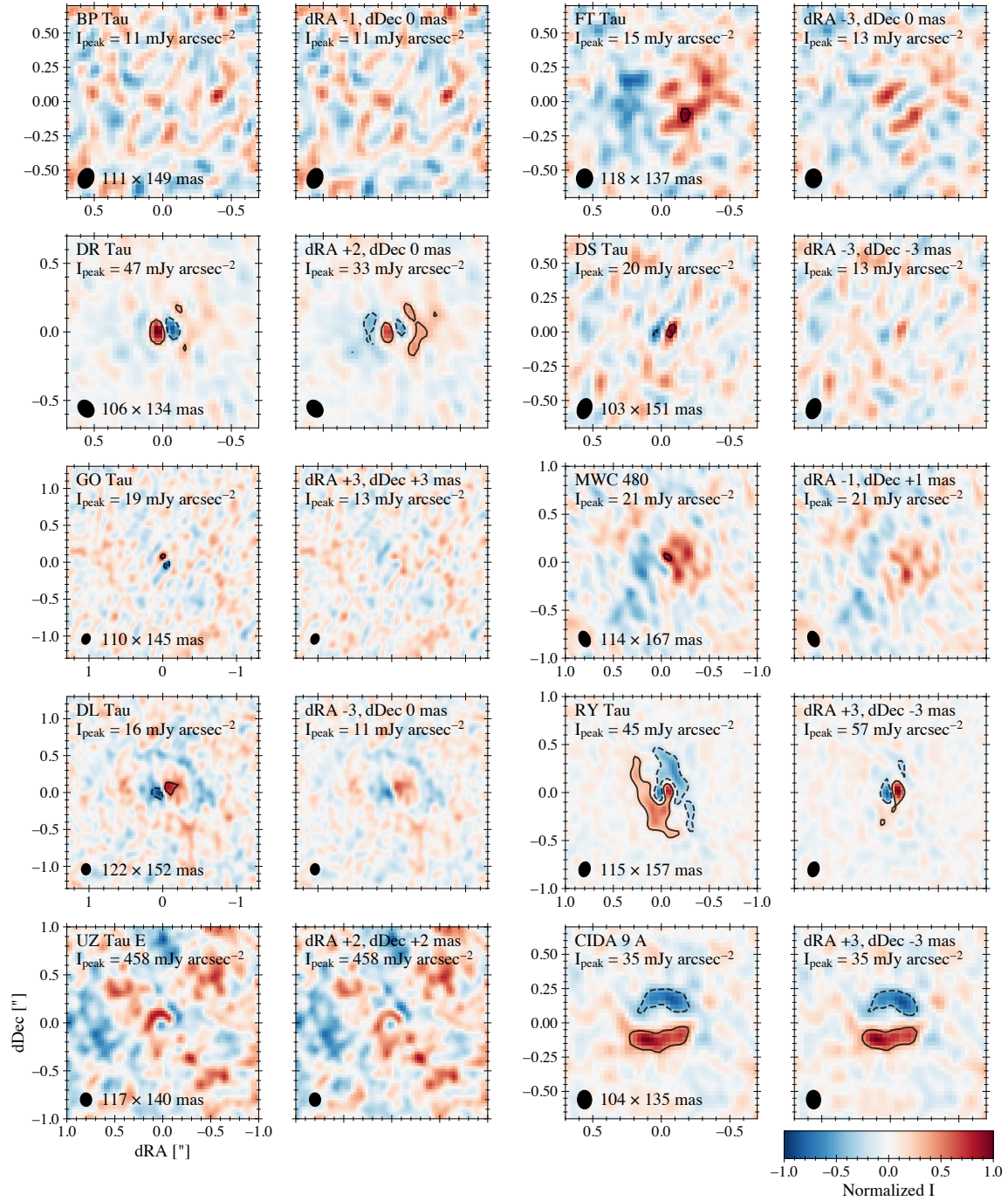


Fig. 4.14. Varying the phase center to minimize the imaged residual visibilities

The imaged frank residual visibilities from the main text for each source in Sec. 4.4, alongside the imaged visibilities obtained by varying the fitted dRA and/or dDec to minimize the absolute image brightness. The images are produced with zero CLEAN iterations; contours are at $-5, +5\sigma$. The peak brightness is given, as is the phase shift applied to minimize the absolute brightness.

peak residual brightness by a factor of ≤ 2 , and in the orientation of the bimodal pattern. But the pattern persists in all cases, and phase shifts that reduce the pattern's brightness (which we may at first interpret as the applied phase center being more accurate) also increase the residual amplitude at larger disk radii. We could expect that this is due to a more complex combination of an incorrect phase center, incorrect inclination and/or position angle, and out-of-plane effects, however this disk is nearly face-on (fitted inclination of 5.4°). The persistence of $> 10\sigma$ features in the residuals thus suggests there is real inner disk structure that the frank fit to these data is not resolving.

To consider the full set of 10 sources in Sec. 4.4, **Fig. 4.14** compares the imaged frank residuals from the main text for each disk with the residuals produced when we shift the phase center to minimize the absolute brightness in the image. In some cases a bimodal asymmetry in the inner disk is weakened, while in others it persists. This suggests these inner disk residual features are not (always) purely an artifact of an incorrect visibility deprojection.

4.7 Appendix B: Parametric fit to DL Tau

Sec. 4.4.2.1 shows a 10 Gaussian parametric fit to DL Tau using `galario`. Here we present the fit in more detail. The model contains 34 free parameters: a centroid, amplitude and standard deviation for each of the 10 Gaussians, as well as the disk geometry (inclination, position angle, and the right ascension and declination offsets). We perform an initial maximum likelihood estimate using the BFGS solver in `scipy.optimize.minimize`, then initialize the MCMC walkers in a Gaussian ball around this estimate (by adding to each parameter value a draw from the standard normal distribution multiplied by 10^{-4}). We run the MCMC with `emcee` (Foreman-Mackey et al., 2013), using 160 walkers (≈ 5 per parameter) and a uniform prior on each parameter in the brightness profile Gaussians, as well as a Gaussian prior on the disk geometry parameters (centered on the published geometry), as listed in **Table 4.2**. We run the MCMC for 3×10^5 steps and then estimate the autocorrelation time τ for each chain at various points in the run. We do not reach convergence across all chains during the run, with the estimate of the autocorrelation time averaged over all dimensions $\hat{\tau}$ continually increasing as a power law in **Fig. 4.15** rather than plateauing. This demonstrates how the high dimensionality of the parameter space would require a significantly larger number of steps to reach sampling convergence.

From the full set of samples we remove a burn-in of $2 \cdot \max(\tau) \approx 6 \times 10^4$ steps, with τ estimated at the last step in the chains. Using the resulting samples, Table 4.2 gives the posterior 16th, 50th and 84th percentiles for each parameter; unsurprisingly the faintest Gaussians (G_3, G_6, G_9, G_{10}) have the highest uncertainty on their width and amplitude.

Table 4.2. Priors and posterior 16th, 50th and 84th percentiles for each parameter in the 10 Gaussian parametric fit to DL Tau. $G(r, \sigma, I)$ denotes a Gaussian of radial position r , standard deviation σ and *logarithmic* brightness I . The disk geometry parameters listed are inclination (inc), position angle (PA), right ascension offset (dRA), and declination offset (dDec).

Priors	
Parameter [unit]	Prior
r_i in $G_i(r_i, \sigma_i, I_i)$ [arcsec]	uniform: $\left\{ \begin{array}{l} (0.00, 0.08), \quad i = 1 \\ (0.08, 0.10), \quad i = 2 \\ (0.10, 0.20), \quad i = 3 \\ (0.20, 0.40), \quad i = 4 \\ (0.40, 0.55), \quad i = 5 \\ (0.55, 0.63), \quad i = 6 \\ (0.63, 0.65), \quad i = 7 \\ (0.65, 0.70), \quad i = 8 \\ (0.70, 0.80), \quad i = 9 \\ (0.80, 0.95), \quad i = 10 \end{array} \right.$
σ_i in $G_i(r_i, \sigma_i, I_i)$ [arcsec]	uniform: (0.00, 0.30) for $i \in [1...10]$
I_i in $G_i(r_i, \sigma_i, I_i)$ [$\log_{10}(\text{Jy sr}^{-1})$]	uniform: (8, 12) for $i \in [1...10]$
inc [deg]	$G(x_0 = 44.95, \sigma_x = 5.0)$
PA [deg]	$G(x_0 = 52.14, \sigma_x = 5.0)$
dRA [mas]	$G(x_0 = 240, \sigma_x = 5)$
dDec [mas]	$G(x_0 = -60, \sigma_x = 5)$
Posteriors	
Brightness profile Gaussians	Disc geometry
$G_1(r = 0.01^{+0.01}_{-0.01}, \sigma = 0.03^{+0.01}_{-0.01}, I = 10.76^{+0.08}_{-0.06})$	inc = $45.10^{+0.32}_{-0.30}$ [deg]
$G_2(r = 0.10^{+0.02}_{-0.01}, \sigma = 0.10^{+0.02}_{-0.02}, I = 10.21^{+0.06}_{-0.07})$	PA = $51.90^{+0.45}_{-0.46}$ [deg]
$G_3(r = 0.14^{+0.04}_{-0.03}, \sigma = 0.05^{+0.10}_{-0.04}, I = 8.90^{+0.86}_{-0.62})$	dRA = 236^{+1}_{-1} [mas]
$G_4(r = 0.31^{+0.01}_{-0.01}, \sigma = 0.03^{+0.01}_{-0.01}, I = 9.86^{+0.05}_{-0.06})$	dDec = -59^{+1}_{-1} [mas]
$G_5(r = 0.49^{+0.00}_{-0.00}, \sigma = 0.01^{+0.01}_{-0.00}, I = 9.80^{+0.24}_{-0.22})$	
$G_6(r = 0.60^{+0.02}_{-0.02}, \sigma = 0.03^{+0.05}_{-0.02}, I = 9.09^{+0.43}_{-0.45})$	
$G_7(r = 0.67^{+0.02}_{-0.02}, \sigma = 0.24^{+0.04}_{-0.09}, I = 9.05^{+0.13}_{-0.22})$	
$G_8(r = 0.73^{+0.01}_{-0.01}, \sigma = 0.02^{+0.01}_{-0.01}, I = 9.58^{+0.23}_{-0.15})$	
$G_9(r = 0.79^{+0.04}_{-0.04}, \sigma = 0.22^{+0.05}_{-0.12}, I = 8.65^{+0.24}_{-0.38})$	
$G_{10}(r = 0.89^{+0.02}_{-0.03}, \sigma = 0.03^{+0.04}_{-0.02}, I = 8.89^{+0.34}_{-0.32})$	

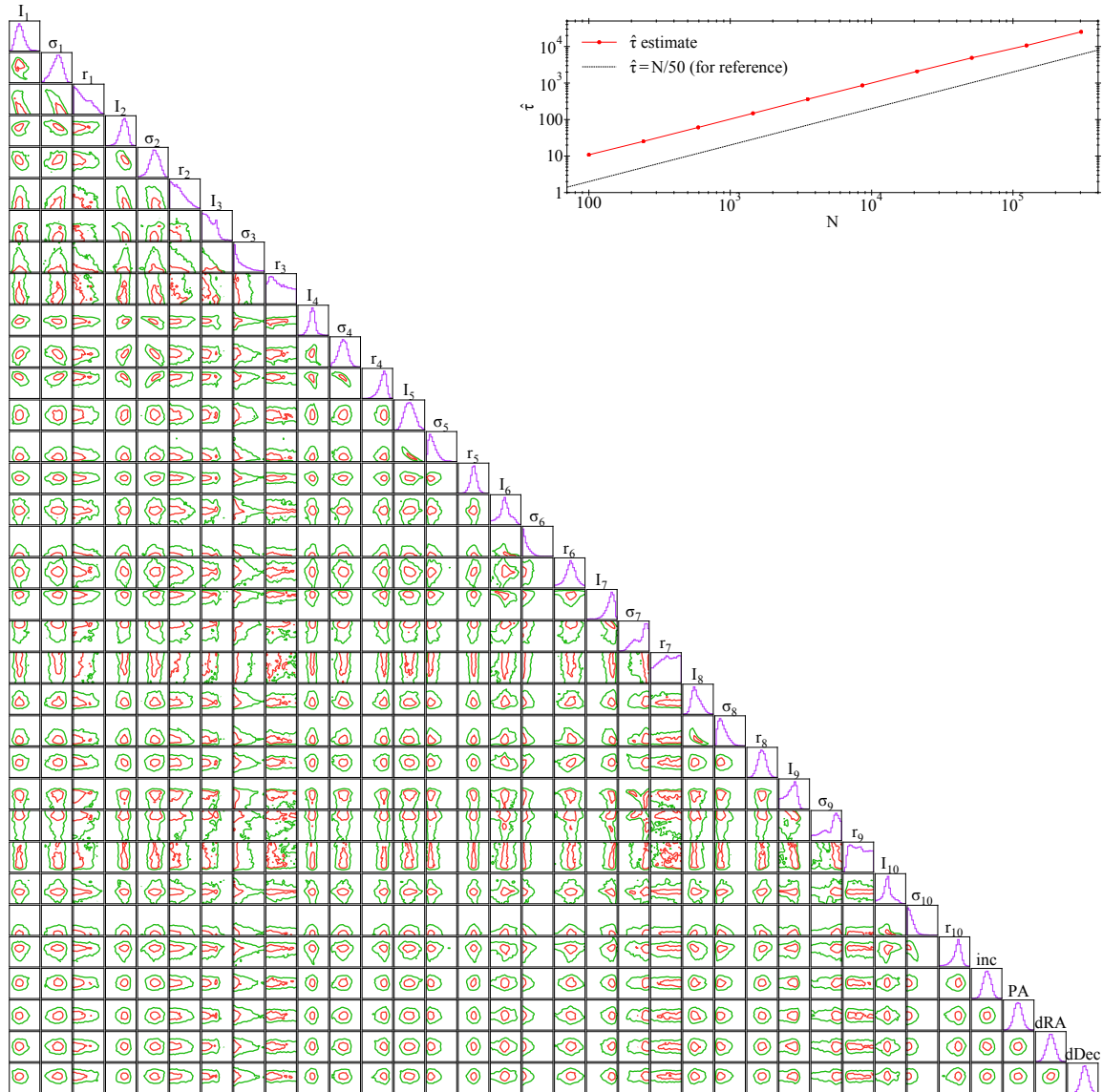


Fig. 4.15. Corner plot for parametric fit to DL Tau

For the parametric fit to DL Tau, a corner plot showing the posterior for each fitted parameter (along the diagonal) and the covariance between parameters (red 1σ and green 2σ confidence intervals). The top-right panel shows the estimate for the autocorrelation time averaged over all dimensions $\hat{\tau}$ as a function of the number of samples N .

Fig. 4.15 shows the corner plot using `corner.py` (Foreman-Mackey, 2016), with few instances of strong covariance in the 2D distributions, but also non-Gaussianity in the 1D distributions for the centroid and the standard deviation of some of the brightness profile Gaussians.

4.8 Appendix C: frank fit to high resolution observations of CI Tau

The `frank` fit to the ≈ 40 mas observations of CI Tau⁷ in **Fig. 4.16** finds new features in the disk's brightness profile: a (very likely underresolved) gap/ring pair at 5 au, structure in the deep gap at 15 au, and a separation of the single ring at 25 au into two rings. The parametric `galarío` profile from Clarke et al. (2018b), also shown in Fig. 4.16, exhibits a change in slope at the location of the 5 au gap in the `frank` fit, giving further credence to this feature. The fast oscillations in the `frank` brightness profile are artifacts of the visibility fit. The `frank` fit shows a large improvement in accuracy in the visibility domain relative to the 1D Fourier transform of a brightness profile extracted from the CLEAN image⁸, with a factor of ≈ 11 lower χ^2 . The `frank` fit to the Taurus survey observations of CI Tau (not shown) does not resolve any indication of the new features seen in the fit to the higher resolution data.

⁷The `frank` fit uses visibilities deprojected and phase centered by $i = 47.3^\circ$, $PA = 14.1^\circ$, $(dRA, dDec) = (330, -93)$ mas. These were determined in `frank` by fitting a 2D Gaussian to the visibilities. The model hyperparameters for the brightness profile fit are $\alpha = 1.05$, $w_{\text{smooth}} = 10^{-4}$, $R_{\text{out}} = 1.5''$, $N = 500$, $p_0 = 10^{-15}$ Jy².

⁸The CLEAN image was generated using `tclean` in CASA 5.6.1-8 with the `multiscale` deconvolver (pixel size of 10 mas and scales of 1, 2, 4, 6 pixels) and Briggs weighting with a robust value of 0.5.

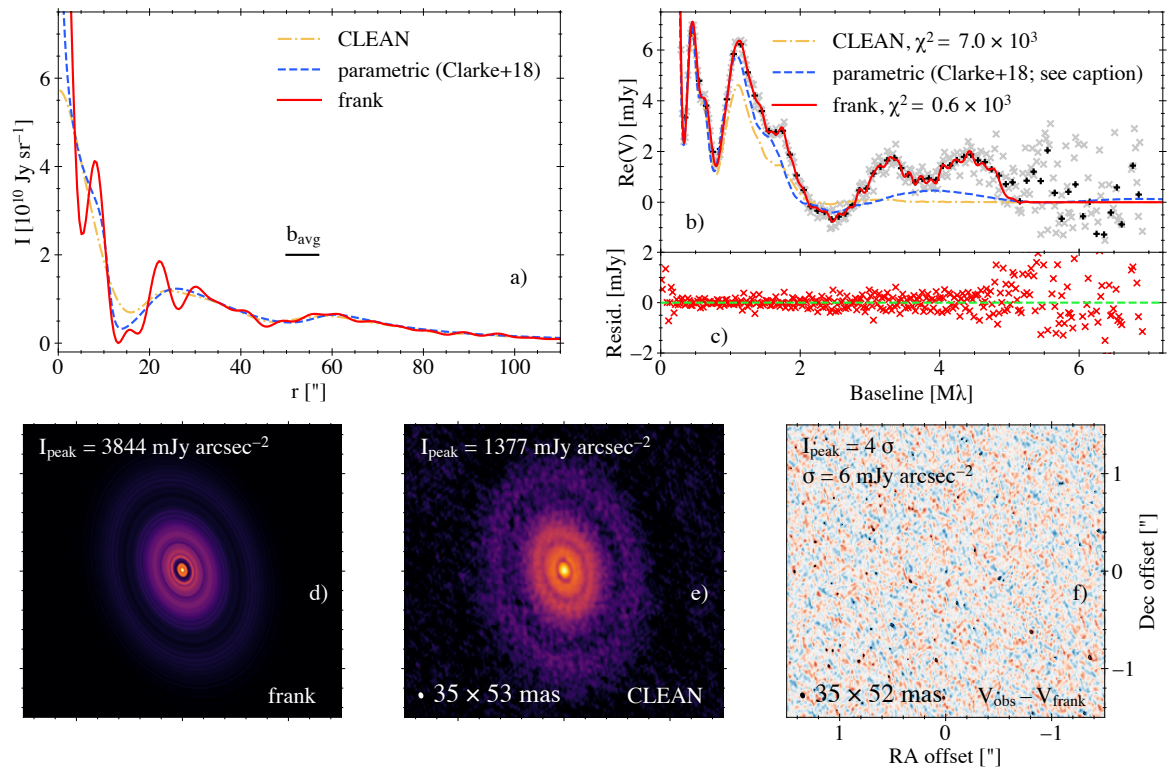


Fig. 4.16. frank fit to high resolution CI Tau observations

a) Brightness profile fits for ≈ 40 mas observations of CI Tau, with the parametric fit from [Clarke et al. \(2018b\)](#), frank fit (which peaks at $16 \times 10^{10} \text{ Jy sr}^{-1}$), and the CLEAN image brightness profile. b_{avg} shows the mean of the CLEAN beam width along its major and minor axes.

b) Observed visibilities (20 and 100 $k\lambda$ bins) and fits corresponding to the brightness profiles in (a). The parametric fit used a different frequency normalization to convert the (u, v) distances to units of $[\lambda]$ and a different geometry to deproject the visibilities, so it is not directly comparable to the data shown here, the frank fit or the CLEAN fit. Hence we do not report a χ^2 .

c) Residuals of the frank visibility fit (20 $k\lambda$ bins).

d)–f) An image of the frank profile swept over 2π and reprojected; the CLEAN image; and the imaged frank residual visibilities (zero CLEAN iterations; contours at $-3, +3\sigma$). The frank and CLEAN images use an arcsinh stretch ($I_{\text{stretch}} = \text{arcsinh}(I/a) / \text{arcsinh}(1/a)$, $a = 0.02$), but different brightness normalization (indicated by the given peak brightness). The imaged frank residuals use a linear stretch symmetric about zero.

Chapter 5

Conclusions

5.1 The frank modeling framework and scientific applications

This thesis presented `frank`, an open source, super-resolution imaging technique for radio interferometric observations, and its application to an ensemble of protoplanetary disk observations to identify and accurately characterize disk substructures. After providing the necessary technical and scientific background and motivation for this tool in Chapter 1, we presented the modeling framework for `frank` in Chapter 2. `frank` is a 1D, nonparametric model that uses a fast Gaussian process to recover the brightness profile of a disk and thus characterize its substructure by directly and accurately fitting the real component of the observed visibilities. `frank` offers an advantage in 1D relative to the community standard imaging approach, `CLEAN`, by consistently recovering higher angular resolution information from a dataset without sacrificing sensitivity. This enables scientific applications for protoplanetary disks including more accurately discerning substructure widths and amplitudes, better resolving the inner disk structure, and isolating disk asymmetries in a residual image.

Considering the ubiquity of disk substructure in bright sources, we next applied `frank` to the high resolution DSHARP survey ([Andrews et al., 2018](#)) in Chapter 3. `frank` super-resolved disk structure relative to `CLEAN` in this analysis by accurately fitting the 1D visibility distribution for each of the 20 DSHARP sources to a mean factor of 4.3 longer baseline than brightness profiles extracted from the `CLEAN` images and a factor of 3.0 longer baseline than the `CLEAN` models. This demonstrated that super-resolution techniques such as `frank` can provide new insights from existing datasets, better informing physical inference without requiring deeper and/or longer baseline interferometric observations. A major scientific

outcome of this analysis was the finding that the DSHARP disks are commonly structured interior to 30 au, a finding not achievable with CLEAN images alone.

Finally in Chapter 4, we applied `frank` to the moderate resolution Taurus survey (Long et al., 2018), finding that disks which appear featureless (or relatively featureless) in CLEAN images are often structured when the data are super-resolved with `frank`. This showed that it is not only bright, large disks that exhibit substructure; instead a lack of substructure in a disk may often be an artifact of a dataset’s or model’s resolution – even a parametric visibility model. This analysis notably found a higher occurrence rate of substructure in compact disks than previously known, and a higher rate of inner disk substructure than previously discovered in this survey, complementing our findings in Chapter 3 with the DSHARP survey.

5.2 The role of super-resolution imaging in future disk science

The scientific findings in Chapters 3 and 4 show the capability of `frank`, and super-resolution techniques generally, to advance our understanding of protoplanetary disk structure. With a sufficiently large sample of disk datasets super-resolved, we will be able to use this substructure characterization to investigate disk physics and the embedded planet population. A subsequent step will be to connect a statistical sample of young planets to the occurrence rates found in the evolved exoplanet population. To these ends, two future directions with `frank` are useful: applying the current version to a larger ensemble of existing datasets and expanding the model’s capabilities.

To immediately advance scientific results for disk science with `frank`, the current version of the model framework could be applied to the large sample of archival ALMA datasets, which constitutes a few tens of disks observed at high resolution (<75 mas) and many tens at moderate resolution (75 - 200 mas). Several of these have been observed across multiple spatial resolutions and wavelengths. Applying `frank` to this large suite of datasets covering a broad range of disk morphologies would enable a statistical analysis of super-resolution trends in disk substructure, with `frank` recovering more information from existing data than previously obtained with CLEAN. Across this sample, leveraging discriminants such as stellar mass, disk mass and age would allow us to address open questions of how substructures form and evolve. This super-resolution characterization of a statistical ensemble of sources could specifically address which substructure morphologies are generated by the dynamical effect of newly-formed planets and which by hydrodynamic disk instabilities.

In terms of expanding `frank`'s capabilities, because the modeling approach has been in 1D, the characterization of azimuthally asymmetric substructure in disks has been limited. Such features are so far found to be less common than annular gaps and rings, although a large diversity of asymmetries may be hidden by the limited resolution in 2D CLEAN images. Examples of known and potential asymmetries include local brightness 'arcs' that simulations find can be produced by eccentric cavities in circumbinary systems (Ragusa et al., 2017), spiral arms whose pitch angles could be measured more accurately with super-resolution imaging to infer the presence of a planet (e.g., Bae and Zhu, 2018); and small 'shoulders' seen on the wings of Gaussian rings in 1D fits (Sec. 4.4.2.2) that may be tracing asymmetries due to planet-induced dust traps (e.g., van der Marel et al., 2013). A 2D version of the `frank` model is thus needed to accurately super-resolve, and conduct physical inference on, a large ensemble of disks observed by ALMA.

To develop this 2D expansion of `frank` will require generalizing the discrete Hankel transform (DHT). The DHT is an analog to the discrete Fourier transform, used in `frank` 1D to translate between the data domain (visibilities) and the real space brightness profile by expressing the profile as a sum of zero-order Bessel functions. The DHT can accurately represent 2D distributions (thus azimuthal disk asymmetries) via a multipole expansion that uses higher order Bessel functions to represent higher moments.

In addition to the continuum emission in the dust, there are a growing number of datasets for the gas component of protoplanetary disks as traced by molecular spectral line emission. The most recent of these data contain high resolution information that remains unleveraged by CLEAN imaging. The MAPS survey measured >50 spectral lines over five disks (Öberg et al., 2021), and in the near-term additional, high spatial resolution gas data in CO, CS and N₂H⁺ will come from the exoALMA, eDisk and AGE-PRO surveys. Super-resolution characterization of molecular line data could probe the molecular inventory at Solar System scales and place tighter constraints on such fundamental properties as the gas disk thermal and kinematic structure, and even the disk chemistry. A 2D version of `frank` could be applied to not only individual images but entire spectral cubes. This would enable a new level of joint high spatial *and* high spectral resolution characterization.

Pairing super-resolution findings in the gas and dust data has the potential to markedly advance our understanding of not only disk physics and chemistry, but also planet formation and orbital evolution. Using a 2D version of `frank` to characterize both gas and dust disk substructures could allow us to constrain the physics and timescales of planet formation, disk-planet interactions, and disk hydrodynamic instabilities that prompt planetesimal growth. Over a sufficiently large sample, this could allow us to holistically and self-consistently assess substructure morphologies, occurrence rates, and origins across multiple tracers. The

resulting trends could have the potential to identify embedded planets across a range of complementary tracers.

Ultimately, these frontiers with `frank` and a statistical census of super-resolved datasets could provide diagnostics that are a unique pathway to advance our understanding of planet formation, the origins of exoplanetary system demographics and giant planet atmospheres. This would further advance connections between our understanding of disks and the compositions of mature exoplanets through a joint analysis of super-resolved dust midplane and spectral line data, bringing us a step closer to a coherent theoretical description of planet formation, disk evolution, and early planetary system evolution.

References

- Ables, J. G. (1974). Maximum Entropy Spectral Analysis. , 15:383.
- Abrantes, F., Lopes, C., Rodrigues, T., Gil, I., Witt, L., Grimalt, J., and Harris, I. (2009). Proxy calibration to instrumental data set: Implications for paleoceanographic reconstructions. *Geochemistry, Geophysics, Geosystems*, 10(9):Q09U07.
- Akiyama, E., Hasegawa, Y., Hayashi, M., and Iguchi, S. (2016). Planetary System Formation in the Protoplanetary Disk around HL Tauri. , 818(2):158.
- Akiyama, K., Ikeda, S., Pleau, M., Fish, V. L., Tazaki, F., Kuramochi, K., Broderick, A. E., Dexter, J., Mościbrodzka, M., Gowanlock, M., Honma, M., and Doeleman, S. S. (2017). Superresolution Full-polarimetric Imaging for Radio Interferometry with Sparse Modeling. , 153(4):159.
- Akiyama, K. and Matthews, L. D. (2019). Exploring regularized maximum likelihood reconstruction for stellar imaging with the ngvla.
- Alexander, R. D., Clarke, C. J., and Pringle, J. E. (2006). Photoevaporation of protoplanetary discs – ii. evolutionary models and observable properties. *Monthly Notices of the Royal Astronomical Society*, 369(1):229–239.
- ALMA Partnership, T., Brogan, C. L., Pérez, L. M., Hunter, T. R., Dent, W. R. F., Hales, A. S., Hills, R. E., Corder, S. A., Fomalont, E. B., Vlahakis, C., Asaki, Y., Barkats, D., Hirota, A., Hodge, J. A., Impellizzeri, C. M. V., Kneissl, R., Liuzzo, E., Lucas, R., Marcelino, N., Matsushita, S., Nakanishi, K., Phillips, N., Richards, A. M. S., Toledo, I., Aladro, R., Brogiere, D., Cortes, J. R., Cortes, P. C., Espada, D., Galarza, F., Garcia-Appadoo, D., Guzman-Ramirez, L., Humphreys, E. M. L., Jung, T., Kamenno, S., Laing, R. A., Leon, S., Marconi, G., Mignano, A., Nikolic, B., Nyman, L.-A., Radiszcz, M., Remijan, A., Rodón, J. A., Sawada, T., Takahashi, S., Tilanus, R. P. J., Vila Vilaro, B., Watson, L. C., Wiklind, T., Akiyama, E., Chapillon, E., De Gregorio-Monsalvo, I., Di Francesco, J., Gueth, F., Kawamura, A., Lee, C.-F., Luong, Q. N., Mangum, J., Pietu, V., Sanhueza, P., Saigo, K., Takakuwa, S., Ubach, C., van Kempen, T. A., Wootten, A., Castro-Carrizo, A., Francke, H., Gallardo, J., Garcia, J., Gonzalez, S., Hill, T., Kaminski, T., Kurono, Y., Liu, H.-Y., Lopez, C., Morales, F., Plarre, K., Schieven, G., Testi, L., Videla, L., Villard, E., Andreani, P., Hibbard, J. E., and Tatematsu, K. (2015). The 2014 ALMA Long Baseline Campaign: First Results From High Angular Resolution Observations Toward the HL Tau Region. *The Astrophysical Journal Letters*, 808(1):L3.
- Andrews, S. M., Elder, W., Zhang, S., Huang, J., Benisty, M., Kurtovic, N. T., Wilner, D. J., Zhu, Z., Carpenter, J. M., Pérez, L. M., Teague, R., Isella, A., and Ricci, L. (2021). Limits

- on Millimeter Continuum Emission from Circumplanetary Material in the DSHARP Disks. *arXiv e-prints*, page arXiv:2105.08821.
- Andrews, S. M., Huang, J., Pérez, L. M., Isella, A., Dullemond, C. P., Kurtovic, N. T., Guzmán, V. V., Carpenter, J. M., Wilner, D. J., Zhang, S., Zhu, Z., Birnstiel, T., Bai, X.-N., Benisty, M., Hughes, A. M., Öberg, K. I., and Ricci, L. (2018). The Disk Substructures at High Angular Resolution Project (DSHARP). I. Motivation, Sample, Calibration, and Overview. , 869:L41.
- Andrews, S. M. and Williams, J. P. (2005). Circumstellar Dust Disks in Taurus-Auriga: The Submillimeter Perspective. *The Astrophysical Journal*, 631:1134.
- Andrews, S. M., Wilner, D. J., Zhu, Z., Birnstiel, T., Carpenter, J. M., Pérez, L. M., Bai, X.-N., Öberg, K. I., Hughes, A. M., Isella, A., and Ricci, L. (2016). RINGED SUBSTRUCTURE AND A GAP AT 1 au IN THE NEAREST PROTOPLANETARY DISK. *The Astrophysical Journal*, 820(2):L40.
- Armitage, P. J. (2007). Lecture notes on the formation and early evolution of planetary systems. *arXiv*, pages astro-ph/0701485.
- Armitage, P. J. (2015). Physical processes in protoplanetary disks. *ArXiv e-prints*.
- Armitage, P. J. (2018). *A Brief Overview of Planet Formation*, page 135.
- Armitage, P. J., Livio, M., Lubow, S. H., and Pringle, J. E. (2002). Predictions for the frequency and orbital radii of massive extrasolar planets. *Monthly Notices of the Royal Astronomical Society*, 334:248–256.
- Arras, P., Frank, P., Leike, R., Westermann, R., and Enßlin, T. A. (2019). Unified radio interferometric calibration and imaging with joint uncertainty quantification. , 627:A134.
- Arras, P., Knollmüller, J., Junklewitz, H., and Enßlin, T. A. (2018). Radio Imaging With Information Field Theory. *arXiv e-prints*, page arXiv:1803.02174.
- Ataiee, S., Pinilla, P., Zsom, A., Dullemond, C. P., Dominik, C., and Ghanbari, J. (2013). Asymmetric transition disks: Vorticity or eccentricity? , 553:L3.
- Baddour, N. and Chouinard, U. (2015). Theory and operational rules for the discrete Hankel transform. *Journal of the Optical Society of America A*, 32:611.
- Bae, J. and Zhu, Z. (2018). Planet-driven Spiral Arms in Protoplanetary Disks. I. Formation Mechanism. , 859(2):118.
- Bae, J., Zhu, Z., and Hartmann, L. (2017). On the Formation of Multiple Concentric Rings and Gaps in Protoplanetary Disks. , 850:201.
- Bai, X.-N. and Stone, J. M. (2014). MAGNETIC FLUX CONCENTRATION AND ZONAL FLOWS IN MAGNETOROTATIONAL INSTABILITY TURBULENCE. *The Astrophysical Journal*, 796(1):31.
- Bai, X.-N., Ye, J., Goodman, J., and Yuan, F. (2016). Magneto-thermal Disk Winds from Protoplanetary Disks. , 818(2):152.

- Bailer-Jones, C. A. L., Rybizki, J., Fouesneau, M., Mantelet, G., and Andrae, R. (2018). Estimating Distance from Parallaxes. IV. Distances to 1.33 Billion Stars in Gaia Data Release 2. , 156(2):58.
- Barclay, T., Pepper, J., and Quintana, E. V. (2018). A Revised Exoplanet Yield from the Transiting Exoplanet Survey Satellite (TESS). , 239(1):2.
- Baruteau, C., Crida, A., Paardekooper, S.-J., Masset, F. S., Guilet, J., Bitsch, B., Nelson, R. P., Kley, W., and Papaloizou, J. C. B. (2014). Planet-Disc Interactions and Early Evolution of Planetary Systems. In *Protostars and Planets VI*, page 24.
- Bate, M. R. (2011). Collapse of a molecular cloud core to stellar densities: the formation and evolution of pre-stellar discs. , 417(3):2036–2056.
- Benisty, M., Bae, J., Facchini, S., Keppler, M., Teague, R., Isella, A., Kurtovic, N. T., Pérez, L. M., Sierra, A., Andrews, S. M., Carpenter, J., Czekala, I., Dominik, C., Henning, T., Menard, F., Pinilla, P., and Zurlo, A. (2021). A circumplanetary disk around PDS70c. *The Astrophysical Journal Letters*, 916(1):L2.
- Birnstiel, T., Dullemond, C. P., and Brauer, F. (2010). Gas- and dust evolution in protoplanetary disks. , 513:A79.
- Booth, R. A. and Ilee, J. D. (2019). Planet-forming material in a protoplanetary disc: the interplay between chemical evolution and pebble drift. .
- Bracewell, R. N. (2000). *The Fourier transform and its applications*.
- Brandl, B. R., Lenzen, R., Pantin, E., Glasse, A., Blommaert, J., Venema, L., Molster, F., Siebenmorgen, R., Boehnhardt, H., and van Dishoeck, E. (2008). METIS: the Mid-infrared E-ELT Imager and Spectrograph. In *Ground-based and Airborne Instrumentation for Astronomy II*, volume 7014 of *Society of Photo-Optical Instrumentation Engineers (SPIE) Conference Series*, page 70141N.
- Casassus, S., Cabrera, G. F., Förster, F., Pearson, T. J., Readhead, A. C. S., and Dickinson, C. (2006). Morphological Analysis of the Centimeter-Wave Continuum in the Dark Cloud LDN 1622. , 639(2):951–964.
- Casassus, S., Christiaens, V., Carcamo, M., Perez, S., Weber, P., Ercolano, B., van der Marel, N., Pinte, C., Dong, R., Baruteau, C., Cieza, L., van Dishoeck, E., Price, D., Absil, O., Arce-Tord, C., Faramaz, V., Flores, C., and Reggiani, M. (2021). A dusty filament and turbulent CO spirals in HD135344B - SAO206462. *arXiv e-prints*, page arXiv:2104.08379.
- Casassus, S., van der Plas, G. M., Perez, S., Dent, W. R. F., Fomalont, E., Hagelberg, J., Hales, A., Jordán, A., Mawet, D., Ménard, F., Wootten, A., Wilner, D., Hughes, A. M., Schreiber, M. R., Girard, J. H., Ercolano, B., Canovas, H., Román, P. E., and Salinas, V. (2013). Flows of gas through a protoplanetary gap. , 493(7431):191–194.
- Chael, A. A., Johnson, M. D., Narayan, R., Doeleman, S. S., Wardle, J. F. C., and Bouman, K. L. (2016). High-resolution Linear Polarimetric Imaging for the Event Horizon Telescope. , 829(1):11.

- Chael, A. A., Johnson, M. D., Narayan, R., Doeleman, S. S., Wardle, J. F. C., and Bouman, K. L. (2016). HIGH-RESOLUTION LINEAR POLARIMETRIC IMAGING FOR THE EVENT HORIZON TELESCOPE. *The Astrophysical Journal*, 829(1):11.
- Chatterjee, S., Ford, E. B., Matsumura, S., and Rasio, F. A. (2008). Dynamical Outcomes of Planet-Planet Scattering. , 686:580–602.
- Cieza, L. A., González-Ruilova, C., Hales, A. S., Pinilla, P., Ruíz-Rodríguez, D., Zurlo, A., Casassus, S., Pérez, S., Cánovas, H., Arce-Tord, C., Flock, M., Kurtovic, N., Marino, S., Nogueira, P. H., Perez, L., Price, D. J., Principe, D. A., and Williams, J. P. (2021). The Ophiuchus Disc Survey Employing ALMA (ODISEA) - III. The evolution of substructures in massive discs at 3-5 au resolution. , 501(2):2934–2953.
- Cieza, L. A., Ruíz-Rodríguez, D., Hales, A., Casassus, S., Pérez, S., Gonzalez-Ruilova, C., Cánovas, H., Williams, J. P., Zurlo, A., Ansdell, M., Avenhaus, H., Bayo, A., Bertrang, G. H. M., Christiaens, V., Dent, W., Ferrero, G., Gamen, R., Olofsson, J., Orcajo, S., Peña Ramírez, K., Principe, D., Schreiber, M. R., and van der Plas, G. (2019). The Ophiuchus Disc Survey Employing ALMA (ODISEA) - I: project description and continuum images at 28 au resolution. , 482(1):698–714.
- Clark, B. G. (1980). An efficient implementation of the algorithm 'CLEAN'. , 89:377.
- Clark, B. G. (1999). Coherence in Radio Astronomy. In Taylor, G. B., Carilli, C. L., and Perley, R. A., editors, *Synthesis Imaging in Radio Astronomy II*, volume 180 of *Astronomical Society of the Pacific Conference Series*, page 1.
- Clarke, C. J., Gendrin, A., and Sotomayor, M. (2001). The dispersal of circumstellar discs: the role of the ultraviolet switch. *Monthly Notices of the Royal Astronomical Society*, 328:485–491.
- Clarke, C. J. and Pringle, J. E. (1988). The diffusion of contaminant through an accretion disc. , 235:365–373.
- Clarke, C. J., Tazzari, M., Juhasz, A., Rosotti, G., Booth, R., Facchini, S., Ilee, J. D., Johns-Krull, C. M., Kama, M., Meru, F., and Prato, L. (2018a). High-resolution Millimeter Imaging of the CI Tau Protoplanetary Disk: A Massive Ensemble of Protoplanets from 0.1 to 100 au. , 866:L6.
- Clarke, C. J., Tazzari, M., Juhasz, A., Rosotti, G., Booth, R., Facchini, S., Ilee, J. D., Johns-Krull, C. M., Kama, M., Meru, F., and Prato, L. (2018b). High-resolution Millimeter Imaging of the CI Tau Protoplanetary Disk: A Massive Ensemble of Protoplanets from 0.1 to 100 au. , 866(1):L6.
- Cornwell, T., Braun, R., and Briggs, D. S. (1999). Deconvolution. In Taylor, G. B., Carilli, C. L., and Perley, R. A., editors, *Synthesis Imaging in Radio Astronomy II*, volume 180 of *Astronomical Society of the Pacific Conference Series*, page 151.
- Cornwell, T. J. (2008). Multiscale CLEAN Deconvolution of Radio Synthesis Images. *IEEE Journal of Selected Topics in Signal Processing*, 2(5):793–801.
- Cornwell, T. J. and Evans, K. F. (1985). A simple maximum entropy deconvolution algorithm. , 143:77–83.

- Cui, C. and Bai, X.-N. (2021). Global Three-Dimensional Simulations of Outer Protoplanetary Disks with Ambipolar Diffusion. *arXiv e-prints*, page arXiv:2106.10167.
- Czekala, I., Zawadzki, B., Loomis, R., Grzybowski, H., Frazier, R., and Quinn, T. (2021). Mpol-dev/mpol: v0.1.1 release.
- de Juan Ovelar, M., Min, M., Dominik, C., Thalmann, C., Pinilla, P., Benisty, M., and Birnstiel, T. (2013). Imaging diagnostics for transitional discs. , 560:A111.
- Dipierro, G., Pinilla, P., Lodato, G., and Testi, L. (2015). Dust trapping by spiral arms in gravitationally unstable protostellar discs. , 451(1):974–986.
- Dong, R., Li, S., Chiang, E., and Li, H. (2017). Multiple Disk Gaps and Rings Generated by a Single Super-Earth. , 843(2):127.
- Dong, R., Liu, S.-y., Eisner, J., Andrews, S., Fung, J., Zhu, Z., Chiang, E., Hashimoto, J., Liu, H. B., Casassus, S., Esposito, T., Hasegawa, Y., Muto, T., Pavlyuchenkov, Y., Wilner, D., Akiyama, E., Tamura, M., and Wisniewski, J. (2018). The Eccentric Cavity, Triple Rings, Two-armed Spirals, and Double Clumps of the MWC 758 Disk. , 860(2):124.
- Dong, R., Najita, J. R., and Brittain, S. (2018). Spiral arms in disks: Planets or gravitational instability? *The Astrophysical Journal*, 862(2):103.
- Duffell, P. C. and MacFadyen, A. I. (2013). Gap Opening by Extremely Low-mass Planets in a Viscous Disk. , 769(1):41.
- Dullemond, C. P., Birnstiel, T., Huang, J., Kurtovic, N. T., Andrews, S. M., Guzmán, V. V., Pérez, L. M., Isella, A., Zhu, Z., Benisty, M., Wilner, D. J., Bai, X.-N., Carpenter, J. M., Zhang, S., and Ricci, L. (2018). The Disk Substructures at High Angular Resolution Project (DSHARP). VI. Dust Trapping in Thin-ringed Protoplanetary Disks. , 869:L46.
- Dutrey, A., Semenov, D., Chapillon, E., Gorti, U., Guilloteau, S., Hersant, F., Hogerheijde, M., Hughes, M., Meeus, G., and Nomura, H. (2014). Physical and Chemical Structure of Planet-Forming Disks Probed by Millimeter Observations and Modeling. In Beuther, H., Klessen, R. S., Dullemond, C. P., and Henning, T., editors, *Protostars and Planets VI*, page 317.
- Enßlin, T. A. and Frommert, M. (2011). Reconstruction of signals with unknown spectra in information field theory with parameter uncertainty. , 83(10):105014.
- Ercolano, B., Clarke, C. J., and Drake, J. J. (2009). X-RAY IRRADIATED PROTOPLANETARY DISK ATMOSPHERES. II. PREDICTIONS FROM MODELS IN HYDROSTATIC EQUILIBRIUM. *The Astrophysical Journal*, 699(2):1639–1649.
- Españolat, C., Muzerolle, J., Najita, J., Andrews, S., Zhu, Z., Calvet, N., Kraus, S., Hashimoto, J., Kraus, A., and D’Alessio, P. (2014). An Observational Perspective of Transitional Disks. In Beuther, H., Klessen, R. S., Dullemond, C. P., and Henning, T., editors, *Protostars and Planets VI*, page 497.

- Event Horizon Telescope Collaboration, Akiyama, K., Alberdi, A., Alef, W., Asada, K., Azulay, R., Baczko, A.-K., Ball, D., Baloković, M., Barrett, J., Bintley, D., Blackburn, L., Boland, W., Bouman, K. L., Bower, G. C., Bremer, M., Brinkerink, C. D., Brissenden, R., Britzen, S., Broderick, A. E., Brogiere, D., Bronzwaer, T., Byun, D.-Y., Carlstrom, J. E., Chael, A., Chan, C.-k., Chatterjee, S., Chatterjee, K., Chen, M.-T., Chen, Y., Cho, I., Christian, P., Conway, J. E., Cordes, J. M., Crew, G. B., Cui, Y., Davelaar, J., De Laurentis, M., Deane, R., Dempsey, J., Desvignes, G., Dexter, J., Doeleman, S. S., Eatough, R. P., Falcke, H., Fish, V. L., Fomalont, E., Fraga-Encinas, R., Freeman, W. T., Friberg, P., Fromm, C. M., Gómez, J. L., Galison, P., Gammie, C. F., García, R., Gentaz, O., Georgiev, B., Goddi, C., Gold, R., Gu, M., Gurwell, M., Hada, K., Hecht, M. H., Hesper, R., Ho, L. C., Ho, P., Honma, M., Huang, C.-W. L., Huang, L., Hughes, D. H., Ikeda, S., Inoue, M., Issaoun, S., James, D. J., Jannuzi, B. T., Janssen, M., Jeter, B., Jiang, W., Johnson, M. D., Jorstad, S., Jung, T., Karami, M., Karuppusamy, R., Kawashima, T., Keating, G. K., Kettenis, M., Kim, J.-Y., Kim, J., Kim, J., Kino, M., Koay, J. Y., Koch, P. M., Koyama, S., Kramer, M., Kramer, C., Krichbaum, T. P., Kuo, C.-Y., Lauer, T. R., Lee, S.-S., Li, Y.-R., Li, Z., Lindqvist, M., Liu, K., Liuzzo, E., Lo, W.-P., Lobanov, A. P., Loinard, L., Lonsdale, C., Lu, R.-S., MacDonald, N. R., Mao, J., Markoff, S., Marrone, D. P., Marscher, A. P., Martí-Vidal, I., Matsushita, S., Matthews, L. D., Medeiros, L., Menten, K. M., Mizuno, Y., Mizuno, I., Moran, J. M., Moriyama, K., Moscibrodzka, M., Müller, C., Nagai, H., Nagar, N. M., Nakamura, M., Narayan, R., Narayanan, G., Natarajan, I., Neri, R., Ni, C., Noutsos, A., Okino, H., Olivares, H., Oyama, T., Özel, F., Palumbo, D. C. M., Patel, N., Pen, U.-L., Pesce, D. W., Piétu, V., Plambeck, R., PopStefanija, A. a., Porth, O., Prather, B., Preciado-López, J. A., Psaltis, D., Pu, H.-Y., Ramakrishnan, V., Rao, R., Rawlings, M. G., Raymond, A. W., Rezzolla, L., Ripperda, B., Roelofs, F., Rogers, A., Ros, E., Rose, M., Roshanineshat, A., Rottmann, H., Roy, A. L., Ruszczyk, C., Ryan, B. R., Rygl, K. L. J., Sánchez, S., Sánchez-Arguelles, D., Sasada, M., Savolainen, T., Schloerb, F. P., Schuster, K.-F., Shao, L., Shen, Z., Small, D., Sohn, B. W., SooHoo, J., Tazaki, F., Tiede, P., Tilanus, R. P. J., Titus, M., Toma, K., Torne, P., Trent, T., Trippe, S., Tsuda, S., van Bemmell, I., van Langevelde, H. J., van Rossum, D. R., Wagner, J., Wardle, J., Weintroub, J., Wex, N., Wharton, R., Wielgus, M., Wong, G. N., Wu, Q., Young, A., Young, K., Younsi, Z., Yuan, F., Yuan, Y.-F., Zensus, J. A., Zhao, G., Zhao, S.-S., Zhu, Z., Farah, J. R., Meyer-Zhao, Z., Michalik, D., Nadolski, A., Nishioka, H., Pradel, N., Primiani, R. A., Souccar, K., Vertatschitsch, L., and Yamaguchi, P. (2019). First M87 Event Horizon Telescope Results. IV. Imaging the Central Supermassive Black Hole. , 875(1):L4.
- Fedele, D., Carney, M., Hogerheijde, M. R., Walsh, C., Miotello, A., Klaassen, P., Bruderer, S., Henning, T., and van Dishoeck, E. F. (2017). ALMA unveils rings and gaps in the protoplanetary system <ASTROBJ>HD 169142</ASTROBJ>: signatures of two giant protoplanets. , 600:A72.
- Fedele, D., Tazzari, M., Booth, R., Testi, L., Clarke, C. J., Pascucci, I., Kospal, A., Semenov, D., Bruderer, S., Henning, T., and Teague, R. (2018). ALMA continuum observations of the protoplanetary disk AS 209. Evidence of multiple gaps opened by a single planet. , 610:A24.
- Fernandes, R. B., Mulders, G. D., Pascucci, I., Mordasini, C., and Emsenhuber, A. (2019). Hints for a Turnover at the Snow Line in the Giant Planet Occurrence Rate. , 874:81.

- Flaherty, K. M., Muzerolle, J., Rieke, G., Gutermuth, R., Balog, Z., Herbst, W., and Megeath, S. T. (2013). Kinks and Dents in Protoplanetary Disks: Rapid Infrared Variability as Evidence for Large Structural Perturbations. , 145:66.
- Flock, M., Nelson, R. P., Turner, N. J., Bertrang, G. H.-M., Carrasco-González, C., Henning, T., Lyra, W., and Teague, R. (2017). Radiation Hydrodynamical Turbulence in Protoplanetary Disks: Numerical Models and Observational Constraints. , 850:131.
- Flock, M., Ruge, J. P., Dzyurkevich, N., Henning, T., Klahr, H., and Wolf, S. (2015). Gaps, rings, and non-axisymmetric structures in protoplanetary disks. From simulations to ALMA observations. , 574:A68.
- Foreman-Mackey, D. (2016). corner.py: Scatterplot matrices in python. *The Journal of Open Source Software*, 1(2):24.
- Foreman-Mackey, D., Hogg, D. W., Lang, D., and Goodman, J. (2013). emcee: The mcmc hammer. *PASP*, 125:306–312.
- Francis, L. and van der Marel, N. (2020). Dust-depleted Inner Disks in a Large Sample of Transition Disks through Long-baseline ALMA Observations. , 892(2):111.
- Ginzburg, S., Schlichting, H. E., and Sari, R. (2018). Core-powered mass-loss and the radius distribution of small exoplanets. , 476:759–765.
- Goldreich, P. and Tremaine, S. (1979). The excitation of density waves at the Lindblad and corotation resonances by an external potential. , 233:857–871.
- Greiner, M., Vacca, V., Junklewitz, H., and Enßlin, T. A. (2016). fastRESOLVE: fast Bayesian imaging for aperture synthesis in radio astronomy. *arXiv e-prints*, page arXiv:1605.04317.
- Gull, S. F. and Daniell, G. J. (1978). Image reconstruction from incomplete and noisy data. , 272(5655):686–690.
- Guzmán, V. V., Huang, J., Andrews, S. M., Isella, A., Pérez, L. M., Carpenter, J. M., Dullemond, C. P., Ricci, L., Birnstiel, T., Zhang, S., Zhu, Z., Bai, X.-N., Benisty, M., Öberg, K. I., and Wilner, D. J. (2018). The Disk Substructures at High Angular Resolution Program (DSHARP). VIII. The Rich Ringed Substructures in the AS 209 Disk. , 869:L48.
- Haffert, S. Y., Bohn, A. J., de Boer, J., Snellen, I. A. G., Brinchmann, J., Girard, J. H., Keller, C. U., and Bacon, R. (2019). Two accreting protoplanets around the young star PDS 70. *Nature Astronomy*, page 329.
- Haisch, K. E. J., Lada, E. A., and Lada, C. J. (2001). Disk Frequencies and Lifetimes in Young Clusters. *The Astrophysical Journal Letters*, 553(2):L153–L156.
- Hall, C., Rice, K., Dipierro, G., Forgan, D., Harries, T., and Alexander, R. (2018). Is the spiral morphology of the Elias 2-27 circumstellar disc due to gravitational instability? , 477(1):1004–1014.
- Hallam, P. D. and Paardekooper, S. J. (2020). Constraining the masses of planets in protoplanetary discs from the presence or absence of vortices - comparison with ALMA observations. , 491(4):5759–5770.

- Hartmann, L., Calvet, N., Gullbring, E., and D'Alessio, P. (1998). Accretion and the Evolution of T Tauri Disks. *Astrophysical Journal* v.495, 495:385–400.
- Hashimoto, J., Muto, T., Dong, R., Liu, H. B., van der Marel, N., Francis, L., Hasegawa, Y., and Tsukagoshi, T. (2021). ALMA Observations of the Asymmetric Dust Disk around DM Tau. , 911(1):5.
- Högbom, J. A. (1974). Aperture Synthesis with a Non-Regular Distribution of Interferometer Baselines. , 15:417.
- Honma, M., Akiyama, K., Uemura, M., and Ikeda, S. (2014). Super-resolution imaging with radio interferometry using sparse modeling. *Publications of the Astronomical Society of Japan*, 66(5). 95.
- Hu, X., Zhu, Z., Okuzumi, S., Bai, X.-N., Wang, L., Tomida, K., and Stone, J. M. (2019). Nonideal MHD Simulation of HL Tau Disk: Formation of Rings. , 885(1):36.
- Huang, J., Andrews, S. M., Dullemond, C. P., Isella, A., Pérez, L. M., Guzmán, V. V., Öberg, K. I., Zhu, Z., Zhang, S., Bai, X.-N., Benisty, M., Birnstiel, T., Carpenter, J. M., Hughes, A. M., Ricci, L., Weaver, E., and Wilner, D. J. (2018a). The Disk Substructures at High Angular Resolution Project (DSHARP). II. Characteristics of Annular Substructures. , 869(2):L42.
- Huang, J., Andrews, S. M., Dullemond, C. P., Öberg, K. I., Qi, C., Zhu, Z., Birnstiel, T., Carpenter, J. M., Isella, A., Macías, E., McClure, M. K., Pérez, L. M., Teague, R., Wilner, D. J., and Zhang, S. (2020). A Multifrequency ALMA Characterization of Substructures in the GM Aur Protoplanetary Disk. , 891(1):48.
- Huang, J., Andrews, S. M., Pérez, L. M., Zhu, Z., Dullemond, C. P., Isella, A., Benisty, M., Bai, X.-N., Birnstiel, T., Carpenter, J. M., Guzmán, V. V., Hughes, A. M., Öberg, K. I., Ricci, L., Wilner, D. J., and Zhang, S. (2018b). The Disk Substructures at High Angular Resolution Project (DSHARP). III. Spiral Structures in the Millimeter Continuum of the Elias 27, IM Lup, and WaOph 6 Disks. , 869(2):L43.
- Ingleby, L., Calvet, N., Bergin, E., Yerasi, A., Espaillat, C., Herczeg, G., Roueff, E., Abgrall, H., Hernández, J., Briceño, C., Pascucci, I., Miller, J., Fogel, J., Hartmann, L., Meyer, M., Carpenter, J., Crockett, N., and McClure, M. (2009). Far-Ultraviolet H₂ Emission from Circumstellar Disks. *The Astrophysical Journal Letters*, 703:L137–L141.
- Isella, A., Huang, J., Andrews, S. M., Dullemond, C. P., Birnstiel, T., Zhang, S., Zhu, Z., Guzmán, V. V., Pérez, L. M., Bai, X.-N., Benisty, M., Carpenter, J. M., Ricci, L., and Wilner, D. J. (2018). The Disk Substructures at High Angular Resolution Project (DSHARP). IX. A High-definition Study of the HD 163296 Planet-forming Disk. , 869(2):L49.
- Jennings, J., Booth, R. A., Tazzari, M., Clarke, C. J., and Rosotti, G. P. (2021). A super-resolution analysis of the DSHARP survey: Substructure is common in the inner 30 au. *arXiv e-prints*, page arXiv:2103.02392.
- Jennings, J., Booth, R. A., Tazzari, M., Rosotti, G. P., and Clarke, C. J. (2020). frankenstein: protoplanetary disc brightness profile reconstruction at sub-beam resolution with a rapid Gaussian process. , 495(3):3209–3232.

- Johansen, A., Youdin, A., and Klahr, H. (2009). ZONAL FLOWS AND LONG-LIVED AXISYMMETRIC PRESSURE BUMPS IN MAGNETOROTATIONAL TURBULENCE. *The Astrophysical Journal*, 697(2):1269–1289.
- Johnson, M. D., Bouman, K. L., Blackburn, L., Chael, A. A., Rosen, J., Shiokawa, H., Roelofs, F., Akiyama, K., Fish, V. L., and Doeleman, S. S. (2017). Dynamical imaging with interferometry. *The Astrophysical Journal*, 850(2):172.
- Jorquera, S., Pérez, L. M., Chauvin, G., Benisty, M., Zhu, Z., Isella, A., Huang, J., Ricci, L., Andrews, S. M., Zhang, S., Carpenter, J., Kurtovic, N. T., and Birnstiel, T. (2020). A search for companions via direct imaging in the DSHARP planet-forming disks. *arXiv e-prints*, page arXiv:2012.10464.
- Junklewitz, H., Bell, M. R., and Enßlin, T. (2015). A new approach to multifrequency synthesis in radio interferometry. , 581:A59.
- Junklewitz, H., Bell, M. R., Selig, M., and Enßlin, T. A. (2016). RESOLVE: A new algorithm for aperture synthesis imaging of extended emission in radio astronomy. , 586:A76.
- Keppler, M., Benisty, M., Müller, A., Henning, T., van Boekel, R., Cantalloube, F., Ginski, C., van Holstein, R. G., Maire, A.-L., Pohl, A., Samland, M., Avenhaus, H., Baudino, J.-L., Boccaletti, A., de Boer, J., Bonnefoy, M., Chauvin, G., Desidera, S., Langlois, M., Lazzoni, C., Marleau, G.-D., Mordasini, C., Pawellek, N., Stolker, T., Vigan, A., Zurlo, A., Birnstiel, T., Brandner, W., Feldt, M., Flock, M., Girard, J., Gratton, R., Hagelberg, J., Isella, A., Janson, M., Juhasz, A., Kemmer, J., Kral, Q., Lagrange, A.-M., Launhardt, R., Matter, A., Ménard, F., Milli, J., Mollière, P., Olofsson, J., Pérez, L., Pinilla, P., Pinte, C., Quanz, S. P., Schmidt, T., Udry, S., Wahhaj, Z., Williams, J. P., Buenzli, E., Cudel, M., Dominik, C., Galicher, R., Kasper, M., Lannier, J., Mesa, D., Mouillet, D., Peretti, S., Perrot, C., Salter, G., Sissa, E., Wildi, F., Abe, L., Antichi, J., Augereau, J.-C., Baruffolo, A., Baudoz, P., Bazzon, A., Beuzit, J.-L., Blanchard, P., Brems, S. S., Buey, T., De Caprio, V., Carbillet, M., Carle, M., Cascone, E., Cheetham, A., Claudi, R., Costille, A., Delboulbé, A., Dohlen, K., Fantinel, D., Feautrier, P., Fusco, T., Giro, E., Gluck, L., Gry, C., Hubin, N., Hugot, E., Jaquet, M., Le Mignant, D., Llored, M., Madec, F., Magnard, Y., Martinez, P., Maurel, D., Meyer, M., Möller-Nilsson, O., Moulin, T., Mugnier, L., Origné, A., Pavlov, A., Perret, D., Petit, C., Pragt, J., Puget, P., Rabou, P., Ramos, J., Rigal, F., Rochat, S., Roelfsema, R., Rousset, G., Roux, A., Salasnich, B., Sauvage, J.-F., Sevin, A., Soenke, C., Stadler, E., Suarez, M., Turatto, M., and Weber, L. (2018). Discovery of a planetary-mass companion within the gap of the transition disk around PDS 70. , 617:A44.
- Keppler, M., Teague, R., Bae, J., Benisty, M., Henning, T., van Boekel, R., Chapillon, E., Pinilla, P., Williams, J. P., Bertrang, G. H.-M., and et al. (2019). Highly structured disk around the planet host pds 70 revealed by high-angular resolution observations with alma. *Astronomy Astrophysics*, 625:A118.
- Kley, W. and Nelson, R. P. (2012). Planet-Disk Interaction and Orbital Evolution. *Annual Review of Astronomy and Astrophysics*, 50(1):211–249.
- Kley, W. and Nelson, R. P. (2012). Planet-Disk Interaction and Orbital Evolution. , 50:211–249.

- Kudo, T., Hashimoto, J., Muto, T., Liu, H. B., Dong, R., Hasegawa, Y., Tsukagoshi, T., and Konishi, M. (2018). A Spatially Resolved au-scale Inner Disk around DM Tau. , 868:L5.
- Kuramochi, K., Akiyama, K., Ikeda, S., Tazaki, F., Fish, V. L., Pu, H.-Y., Asada, K., and Honma, M. (2018). Superresolution Interferometric Imaging with Sparse Modeling Using Total Squared Variation: Application to Imaging the Black Hole Shadow. , 858(1):56.
- Kurtovic, N. T., Pérez, L. M., Benisty, M., Zhu, Z., Zhang, S., Huang, J., Andrews, S. M., Dullemond, C. P., Isella, A., Bai, X.-N., Carpenter, J. M., Guzmán, V. V., Ricci, L., and Wilner, D. J. (2018). The Disk Substructures at High Angular Resolution Project (DSHARP). IV. Characterizing Substructures and Interactions in Disks around Multiple Star Systems. , 869(2):L44.
- Kurtovic, N. T., Pinilla, P., Long, F., Benisty, M., Manara, C. F., Natta, A., Pascucci, I., Ricci, L., Scholz, A., and Testi, L. (2021). Size and structures of disks around very low mass stars in the Taurus star-forming region. , 645:A139.
- Lin, D. N. C. and Papaloizou, J. (1986). On the Tidal Interaction between Protoplanets and the Protoplanetary Disk. III. Orbital Migration of Protoplanets. , 309:846.
- Lin, D. N. C. and Papaloizou, J. C. B. (1986). On the tidal interaction between protoplanets and the protoplanetary disk. III. Orbital migration of protoplanets. *The Astrophysical Journal*, 309:846–857.
- Lodato, G., Dipierro, G., Ragusa, E., Long, F., Herczeg, G. J., Pascucci, I., Pinilla, P., Manara, C. F., Tazzari, M., Liu, Y., Mulders, G. D., Harsono, D., Boehler, Y., Ménard, F., Johnstone, D., Salyk, C., van der Plas, G., Cabrit, S., Edwards, S., Fischer, W. J., Hendler, N., Nisini, B., Rigliaco, E., Avenhaus, H., Banzatti, A., and Gully-Santiago, M. (2019). The newborn planet population emerging from ring-like structures in discs. , 486:453–461.
- Long, F., Herczeg, G. J., Harsono, D., Pinilla, P., Tazzari, M., Manara, C. F., Pascucci, I., Cabrit, S., Nisini, B., Johnstone, D., Edwards, S., Salyk, C., Menard, F., Lodato, G., Boehler, Y., Mace, G. N., Liu, Y., Mulders, G. D., Hendler, N., Ragusa, E., Fischer, W. J., Banzatti, A., Rigliaco, E., van de Plas, G., Dipierro, G., Gully-Santiago, M., and Lopez-Valdivia, R. (2019). Compact Disks in a High-resolution ALMA Survey of Dust Structures in the Taurus Molecular Cloud. , 882(1):49.
- Long, F., Pinilla, P., Herczeg, G. J., Harsono, D., Dipierro, G., Pascucci, I., Hendler, N., Tazzari, M., Ragusa, E., Salyk, C., Edwards, S., Lodato, G., van de Plas, G., Johnstone, D., Liu, Y., Boehler, Y., Cabrit, S., Manara, C. F., Menard, F., Mulders, G. D., Nisini, B., Fischer, W. J., Rigliaco, E., Banzatti, A., Avenhaus, H., and Gully-Santiago, M. (2018). Gaps and Rings in an ALMA Survey of Disks in the Taurus Star-forming Region. , 869:17.
- Longarini, C., Lodato, G., Toci, C., and Aly, H. (2021). Dynamical dust traps in misaligned circumbinary discs: analytical theory and numerical simulations. , 503(4):4930–4941.
- Lu, R.-S., Broderick, A. E., Baron, F., Monnier, J. D., Fish, V. L., Doeleman, S. S., and Pankratius, V. (2014). IMAGING THE SUPERMASSIVE BLACK HOLE SHADOW AND JET BASE OF m87 WITH THE EVENT HORIZON TELESCOPE. *The Astrophysical Journal*, 788(2):120.

- Lynden-Bell, D. and Pringle, J. E. (1974). The Evolution of Viscous Discs and the Origin of the Nebular Variables. *Monthly Notices of the Royal Astronomical Society*, 168:603–637.
- Macías, E., Espaillat, C. C., Ribas, Á., Schwarz, K. R., Anglada, G., Osorio, M., Carrasco-González, C., Gómez, J. F., and Robinson, C. (2018). Multiple Rings in the Transitional Disk of GM Aurigae Revealed by VLA and ALMA. , 865(1):37.
- Macías, E., Guerra-Alvarado, O., Carrasco-González, C., Ribas, Á., Espaillat, C. C., Huang, J., and Andrews, S. M. (2021). Characterizing the dust content of disk substructures in TW Hydrae. , 648:A33.
- Macintosh, B., Graham, J. R., Ingraham, P., Konopacky, Q., Marois, C., Perrin, M., Poyneer, L., Bauman, B., Barman, T., and Burrows, A. S. (2014). First light of the Gemini Planet Imager. *Proceedings of the National Academy of Science*, 111(35):12661–12666.
- Manara, C. F., Rosotti, G., Testi, L., Natta, A., Alcalá, J. M., Williams, J. P., Ansdell, M., Miotello, A., van der Marel, N., and Tazzari, M. (2016). Evidence for a correlation between mass accretion rates onto young stars and the mass of their protoplanetary disks. , 591:L3.
- Manger, N. and Klahr, H. (2018). Vortex formation and survival in protoplanetary discs subject to vertical shear instability. , 480(2):2125–2136.
- Marino, S., Perez, S., and Casassus, S. (2015). Shadows Cast by a Warp in the HD 142527 Protoplanetary Disk. , 798:L44.
- Meru, F., Juhász, A., Ilee, J. D., Clarke, C. J., Rosotti, G. P., and Booth, R. A. (2017). On the Origin of the Spiral Morphology in the Elias 2-27 Circumstellar Disk. , 839(2):L24.
- Meru, F., Rosotti, G. P., Booth, R. A., Nazari, P., and Clarke, C. J. (2018). Is the ring inside or outside the planet?: the effect of planet migration on dust rings. *Monthly Notices of the Royal Astronomical Society*, 482(3):3678–3695.
- Miranda, R. and Rafikov, R. R. (2019). On the planetary interpretation of multiple gaps and rings in protoplanetary disks seen by ALMA. *arXiv e-prints*.
- Morbidelli, A. and Raymond, S. N. (2016). Challenges in planet formation. *Journal of Geophysical Research (Planets)*, 121(10):1962–1980.
- Müller, A., Keppler, M., Henning, T., Samland, M., Chauvin, G., Beust, H., Maire, A. L., Molaverdikhani, K., van Boekel, R., and Benisty, M. (2018). Orbital and atmospheric characterization of the planet within the gap of the PDS 70 transition disk. , 617:L2.
- Nakazato, T., Ikeda, S., Akiyama, K., Kosugi, G., Yamaguchi, M., and Honma, M. (2019). A New Synthesis Imaging Tool for ALMA Based on Sparse Modeling. In Teuben, P. J., Pound, M. W., Thomas, B. A., and Warner, E. M., editors, *Astronomical Data Analysis Software and Systems XXVII*, volume 523 of *Astronomical Society of the Pacific Conference Series*, page 143.
- Narayan, R. and Nityananda, R. (1986). Maximum entropy image restoration in astronomy. , 24:127–170.

- Nazari, P., Booth, R. A., Clarke, C. J., Rosotti, G. P., Tazzari, M., Juhasz, A., and Meru, F. (2019). Revealing signatures of planets migrating in protoplanetary discs with ALMA multiwavelength observations. , 485(4):5914–5923.
- Nelson, R. P. (2018). *Planetary Migration in Protoplanetary Disks*, page 139.
- Norfolk, B. J., Maddison, S. T., Pinte, C., van der Marel, N., Booth, R. A., Francis, L., Gonzalez, J.-F., Ménard, F., Wright, C. M., van der Plas, G., and Garg, H. (2021). Dust traps and the formation of cavities in transition discs: a millimetre to sub-millimetre comparison survey. , 502(4):5779–5796.
- Öberg, K. I., Guzmán, V. V., Walsh, C., Aikawa, Y., Bergin, E. A., Law, C. J., Loomis, R. A., Alarcón, F., Andrews, S. M., Bae, J., Bergner, J. B., Boehler, Y., Booth, A. S., Bosman, A. D., Calahan, J. K., Cataldi, G., Cleeves, L. I., Czekala, I., Furuya, K., Huang, J., Ilee, J. D., Kurtovic, N. T., Le Gal, R., Liu, Y., Long, F., Ménard, F., Nomura, H., Pérez, L. M., Qi, C., Schwarz, K. R., Sierra, A., Teague, R., Tsukagoshi, T., Yamato, Y., van't Hoff, M. L. R., Waggoner, A. R., Wilner, D. J., and Zhang, K. (2021). Molecules with ALMA at Planet-forming Scales (MAPS). I. Program Overview and Highlights. , 257(1):1.
- Ogilvie, G. I. and Lin, D. N. C. (2004). Tidal Dissipation in Rotating Giant Planets. , 610:477–509.
- Okuzumi, S., Momose, M., Sirono, S.-i., Kobayashi, H., and Tanaka, H. (2016). Sintering-induced Dust Ring Formation in Protoplanetary Disks: Application to the HL Tau Disk. , 821(2):82.
- Oppermann, N., Selig, M., Bell, M. R., and Enßlin, T. A. (2013). Reconstruction of Gaussian and log-normal fields with spectral smoothness. , 87(3):032136.
- Owen, J. E. and Wu, Y. (2017). The Evaporation Valley in the Kepler Planets. , 847(1):29.
- Pérez, L. M., Benisty, M., Andrews, S. M., Isella, A., Dullemond, C. P., Huang, J., Kurtovic, N. T., Guzmán, V. V., Zhu, Z., Birnstiel, T., Zhang, S., Carpenter, J. M., Wilner, D. J., Ricci, L., Bai, X.-N., Weaver, E., and Öberg, K. I. (2018). The Disk Substructures at High Angular Resolution Project (DSHARP). X. Multiple Rings, a Misaligned Inner Disk, and a Bright Arc in the Disk around the T Tauri star HD 143006. , 869(2):L50.
- Pérez, L. M., Carpenter, J. M., Andrews, S. M., Ricci, L., Isella, A., Linz, H., Sargent, A. I., Wilner, D. J., Henning, T., Deller, A. T., Chandler, C. J., Dullemond, C. P., Lazio, J., Menten, K. M., Corder, S. A., Storm, S., Testi, L., Tazzari, M., Kwon, W., Calvet, N., Greaves, J. S., Harris, R. J., and Mundy, L. G. (2016). Spiral density waves in a young protoplanetary disk. *Science*, 353(6307):1519–1521.
- Pérez, S., Casassus, S., Baruteau, C., Dong, R., Hales, A., and Cieza, L. (2019a). Dust unveils the formation of a mini-Neptune planet in a protoplanetary ring. *arXiv e-prints*.
- Pérez, S., Casassus, S., Baruteau, C., Dong, R., Hales, A., and Cieza, L. (2019b). Dust unveils the formation of a mini-Neptune planet in a protoplanetary ring. *arXiv e-prints*.

- Perkins, S., Marais, P., Zwart, J., Natarajan, I., Tasse, C., and Smirnov, O. (2015). Montblanc1 <https://github.com/ska-sa/montblanc>.: Gpu accelerated radio interferometer measurement equations in support of bayesian inference for radio observations. *Astronomy and Computing*, 12:73 – 85.
- Petigura, E. A., Howard, A. W., Marcy, G. W., Johnson, J. A., Isaacson, H., Cargile, P. A., Hebb, L., Fulton, B. J., Weiss, L. M., and Morton, T. D. (2017). The California-Kepler Survey. I. High-resolution Spectroscopy of 1305 Stars Hosting Kepler Transiting Planets. , 154(3):107.
- Pfeil, T. and Klahr, H. (2020). The Sandwich Mode for Vertical Shear Instability in Protoplanetary Disks. *arXiv e-prints*, page arXiv:2008.11195.
- Pinilla, P., Birnstiel, T., Ricci, L., Dullemond, C. P., Uribe, A. L., Testi, L., and Natta, A. (2012). Trapping dust particles in the outer regions of protoplanetary disks. , 538:A114.
- Pinilla, P., Flock, M., Ovelar, M. d. J., and Birnstiel, T. (2016). Can dead zones create structures like a transition disk? , 596:A81.
- Pinilla, P., Kurtovic, N. T., Benisty, M., Manara, C. F., Natta, A., Sanchis, E., Tazzari, M., Stammler, S. M., Ricci, L., and Testi, L. (2021). A bright inner disk and structures in the transition disk around the very low-mass star CIDA 1. , 649:A122.
- Pinte, C., Price, D. J., Ménard, F., Duchêne, G., Christiaens, V., Andrews, S. M., Huang, J., Hill, T., van der Plas, G., Perez, L. M., Isella, A., Boehler, Y., Dent, W. R. F., Mentiplay, D., and Loomis, R. A. (2020). Nine Localized Deviations from Keplerian Rotation in the DSHARP Circumstellar Disks: Kinematic Evidence for Protoplanets Carving the Gaps. , 890(1):L9.
- Pinte, C., Price, D. J., Ménard, F., Duchêne, G., Dent, W. R. F., Hill, T., de Gregorio-Monsalvo, I., Hales, A., and Mentiplay, D. (2018). Kinematic evidence for an embedded protoplanet in a circumstellar disk. *The Astrophysical Journal*, 860(1):L13.
- Pinte, C., van der Plas, G., Ménard, F., Price, D. J., Christiaens, V., Hill, T., Mentiplay, D., Ginski, C., Choquet, E., Boehler, Y., Duchêne, G., Perez, S., and Casassus, S. (2019). Kinematic detection of a planet carving a gap in a protoplanetary disk. *Nature Astronomy*, page 419.
- Price, D. J., Cuello, N., Pinte, C., Mentiplay, D., Casassus, S., Christiaens, V., Kennedy, G. M., Cuadra, J., Sebastian Perez, M., Marino, S., Armitage, P. J., Zurlo, A., Juhasz, A., Ragusa, E., Laibe, G., and Lodato, G. (2018). Circumbinary, not transitional: on the spiral arms, cavity, shadows, fast radial flows, streamers, and horseshoe in the HD142527 disc. *Monthly Notices of the Royal Astronomical Society*, 477(1):1270–1284.
- Pringle, J. E. (1981). Accretion Discs in Astrophysics. *Annual Review of Astronomy and Astrophysics*, 19:137–162.
- Ragusa, E., Dipierro, G., Lodato, G., Laibe, G., and Price, D. J. (2017). On the origin of horseshoes in transitional discs. , 464(2):1449–1455.
- Ragusa, E., Rosotti, G., Teyssandier, J., Booth, R., Clarke, C. J., and Lodato, G. (2018). Eccentricity evolution during planet-disc interaction. , 474(4):4460–4476.

- Rasmussen, C. E. and Williams, C. K. I. (2006). *Gaussian Processes for Machine Learning*.
- Remijan, A., Biggs, A., Cortes, P., Dent, B., Di Francesco, J., Fomalont, E., Hales, A., Kamenno, S., Mason, B., Philips, N., Saini, K., Stoehr, F., Vila Vilaro, B., and Villard, E. (2019). *ALMA Doc. 7.3, ver. 1.0*.
- Ricci, L., Liu, S.-F., Isella, A., and Li, H. (2018). Investigating the Early Evolution of Planetary Systems with ALMA and the Next Generation Very Large Array. , 853(2):110.
- Ricker, G. R., Winn, J. N., Vanderspek, R., Latham, D. W., Bakos, G. Á., Bean, J. L., Berta-Thompson, Z. K., Brown, T. M., Buchhave, L., Butler, N. R., Butler, R. P., Chaplin, W. J., Charbonneau, D., Christensen-Dalsgaard, J., Clampin, M., Deming, D., Doty, J., De Lee, N., Dressing, C., Dunham, E. W., Endl, M., Fressin, F., Ge, J., Henning, T., Holman, M. J., Howard, A. W., Ida, S., Jenkins, J. M., Jernigan, G., Johnson, J. A., Kaltenegger, L., Kawai, N., Kjeldsen, H., Laughlin, G., Levine, A. M., Lin, D., Lissauer, J. J., MacQueen, P., Marcy, G., McCullough, P. R., Morton, T. D., Narita, N., Paegert, M., Palle, E., Pepe, F., Pepper, J., Quirrenbach, A., Rinehart, S. A., Sasselov, D., Sato, B., Seager, S., Sozzetti, A., Stassun, K. G., Sullivan, P., Szentgyorgyi, A., Torres, G., Udry, S., and Villaseñor, J. (2015). Transiting Exoplanet Survey Satellite (TESS). *Journal of Astronomical Telescopes, Instruments, and Systems*, 1(1):014003.
- Rosotti, G. P., Juhasz, A., Booth, R. A., and Clarke, C. J. (2016). The minimum mass of detectable planets in protoplanetary discs and the derivation of planetary masses from high-resolution observations. , 459(3):2790–2805.
- Rosotti, G. P., Teague, R., Dullemond, C., Booth, R. A., and Clarke, C. J. (2020). The efficiency of dust trapping in ringed protoplanetary discs. , 495(1):173–181.
- Schlichting, H. E., Sari, R., and Yalinewich, A. (2015). Atmospheric mass loss during planet formation: The importance of planetesimal impacts. , 247:81–94.
- Selina, R. J., Murphy, E. J., McKinnon, M., Beasley, A., Butler, B., Carilli, C., Clark, B., Erickson, A., Grammer, W., and Jackson, J. (2018). The Next-Generation Very Large Array: a technical overview. In *Ground-based and Airborne Telescopes VII*, volume 10700 of *Society of Photo-Optical Instrumentation Engineers (SPIE) Conference Series*, page 107001O.
- Shakura, N. I. and Sunyaev, R. A. (1973). Black Holes in Binary Systems. Observational Appearance. *Astronomy and Astrophysics*, 24:337–355.
- Sheehan, P. D. and Eisner, J. A. (2018). Multiple Gaps in the Disk of the Class I Protostar GY 91. , 857(1):18.
- Sierra, A., Lizano, S., Macías, E., Carrasco-González, C., Osorio, M., and Flock, M. (2019). An Analytical Model of Radial Dust Trapping in Protoplanetary Disks. , 876(1):7.
- Simon, J. B. and Armitage, P. J. (2014). Efficiency of Particle Trapping in the Outer Regions of Protoplanetary Disks. , 784(1):15.
- Sutter, P. M., Wandelt, B. D., McEwen, J. D., Bunn, E. F., Karakci, A., Korotkov, A., Timbie, P., Tucker, G. S., and Zhang, L. (2013). Probabilistic image reconstruction for radio interferometers. *Monthly Notices of the Royal Astronomical Society*, 438(1):768–778.

- Sutton, E. C. and Wandelt, B. D. (2006). Optimal Image Reconstruction in Radio Interferometry. , 162(2):401–416.
- Takeuchi, T. and Lin, D. N. C. (2002). Radial Flow of Dust Particles in Accretion Disks. , 581:1344–1355.
- Takeuchi, T., Miyama, S. M., and Lin, D. N. C. (1996). Gap Formation in Protoplanetary Disks. , 460:832.
- Tazzari, M. (2017). `mtazzari/uvplot`.
- Tazzari, M., Beaujean, F., and Testi, L. (2018). GALARIO: a GPU accelerated library for analysing radio interferometer observations. , 476:4527–4542.
- Teague, R., Bae, J., Bergin, E. A., Birnstiel, T., and Foreman-Mackey, D. (2018). A Kinematical Detection of Two Embedded Jupiter-mass Planets in HD 163296. , 860(1):L12.
- Terquem, C. and Ajmia, A. (2010). Eccentricity pumping of a planet on an inclined orbit by a disc. , 404(1):409–414.
- Thompson, A. R. (1999). Fundamentals of Radio Interferometry. In Taylor, G. B., Carilli, C. L., and Perley, R. A., editors, *Synthesis Imaging in Radio Astronomy II*, volume 180 of *Astronomical Society of the Pacific Conference Series*, page 11.
- Thompson, A. R., Moran, J. M., and Swenson, Jr., G. W. (2017). *Interferometry and Synthesis in Radio Astronomy, 3rd Edition*.
- Toci, C., Rosotti, G., Lodato, G., Testi, L., and Trapman, L. (2021). On the secular evolution of the ratio between gas and dust radii in protoplanetary discs. *arXiv e-prints*, page arXiv:2107.09914.
- Tsukagoshi, T., Muto, T., Nomura, H., Kawabe, R., Kanagawa, K. D., Okuzumi, S., Ida, S., Walsh, C., Millar, T. J., Takahashi, S. Z., Hashimoto, J., Uyama, T., and Tamura, M. (2019). Discovery of An au-scale Excess in Millimeter Emission from the Protoplanetary Disk around TW Hya. , 878(1):L8.
- van der Marel, N., Dong, R., di Francesco, J., Williams, J. P., and Tobin, J. (2019). Protoplanetary Disk Rings and Gaps across Ages and Luminosities. , 872(1):112.
- van der Marel, N., van Dishoeck, E. F., Bruderer, S., Birnstiel, T., Pinilla, P., Dullemond, C. P., van Kempen, T. A., Schmalzl, M., Brown, J. M., Herczeg, G. J., Mathews, G. S., and Geers, V. (2013). A Major Asymmetric Dust Trap in a Transition Disk. *Science*, 340(6137):1199–1202.
- Varnière, P. and Tagger, M. (2006). Reviving Dead Zones in accretion disks by Rossby vortices at their boundaries. , 446(2):L13–L16.
- Vigan, A., Bonnefoy, M., Ginski, C., Beust, H., Galicher, R., Janson, M., Baudino, J. L., Buenzli, E., Hagelberg, J., and D’Orazi, V. (2016). First light of the VLT planet finder SPHERE. I. Detection and characterization of the substellar companion GJ 758 B. , 587:A55.

- Williams, J. P. and Cieza, L. A. (2011). Protoplanetary Disks and Their Evolution. , 49(1):67–117.
- Winn, J. N. and Fabrycky, D. C. (2015). The Occurrence and Architecture of Exoplanetary Systems. , 53:409–447.
- Wyatt, M. C. (2018). *Debris Disks: Probing Planet Formation*, page 146.
- Wyatt, M. C. and Jackson, A. P. (2016). Insights into Planet Formation from Debris Disks. II. Giant Impacts in Extrasolar Planetary Systems. , 205(1-4):231–265.
- Yamaguchi, M., Akiyama, K., Tsukagoshi, T., Muto, T., Kataoka, A., Tazaki, F., Ikeda, S., Fukagawa, M., Honma, M., and Kawabe, R. (2020). Super-resolution imaging of the protoplanetary disk HD 142527 using sparse modeling. *The Astrophysical Journal*, 895(2):84.
- Yamaguchi, M., Tsukagoshi, T., Muto, T., Nomura, H., Nakazato, T., Ikeda, S., Tamura, M., and Kawabe, R. (2021). ALMA Super-resolution Imaging of T Tau: $r = 12$ au Gap in the Compact Dust Disk around T Tau N. , 923(1):121.
- Zhang, K., Bergin, E. A., Blake, G. A., Cleeves, L. I., Hogerheijde, M., Salinas, V., and Schwarz, K. R. (2016). On the Commonality of 10-30 AU Sized Axisymmetric Dust Structures in Protoplanetary Disks. , 818:L16.